Imperial College London

Optical and Semiconductor Devices Group

Department of Electrical and Electronic Engineering

Imperial College London

Monitoring System for Long-Distance Pipelines Subject to Destructive Attack

By: Aiman Noorwali

Supervised by: Prof. Richard Syms

A thesis submitted in fulfillment for the degree of

Doctor of Philosophy

March 2022

Declaration of Originality

I certify that all material in this thesis entitled, 'Monitoring System for Long-Distance Pipelines Subject to Destructive Attack', is my original own work under the supervision of Professor Richard Syms. Other material that is not my own has been appropriately referenced and acknowledged.

Aiman Noorwali

Declaration of Copyright

Abstract

In an era of terrorism, it is important to protect critical pipeline infrastructure, especially in countries where life is strongly dependent on water and the economy on oil and gas. Structural health monitoring (SHM) using acoustic waves is one of the common solutions. However, considerable prior work has shown that pipes are cylindrical acoustic waveguides that support many dispersive, lossy modes; only the torsional T(0, 1) mode has zero dispersion. Although suitable transducers have been developed, these typically excite several modes, and even if they do not, bends and supports induce mode conversion. Moreover, the high-power transducers that could in principle be used to overcome noise and attenuation in long distance pipes present an obvious safety hazard with volatile products, making it difficult to distinguish signals and extract pipeline status information. The problem worsens as the pipe diameter increases or as the frequency rises (due to the increasing number of modes), if the pipe is buried (due to rising attenuation), or if the pipe carries a flowing product (because of additional acoustic noise). Any system is therefore likely to be short-range.

This research proposes the use of distributed active sensor network to monitor long-range pipelines, by verifying continuity and sensing small disturbances. A 4-element cuboid Electromagnetic Acoustic Transducer (EMAT) is used to excite the longitudinal L(0,1) mode. Although the EMAT also excites other slower modes, long distance propagation allows their effects to be separated. Correlation detection is exploited to enhance signal-to-noise ratio (SNR), and code division multiplexing access (CDMA) is used to distinguish between nodes in a multi-node system. An extensive numerical search for multiphase quasi-orthogonal codes for different user numbers is conducted. The results suggest that side lobes degrade performance even with the highest possible discrimination factor. Golay complementary pairs (which can eliminate the side lobes completely, albeit at the price of a considerable reduction in speed) are therefore investigated as an alternative.

Pipeline systems are first reviewed. Acoustic wave propagation is described using standard theory and a freeware modeling package. EMAT modeling is carried out by numerical calculation of electromagnetic fields. Signal propagation is investigated theoretically using a full system simulator that allows frequency-domain description of transducers, dispersion, multi-mode propagation, mode conversion and multiple reflections. Known codes for multiplexing are constructed using standard algorithms, and novel codes are discovered by an efficient directed search. Propagation of these codes in a dispersive system is simulated. Experiments are carried out using small, unburied air-filled copper pipes in a frequency range where the number of modes is small, and the attenuation and noise are low. Excellent agreement is obtained between theory and experiment. The propagation of pulses and multiplexed codes over distances up to 200 m are successfully demonstrated, and status changes introduced by removable reflectors are detected.

Acknowledgments

During my PhD studies, I have received great support and assistance that I would like to mention.

First and foremost, I would like to express my deepest gratitude and appreciation to my supervisor, Prof. Richard Syms, head of the Optical and Semiconductor Devices Group, for his dedicated support and immense knowledge. This research would not have been possible without his guidance, motivation, and patience. I have gained valuable knowledge and skills from him that go beyond my PhD.

I would like to give my heartfelt thanks to Phil Jones for his great support and valuable suggestions to design the experiments and make them work. Also, I would like to thank Victor Boddy and Amine Halimi for their appreciated assistance and advice. I am thankful to Dr. Imad Jaimoukha for his kind support. I am also grateful to many more people, staff and students, in the OSD group and in the EEE department for their help.

In addition, my sincere thanks to my sponsor, King Abdulaziz City for Science and Technology in Saudi Arabia. I am really grateful to its people for providing me with this generous opportunity.

Last but not least, my special gratitude to my parents and my little family for their patience, emotional support, and best wishes and prayers.

Contents

List of Figures

List of Tables

Introduction

In this introductory Chapter, gas, oil, and water pipelines will first be reviewed. The importance of monitoring systems will then be highlighted in each domain, especially in countries that are arid and, therefore, heavily dependent on water, and countries that are rich in energy resources, and consequently having an economy dependent on extraction and transportation of oil and gas. This will be followed by a discussion of the risk of terrorism. Pipeline monitoring systems will then be reviewed. And finally, the research gap and aim will be presented.

1 Pipelines

Pipelines have thousands of years of history that go back to the ancient Chinese and Egyptian eras. The industrial revolution improved pumping techniques and facilitated the expansion of long-distance pipelines across continents to transport different products. Today, most cities have underground pipeline networks as a vital component of urban planning, and many countries have thousands of kilometers of underground and above ground pipelines which are used to transport gas, oil, water, and sewage. The importance of pipelines in daily life raises many challenges in pipeline safety and health. Therefore, increasing interest is developing in efficient monitoring systems. Pipeline systems include, in addition to the pipe itself, transported product, pumps, valves, monitoring instruments, bends, branches, supports, and surrounding media. All play a role in integrity.

1.1 Gas, Oil and Water pipelines

Gas and oil pipes vary according to the transported product and the stage of the transportation (for example, from wells to processing units or from processing units to distribution). Figure 1.1 shows an example of modes of transportation from the field to customers [1]. It shows two types of pipelines, for gathering and transmission of product, respectively. Gathering pipes are relatively short and have small diameter (hundreds of meters, with a 50-100mm diameter). Transmission pipes are very long (hundreds of kilometers, with a diameter of 300-600 mm for gas and 1000-1220 mm for oil). Distribution and plant pipes are shorter and smaller and have more types of supports and fittings such as bends, elbows, tees, and branches.

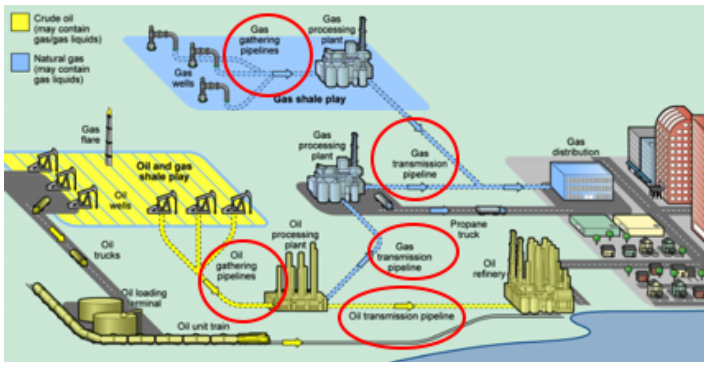

Figure 1.1: Gas and oil transportation systems. Transmission pipelines and gathering pipelines are highlighted with red circles [1].

Generally, pipes are made of metals such as iron, copper, carbon steel, and stainless steel or non-metallic materials such as poly-vinyl chloride (PVC), fiberglass, or concrete. In the US, 98% of natural gas pipelines are carbon steel. The rest are made of polyethylene (PE) and cast iron [2]. Oil pipelines are steel or fiberglass. Gas pipelines have compression stations every 50-100 miles, while oil pipelines require regular pumping stations to move a viscous product. Both have valves and fittings made from the pipe material. Gas and oil pipelines are either installed above ground or buried underground (as required by government regulations, environmental restrictions, and land topography). Underground pipes are supported by a sand pillow or spray-in foam to protect them from ovality and denting and to elevate the pipe in rocky trenches. For overground pipes, support is provided by regular mechanical arrangements such as anchors, rests, or guides. Thus, the area of support contact is much larger in underground pipes. Moreover, oil pipes are bigger and heavier than dry gas pipes, and consequently require stronger and more frequent supports. Figure 1.2 shows typical examples of overground, underground, and plant pipes [4 - 6].

a)  b)  c) 

Figure 1.2: a) Over ground gas pipelines, b) underground water pipeline and c) plant pipes [4 - 6].

Water pipeline networks contain pumping stations, terminal stations, mixing stations, reservoirs, vent and drain stations, and closing valves in addition to pipes. The pipes are larger, with an average diameter of 1-2 m. Many different materials are used, including cast iron, ductile iron, steel, polyethylene (PE), PVC, glass-reinforced plastic GRP and concrete [3]. Because of their large size, they generally require continuous burial and more frequent above-ground supports than gas and oil pipes.

Finally, the transported product has special physical and chemical properties in addition to density and volume, such as viscosity, flammability, and explosivity. This can affect the overall design; for example, gases need different pumping specifications than high viscosity liquids. Since gases are highly pressurized and oil is highly flammable, gas and oil pipelines have more safety concerns than water pipes.

1.2 Importance of pipeline monitoring systems

Continuous monitoring is required to maintain the integrity of the pipe and its transported product. Integrity is vital when transporting economic necessities such as gas and oil or life necessities such as water. In the literature, non-destructive testing (NDT) and structural health monitoring (SHM) fields are increasingly concerned about the integrity of pipes and monitoring methods. NDT includes analysis methods to evaluate the properties of a material without disturbance while SHM monitors the integrity of structures continuously. Before exploring monitoring methods, this section will emphasize the importance of pipe monitoring systems by discussing hazards and their consequences. Special attention is devoted to pipelines in arid and gas and oil-dependent countries. Lastly, the problem of terrorism will be discussed.

1.2.1 Gas and Oil Pipe Hazards

Explosions and health hazards are associated with gas and oil pipeline damage and leaks in addition to the obvious economic loss. Many disastrous events have been caused by leaks of flammable products. For instance, 52 people were killed by an explosion of a gas pipeline in 1978 in Mexico. An oil pipe explosion in the same country in 2010 killed 27 people and injured more than 50. A gasoline pipeline explosion in Mexico killed 96 people in 2019. Another gas pipe incident in the U.S. killed 1 and injured 5. In Malaysia, a gas pipeline explosion resulted in an evacuation of many villagers in 2014 [7]. In addition, inhalation of

gases like ethane, propane or natural gas from damaged pipes can be substantially harmful or even fatal. Therefore, assuring the safety of gas and oil pipeline infrastructure has become a critical need for the energy sector.

1.2.2 Water Pipe Damage

The main issue with damage to water pipes is waste, potentially leading to a catastrophic water shortage. Although some countries are blessed with an excessive amount of freshwater, others face water scarcity. Figure 1.3 shows data from the Food and Agriculture Organization (FAO) of the United Nations (UN) for total renewable water resources per capita in different countries [8]. The table shows how much renewable water a country has, including precipitation, surface, and underground water. Countries are chosen to highlight the difference between fortunate and unfortunate countries. Arabian Peninsula countries such as Saudi Arabia, the United Arab Emirates and Kuwait depend very heavily on desalinated water to cover their freshwater needs. Multiple water pipe burst events in countries facing water scarcity have circulated in recent news [9]. In each case, the incident took days to be repaired which is a long time for such an essential product.

a)

Country	Total renewable water resources per capita (K m3/inhab/year)
Egypt	637.1
Chad	3256
Libya	111.5
Morocco	843.6
Mauritania	2802
Niger	1711
Nigeria	1571
Somalia	1363
Italy	3199
Kuwait	5.139
Qatar	25.95
Saudi Arabia	76.09
Emirates	16.38
Yemen	78.26

b)

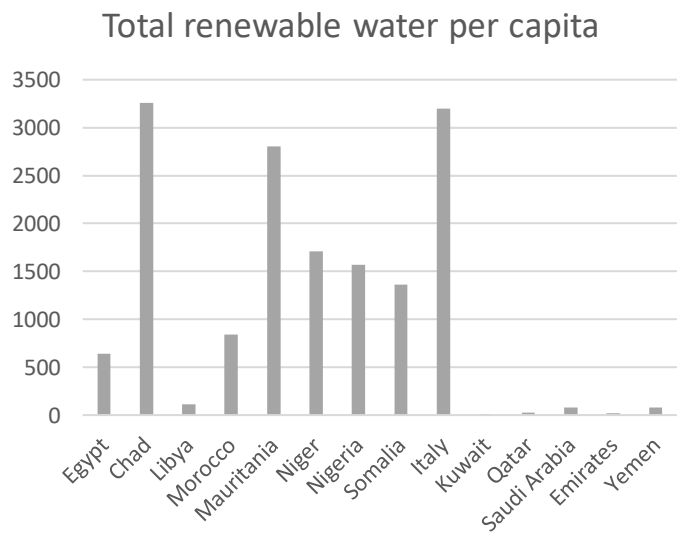

Figure 1.3: FAO data in a) numerical form and b) as a bar chart of total renewable water resources per capita in different countries [8].

1.2.3 Critical pipeline networks

Several countries with scarce water supplies are also economically highly dependent on energy resources; examples include Saudi Arabia, Kuwait, Emirates, Qatar, and Libya. Hence, their gas, oil and water pipelines networks are critical both the welfare of their population and for their economy [10].

Saudi Arabia is a good example of a country that can be harmed seriously by damage to gas, oil, and water pipelines. Its area is 2.15 million km with a population of 32.5 million that is expected to grow to 42 million by 2040 [8]. Saudi is the second-largest holder in the world of proved oil reserves and the largest exporter of petroleum. The country's economy is highly dependent on oil and gas, representing 75% of total export and 60% of revenue [10]. To highlight the gas and oil infrastructure, according to the Central Intelligence Agency (CIA), Saudi has 10,600 km of gas and oil pipelines [11] that cross from East to West and North. A small part of the oil and gas pipeline network is underground, and the rest is above-ground. Figure 1.4.a shows the gas and oil network in Saudi Arabia [10]. The map shows 7 refineries distributed in East and West coasts with pipelines between them. In February 2020, Saudi announced an investment of $110bn to develop the Jafurah Field which is expected to be the largest gas field in the world [12].

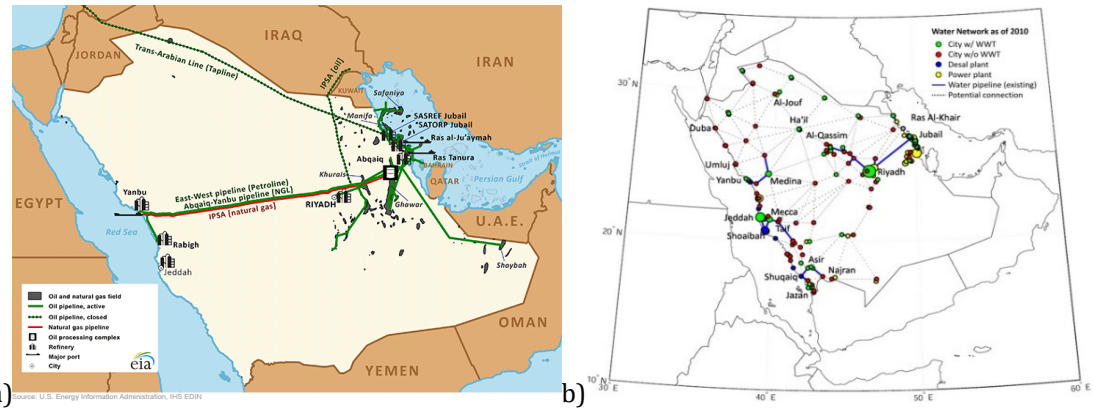

Figure 1.4: Saudi Arabia: a) oil and gas infrastructure, b) current/future water networks [10].

This arid country has no rivers or other natural freshwater sources except rain and underground water. Drinkable water is provided by desalination of seawater, making Saudi Arabia the largest desalinated water producer in the world [8]. Total water demand is 18.51

billion cubic meters per year (BCM/year) in 2009. 11.6 BCM/year is consumed from non-renewable groundwater sources, which are depleting in an alarming rate [13]. Consequently, water in Saudi is extremely precious and any threat to water resources is taken seriously. The country has 27 desalination stations. The current network of water pipelines is at the maximum length of 932 km. Figure 1.4.b shows the current and future water pipeline network which is covering most populated cities.

In contrast, some countries are rich in water and energy resources. Examples include the Russian Federation, the largest country by landmass and producing more than 10M oil barrel per day with half of its exports in energy, and Canada, the second-largest country, producing 4.8M oil barrel per day [14]. Both have a vast gas and oil pipeline network with 251,800 km of pipelines in Russia and 110,000 km of pipelines in Canada. Other large pipeline networks are in China, which has about 213,000 km of gas and oil pipelines, and Venezuela, which has over 16,000 km of gas and oil pipelines [10]. These examples show that pipeline monitoring systems are significant for many countries around the world.

1.2.4 Terrorist Attacks

Because of their significance and extended nature, pipelines are particularly vulnerable to terrorist attacks. Researchers from Carnegie Melon University and Igarapé Institute think tank developed maps that show the number of deaths from terrorism for the last 20 years [15]. The red areas in Figure 1.5.a represent deaths by terrorist attacks in 2016, demonstrating that North Africa, Europe, and South and East Asia are targeted the most. There have been more than 60 terrorist attack incidents in Saudi Arabia since 2001 [19]. In the Global Terrorism Database, an open-source database to record all terrorist events since 1970, 1558 terrorist attacks on pipelines are recorded, mostly in the Middle East, Sub Saharan Africa, and South Asia [16]. Figure 1.5.b shows the rise of pipeline terrorist attacks in recent years. Figure 1.5.c shows an example of a gas pipe explosion in the US in 2010 [18]. Figure 1.5.d shows a 2019 attack on Saudi gas and oil infrastructure by drones [17]. Figure 1.5.e shows a water pipeline blast in the recent war in Libya which interrupted the water supply to the capital Tripoli [19]. All illustrate the increasing threat posed by terrorism, particularly in countries already dependent on the energy sector or facing water scarcity.

a)  b) 

c)  d) 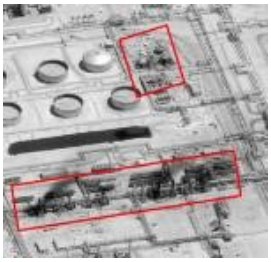 e) 

Figure 1.5: Terrorist attacks: a) deaths in 2016 (Igarapé 2017) [15], b) Terrorist attacks on pipelines from 1970 [16], c) An explosion in a gas pipeline in the US [18], d) an attack on Saudi gas and oil infrastructure [17], e) an attack on a water pipeline in Libya [19].

1.3 Pipeline Monitoring Systems

Different abnormalities can affect pipelines such as damage, leaks, bursts, blockage, and corrosion. Here, the focus will be on monitoring continuity and anticipating potentially deliberate damage. Figure 1.6 illustrates the general monitoring process. When a destructive event or a potentially dangerous change occur on the pipe, a signal is generated. This signal can be detected and processed to extract information about the event and its location. In the literature, little attention has so far been paid to monitoring systems for structural damage in pipes. Any such studies (mostly on the effects of earthquakes or permanent ground deformation (PGD)), mainly focus on precautionary solutions such as pipe material selection or tolerant designs. In contrast, leak detection methods have been very well researched. NDT and SHM overlap with leak detection methods when concerned specifically with pipes. We therefore now briefly review the potential for adapting leak detection methods.

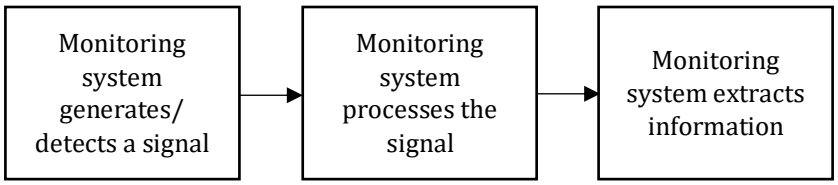

Figure 1.6: Major functions of a general monitoring system.

Pipeline monitoring methods can be separated into two groups appropriate for gas and oil pipe and water pipes. They can also be divided into hardware-based methods (generating and detecting a signal) and methods using software tools (processing and extracting information). Thus, most computational methods utilize a minimum of hardware methods for sensing.

For hardware-based methods, pipeline monitoring systems general exploit acoustic, hydraulic, or electromagnetic signals [20-24]. A century-old paper [25] reviewed primitive detection methods for underground pipes such as observing luxuriant growth of vegetation, using sound rods in direct contact with the pipe or similar devices to observe changes in pipe noise caused by changes inflow. More advanced techniques to detect leaks without localization include analyzing hydraulic readings of pressure and flow in steady state [26] or transient situations [27]. However, damage and leaks are still often identified by non-technical methods such as patrolling and inspecting over-ground pipes or using sniffer dogs to detect gas leaks. In the following, monitoring methods for general pipelines will be reviewed with a focus on acoustics.

1.3.1 Acoustic Pipelines Monitoring Methods

The most-commonly used signal for monitoring systems is acoustic, which can be used not only to detect a change but to locate it as well. Acoustic waves propagate either as bulk waves or as surface waves. Famous scientists and engineers who have worked on wave propagation in elastic solids include Stokes, Poisson, Rayleigh, Navier, Hopkinson, Pochhammer, Lamb, Love, Davies, Mindlin, Viktorov, Graff, Miklowitz and Auld [28]. Many theoretical studies have covered acoustic propagation in pipes [29-31]. Jacobi studied transmission along axisymmetric liquid cylinders with rigid, thin, liquid, and pressure-release walls. Greenspon [32] described acoustic propagation in nonaxisymmetric hollow pipes. Gazis [33] studied the characteristics of wave propagation and energy distributions

in nonaxisymmetric cylindrical elastic shells filled with fluid. Fuller et al. [34] studied leak noise propagation and attenuation in submerged plastic water pipes.

The earliest acoustic methods for detecting leaks simply observed sound changes in oil [35] or gas [36] pipes. A related technique known as acoustic emission (AE) analyzed elastic waves emitted from defects in the structure or pipe [37]. Although this technique is passive, it is used for monitoring structural health in addition to leaks. More advanced methods use acoustic transducers to excite and detect acoustic waves. Common transducers include piezoelectric and electromagnetic types. In fact, acoustic NDT was not possible until the Curie brothers discovered the piezoelectric effect in 1880 [38]. One of the earliest examples of acoustic NDT dates from 1949, utilizing acoustic longitudinal waves on concrete plates [39]. Subsequent investigations have involved steel [40] or aluminum [41, 42] plates, and pipes in similar materials [43, 44]. Internally generated guided waves have been used for pipe inspection [45] and transducers arrays have been used to reduce the number of modes excited [46, 47].

A brief introduction to transducers and wave propagation now be given; these will be covered in more depth in later Chapters. An electromagnetic acoustic transducer (EMAT) consists of a permanent magnet and an induction coil. It generates acoustics in metals using one of three different mechanisms: Lorentz force, magnetization force, or magnetostriction. Piezoelectric transducers are based on piezoelectric crystals or ceramics that change their shapes when an electric field is applied on them in a reversible process. Figure 1.7 shows a simplified view of both types. Both can generate bulk, surface, or guided acoustic waves and guided waves are a major growth area for NDT [28].

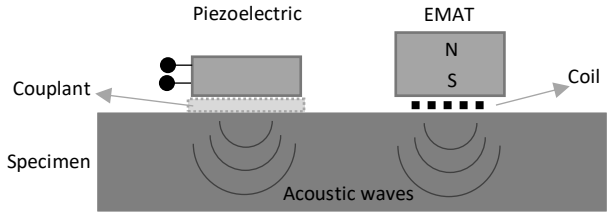

Figure 1.7: Piezoelectric and EMAT acoustic transducers.

The propagation of guided waves in plates, rods, and pipes is susceptible to attenuation, dispersion and multimode effects, and reflection from discontinuities. The pipe material and the contact between the pipe and its surround both cause attenuation. Metallic materials have lower attenuation. Attenuation increases with frequency, and flowing contents generate acoustic noise, leading to a low signal-to-noise ratio. There are generally multiple propagating modes, either excited directly by the transducer or by mode conversion effects. Longitudinal and flexural modes are dispersive while the torsional mode T(0,1) is non-dispersive. The number of modes rises when the size of the pipe and the frequency increases, or when the walls of the pipe are flexible. The surrounding medium (e.g. sand in buried pipes) and liquid fill (water or oil) also affect the number of modes and their dispersion [48], However, coating with a viscous material can reduce leaky modes. In contrast, gas fills leave dispersion characteristics largely unaffected. However, interaction with different features in the pipe such as welds, bends, and defects generally cause reflections and mode conversion.

In gas, oil and water pipes, the pipe fill is normally used for acoustic wave propagation [53]. A recent study [49] reviewed detection by acoustic signals, which have significantly better performance in metal pipes than plastic ones. Watanabe et al. [22] considered a gas pipeline as a wind instrument, and measured inlet-outlet pipeline variables such as pressure and flow rate and the changes to the impulse response caused by a leak. Distributed monitoring units along the pipeline were proposed in [50]. The system could discriminate between leaks and man-made and non-leak signals up to 300m in a buried pipeline of 40 miles, 7 inches inner diameter, and 0.5 inches thickness. Weiguo et al. [51] validated the feasibility of detecting leaks in gas pipelines in transient and continuous cases. They transmitted a low-frequency acoustic signal in a long compressed-air pipe with a piezoelectric transducer. Figure 1.8 shows their experimental setup, which contains a transducer connected to signal sampling and storage, a 400 m-long tube connected to an air pump, and some galvanized pipe. However, the leakage rate in a transient case needed more analysis to distinguish it from position and time effects.

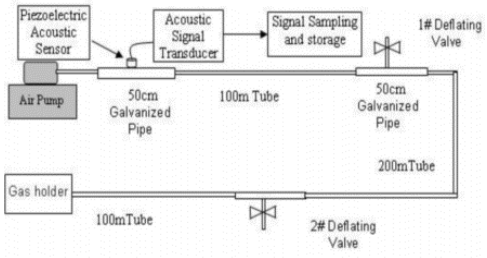

Figure 1.8: Lab-based monitoring system for a compressed air pipeline [51].

Xu et al. [52] developed a leak detection system based on aeroacoustics. They used the Wavelet Packet Transform method and Fuzzy Support Vector Machine pattern classification and demonstrated that the system can identify small leaks while avoiding false alarms. Figure 1.9 shows schematics and photographs of their lab setup.

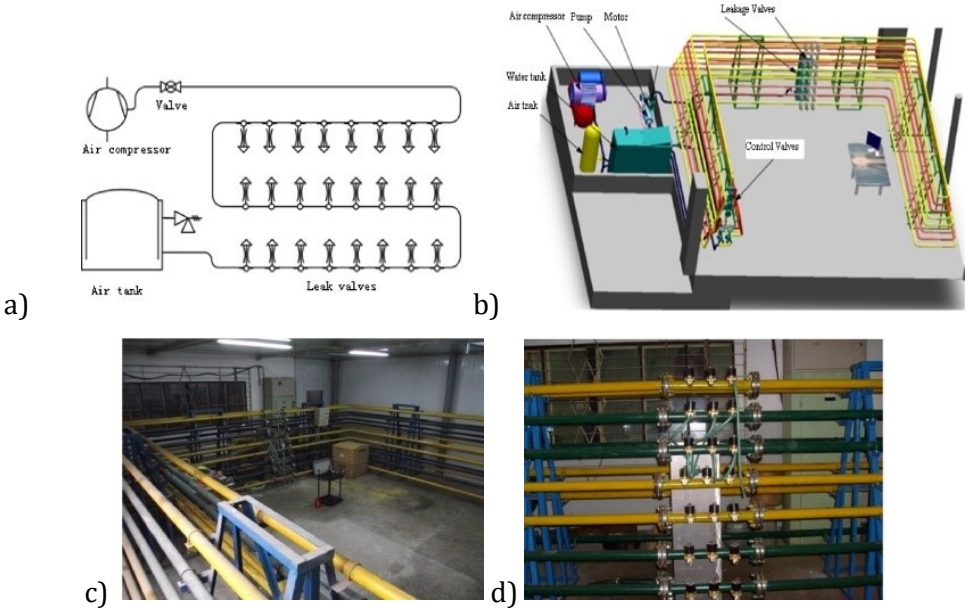

Figure 1.9: a) Experiment to detect small leaks consists of gas pipe, leak valves, air compressor and air tank, b) Lab setup 3D drawing, c) and d) lab setup [52].

Non-metallic pipes have also been studied [53, 57], For example, [57] studied the characteristics of acoustic leak signals in water plastic pipes and showed that attenuation becomes negligible in low frequency. Their test setup used 200 m buried polyvinyl chloride (PVC) pipe, 2 fire hydrants, and a piezoelectric accelerometer as a vibration sensor and hydrophone as an acoustic sensor. Sensors were connected to a digital tape recorder and PC processor to perform anti-aliasing filtering, analog to digital converting, FFT, and cross-

correlation. In fact, sensors, filters, and digital processors are the major units in any monitoring system. Figure 1.10 shows photographs of the setup; a) shows a piezoelectric accelerometer attached magnetically to the top surface of fire hydrants and b) shows a hydrophone attached to fire hydrants through a special pipe fitting.

a) 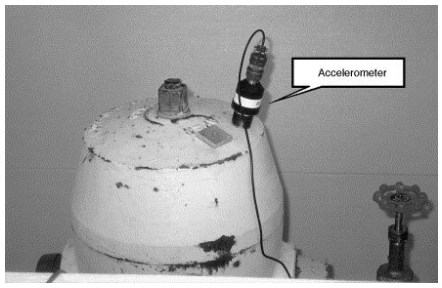

b) 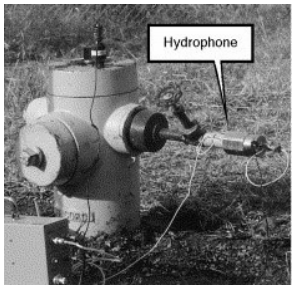

Figure 1.10: Attachment of a) an accelerometer and b) a hydrophone to a fire hydrant that is connected to a buried PVC pipe [57].

1.3.2 Other Pipeline Monitoring Methods

The use of electromagnetic (EM) waves for pipeline monitoring and change detection has received little. However, the propagation of EM in tunnels, which share some similarities with pipelines, has been studied [54]. Different models such as modal theory, exact resolution of Maxwell's equation, ray concept, and measurement results have been used to analyze EM propagation. Leak detection has been demonstrated in an iron water pipe using an EM sensor, but without localization [56]. Figure 1.11 shows their lab setup which consists of a vertical cast iron pipe filled with water. The pipe has a length of 1.5 m and is cracked from the middle. An EM sensor at the top is connected to a vector network analyzer. A study of EM propagation at 2.4-2.5 GHz shows that the attenuation of EM waves in water pipes is very high in comparison with air and oil pipes due to the conductivity and permeability of the medium [55]. Despite this, little attention has been paid to EM propagation in non-metallic pipes like GRP.

Figure 1.11: Lab setup for EM detection of leaks in a cast-iron pipe [56].

Another method used for pipeline monitoring is ground penetrating radar (GPR), which can penetrate through solid material [58]. GPR uses electromagnetic waves (EM) to detect changes in buried pipes of any material by identifying reflections from product-saturated soils around leaks. However, sites with soft or wet clay can pose difficulties because of their conductivity and attenuation [58], and interpretation of GPR data is often subjective.

Infrared thermography is another common monitoring method, which identifies thermal changes that are inconsistent with the expected pipe temperature. Leaks can be detected by computer-enhanced thermography from mobile vehicles, helicopters, or man-portable systems for several miles [59]. However, there are many challenges for accurate detection in real applications due to geographic and climatic factors.

Autonomous detection methods can be based on static sensor networks or mobile sensors carried by a flow. Wireless sensor networks have been developed to collect hydraulic and acoustic data [60]. Figure 1.12 shows their laboratory rig which consists of a PVC pipe, sensor motes, and a wired data acquisition unit for reference. The motes are battery powered and have accelerometers and Intel mote nodes for data acquisition, storage, local processing, and GPS wireless communication for time reference. A framework of a wireless sensor network is presented with multiple network architectures and routing protocols in [61]. Jawhar et al. [62] introduced the TriopusNet monitoring system, which installed sensor nodes autonomously from a central repository using water flow and attached them to

targeted locations. Although autonomous sensors appear an elegant solution, many factors must be considered for them to be deployed cost-effectively outside the laboratory.

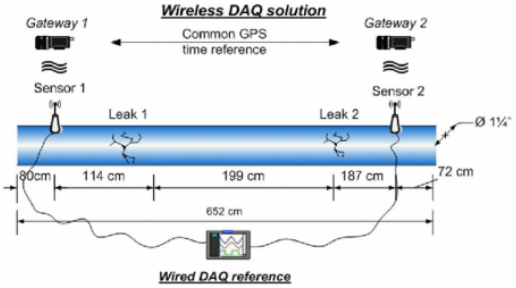

Figure 1.12: Autonomous sensor system including PVC pipe, motes with wireless time reference, and wired data acquisition unit [60].

Other leak detection methods include chemical sensors, which can detect specific gases by a semi-permeable sensor tube near the pipeline [52], and optical fiber sensors. Optical fibers can be used with acoustic waves or temperature to detect and locate a change. For example, a distributed fiber optic acoustic sensor adapted a Sagnac interferometer commonly used in fiber optic gyroscopes to measure and locate a leak in fluid-filled high voltage distribution pipes [63]. The fibers are placed inside the pipe and used to listen to the sound of leaks. Another optical fiber application is distributed temperature sensing (DTS). As the optical fiber runs the whole length of the pipe, a continuous temperature profile can be obtained rather than a set of discrete points. The fiber glass is sensitive to temperature, which causes light scattering at the leak point [64].

In addition to hardware methods, there are also computational monitoring methods. For example, Shibata et al. [7] proposed the FFT method to detect pipe leak positions through analysis of data obtained at a given distance from the leakage point. Adrian-Martinez et al. [65] used cross-correlation for acoustic signal detection. Gao et al. [66] proposed a differentiation method to cross-correlation for a leak signal to increase its sensitivity. The Haar wavelet transformation of a negative pressure signal caused by a leak has been used to overcome noise [67]. The harmonic wavelet has been used to identify small leaks in high noise [68]. Wang et al. [69] used Kalman filters to extract pressure wave inflection information, and Lay-Ekuakille et al. [70] proposed a filter diagonalization method (FDM) as an alternative to FFT for leak detection.

1.4 Discussion of Monitoring Systems

From the above, two things can be concluded. First, few methods monitor structural damage; most are for leak detection. However, leak detection methods can be exploited to generate or detect signals and process them to anticipate, detect, and locate a destructive event. Second, although most methods are been used for some time, each has a significant limitation. For example, GPR is not efficient for long-distance pipelines; neither is infrared thermography. Fiber optics and DTS are vulnerable to blast events since they also require continuity. More importantly, all these techniques except AE and DTS work on filled pipes as they use the pipe fill to carry information. Table 1.1 summarizes current methods. Acoustic methods are the most suitable for further exploitation, due to the possibility of long-distance propagation. However, acoustic waves are susceptible to multimode effects, dispersion, the effects of surrounds and fills on propagation, and noise. Distributed sensor networks may also be useful, as they do not require full continuity, and can compensate for the propagation range of acoustic waves.

Method	Strength	Limitations	References
Acoustic waves	Low attenuation at low frequency. AE doesn't rely on pipe fill	Multimode propagation, mode conversion, dispersion	[29 - 53, 57, 71]
Electromagnetic waves	Non-dispersive	Needs conductive materials and has high attenuation	[54 - 56]
Ground-penetrating radar	Timely detection of damages and comprehensive information	Restricted to buried pipes, not efficient for long-distances; lengthy image processing	[58]
Infrared thermography	Fast response	Impractical in remote areas; low-noise immunity;	[59]
Autonomous sensors	Enable real-time monitoring. Wireless distributed sensors do not rely on pipe continuity	Many factors to be considered such as cost, size, and power.	[60 - 62]
Fiber optics	Provide a continuous profile of the pipe temperature. DTS doesn't rely on pipe's product,	Require full continuity	[63 - 64]
Computational methods	Can enhance signals in noisy and dispersive pipes	Requires hardware sensors and computational power	[7, 65 - 70]

Table 1.1: Summary of pipeline monitoring methods.

A hypothetical example will demonstrate the inability of conventional monitoring systems to detect destructive events where the pipe has sustained severe damage in multiple locations. Let us assume a long pipeline that is located between two compression or pumping stations. Then, assume a destructive event has occurred somewhere along the pipe, conventional monitoring methods could locate the damage effectively from one of the stations. If further damage occurred elsewhere along the pipe, the other station can compress or pump products and locate the second damage site. However, if the first event has emptied the pipe or interrupted a wired monitoring system, subsequent damage will be undetectable. Furthermore, existing systems are unlikely to anticipate a potential attack by detecting the change caused by (for example) attaching explosives to a pipe wall. This limitation exists in empty or full pipes due to the poor signal to noise ratio induced by the change.

Previously mentioned problems of acoustic modes, attenuation and dispersion can be mitigated by choosing a proper pipe type. In addition, a thorough comparison can be found in [71] of longitudinal mode attenuation in 5 mm steel pipes filled with various products such as air, water, diesel oil, castor oil, and glycerin up to 5 MHz. Air-filled pipes have the lowest attenuation in the evaluated range with 6.89 dB at 1 MHz, while diesel oil-filled pipes attenuation is 16.61 dB, and water-filled pipes attenuation is the highest among the three with 21.49 dB at the same frequency. Table 1.2 summarizes earlier details of pipeline types and acoustic challenges. Underground pipes suffer from high attenuation, since the area of contact with trench material. Moreover, laminar and turbulent flows will generate noise. Turbulent flow (expected near compression and pumping stations) is likely to cause mode conversions as well. Mode conversions and reflections can also be caused by above-ground supports. However, above-ground gas pipes are lighter and have less frequent supports. They are also smaller, and consequently support fewer modes. Rigid metallic above ground gas pipes have lower attenuation and fewer modes. On the other hand, due to the high inflammability or explosivity of the products in gas and oil pipes, industry has strict electrical safety rules on the sensors and monitoring systems designs. Considering all these aspects, small diameter, above-ground metallic gas pipes are suitable for this research.

Type	Size	Material	Method of Support	Attenuation	Effects of fill and surround	No. of Modes	Dispersion	Mode conversion
Gas	Small (300-600 mm)	Metallic (carbon steel) or non-metallic (PE)	Above or underground	Lowest for metallic (7 dB for 5 mm steel pipe)	No, for above ground No, for above ground	Low (2-15 modes below 100 kHz for 15mm Cu pipes)	Yes, for L and F modes. No dispersion for T modes	Yes, for above ground or in turbulent flow
Oil	Big (1000-1220 mm)	Metallic (steel) or non-metallic (fiberglass)	Above or underground	Medium for metallic (17 dB for 5 mm steel pipe)	Yes Yes	High (2-40 modes below 100 kHz for 15mm Cu pipes)		
Water	Biggest (1000-2000 mm	Metallic (cast iron, copper) or Non-metallic (concrete, GRP)	underground	High (22 dB for 5 mm steel pipe)	Yes Yes	High (2-40 modes below 100 kHz for Cu 15mm pipes)		

Table 1.2: Comparison between different gas oil and water pipe types and their acoustic characteristics [1 - 6, 29 - 53, 57, 71].

1.5 Research Aim and Conclusion

The importance of protecting critical pipeline infrastructure in an era of terrorism, has been highlighted. A review of pipeline monitoring systems has been presented including the acoustic method, one of the most common solutions. However, there is a gap in the literature in addressing severe damage problems, particularly destructive attacks. The limitation in current systems is mainly due to the use of flowing products either as a signal carrier or sensing object. This product could be absent in destructive attacks. Moreover, acoustic propagation suffers from the dispersion nature of the pipe and the lossy modes generation and conversion which make it difficult to disentangle signals and extract information. The problem worsens as the diameter increases or as the frequency rises (more modes), if the pipe is buried (higher attenuation and leaky modes), or if the pipe carries a flowing liquid (noise and more modes).

Accordingly, this research will develop an approach that may remain functional in destructive attacks and effective in remote areas based on acoustic wave propagation in pipe walls. To mitigate problems associated with multiple modes, high attenuation, and noise, work will be carried out with small, unburied metal gas-filled pipes. Such pipes are suitable for lab experiments using electromagnetic acoustic transducers EMATs, and experimental data is likely to confirm theory. A frequency range will be used where the number of modes is limited, and the dispersion of some modes is low. Sensing in

transmission or reflection schemes may then be used to verify continuity and mode conversion to detect disturbances and scattering events. This approach will be implemented in a distributed sensor network, using a code division multiplexed (CDMA) in-pipe communication scheme among sensor nodes to distinguish signals from different nodes via correlation detection. Quasi orthogonal codes and complementary pairs may be exploited to improve multi-node discrimination performance and signal to noise ratio.

Figure 1.13 shows the basic concept. Distributed sensors network sends and receives multiplexed acoustic signals along pipe walls. Each node has a code that is different from its neighbors. The number of nodes that has a unique code can be selected based on the attenuation. Let's assume a case where attenuation allows every node to hear only the 2 neighbors. Consequently, in Figure 1.13.a, transmissions from node *n*-1 will only reach nodes *n* and *n*-2. In Figure 1.13.b, when node *n*-1 and node *n*+1 transmit their codes simultaneously, node *n* must distinguish between them to verify the pipe continuity. In addition, the node could also receive back scattered signals (grey arrows). In Figure 1.13.c, when there is a break between nodes *n*-1 and *n*, node *n* will no longer receive the code of node *n*-1, while node *n*-1 will receive its echo. Thus, three distinguishable codes (orthogonal) are required. However, the system can be more complicated in a low attenuation case, where transmissions from nodes *n* can reach as far as nodes *n*-2 and *n*+2 or more. The distinguishment of multi-node can also be exploited in partial breaks or changes that create extra signals.

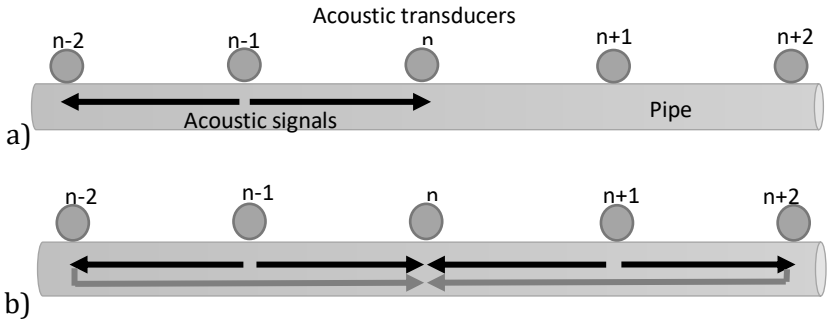

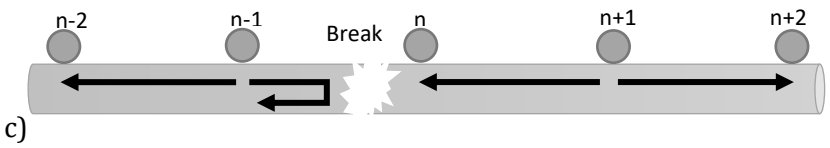

Figure 1.13: Proposed multiplexed distributed monitoring system: a) transmission from node n-1, b) transmission from nodes n-1 and n+1, c) after a break occurs.

Figure 1.14 shows the basic building blocks of a multiplexed communication system. At the transmitter, the signal is encoded, up-converted and amplified, transduced into the acoustic domain using an EMAT, and then propagated through the pipe. At the receiver, the signal transduced back to the electrical domain, down-converted and decoded by correlation detection. Additional software is then used to extract pipe status information.

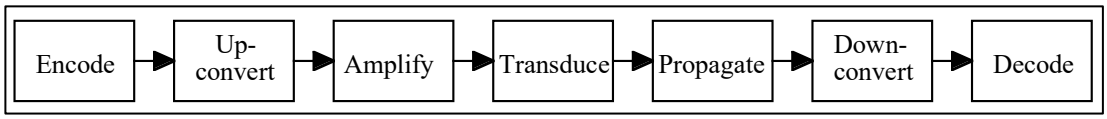

Figure 1.14: Basic block diagram of a multiplexed communication system.

For example, Figure 1.15 presents a further example showing 4 possible timing diagrams involving transmission between adjacent nodes. Figure 1.15a shows the pipe itself in a transmission scheme. Figure 1.15b shows the ideal case, where a single mode with no dispersion and limited attenuation is excited using a pulse at $t = 0$. This pulse will be received at time T, but may in a low-attenuation system be reflected back and received again at time $3T$. The received pulse has a lower amplitude than the transmitted pulse due to the attenuation, while the multiply reflected pulse has a lower amplitude still.

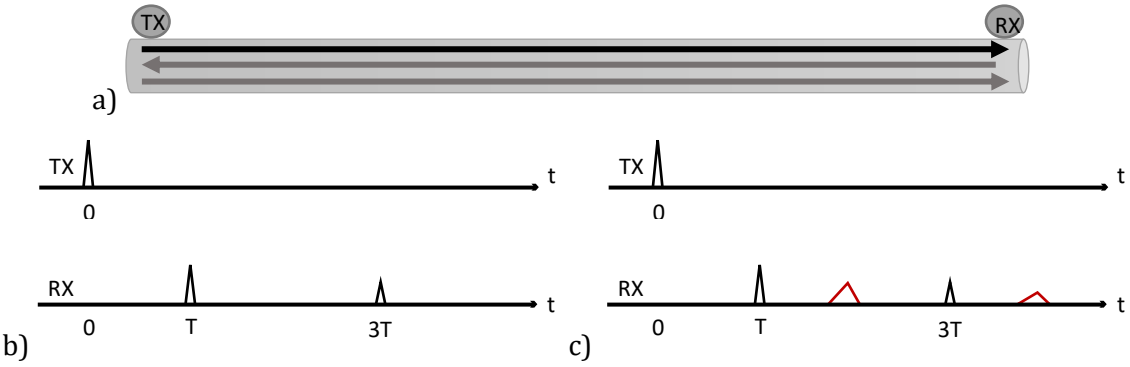

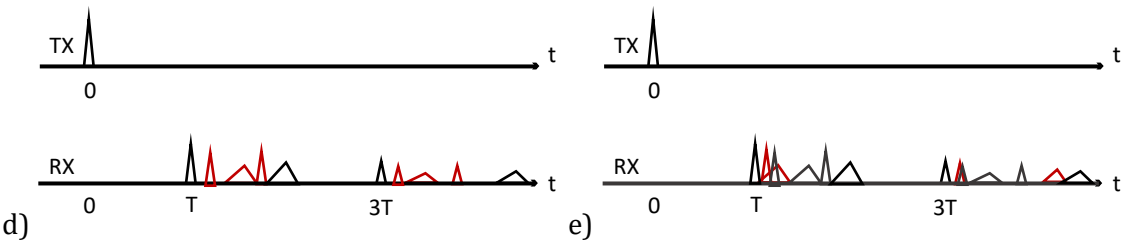

Figure 1.15: a) Pipeline communication system in a transmission scheme; time diagrams of pulse transmission in b) ideal case, c) a 2-moded system, d) a 2-moded system with a joint, e) effect of a change.

Figure 1.15c shows an even more realistic example. Now, two modes are launched by the transducer. One might be the L(0,1) longitudinal mode, which has a relatively high group velocity and little group dispersion at low frequency. The other might be the F(1,1) flexural mode, which has lower velocity and higher group dispersion. The red signals show that the F(1,1) components appear as a delayed, dispersed copies of the main signal. Figure 1.15d shows a more realistic example still, when there is a joint or support that converts the signal from one mode to another (either from L(0,1) to F(1,1) or vice versa) in addition to act as a reflector. Therefore, two converted modes of various velocities and at least one reflection might appear in the time diagram together with their delayed echoes. Finally, Figure 1.15e shows that additional signals may appear if there are any changes to the pipe. In principle, this change may be detected. However, the effects of dispersion, mode conversion and reflection rapidly make the problem complicated. Moreover, more spurious signals may exist in a multi-node system where codes are transmitted instead of pulses. These codes if they are not perfectly orthogonal may have side lobes signals which overlap with other signals resulting in complicating the problem further. Figure 1.16 shows the pipe in a reflection scheme. All previous effects may happen in this scheme as well. Since the signals travel longer, inferior signal to noise ratio is expected because of higher attenuation and dispersion while the overlaps are less severe.

Figure 1.16: Pipeline communication system in a reflection scheme.

The remaining chapters of this thesis will present in detail the building blocks of the proposed system, including numerical and experimental implementations. Chapter 2 will first review the principles of acoustic wave propagation in cylindrical waveguides including acoustic modes, dispersion characteristics and effects of bends, defects and other surrounds. A freeware numerical solver will be used to compute dispersion curves for small diameter pipes. The chapter will highlight the possibility of limiting the number of modes and reducing dispersion by controlling the pipe diameter and the frequency. Chapter 3 will discuss the principles of piezoelectric and electromagnetic acoustic transducers, with a focus on EMAT design including analytical and numerical model for coils and permanent magnets. The results will show that 4-element cuboid EMAT predominantly excites the longitudinal L(0,1) mode. An attempt to shape the cuboids to improve magnetic field uniformity results in weakening the field strength, potentially allowing design tradeoffs.

Chapter 4 will develop analytically and numerically a dispersion-less signal propagation model, containing additional features such as multiple reflectors. The ability to enhance SNR by correlation detection using a matched filter and increase the processing gain by increasing the bit rate will be highlighted. A more realistic model containing transducer responses, dispersion, multi-mode propagation and mode conversion will then be developed. The numerical results will emphasize the necessity for pulse compression to increase SNR, and reduce signal overlap effects.

Chapter 5 will first introduce techniques for pulse compression and multiplexing in asynchronous CDMA. The most common bipolar pulse-compression codes - Barker codes - will first be reviewed. An efficient algorithm will then be constructed to search for analogous quasi-orthogonal (QO) multiphase codes capable of supporting 2-4 users in a multimode system. The most effective sets are shown to be based on six-phase codes. However, because of the side lobes inherent in any QO system, discrimination is limited. Golay complementary pairs (GCP) are then presented as an alternative that provides full orthogonality, at the price of significantly increasing the number of codes that must be transmitted. Chapter 6 presents a full system model of QO and GCP code propagation in a dispersive system with multiplexing communication. The results confirm that QO multiphase codes are likely to allow rapid communication between nodes, while GCPs are more appropriate for accurate sensing of pipe status.

Chapter 7 describes laboratory apparatus to demonstrate coded propagation, and compares the results with earlier theoretical predictions. Excellent agreement validates the analysis presented in previous chapters, and the results confirm the first aim of the thesis, namely a system to verify the continuity of long-distance pipelines using active acoustic sensor nodes, despite the adverse effects of noise, dispersion, multimode propagation, mode conversion and multiple reflections. Chapter 8 investigates the second thesis aim, namely a system to detect disturbances. Experiments are conducted using removable reflectors, and the signal changes caused by mode conversion and reflection are correlated with theoretical predictions. Excellent agreement is again obtained, but largely because of the small number of modes propagating. Chapter 9 concludes by summarizing what has been learnt and presenting suggestions for further work. Finally, the MATLAB algorithms used to model the dispersive channel and search for QO pairs and triplets are supplemented in the Appendices.

Part of this research has been published in the following journal:
Syms R, Noorwali A, Polyphase Codes for Multiplexed Acoustic Signalling and Sensing on Pipes, *Smart Materials and Structures*, ISSN:0964-1726, 2022.

2 Acoustic Waves

In this chapter, the wave equation for acoustic waves will be presented with its assumed solution. The considerably more complicated equation for waves in a cylindrical acoustic waveguide and its solutions will be also explored, with a focus on solutions provided by a freeware numerical solver PCDisp. In addition, the wide range of different acoustic modes and dispersion and other effects such as mode conversion in joints, fittings, and bends will be discussed.

Acoustic waves are mechanical perturbations on a medium that carries the wave. They can be bulk or guided waves. Unlike guided waves, bulk waves propagate in an infinite media with no dispersion and no boundaries that causing reflections. The bulk wave equation for any wave in one dimension can be written as:

$$\frac{\partial^2 u}{\partial x^2} = \frac{1}{v^2}\frac{\partial^2 u}{\partial t^2} \tag{2.1}$$

Where u is the displacement field, t is the time, x is the position and v is the velocity. In general, the velocity is related to the wavelength λ and frequency f by:

$$v = \lambda f \tag{2.2}$$

This velocity is the speed of single wave, and it is more generally known as the phase velocity. For a bulk acoustic wave, the phase velocity is related to the elasticity modulus E and density ρ of the medium (solid, water or gas) by:

$$v = \sqrt{\frac{E}{\rho}} \tag{2.3}$$

The solution for the longitudinal displacement field $u(x,t)$ with pressure amplitude A, angular frequency ω and propagation constant (wavenumber) k for a lossless wave is:

$$u(x,t) = Ae^{j(kx-\omega t)}$$

(2.4)

The propagation constant k is the spatial frequency of a wave, measured in cycles per unit distance or radians per unit distance, given by:

$$k = \frac{2\pi}{\lambda}$$

(2.5)

Unlike liquids and gases, solids can in addition support transverse waves, in which the displacement has a component perpendicular to the propagation direction. There are more types of waves that will be explored later.

Acoustic waves are affected by propagation loss due to absorption and geometric spreading. Geometric spreading loss is caused by diffraction. Absorption loss is caused by dissipation of energy as friction in the medium. It is the most limiting factor and can be included in the waveform by making the wavenumber complex. Let $k = k' + jk''$, where k' represents the propagation constant and k'' represents attenuation as: $\alpha_k = -k''$. Thus, the lossy wave equation is,

$$u(x,t) = Ae^{(-k''x)}e^{j(k'x-\omega t)}$$

(2.6)

Guided waves in cylindrical structures are more complicated than bulk waves due to the wide range and large number of propagating modes and the non-linear relation between frequency and wavenumber known as dispersion. The next section will describe the propagation in cylindrical waveguides.

2.1 Propagation in Cylindrical Waveguides

Acoustic waves in cylindrical waveguides have received considerable attention, due to their importance in pipeline inspection. The original theory was developed in the 1800s by Pochhammer [72] and Chree [73], who derived the dispersion equation by transforming the three-dimensional equation of motion of a solid rod into cylindrical coordinates and applying the boundary conditions for traction-free surfaces. Multiple studies [74, 75] then investigated propagation in detail, however, these faced high complexity due to the multimode, dispersive nature of wave propagation. The development of computers allowed

Gazis [76, 77] to present the first exact numerical solution to the Pochhammer-Chree equations and describe acoustic modes in isotropic cylindrical tubes. Following Gazis's analysis, multiple additional factors have been explored. For example, Mirsky [78] investigated anisotropic waveguides and the effect of a viscous fluid in anisotropic tubes [79]. Fuller and Fahy [80] studied wave propagation in fluid-filled cylindrical shells, and the effect of burial in a surrounding medium was explored in [81].

Guided waves require boundaries for propagation. These can be provided in rod or tube geometries. Guide waves are governed by similar partial differential equations, but unlike bulk waves are highly dispersive. For an elastic isotropic hollow cylinder with traction-free surface boundary conditions, the Navier equation for guided wave propagation is:

$$\mu\nabla^2\vec{u} + (\lambda' + \mu)\nabla\nabla.\vec{u} = \rho(\frac{\partial^2\vec{u}}{\partial t^2}) \tag{2.7}$$

Here $\vec{u}$ is the displacement field and a function in three cylindrical coordinates and time, t is time, and λ' and μ are Lame's constants. These can be used to find the longitudinal and shear bulk wave velocities v_1 and v_2 as:

$$v_1 = \sqrt{\frac{\lambda'+2\mu}{\rho}} \tag{2.8}$$

$$v_2 = \sqrt{\frac{\mu}{\rho}} \tag{2.9}$$

Simplification can be achieved for an isotropic cylinder through a Helmholtz decomposition, using a longitudinal scalar potential and an equi-voluminal vector potential. Boundary conditions can then be applied for an infinitely long hollow cylinder, assuming gauge invariance (constant volume) and avoiding the need for end-conditions.

For cylindrical coordinates. Gazis then assumed a separated solution [28] for the displacement vector $\hat{u}$ and stress tensor $\hat{\sigma}$ as:

$$\hat{u}(r,\theta,z) = \tilde{u}(r,\theta)e^{j\mathrm{kz}} = u(r)e^{j\mathrm{n}\theta}e^{j\mathrm{kz}} \tag{2.10}$$

$$\hat{\sigma}(r,\theta,z) = \tilde{\sigma}(r,\theta)e^{j\mathrm{kz}} = \sigma(r)e^{j\mathrm{n}\theta}e^{j\mathrm{kz}} \tag{2.11}$$

Here (r,θ,z) are the coordinates, (e_r, e_θ, e_z) are the unit vector for the cylindrical system, u and σ are displacement and stress and n is an integer for the circumferential order that quantifies the symmetry of the solution in the azimuthal direction. The radial components $u(r)$ and $\sigma(r)$ can be written as:

$$u(r) = \begin{bmatrix} u_r(r) \\ u_\theta(r) \\ u_z(r) \end{bmatrix} = D^u(r).A = D^u(r).\begin{bmatrix} L+ \\ L- \\ SV+ \\ SV- \\ SH+ \\ SH- \end{bmatrix} \tag{2.12}$$

$$\sigma(r) = \begin{bmatrix} \sigma_{rr}(r) \\ \sigma_{\theta\theta}(r) \\ \sigma_{zz}(r) \\ \sigma_{\theta z}(r) \\ \sigma_{rz}(r) \\ \sigma_{r\theta}(r) \end{bmatrix} = D^\sigma(r).A = D^\sigma(r).\begin{bmatrix} L+ \\ L- \\ SV+ \\ SV- \\ SH+ \\ SH- \end{bmatrix} \tag{2.13}$$

Where A is the amplitude coefficient vector of longitudinal (L), shear vertical (SV), and horizontal (SH) deformation components, + indicates a perturbation propagating to increasing radius and – to decreasing radius.

The coefficients of matrices $D^u(r)$ and $D^\sigma(r)$ can be found in [76] for mechanically isotropic material. These consist of 36 and 66 coefficients respectively, and have been implemented in a numerical solver, PCDisp, which will be discussed later.

2.2 Acoustic Modes

Many studies have focused on the range of acoustic modes that can exist in cylindrical pipe geometries. These have been called by different names and will be presented here using notation from the 1970s [83]. Figure 2.1 shows the main three mode types, which are known as longitudinal, torsional and flexural modes because of the dominant mechanical motions

involved. Longitudinal mode has axial and radial displacements but no circumferential displacements. Torsional mode has purely radial displacements, while flexural mode has circumferential and radial displacements but no axial displacements. Thus, longitudinal and torsional modes are axisymmetric while flexural mode is non-axisymmetric.

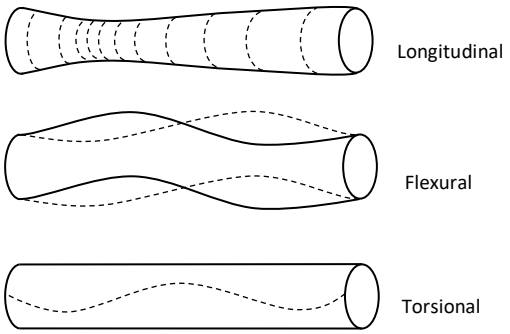

Figure 2.1: Guided acoustic modes.

The longitudinal modes, L(0,m), where, m = 1,2,3,4,… are similar to Lamb waves in thin flat plates which were discovered by Horace Lamb in 1917. Displacement fields of Lamb waves can exist either as a symmetric mode, S0, or antisymmetric mode, A0. For example, Figure 2.2 shows that the L(0,1) mode is comparable to the A0 Lamb mode , while the L(0,2) is comparable to S0 Lamb mode [84].

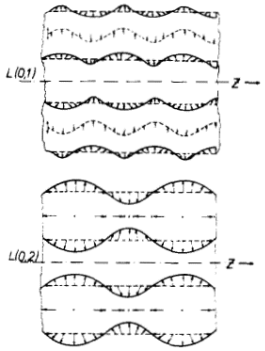

Figure 2.2: Particle motions in the L(0,1) and L(0,2) modes [84].

The torsional mode, T(0,m), is extremely important mode and similar to a simple SH wave in a plate and can be thought of as wave that twists the waveguide. The flexural mode is denoted by F(n,m), where n=1,2,3,4 ... In some references [28], these modes have been called L(n,m), $n \neq 0$. The integer parameter m reflects the circumferential order or the modes of vibration within the wall of the tube, while the parameter n reflects the radial order or the modes of flexing of the tube as a whole. Figure 2.3 is a simplified representation of the

displacement patterns associated with wave modes and caused by circumferential and radial contributions. The figure shows patterns for circumferential orders *m*, from 0 through 3, and radial orders *n*, from 0 through 3 [85].

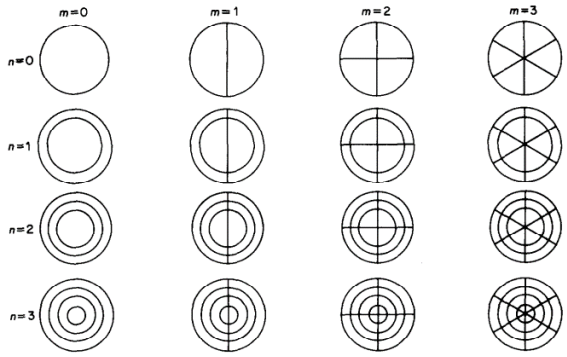

Figure 2.3: Simplified representation of modes in terms of order numbers [85].

Modes that have *n*=0 in Equations 2.10 and 2.11 are axisymmetric and have no dependencies on the azimuthal coordinate θ. Non-null components for longitudinal modes are $(L\pm, SV\pm)$ for amplitude coefficients, (u_r, u_z) for displacement vectors and $(\sigma_{rr}, \sigma_{\theta\theta}, \sigma_{zz}, \sigma_{rz})$ for stress vectors. For torsional mode, non-null components are $(SH\pm)$, for amplitude coefficients (u_θ) for displacement vectors and $(\sigma_{\theta z}, \sigma_{r\theta},)$ for stress vectors. For flexural modes, non-null components are $(L\pm, SV\pm, SH\pm)$ for amplitude coefficients, (u_r, u_θ, u_z) for displacement vectors and $(\sigma_{rr}, \sigma_{\theta\theta}, \sigma_{zz}, \sigma_{rz}, \sigma_{\theta z}, \sigma_{r\theta},)$ for stress vectors.

It is worth mentioning that Lamb waves in the low-frequency range, when the wavelength is greater than the plate thickness, are also called extensional modes (particle motions are in the plane) and flexural modes (particle motions are perpendicular to the plane) [86]. Extensional and flexural modes terminology have been used in structural health monitoring literature [87-89]. Other terminologies such as Rayleigh and Love waves (both surface) waves are significant in multilayer media but will not be used here.

2.3 Dispersion

Many studies have investigated mode dispersion. Oliver [90] studied the dispersion by a wide-band short-pulse dispersion technique. Sachse et. al. [91] proposed a simpler technique to measure the phase and group velocities in dispersive solids. Pialucha and his group proposed an amplitude spectrum method to measure phase velocity in [92]. Two-

dimensional Fourier transform method have been proposed to measure multimode signals [93], and a short-time Fourier transform has been used to analyze dispersive waves [94].

Three main parameters describe dispersion: the wavenumber, the phase velocity, and the group velocity. The first two have previously been introduced for bulk waves. For guided waves, the phase velocity is given more generally by:

$$\mathrm{v}_{ph} = \frac{\omega}{k} \tag{2.14}$$

The group velocity is the velocity of a group of waveforms or wave packets propagating. The group velocity is generally slower than the individual wave velocities and is given by:

$$\mathrm{v}_{g} = \frac{d\omega}{\mathrm{dk}} \tag{2.15}$$

Figure 2.4 illustrates the difference between phase and group velocities in a modulated waveform [28]. The phase velocity is the speed of the carrier, while the group velocity the speed of the envelope. The group velocity is generally the most important factor, as it describes the velocity of information. When the phase velocity and group velocity are equal, such as in bulk waves, the wave is dispersion-less. When the group and phase velocities are not equal, which is commonly in guided waves, the wave is dispersive. The most damaging effect is group velocity dispersion, which alters the shape of the envelope.

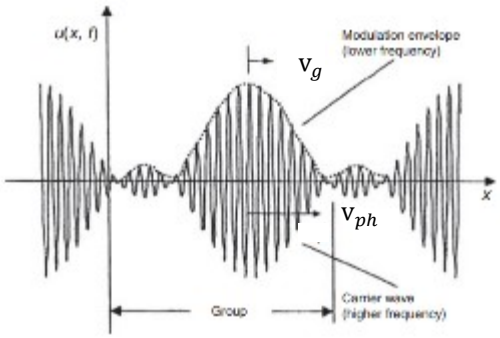

Figure 2.4: Phase and group velocity in a modulated wave [28].

Figure 2.5 shows an example of a) non-dispersive and b) dispersive waves [28]. The dispersive wave spreads more and more the further it travels. Some guided acoustic waves have much higher dispersion than other; however, the severity of the problem can depend on the mode and the frequency range. Before exploring dispersion in any detail, numerical dispersion equation solvers will be discussed.

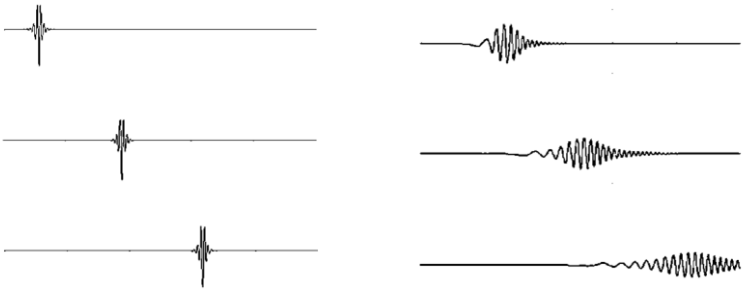

a) b)

Figure 2.5: a) Non-dispersive and b) dispersive wave propagation [28].

2.3.1 PCDisp Numerical Solver

Dispersion characteristics of cylindrical tubes appear highly consistent, despite the use of different tube materials [40, 77, 83, 84, 95]. Many different methods have been used to calculate the dispersion curves in multi-layered composite materials. Examples include the Global Matrix method (GMM), the Finite Element method (FE) and the Semi-Analytical Finite Element method (SAFE). The FE method is relatively time-consuming [96]. Commercial software based on GMM (DISPERSE) is available [96, 97], as is freeware (GUIGUW) based on SAFE [98]. Here, we shall base the discussion on a MATLAB based toolbox (PCDisp) is designed to allow of propagation in addition to calculating dispersion [82].

PCDisp is based on Pochhammer-Chree (PC) theory. Its methodology is to simulate the waveguide behaviour in 4 stages. The first stage involves assembly of a description matrix, which contains the necessary information to study the mechanical behaviour of the waveguide and is built by matching the displacement vector and stress tensor between adjacent layers and then applying the external boundary condition. The other stages involve tracing the frequency-wavenumber curves, computing mode shapes and using the modal analysis to determine the response to excitations. The last step involves modal analysis, a mathematical technique which allows the dynamic response of a waveguide subject to arbitrary external forces to be found as an over the normal modes.

Gazis [76, 77] showed that the traction part of the stress tensor is nulled by the boundary conditions in both surfaces of a single layer isotropic tube. Such a tube will typically have an inner radius r_{int} and an outer radius r_{ext} in vacuum or air, therefore:

$$\sigma_t = \sigma . e_r = \begin{bmatrix} \sigma_{rr} \\ \sigma_{r\theta} \\ \sigma_{rz} \end{bmatrix} = 0 \quad for\, r = r_{int}, r_{ext} \tag{2.16}$$

Thus:

$$\det D(\omega, k) = det \begin{bmatrix} D^{\sigma t}(\mathrm{r}_{int}) \\ D^{\sigma t}(ext) \end{bmatrix} = 0 \quad D^{\sigma t} = D_{ij}^{\sigma} \quad i = 1,5,6 \tag{2.17}$$

The previous equation is the frequency equation of the waveguide, and its roots (ω, k) determine the modes supported. The coefficients of matrices $D^u(r)$ and $D^\sigma(r)$ can be defined using α and β as:

$$\alpha^2 = \frac{\omega^2}{{v_{vol}}^2} - k^2 \tag{2.18}$$

$$\beta^2 = \frac{\omega^2}{{v_{rot}}^2} - k^2 \tag{2.19}$$

Where v_{vol} is the volumetric velocity and v_{rot} is the rotational velocity.

Functions $Z_n(x)$ and $W_n(x)$ are used as independent solutions for Bessel-type differential equations to define the coefficients with $x = \alpha r, \beta r$. Ordinary Bessel functions, $J_n(x)$ and $Y_n(x)$, are employed for real arguments and the modified Bessel functions, $I_n(x)$ and $k_n(x)$ for imaginary arguments to increase the numerical stability of the frequency equation determinant. Thus, Bessel functions for real wavenumber of coefficients $\alpha^2, \beta^2 < 0$ and $\lambda_1, \lambda_2 = -1$ for the frequency range $\frac{\omega}{k} < v_{rot}, v_{vol}$ are:

$$Z_n(\alpha r) = I_n(\alpha r) W_n(\alpha r) = K_n(\alpha r) \tag{2.20}$$

$$Z_n(\beta r) = I_n(\beta r)W_n(\beta r) = K_n(\beta r) \tag{2.21}$$

While the Bessel functions for the real wavenumber of coefficients $\alpha^2 < 0, \beta^2 > 0$, and $\lambda_1 = -1, \lambda_2 = 1$ for the frequency range $v_{rot} < \frac{\omega}{k} < v_{vol}$ is:

$$Z_n(\alpha r) = I_n(\alpha r)W_n(\alpha r) = K_n(\alpha r) \tag{2.22}$$

$$Z_n(\beta r) = J_n(\beta r)W_n(\beta r) = Y_n(\beta r) \tag{2.23}$$

The Bessel functions for the real wavenumber of coefficients $\alpha^2, \beta^2 > 0$ and $\lambda_1, \lambda_2 = 1$ for the frequency range $\frac{\omega}{k} > v_{rot}, v_{vol}$, for the imaginary wavenumber of the same coefficients in any frequency range, and for complex wavenumber of complex α^2, β^2 coefficients and $\lambda_1, \lambda_2 = 1$ for any frequency range are:

$$Z_n(\alpha r) = J_n(\alpha r)W_n(\alpha r) = Y_n(\alpha r) \tag{2.24}$$

$$Z_n(\beta r) = J_n(\beta r)W_n(\beta r) = Y_n(\beta r) \tag{2.25}$$

As mentioned, these Bessel functions are used to define the coefficients of displacement matrix $D^u(r)$ and stress matrix $D^\sigma(r)$. Using these, the amplitude coefficients A can be found from:

$$D(\omega, k).A = 0 \tag{2.26}$$

The matrix A is computed by a method called Singular Value Decomposition (SVD). Then, u_r and σ_r can be found from Equations 2.12 and 2.13.

PCDisp computes dispersion curves and wave propagation for multilayer waveguides using the Multiple Layer Matrix by assembling a system of linear equations for each individual layer. The equations match the displacement and traction stresses at the interface between adjacent layers and also satisfy the boundary conditions. PCDisp uses a routine 'pcmat' to compute $D^u(r)$ and $D^\sigma(r)$ and a routine 'pcmatdet' to assemble and solve the waveguide

description matrix. The 'pcdisp' routine plots the phase and group velocity variations for the physical parameters defined in the routine 'pcwaveguide'.

2.3.2 Dispersion Curves

To understand typical dispersion curves, Figure 2.6 shows an example of a phase velocity dispersion curve of longitudinal mode L(0,1) calculated using PCDisp up to 100 kHz for a copper pipe with 15 mm outer diameter (OD) and 1 mm wall thickness. The standard mechanical parameters for copper that used are 3580m/s for bar speed, 0.34 for Poisson's ratio, and 8940 kg/m^3 for copper density. At low frequencies, the variation shows little dispersion, with a phase velocity of around 3580m/s at low frequencies. As the frequency increases further, the velocity starts to decrease, falling rapidly at around 70 kHz. In this frequency range, there must be high dispersion, leading to significant distortion of any modulated wave.

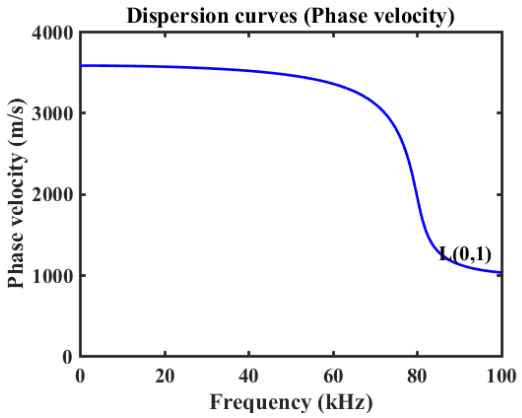

Figure 2.6: Example of phase velocity variation for the L(0, 1) longitudinal mode up to 100 kHz for a copper pipe with 15 mm OD and 1mm wall thickness.

Figure 2.7 shows modes dispersion curves of a) phase velocities and b) group velocities of a copper pipe with 15mm OD and 1mm wall thickness up to 100 kHz. Here, the longitudinal modes are in blue, the flexural modes are in green, and the torsional mode is in red. Below 10 kHz range, only the L(0,1), F(1,1) and T(0,1) modes exist. The L(0,1) mode is the fastest. The torsional mode T(0,1) is the only non-dispersive mode, and its phase and group velocities are invariant. However, it needs a special configuration for the transducers to be excited. Increasing the frequency clearly increases the number of modes rapidly, and there is a considerable range of phase and group velocity.

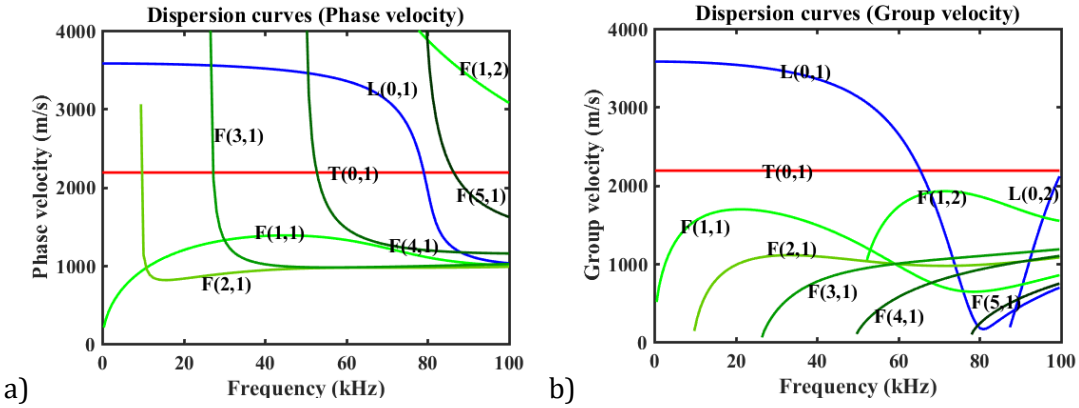

Figure 2.7: Dispersion curves of a) phase velocity and b) group velocity up to 100 kHz for a copper pipe with 15 mm OD and 1mm wall thickness.

Figure 2.8 shows this effect more clearly. Here the variations of a) phase and b) group velocity are calculated up to 1 MHz for the same previous pipe dimensions. Again, the longitudinal modes are in blue, the flexural modes are in green, and the torsional mode is in red. The emergence of large numbers of higher-order flexural modes are particularly noticeable as the frequency increases. Note that flexural modes in a circularly symmetric pipe are effectively degenerate pairs of modes, corresponding to bending about two perpendicular axes.

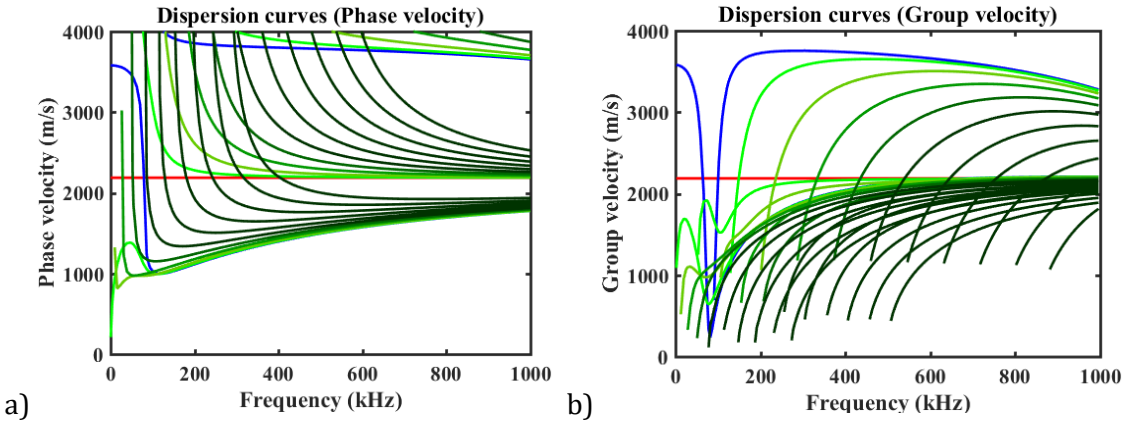

Figure 2.8: Dispersion curves of a) phase velocity and b) group velocity up to 1 MHz for a copper pipe with 15 mm OD and 1mm wall thickness.

Dispersion curves follow well-known scaling laws and are often presented in terms of a frequency-diameter product [99]. In general, when increasing the diameter of the pipe, the

number of longitudinal, torsional and flexural modes increases rapidly, and flat ranges of the curves decrease. Figure 2.9 shows the a) phase and b) group dispersion curves of a copper pipe with 120mm OD and 3mm wall thickness this time. The longitudinal modes are in blue, the flexural modes are in green, and the torsional modes are in red. There are many more modes in the same range of frequencies compared to the smaller pipe discussed before. Moreover, the range of constant phase velocity of the L(0,1) mode, where the minimum dispersion occurs, becomes much smaller. Therefore, larger pipes are likely to suffer much more severely from multi-mode effects.

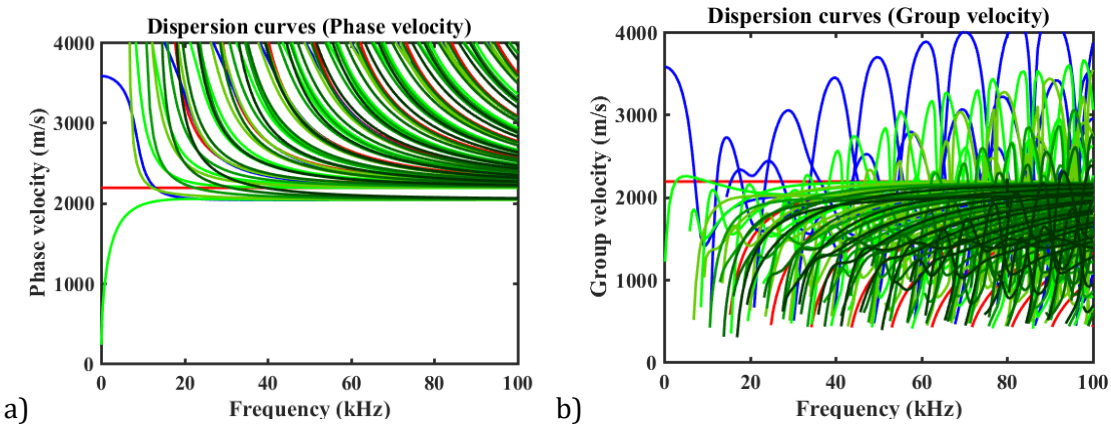

Figure 2.9: Dispersion curves of a) phase velocity and b) group velocity up to 100 kHz for a copper pipe with 120 mm OD and 3mm wall thickness.

Kwun and Bartels [100] cite an equation for the turning point in the phase velocity variation of the first longitudinal mode L(0,1) as $Vo/2\pi a$, where a is the mean radius of the shell and $Vo = \sqrt{(E/\rho)}$. For a copper pipe with 15 mm OD, this frequency is around 70 kHz in agreement with the PCDisp calculations. Solutions of the dispersion equation become numerically unstable when the product of frequency times and waveguide size is high [82]. Physically, this phenomenon arises because the standing waves, established in the radial direction of the waveguide, are formed by a combination of terms that increase exponentially with the radius and others that decrease exponentially.

Other authors have emphasized the importance of having a small bandwidth to generate a pure Lamb mode [40]. While increasing the pulse width can reduce the bandwidth and improve the signal to noise ratio, the pulse width is limited by the length of the pipe as the incident signal will quickly merge with any echoes. One common technique to reduce the

bandwidth is to use a windowed tone-burst. Another is to reduce the excitation zone in the phase velocity dispersion curve by varying the angle beam of a piezoelectric transducer or controlling the spacing of excitation coils in an EMAT.

2.4 Additional Effects

Other effects in acoustic waveguides that have been studied include the relation between attenuation and dispersion [101, 102]. Long [103] investigated the attenuation of the fundamental modes due to leakage into the surrounding medium and the scattering of the modes from the pipe joints and fitting. Even in unburied pipes, pipe features such as welds, flanges, and bends complicate wave propagation. For example, axisymmetric modes, such as L(0,1) and T(0,1), have even displacements distribution around the circumference. Consequently, axisymmetric features in the pipe (such as uniform axisymmetric changes in wall thickness) will cause axisymmetric reflections without mode conversion. Unfortunately, non-uniformly features such as joints and fittings are extremely common and cause non-axisymmetric mode conversions. Figure 2.10 shows examples of typical effects. Figure 2.10 a) shows a reflection due to an axisymmetric connector. Figure 2.10 b) shows mode conversion due to a non-axisymmetric support. Mode conversion can be minimized by increasing the area of contact between the support and the pipe.

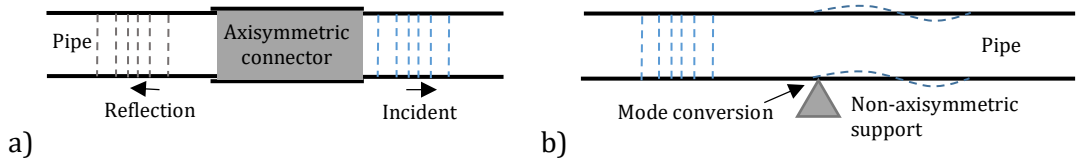

Figure 2.10: Examples of a) a reflection due to an axisymmetric connector and b) a mode conversion due to a non-axisymmetric support.

Bends have been studied for almost a century; Lord Rayleigh reported propagation of acoustic waves in curved pipes in 1912 [104], and more recent studies in [97]. The main differences are as follows. Axisymmetric modes in toroidal shells have an uneven displacement distribution around the circumference. Flexural modes split into two modes with different characteristics. Figure 2.11 shows effects on the flexural and longitudinal modes caused by pipe bend (a toroid) [97]. In the Figure, the un-deformed shape shows the original position of the pipe and the line SS is the plane of symmetry of the pipe. Figure 2.11a shows a split of the flexural mode, F(1,3), into antisymmetric $F(1,3)_A$ and symmetric $F(1,3)_S$

modes in a toroidal pipe. Figure 2.11b shows the longitudinal mode, L(0,2), in a straight pipe is axisymmetric while the longitudinal mode, $L(0,2)_T$, in a toroidal pipe is not axisymmetric but it has a bigger displacement on the outside of the toroid.

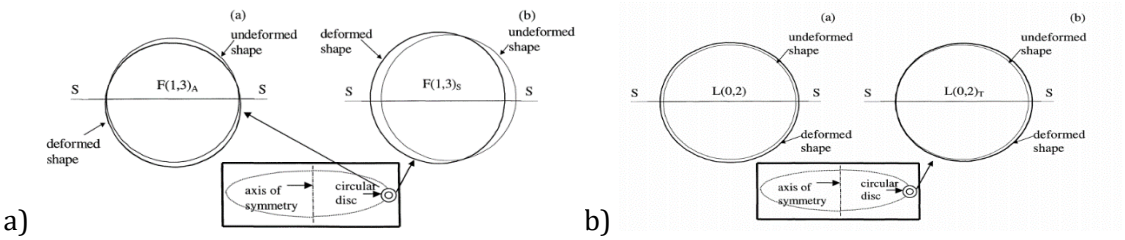

a) b)

Figure 2.11: Effect of bends on flexural modes and longitudinal modes. a) A split of antisymmetric F(1,3)A and symmetric F(1,3)S modes from F(1,3) in a toroidal pipe, b) A comparison between L(0,2) in a straight pipe and L(0,2)T in a toroidal pipe [97].

Figure 2.12 shows a comparison between the dispersion curves of L(0,2) and F(1,3) modes in a) a straight and b) toroidal pipes. The effect of bending is to separate the F(1,3) characteristic into two very similar curves. The length of the bend, the bend diameter, and the pipe geometry all affect the overall transmission coefficient. Bends may also cause mode conversion [105], with the amplitude of the F(1, 1) mode converted from the L(0, 1) mode increasing with the bending angle [106-108]. The only solution is large bend radii.

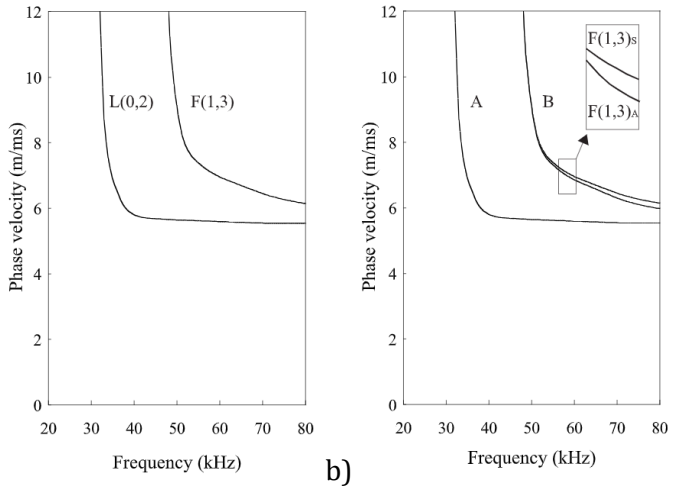

a) b)

Figure 2.12: Comparison between dispersion curves for a) straight and b) toroidal pipes, showing splitting of the F(1, 3) mode [97].

Interaction of guided waves with defects have been studied [109, 110]. In [110], the authors simulated interaction Lamb waves with defects. They reported that sensitivity to a particular defect is dependent on the frequency-thickness product, the mode type (symmetric or antisymmetric), the mode order, and the geometry of the defect. In [111], the same authors studied the effects of standard features in pipelines such as welds, supports, and flanges and showed that the longitudinal mode L(0,1) can be converted to L(0,2) by different features. Another recent study showed that defects can cause mode conversion between the S0 Lamb wave and the SH0 plate wave [112].

Another effect worth mentioning is non-propagating modes, which can arise when a wave is reflected from the end of a finite structure [113, 114]. A thesis by [115] measured the displacement field of the non-propagating modes at the free end using a laser interferometer. Identifying non-propagating modes was essential to correct receiver positioning. In mathematical terms, non-propagating mode exists when the wavenumber contains an imaginary part. Moving the detector away from the end can therefore minimise detection these modes. Free ends also cause mode conversion [116]. Despite this, defect localisation by mode conversion is a significant application [117-119].

2.5 Longitudinal Wave Excitation

In general, the focus is on generating longitudinal waves that are the fastest, and easiest to generate and detect. Silk and Bainton [83] demonstrated Lamb wave generation using conventional piezoelectric crystals with liquid coupling to a steel pipe. They distinguished between longitudinal modes through arrival times, and found that the L(0,1) mode was more efficiently excited than the L(0,2) mode. Alleyne and Cawley [95] excited Lamb waves, L(0,2), at 70 kHz using dry coupled piezoelectric transducers. The authors mentioned the difficulty of generating a single mode, as there are at least two modes at any given frequency. The excitation signal was a 10-cycle tone burst at a frequency, *fo*, which had 40 dB points at about 0.8*fo* and 1.2*fo* to control bandwidth. The authors discussed the importance of controlling bandwidth. At 70 kHz, longitudinal and flexural modes are expected. However, the authors mentioned that if a series of elements were attached in a ring round the pipe, it should be possible to suppress the nonaxisymmetric F(m,n) modes. They found 12 elements to be sufficient and proposed that longitudinally extended transducers could further suppress unwanted modes.

2.6 Conclusion

Dispersion analysis shows that high frequencies, large diameters, bends, supports, liquid fills and surrounds all increase the number of acoustic modes rapidly. However, the combination of low frequency and small pipe diameter can allow a system supporting only a small number of modes. It may then be possible to use sensing in transmission or reflection schemes and mode conversion as methods of monitoring pipeline continuity and disturbance. The next chapter will discuss the excitation of acoustic waves using EMATs including a simulation of magnetic fields and volumetric force generation by the Lorentz effect.

3 Acoustic Transducers

In this chapter, the principles of piezoelectric and electromagnetic acoustic transducers (EMATs) will be described, which have been introduced briefly in Chapter 1. A specific focus will be on EMAT design to excite the longitudinal L(0,1) mode, including analytical and numerical models for coils and permanent magnets. Then, there will be an attempt to shape the design to improve the uniformity and strength of the DC and AC magnetic fields.

3.1 Piezoelectric transducers

We start with piezoelectric transducers, which transfer energy between electromagnetic and mechanical domains. Piezoelectric materials change their condition from neutral to positive or negative charge when mechanical stress is applied. The process is reversible, so the introduction of a charge distribution generates a stress. This effect occurs in certain natural materials such as quartz and topaz crystals and synthetic materials such as lead zirconate titanate (PZT) ceramics. Figure 3.1 shows a piezoelectric crystal that is connected to electrodes to collect or apply charges. The dashed lines show an exaggeration of the deformation of the crystal [120].

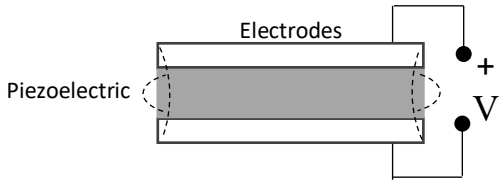

Figure 3.1: A piezoelectric crystal with control electrodes [120].

The effect can be described mathematically using the linear electrical behavior of the material and Hooke's law to couple the elastic and the electromagnetic fields as follows [120]:

$$\underline{S} = \mathbb{s}\underline{T} + \mathbb{d}\underline{E} \tag{3.1}$$

$$\underline{D} = \mathbb{s}\underline{T} + \mathcal{E}\underline{E} \tag{3.2}$$

Where $\underline{S}$ is the strain vector, $\underline{T}$ is the stress vector, $\mathbb{s}$ is the compliance coefficients matrix, $\mathbb{d}$ is the piezoelectric strain constants matrix (the ratio of developed free strain to the applied electric field), $\underline{E}$ is the electric field strength vector, $\underline{D}$ is the electric charge density displacement vector and $\mathcal{E}$ is the permittivity matrix. Equation 3.1 shows that the total strain is the sum of the strains caused by the mechanical stress and the applied voltage and describes the effect when the transducer is used as an actuator. Equation 3.2 shows that the total electric charge density displacement is the sum of the displacements due to the mechanical stress applied and the electric field when the transducer is used as a sensor. Because piezoelectric transducers can impose a wave-type disturbance on the material, it is relatively simple to excite only a small number of modes. However, piezoelectric transducers require liquid couplant to reduce impedance mismatch. Because it is difficult to contain a liquid in many applications, dry coupled transducers have been developed.

3.2 EMATs

We now consider EMATs, which generally require a conducting material (although ferromagnetic materials can also be used). The basic mechanism involves the formation of an eddy current using a time-varying magnetic field, followed by the generation of a volumetric force through the action of a static magnetic field on the moving carriers. The key advantage is the lack of any requirement for the contact between the transducer and the material. Unfortunately, because EMATs typically impose a concentrated disturbance, it is more difficult to generate a pure single mode using an EMAT than using an angled piezoelectric transducer [121]. However, array-type EMATs containing periodically spaced elements have been developed to solve this problem.

A variety of different EMAT arrangements have been developed [122-124]. Figure 3.2 shows in cross-sectional views the biasing magnet, the coil, and the force, in a number of configurations used to generate different acoustic modes in plates. Fig 3.2a) shows a spiral coil EMAT used to excite shear waves propagating normal to the surface, b) shows a tangential field EMAT to excite longitudinal waves normal to the surface, c) shows a normal field EMAT to excite shear waves normal to the surface, and finally d) shows a meander coil EMAT to excite longitudinal, SV waves (shear wave in a vertical plane) or Rayleigh (surface) waves. Some of these configurations have also been adapted to cylinders, pipes, and other geometries.

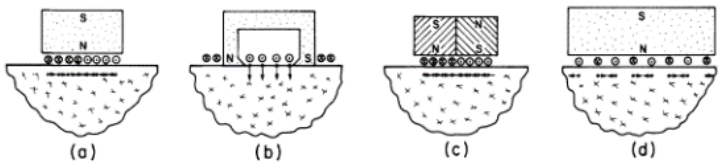

Figure 3.2: EMAT configurations: a) a spiral coil, b) tangential EMAT, c) normal field EMAT, d) meander coil EMAT [122].

EMATs can be configured to exploit the Lorentz force, magnetization force, or magnetostriction mechanisms. Mathematical models have been developed to analyze Lamb wave generation using both linear [125] and non-linear [126, 127] effects. Even in the linear case, the Lorentz force is strongly dependent on the coil geometry, and different modes can be excited depending on the relative similarity between the excitation and the mode concerned. Figure 3.3 shows a) spiral coils and b) meander line coils fabricated using printed circuit techniques and designed to excite different modes [128].

a) 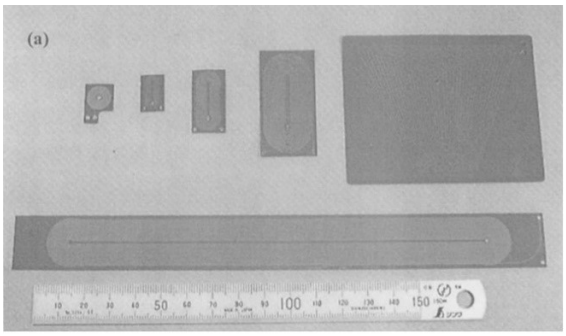

b) 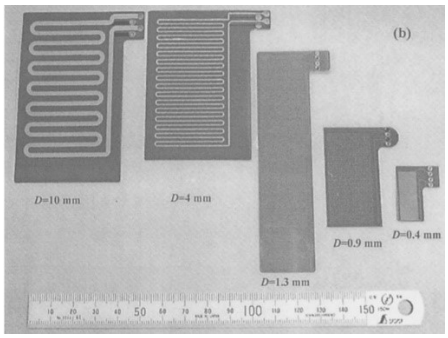

Figure 3.3: Printed circuit coils: a) spiral and b) meander-line coils [128].

U-shaped EMATs based on the alternative magnetostriction mechanism have also been used to generate different modes in a cold-rolled steel rod [129]. For example, Figure 3.4 shows longitudinal, torsional, and flexural waves generated by the exact same transducer. The different modes may be identified by their group velocities during pulse excitation; however, propagation distances must clearly be sufficient to separate out the different contributions, a major difficulty with all acoustic systems involving multi-mode propagation and a recurring theme of later chapters.

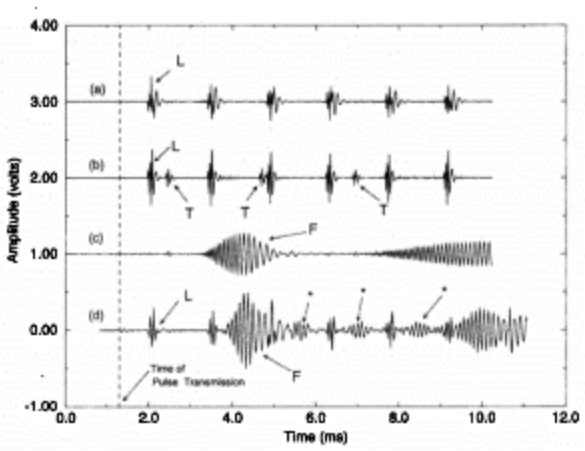

Figure 3.4: Longitudinal L, torsional T, and flexural F modes generated by U-shaped magnetostrictive EMAT [129].

Several factors affect the proportions with which different modes are excited. These include the separation from the material (known as the lift-off distance) and the number of EMAT elements or poles. For example, Wang et al. [130] studied the effect of varying the number of elements using a periodic permanent magnet to find the optimum number for a given pipe. Increasing the number led to a more symmetrical excited volume, which maximized axisymmetric modes while suppressing non-axisymmetric modes.

3.3 EMAT Design

Figure 3.5 shows a single pole of the multipole EMAT design used here. It consists of a permanent magnet and a solenoid coil to form static (bias) and dynamic magnetic fields respectively. The magnet bars and coils are both initially assumed to be cuboids to match later experiments. The configuration parameters, which include the position of the magnet relative to the pipe, the current direction, and the lift-off distance, were chosen to produce longitudinal waves propagating along the pipe in an axial direction.

The excitation occurs through multiple steps starting from the AC voltage source, which generates an AC current in the coil. This in turn generates a dynamic magnetic field in the axial direction. The dynamic field creates an electric field that induces an eddy current in the circumferential direction in the pipe wall. The permanent magnet creates a static field in the radial direction, which acts on the eddy current to create a volumetric Lorentz force, which excites acoustic waves in the longitudinal direction. However, as we show below, it is not possible to generate an ideal, uniform static field.

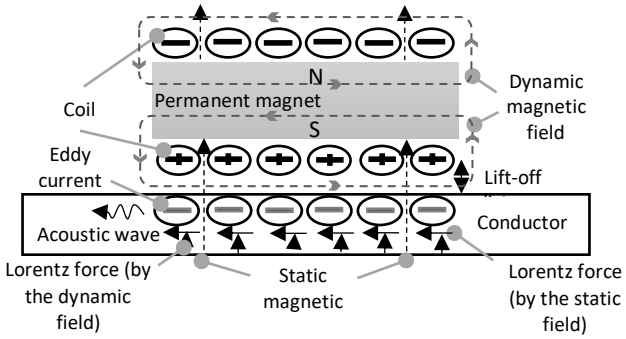

Figure 3.5: EMAT configuration used here. Dashed arrows are for magnetic fields, solid arrows are for Lorentz forces and signs in circles are for the current direction.

Figure 3.6 shows a) on (z, y) plane, and b) in three-dimensional space how an arrangement of four similar poles equally spaced around the pipe and driven in parallel can be used to improve symmetry and increase the acoustic wave amplitude. Here it is again assumed that the magnets and solenoids are all cuboids to match later experiments. Since the static magnetic field is perpendicular to the pipe, the main mode is longitudinal. In a linear model, the acoustic mode has the same frequency as the drive.

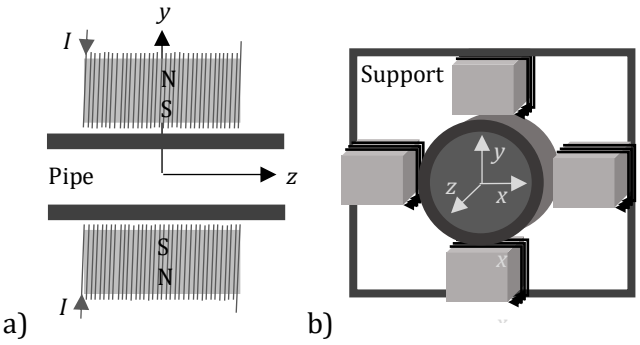

Figure 3.6: 4-element EMAT a) on (z, y) plane, and b) in three-dimensional space.

Analysis of even a simple EMAT is complicated by coupling between the different physical effects. The first difficulty is that when there is a permanent magnet in the coil core, the solenoid field modifies. There is a strong focus in the literature on air-cored solenoids [131], but limited attention has been paid to other core materials. The external field of the linear solenoid occupies a large volume of space. Lerner [132] derived field solutions for spheroidal solenoids that have core permeability different from free space. In specific applications, iron-core coils have an important advantage [133]. These authors described the construction, modeling, and testing of an iron-core coil that reduces power

requirements and heat generation substantially, while improving the penetration of the magnetic field for brain-stimulating applications. The second difficulty is when the magnetic field created by the eddy current is generated, the dynamic magnetic field modifies. The resulting coupled problem was solved by Dodd and Deeds [134]; however, an exact solution is only obtained in terms of the magnetic vector potential. The third difficulty is when a permanent magnetic field acts on the eddy current, the current distribution modifies. To solve this coupled problem, [135] and [136] simulated an EMAT with a meander line coil numerically. Here we use a simpler uncoupled analysis.

3.4 Cuboid EMAT Model

Before the widespread availability of computers, calculations based on power series solutions [137] were used to analyze non-cylindrical solenoid geometries. The development of computers allowed exact methods such as the boundary-element method (BEM) and finite-element method (FEM) [138, 139] to be used. Today, commercial finite element solvers such as COMSOL® are often used. However, a simplified mathematical analysis will be presented here to model cuboid coils and magnets.

3.4.1 Mathematical Model

The EMAT proposed here has four elements, each consisting of a cuboid solenoid surrounding a cuboid permanent magnet core. The axes of the solenoids are axial (i.e., parallel to the pipe) and the main fields of the magnets are radial. The magnetic fields generated by each coil and magnet may be found by summing the fields of rectangular current loops. We start by considering a small filament of current $I\ d\underline{L}$. Figure 3.7 shows the filament and an arbitrary point P in space where its field is to be calculated.

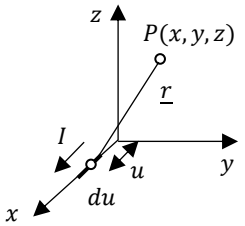

Figure 3.7: Geometry used to calculate the magnetic field due to a small filament of current.

The Biot-Savart law [140] that describes the magnetic flux of a current-carrying wire is:

$$\underline{B} = \left(\frac{\mu_o I}{4\pi}\right) \int \frac{d\underline{L} \times \underline{r}}{r^2}$$

(3.3)

Where $\underline{B}$ is the magnetic flux density, μ_o is the permeability of free space, $\underline{r}$ is a unit vector towards P, and r is the distance to P. For a short segment of a wire, the elementary flux contribution $d\underline{B}$ is:

$$d\underline{B} = \left(\frac{\mu_o I}{4\pi}\right) \frac{d\underline{L} \times \underline{r}}{r^2}$$

(3.4)

When the filament is a short section $du\ \underline{i}$ located at distance u along the x-axis, we can obtain the component parts of 3.4 as:

$$\begin{aligned} d\underline{L} &= du\ \underline{i} \\ \underline{r} &= (x-u)\underline{i} + y\underline{j} + z\underline{k} \\ |\underline{r}| &= \{(x-u)^2 + y^2 + z^2\}^{1/2} \\ d\underline{L} \times \underline{r} &= 0\underline{i} - z\ du\ \underline{j} + y\ du\ \underline{k} \end{aligned}$$

(3.5)

Substitution then gives:

$$\begin{aligned} dB_y &= \left(\frac{\mu_o I}{4\pi}\right) \frac{-z\ du}{\{(x-u)^2 + y^2 + z^2\}^{3/2}} \\ dB_z &= \left(\frac{\mu_o I}{4\pi}\right) \frac{y\ du}{\{(x-u)^2 + y^2 + z^2\}^{3/2}} \end{aligned}$$

(3.6)

Figure 3.8 shows the arrangement when the filament is a complete line segment of length $2a$ symmetrically placed along the x-axis.

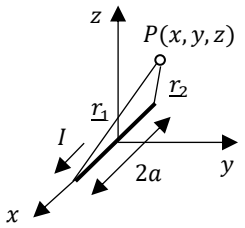

Figure 3.8: Geometry used to calculate the magnetic field due to a current-carrying wire.

In this case, the *y* and *z* components of magnetic flux density can be found as:

$$B_y = \left(\frac{\mu_o I}{4\pi}\right) \int_{-a}^{a} \frac{-z\, du}{\{(x-u)^2 + y^2 + z^2\}^{3/2}}$$
$$B_z = \left(\frac{\mu_o I}{4\pi}\right) \int_{-a}^{a} \frac{y\, du}{\{(x-u)^2 + y^2 + z^2\}^{3/2}}$$

(3.7)

Integration then yields:

$$B_y = \left(\frac{\mu_o I}{4\pi}\right)\left(\frac{z}{y^2 + z^2}\right)\left(\frac{1}{r_1} - \frac{1}{r_2}\right)$$
$$B_z = \left(\frac{\mu_o I}{4\pi}\right)\left(\frac{-y}{y^2 + z^2}\right)\left(\frac{1}{r_1} - \frac{1}{r_2}\right)$$

(3.8)

With the radii given as:

$$r_1 = \{(x-a)^2 + y^2 + z^2\}^{1/2}$$
$$r_2 = \{(x+a)^2 + y^2 + z^2\}^{1/2}$$

(3.9)

The same approach can be extended to calculate the magnetic field of more complicated geometries containing wire sections. For example, Figure 3.9 shows a current-carrying rectangular wire loop. In this case, the overall field can be obtained by repeating the analysis above for different current directions, wire orientations, and origins and summing the result around the perimeter of the loop.

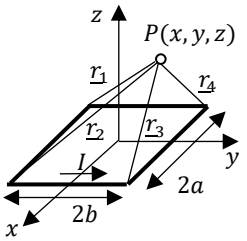

Figure 3.9: Geometry used to calculate the magnetic field due to a current-carrying loop.

Weber [141] and Misakian [142] analyzed the magnetic effect of single and multiple rectangular current loops in this way. For a single loop centered on point (0,0,0) and with dimensions $2a$ in the x-direction and $2b$ in the y-direction, the flux density at P is given by:

$$B_x = \left(\frac{\mu_o I}{4\pi}\right)\sum_{n=1}^{4}\left[\frac{(-1)^{n+1}z}{r_n[r_n + d_n]}\right]$$
$$B_y = \left(\frac{\mu_o I}{4\pi}\right)\sum_{n=1}^{4}\left[\frac{(-1)^{n+1}z}{r_n[r_n + (-1)^{n+1}c_n]}\right]$$
$$B_z = \left(\frac{\mu_o I}{4\pi}\right)\sum_{n=1}^{4}\left[\frac{(-1)^{n}d_n}{r_n[r_n + (-1)^{n+1}c_n]} - \frac{c_n}{r_n[r_n + d_n]}\right]$$

(3.10)

Where the constants are given by:

$$c_1 = -c_4 = a + x;\ c_2 = -c_3 = a - x$$
$$d_1 = d_2 = y + b;\ d_3 = d_4 = y - b$$

(3.11)

And the radii are given by:

$$r_1 = \sqrt{(a+x)^2 + (y+b)^2 + z^2}$$
$$r_2 = \sqrt{(a-x)^2 + (y+b)^2 + z^2}$$
$$r_3 = \sqrt{(a-x)^2 + (y-b)^2 + z^2}$$
$$r_4 = \sqrt{(a+x)^2 + (y-b)^2 + z^2}$$

(3.12)

The magnetic field of a multi-turn solenoid coil can be estimated by adding the fields of multiple loops after shifting their coordinate origins and rotating their axes as required. Figure 3.10 shows a stack of loops forming a rectangular coil in this way. The magnetic field of a permanent magnet can in turn be modeled as the field of a solenoid coil [143], adjusting the 'current' to obtain a realistic magnetic field.

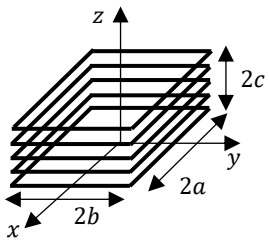

Figure 3.10: Multiple rectangular current loops used to model a coil or permanent magnet.

Since the generated magnetic field passes through materials that could contribute internal magnetic fields, the field strength $\underline{H}$ is commonly used to find the magnetic effect without the material's contribution. It can be found with the following well-known relationship:

$$\underline{H} = \underline{B}/\mu \tag{3.13}$$

Where μ is the magnetic permeability of the material.

3.4.2 Numerical Simulation

The approach above was used to construct a general modeling tool, implemented in MATLAB. General vector fields were first calculated by summation of the contribution of individual wires. The current amplitude was assumed to be 1 Amp in each element. The results were formed into data arrays from which important field variations were extracted. Results were plotted contour plots and streamlines on 2D planes, or as graphs on linear or circumferential loci.

For example, Figure 3.11a shows the magnetic field of a single cuboid solenoid on the central (z, y) and (x, y) planes (i.e., on axial and transverse planes, respectively). The colors indicate the modulus of the magnetic field strength (darkest is 0 while brightest is above 1000 A/m) and the streamlines show the direction of the field. The field is clearly very similar to that of a cylindrical solenoid, being predominantly axial, uniform, and strong along the centerline of the solenoid, but weaker and spatially varying outside. Figure 3.11b shows the magnetic field of a single cuboid solenoid in the position it would occupy in an EMAT. Here, the additional white lines represent the outline of a non-metallic transducer support clamped around a central cylindrical pipe. This field is clearly similar to 3.11a but shifted. Figure 3.11c shows the magnetic field of a 4-element EMAT, containing four cuboid solenoids

arranged symmetrically around the pipe. In this simulation, the solenoid length and width ratio, the lift-off distance, and the number of turns (90) are chosen to match later experiments. The field is predominantly axial and uniform throughout the space between the coils. Consequently, the time-varying field that would be generated with an AC current is correctly oriented to generate eddy currents circulating circumferentially around an annular conducting pipe by magnetic induction.

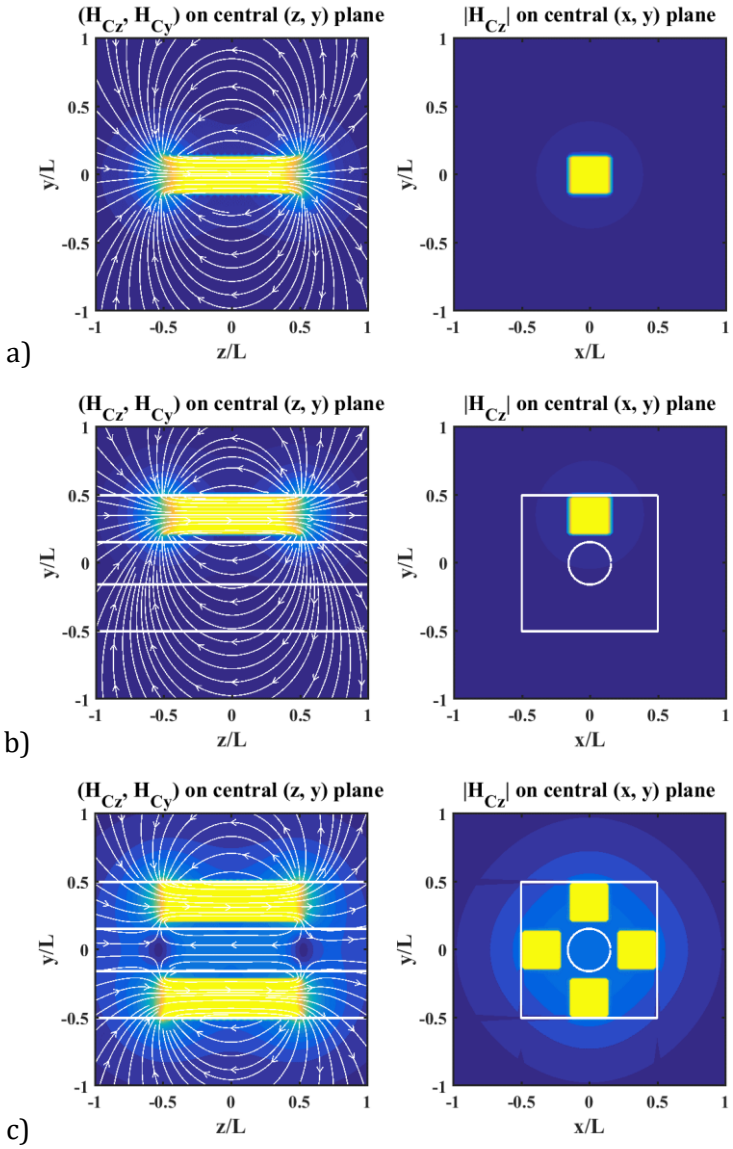

Figure 3.11: Magnetic field strength simulations on the (z, y) and (x, y) planes of a) a single cuboid solenoid at the center, b) a shifted solenoid, and c) a 4-element solenoid array. Color modulus is between 0 and 1200 A/m.

Figure 3.12a shows the magnetic field of a single cuboid permanent magnet on the central (z, y) and (x, y) planes, modeled as an equivalent solenoid. In this case, there is no equivalent experimental value for the number of turns, which is simply assumed to be 50. The field lines are close together, uniformly spaced, and parallel along the centerline of the magnet, flowing from the North to the South pole, but are further apart and spatially varying outside. Figure 3.12b shows the magnetic field of a single cuboid magnet in the location it would occupy in an EMAT; here, the field lines and colors are again simply shifted into the new position. Figure 3.12c shows the magnetic field of a 4-element EMAT, containing four cuboid magnets arranged symmetrically around the pipe. The field lines flow radially outward beneath each magnet but reverse direction to flow radially inwards between them.

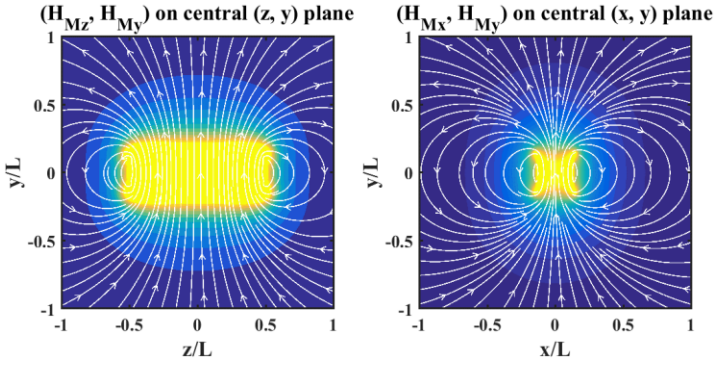

a)

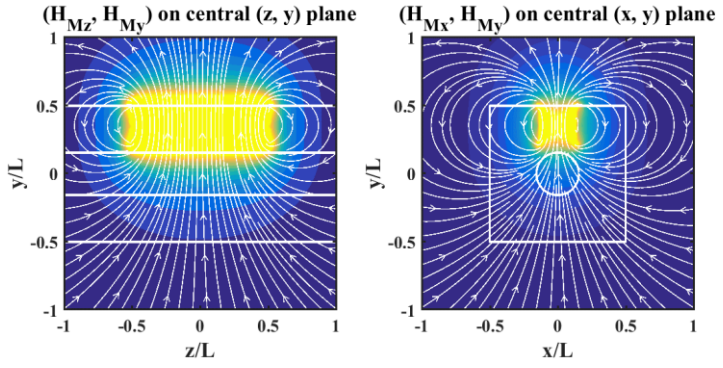

b)

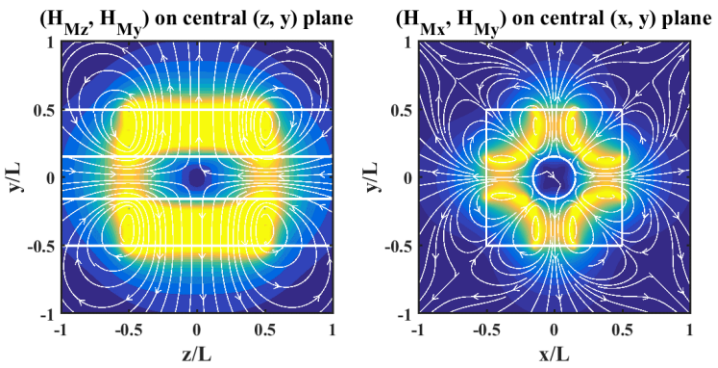

c)

Figure 3.12: Magnetic field strength simulations on the (z, y) and (x, y) planes of a) a single cuboid permanent magnet at the center, b) a shifted magnet, and c) a 4-magnet array. Color modulus is between 0 and 4300 A/m.

Increasing the number of magnets essentially increases the number of similar poles, and it is impossible to obtain a field that is uniformly directed inward or outward. Since the arrangement will induce a radial static magnetic field on the eddy currents that are circulating circumferentially around the annular conducting pipe, the effect will then be to induce an axial volumetric force according to the Lorentz law that varies in direction. Excitation of longitudinal waves will therefore be inefficient.

To illustrate these variations further, Figure 3.13 shows the variation of magnetic field strength H_{Cnz} around circular trajectories of different normalized radii r/R_E on the x-y plane for multipole EMATS containing a) 2 and b) 4 cuboid solenoids. Here R_E is the radius of the pipe. With the specific parameters mentioned above, the average magnetic field strength around the pipe is approximately 200 A/m. The field strength varies periodically with the angle between poles and the variation reduces at a small radius. However, increasing the number of solenoids from 2 to 4 almost doubles the field strength, reduces the periodicity of the oscillations, and improves the field uniformity.

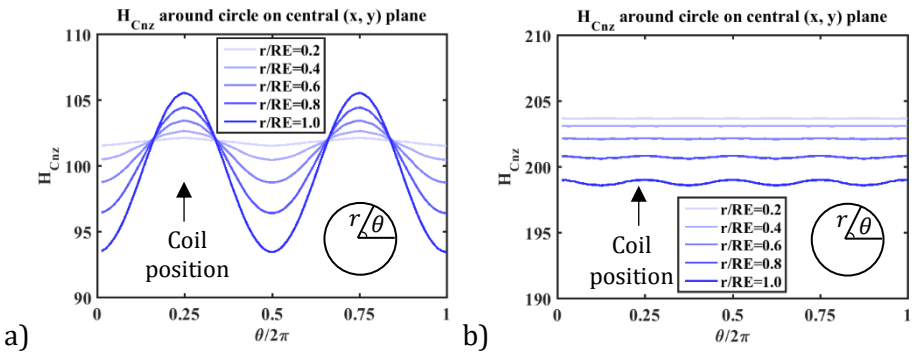

Figure 3.13: Variation of magnetic field strength around circular trajectories for EMATS containing a) 2 and b) 4 cuboid solenoids.

Similarly, Figure 3.14 shows the magnetic field strength H_{Mnr} around circular trajectories of different normalized radii r/R_E on the x-y plane for multipole EMATs containing a) 2 and b) 4 cuboid permanent magnets. As for the solenoids, the magnetic field strength varies periodically with the angle between poles and the variation reduces at a small radius. However, the field clearly reverses in sign between poles. As the number of poles increases, the field variation reduces. The field is maximized immediately beneath each pole. Since this is also the location where the solenoid field is maximized, a non-zero longitudinal volumetric Lorentz force might be expected, allowing the excitation of the L(0, 1) longitudinal mode despite field reversal.

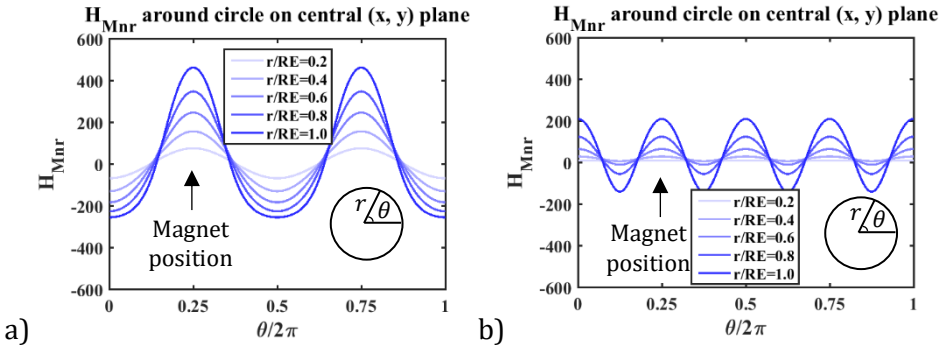

Figure 3.14: Variation of magnetic field strength around circular trajectories for EMATS containing a) 2 and b) 4 cuboid permanent magnets.

3.4.3 Eddy Current and Volumetric Lorentz Force

We now consider the excitation of longitudinal waves in more detail. An eddy current is generated when the solenoids are driven with AC current, so that their field is time-varying. As we have shown in the static case, this field is high, reasonably uniform, and largely axial

in the space between the four solenoids. Assuming that the field varies harmonically at angular frequency ω. we can write:

$$\underline{\boldsymbol{B}}_{cz} = B_{cz} e^{j\omega t} \underline{z} \tag{3.14}$$

Where t is the time. We now assume that the time-varying magnetic field must have an associated electric field. Since this must vary at the same frequency, we assume the form:

$$\underline{\boldsymbol{E}} = \underline{E} e^{j\omega t} \tag{3.15}$$

The exact field can be found from Faraday's law, which for harmonic fields is given by:

$$\nabla \times \underline{\boldsymbol{E}} = -\frac{\partial \underline{\boldsymbol{B}}}{\partial t} = -j\omega \underline{\boldsymbol{B}} \tag{3.16}$$

Substitution of the assumed solutions 3.14 and 3.15 allows the complex exponential terms to be canceled, so that the remainder of the analysis can be carried out using the time-independent fields in normal type. As the magnetic flux density is only on the z-axis, only the z-component of the curl term is important. Equating the two we get:

$$\frac{1}{r}\left\{\frac{\partial (rE_\theta)}{\partial r} - \frac{\partial E_r}{\partial \theta}\right\} = -j\omega B_{cz} \tag{3.17}$$

Here E_r and E_θ are the radial and circumferential components respectively. If there are no angular variations in E, then we can neglect $\frac{\partial E_r}{\partial \theta}$ to get:

$$\frac{1}{r}\left\{\frac{\partial (rE_\theta)}{\partial r}\right\} = -j\omega B_{cz} \tag{3.18}$$

Integrating from 0 to r we then obtain:

$$rE_\theta = -j(\omega \frac{r^2}{2}) B_{cz} \tag{3.19}$$

Re-arranging, we can find the induced electric field as:

$$E_\theta = -j(\omega \frac{r}{2}) B_{cz} \tag{3.20}$$

In a material of conductivity σ, such as a conducting pipe wall, this field will induce a circumferential eddy current, given by:

$$J_\theta = -j(\omega\sigma \frac{r}{2}) B_{cz} \tag{3.21}$$

A more detailed analysis would also consider skin effects. and show that the induced current is non-uniform and concentrated in a superficial portion of the material close to the outer and inner pipe walls. The effective current-carrying region is the skin depth δ, which can be defined for a non-magnetic material as:

$$\delta = \frac{1}{\sqrt{\pi f \sigma \mu_0}} \tag{3.22}$$

Here $\mu_0 = 4\pi \times 10^{-7}\ N/A^2$ is the permeability of free space. Figure 3.15 shows the variation with frequency of the skin depth in copper (σ =6 × 10^7 $(\Omega m)^{-1}$). The skin depth clearly decreases significantly with frequency. However, for a pipe of 1mm wall thickness, as used in later experiments, the value of δ at frequencies below 20 kHz is above 0.25mm. Therefore, skin effects should be relatively insignificant in the proposed design.

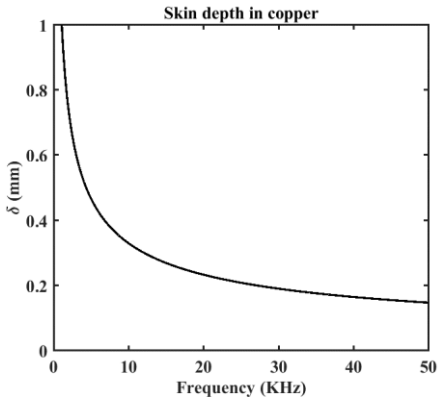

Figure 3.15: Frequency dependence of skin depth in copper.

Based on the simulation results above, the volumetric Lorentz force can be estimated. Figure 3.16a) shows a cross-sectional view of the EMAT in the (z, y) plane. Here the bold lines show the direction of the static magnetic field while the thin lines show the direction of the dynamic field. Each element is located at equal angular separation around the pipe, to give the most uniform longitudinal magnetic field B_{cz} over the whole pipe cross-section. Figure 3.16b) shows the lines of the radial magnetic fields B_{Mr} between the coils, which are inward immediately beneath poles and outward between poles. Figure 3.16c) shows the lines of the Lorentz force in the z-direction which are alternating in sign. The Lorentz force arises from the interaction between B_{cz} and B_{Mr}. Therefore, the direction of the Lorentz force indicates an excitation in an axial direction, which is likely to generate the L(0,1) mode at low frequencies. However, we might expect that interaction between non-uniform and fringing fields may excite other flexural modes as well.

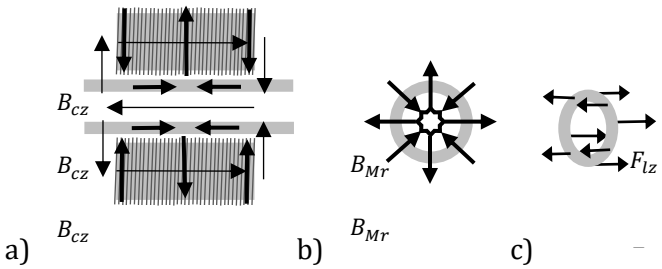

Figure 3.16: a) Cross-section of a 4- element EMAT, b) lines of radial magnetic fields B_{Mr} between the coils, and c) lines of axial Lorentz force in the z-direction.

The Lorentz force on a charge q moving at velocity $\underline{v}$ in a flux density $\underline{B}$ is given by:

$$\underline{F_l} = q(\underline{v} \times \underline{B}) \tag{3.23}$$

Through the action of the dynamic magnetic field of the solenoid, the charges in the skin depth of the conducting pipe are accelerated to the mean velocity to form an eddy current. The charges then experience a Lorentz force due to the static magnetic field of the permanent magnets. The Lorentz force $\underline{F_{l(puv)}}$ for n charges per unit volume is given by:

$$\underline{F_{l(puv)}} = nq(\underline{v} \times \underline{B}) = \underline{J} \times \underline{B} \tag{3.24}$$

Here $\underline{J}$ is the eddy current density, which can be written as:

$$\underline{J} = J_\theta \underline{\theta}$$

(3.25)

Assuming the radial magnetic force B_{Mr} due to the permanent magnets, the volumetric Lorentz force is given by:

$$\underline{F_{l(puv)}} = J_\theta B_{Mr} \underline{\theta} \times \underline{r} = -J_\theta B_{Mr} \underline{z}$$

(3.26)

Since the current density is related to the dynamic magnetic flux density by:

$$J_\theta = -\mathrm{j}(\frac{\omega \sigma r}{2}) B_{Cz}$$

(3.27)

We then obtain the volumetric force as:

$$\underline{F_{l(puv)}} = +\mathrm{j}(\frac{\omega \sigma r}{2}) B_{Cz} B_{Mr} \underline{z}$$

(3.28)

The last equation shows that the interaction between B_{Cz} and B_{Mr} causes a volumetric force in an axial direction to the pipe that alternates in sign at angular frequency ω. From the dispersion curves previously presented in chapter 2, we would then expect the EMAT to excite the L(0,1) mode at frequencies below 20kHz for a copper pipe with 15mm OD and 1mm wall thickness.

3.5 Shaped EMAT Model

An EMAT design with cuboid elements is not a natural fit to a cylindrical pipe, and the magnetic field strength will vary around the pipe circumference. In addition to the sign reversal of the fringing field, the edges and center of the cuboid induce different magnetic fields due to their variable separation from the pipe wall. This variation could induce unwanted effects, such as the excitation of higher acoustic modes. Improvements might follow from the use of wider cuboid elements or curved poles, and we now investigate this

possibility. Figure 3.17 compares a) cuboid EMATs with non-uniform lift-off distance (red and green arrows), and b) curved pole EMATs with improved uniformity (green arrows).

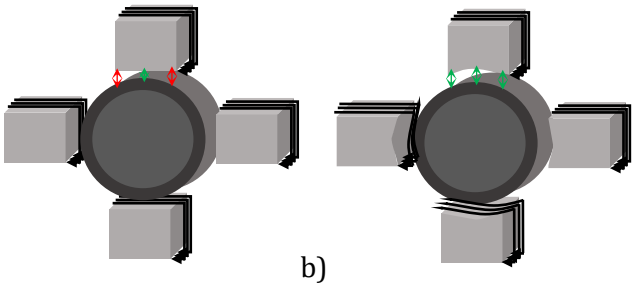

a) b)

Figure 3.17: Comparison of a) cuboid, and b) curved pole EMATs.

The curved side of the coil may be approximated using a more complex wire arrangement. Figure 3.18 shows an example of a single current-carrying wire loop with a wire staircase forming a stepped approximation to a curved pole. The number of steps can be increased to improve the smoothness of the curve and even out the lift-off distance to the pipe.

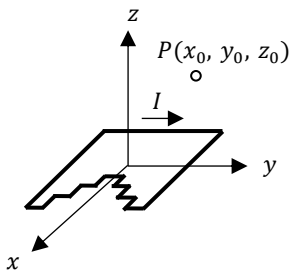

Figure 3.18: Stepped approximation to single loop with a curved end face.

To describe the magnetic field in this case, Equations (3.7-3.9) can simply be modified to describe magnetic flux densities created by the new distribution of wires. The necessary formulae can be constructed by origin shifting and summation. For example, the flux components for a wire of length *2a* parallel to the x-axis and located at $(x_0,\ y_0, z_0)$ are:

$$B_y = \left(\frac{\mu_0 I}{4\pi}\right)\left(\frac{z'}{y'^2 + z'^2}\right)\left(\frac{(x'-a)}{r'_{1x}} - \frac{(x'+a)}{r'_{2x}}\right)$$
$$B_z = \left(\frac{\mu_0 I}{4\pi}\right)\left(\frac{-y'}{y'^2 + z'^2}\right)\left(\frac{(x'-a)}{r_{1x}} - \frac{(x'+a)}{r_{2x}}\right) \quad (3.29)$$

With:

$$r'_{1x} = \{(x' - a)^2 + y'^2 + z'^2\}^{1/2}$$
$$r'_{2x} = \{(x' + a)^2 + y'^2 + z'^2\}^{1/2}$$

(3.30)

Where $x' = x - x_0$, $y' = y - y_0$ and $z' = z - z_0$. Similarly, the flux components for a wire of length $2b$ parallel to the y-axis and located at $(x_0,\ y_0, z_0)$ are:

$$B_x = \left(\frac{\mu_0 I}{4\pi}\right)\left(\frac{-z'}{x'^2 + z'^2}\right)\left(\frac{(y' - b)}{r'_{1y}} - \frac{(y' + b)}{r'_{2y}}\right)$$
$$B_z = \left(\frac{\mu_0 I}{4\pi}\right)\left(\frac{x'}{x'^2 + z'^2}\right)\left(\frac{(y' - b)}{r'_{1y}} - \frac{(y' + b)}{r'_{2y}}\right)$$

(3.31)

With:

$$r'_{1y} = \{x'^2 + (y' - b)^2 + z'^2\}^{1/2}$$
$$r'_{2y} = \{x'^2 + (y' + b)^2 + z'^2\}^{1/2}$$

(3.32)

Finally, the flux components for a wire of length $2c$ parallel to the z-axis and located at $(x_0,\ y_0, z_0)$ must be:

$$B_x = \left(\frac{\mu_0 I}{4\pi}\right)\left(\frac{y'}{x'^2 + y'^2}\right)\left(\frac{(z' - c)}{r'_{1z}} - \frac{(z' + c)}{r'_{2z}}\right)$$
$$B_y = \left(\frac{\mu_0 I}{4\pi}\right)\left(\frac{-x'}{x'^2 + y'^2}\right)\left(\frac{(z' - c)}{r'_{1z}} - \frac{(z' + c)}{r'_{2z}}\right)$$

(3.33)

With:

$$r'_{1z} = \{x'^2 + y'^2 + (z' - c)^2\}^{1/2}$$
$$r'_{2z} = \{x'^2 + y'^2 + (z' + c)^2\}^{1/2}$$

(3.34)

As before, addition of the fields of multiple loops may be used to estimate the magnetic field of a multi-turn curved pole solenoid. Figure 3.19a shows the general arrangement. However, the same approach cannot be used for a permanent magnet because the curve and the

stacked loops are in different planes. Instead, a cascade of rectangular loops with different dimensions must be used. Figure 3.19b shows the arrangement needed in this case.

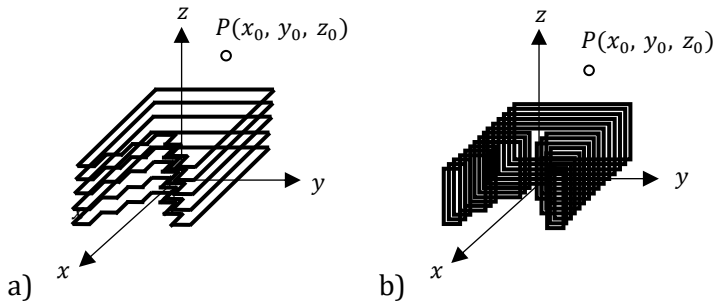

Figure 3.19: Stacked loops used to model a) coils and b) magnets with curved poles.

To illustrate likely effects, we start by simulating an elementary discrete approximation to a curved pole based on a 2-level staircase. In this simulation, 13 small wires are used to approximate the curved pole of the solenoid and 15 small loops out of a total of 50 are used to approximate the curved pole of the magnet. Each step in the pole perimeter has the same depth while its width is varied to match the true circular shape. Increasing the number of levels to obtain a smoother approximation will increase the computation time significantly. Consequently, the discrete approximation to the solenoid is expected to reduce the anticipated uniformity in lift-off distance, while the roughness of the permanent magnet surface is expected to produce unwanted effects from additional fringing fields.

Figure 3.20 shows numerical simulations for a) narrow cuboid, b) wider cuboid, c) curved pole, and d) wider curved pole solenoids. In each case, we assume 4 poles, constant currents, and constant numbers of turns. All simulations have the same lift-off distance except in Figure 3.20c where the lift-off is minimized to take advantage of the curved pole shape. In each case, the wire arrangement (including the current direction), the magnetic field on the (x, y) plane, and the variation of magnetic field H_{Cnz} around circular trajectories of different normalized radii r/R_E on the x-y plane are presented, reading from left to right.

For a clear comparison, the parameters of the narrow cuboid solenoids are as before, with an average field strength around the pipe of approximately 200 A/m. The average field strength rises to 275 A/m when the solenoid width is increased as far as possible without changing the lift-off distance. Compared with the original narrow cuboid solenoid, the

average field strength increases from 200 A/m to approximately 211 A/m when the solenoid pole is curved, and the lift-off distance is reduced to the minimum. Compared with the wider cuboid solenoid, the average field strength decreases from 275 A/m to approximately 255 A/m when the wider solenoid is curved, and the lift-off remains constant. However, the lift-off distance at the middle of the element is clearly increased by the curved pole shape. The results suggest that widening the elements or decreasing the lift-off distance increase the magnetic field strength while curving the pole has a relatively negative impact. On the other hand, the reduction in the periodic variations of the field strength, which indicates an improvement in uniformity, is hardly noticeable in this scale.

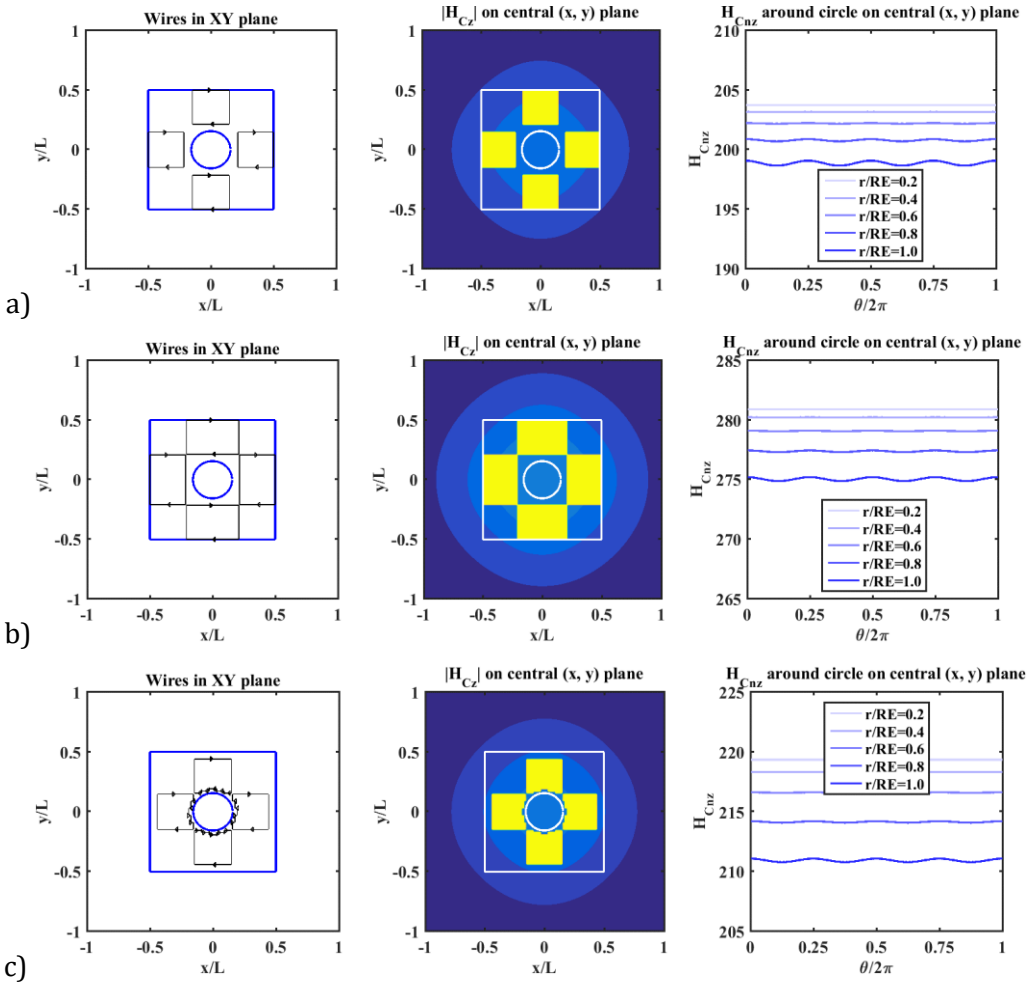

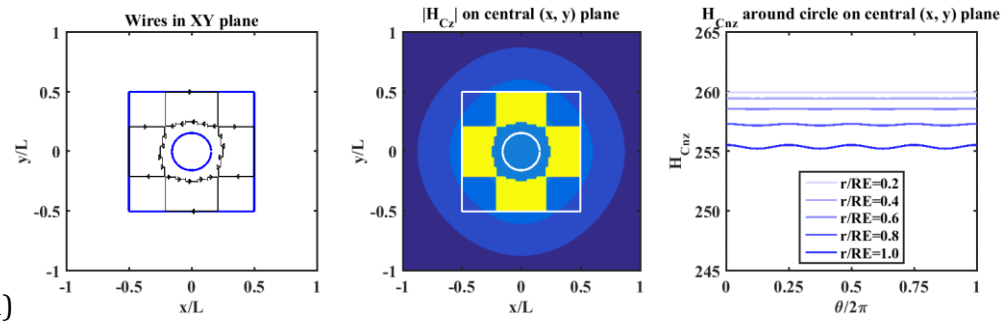

d)

Figure 3.20: Simulations on (x,y) plane of wire arrangement, magnetic field strength, and field strength around circles of different radii for 4-pole EMATs based on a) cuboid, b) wider cuboid, c) curved pole, and d) wider curved pole solenoids.

To analyze field uniformity further, Figure 3.21 compares, in a normalized scale, the variation of normalized magnetic field H_{Cnz} around circular trajectories of normalized radii r/R_E = 1 on the x-y plane. The comparisons are between a) narrow cuboid (black) and curved pole (blue) solenoids, and between b) wider cuboid (black) and wider curved pole (blue) solenoids. The narrow curved pole with a minimum lift-off distance shows a clear reduction in the periodic variations of the field when compared with the narrow cuboid. The wider curved pole also shows some reduction in the periodic variations when compared with the wider cuboid, although this is less obvious. These results indicate that curved pole solenoids do produce a more uniform magnetic field strength. The uniformity is expected to improve further not only if the lift-off distance is minimized, but also if the curve is smoother.

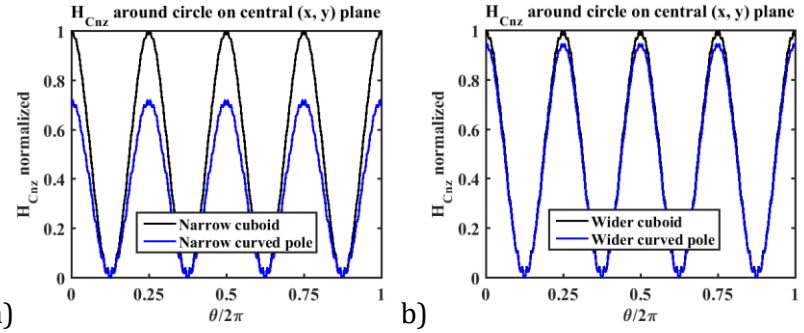

a) b)

Figure 3.21: Comparison of periodic variations of normalized magnetic field around circular trajectories for a) narrow cuboid and curved pole, and b) wider cuboid and wider curved pole solenoids.

Figure 3.22 shows similar simulation results on (x,y) plane for a) narrow cuboid, b) wider cuboid, c) curved pole (minimum lift-off distance), and d) wider curved pole permanent magnets, again with 4 poles. Compared with the cuboid permanent magnet, the maximum magnetic field is decreased by increasing the magnet width. When the narrow cuboid magnet is curved and the lift-off distance is minimized, the maximum field is slightly reduced. When the wider cuboid magnet is curved, the maximum field reduces even further. These results suggest that both curved pole magnets have a negative impact on field strength regardless of the lift-off distance. As expected, there are still sign reversals of field for all shaped permanent magnets. However, periodic variations reduce when the field reduces. The rough curved pole also introduces local sign reversals that cause slight shifts in the periodic field variations.

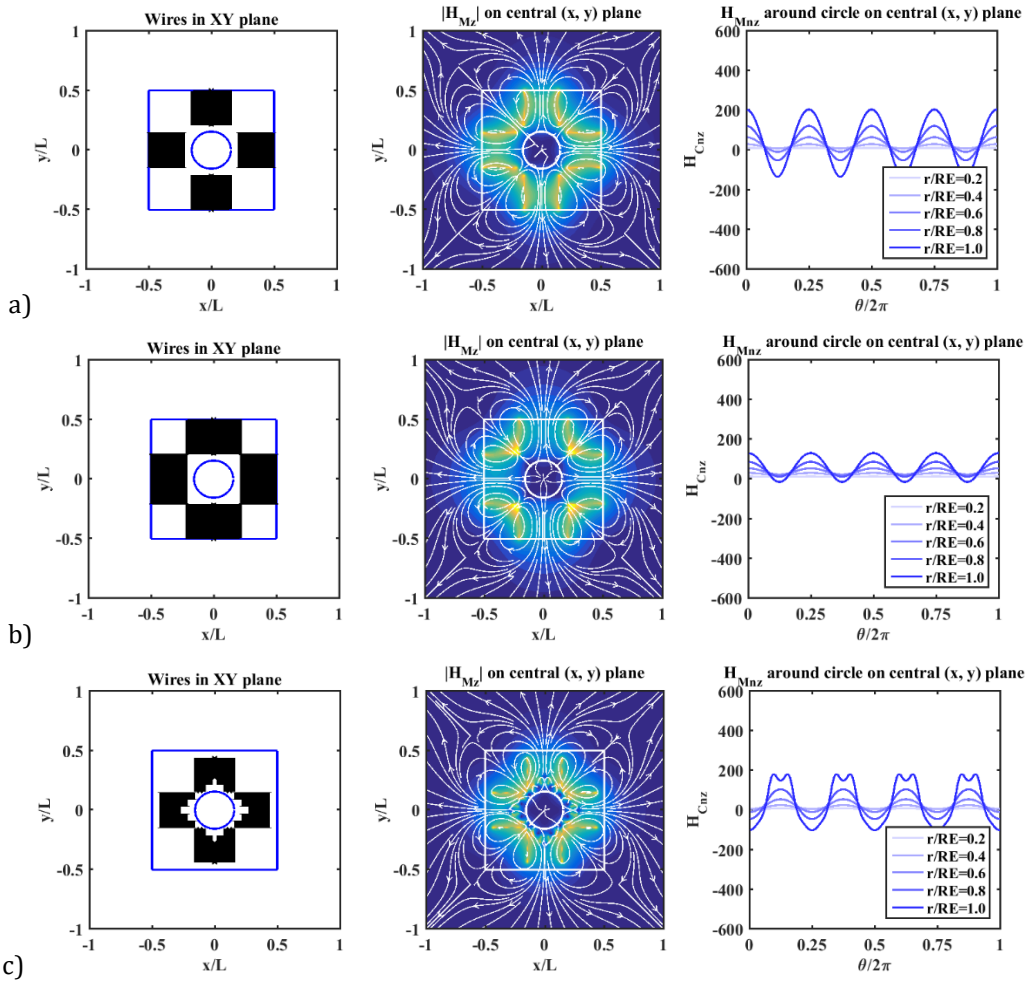

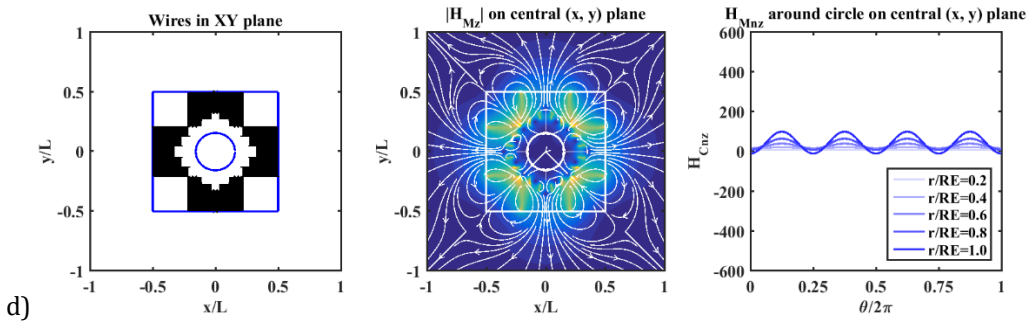

d)

Figure 3.22: Simulations on (x,y) plane of wire arrangement, magnetic field strength, and field strength around circles of different radii for 4-pole EMATs based on a) cuboid, b) wider cuboid, c) curved pole, and d) wider curved pole permanent magnets.

Two main features determine EMAT performance, the strength of the magnetic field and its uniformity. A stronger field maximizes the acoustic power, which is important to overcome noise and attenuation. Maximizing the acoustic power is more critical in oil and gas pipelines where the drive power is strictly limited to avoid catastrophic events. The narrow curved pole solenoids allow the lift-off distance to be minimized, which then increases the magnetic field strength to some extent. However, the wider cuboid solenoids produce the strongest average magnetic field among the reviewed shapes above.

Uniform fields pipe reduces the chance of exciting higher-order modes. Increasing the lift-off distance and the number of elements are obvious ways to improve uniformity. The results above suggest curved pole EMATs do offer some improvements, but these are marginal. A combination of wider cuboid solenoids and narrow cuboid magnets may produce a larger acoustic signal. Alternatively, curved pole EMATs with minimum lift-off distance or a combination of curved pole solenoids and wider cuboid magnets may maximize the longitudinal acoustic mode. These benefits require further analysis, which is beyond the scope of this thesis, and we conclude that cuboid elements may be sufficient.

3.6 Conclusion

In this chapter, the principles of piezoelectric and EMAT transducers have been introduced. EMAT has no-contact and no-couplant advantages over a piezoelectric transducer which makes it suitable for this research. A 4-element cuboid EMAT has been designed to excite mainly longitudinal modes. Mathematical models and simulations of air-cored cuboid

solenoids and permanent magnets have been presented, based on the summation of field contributions from rectangular current loops. The results show the fields of solenoids and magnets are correctly oriented to generate an axial volumetric force likely to excite the longitudinal mode. However, the magnet fields have sign reversals that may excite other modes. Modifying the cuboid shape for a better fit around the pipe involves a trade-off between improving uniformity and improving magnetic field strength. The results have shown wider cuboid solenoids and narrow cuboid magnets enlarge the acoustic signal, while curved-pole solenoids and magnets improve the uniformity. However, the advantages appear limited for this research. The next chapter will discuss time-and frequency-domain modeling of the general system, including transduction, propagation, and effects such as noise, reflections, dispersion, multi-mode propagation, and mode conversion.

4 General System Model

In this chapter, a system model will be presented. First, a simple transfer function will be developed to model dispersion-less single-mode transmission between two sensor nodes in a pipe. A single Fabry-Perot cavity then will be incorporated to model reflections. Then, a more realistic model will be explored, where dispersion and multi-mode propagation have a significant effect. The dispersive model will be built on top of the dispersion-less model. Numerical examples obtained from both models will be presented for a carrier frequency at 20 kHz and a propagation distance of 24.4 m, to match results obtained experimentally in later chapters. This distance is sufficient to mitigate the adverse effects of acoustic propagation, allowing the system to verify status for the specified frequency and pipe.

Figure 4.1 shows the system block diagram in transmission. The starting point is a baseband signal which is up-converted and transmitted as an acoustic signal on a pipe. The delayed signal is detected by correlation and then down-converted.

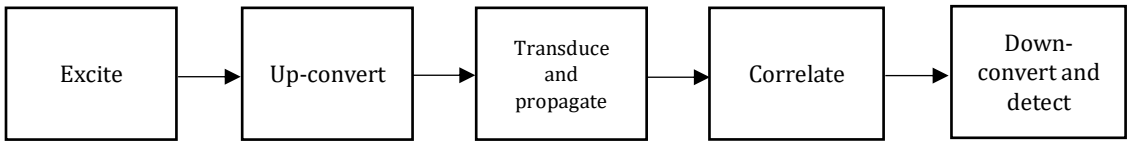

Figure 4.1: Block diagram of the general system model.

4.1 Dispersion-less Model Analysis

To begin with, a simple system is considered with reflections and noise, but without dispersion and multi-mode propagation. The input is a time-varying signal $x(t)$, which may be described using Fourier transformation as a set of sinusoidal signals with different amplitudes and frequencies $X(\omega)$ as:

$$X(\omega) = \int_{-\infty}^{\infty} x(t) e^{-j\omega t} dt \tag{4.1}$$

Where t is the time and ω is the angular frequency. As a specific example, $x(t)$ might be a rectangular function of width T and amplitude A, defined as:

$$x(t) = \begin{cases} 0, & |t| > \frac{T}{2} \\ A, & |t| \leq \frac{T}{2} \end{cases}$$

(4.2)

Its Fourier transform is therefore given by:

$$X(\omega) = AT\ \mathrm{sinc}(\frac{\omega T}{2})$$

(4.3)

If x is used to modulate a carrier of angular frequency ω_c, the up-converted signal x' is:

$$x'(t) = x(t)e^{j\omega_c t}$$

(4.4)

The shift theorem then implies that the upconverted signal in the frequency domain is:

$$X'(\omega) = X(\omega + \omega_c)$$

(4.5)

In a non-dispersive single-mode channel, the signal propagates a distance d with constant phase velocity v_{ph}. The channel transfer function $T_{ch}(\omega)$ is therefore:

$$T_{ch}(\omega) = e^{-j\mathrm{k}d} = e^{-j\frac{\omega}{v_{ph}}d}$$

(4.6)

Where k is the wavenumber. The spectrum after propagating a distance d is therefore:

$$X_i''(\omega) = X(\omega + \omega_c)T_{ch}(\omega)$$

(4.7)

In the time domain, the delayed signal is the inverse Fourier transform of $X''(\omega)$ namely:

$$x_i''(t) = x'(t - t_{\mathrm{d}})$$

(4.8)

Where the time delay t_{d} is clearly:

$$t_{\mathrm{d}} = \frac{d}{v_{ph}}$$

(4.9)

More generally, a pipeline system will have internal joints and additional terminating features. Both will cause reflections of any propagating acoustic wave, and both may be modeled as Fabry-Perot cavities, by analogy with effects that occur in optics [144, 145] and ultrasonics [146, 147]. We first consider, an internal cavity formed from two reflectors separated by a distance *d*. Figure 4.2 shows a schematic of such a cavity. In this case, multiple reflections will be generated at $3t_{\mathrm{d}}$, $5t_{\mathrm{d}}$, $7t_{\mathrm{d}}$ and so on.

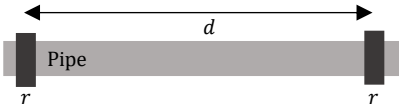

Figure 4.2: Schematic of a pipe with 2 reflectors forming a Fabry-Perot cavity.

If the transmission and reflection coefficients are T and R at each reflector, the amplitude that passes straight through both reflectors is given by:

$$A_{ch} = T^2 e^{-j\mathrm{k}d}$$

(4.10)

The amplitude for a wave that travels up and down the cavity, bouncing off each reflector once and traveling a distance *3d* is:

$$A_{TR1} = T^2 R^2 e^{-3j\mathrm{k}d}$$

(4.11)

Similarly, the amplitude that follows a zig-zag path, bouncing off each reflector twice and traveling a distance *5d* is:

$$A_{TR2} = T^2 R^4 e^{-5j\mathrm{k}d}$$

(4.12)

There is an infinite number of higher-order paths that have similar forms. The overall transfer function of the channel can be found as the sum of all such paths, as:

$$T_{ch,r} = A_{ch} + A_{TR1} + A_{TR2} + \cdots = T^2 e^{-j\mathrm{k}d} + T^2 R^2 e^{-3j\mathrm{k}d} + T^2 R^4 e^{-5j\mathrm{k}d} + \cdots \tag{4.13}$$

This series may be re-arranged to give:

$$T_{ch,r} = T^2 e^{-j\mathrm{k}d}\left(1 + R^2 e^{-2j\mathrm{k}d} + R^4 e^{-4j\mathrm{k}d} + \cdots\right) \tag{4.14}$$

Summing the infinite series, we get:

$$T_{ch,r} = \frac{T^2 e^{-j\mathrm{k}d}}{(1 - R^2 e^{-2j\mathrm{k}d})} \tag{4.15}$$

More realistically, any pipeline will have multiple joints, with each joint consisting of the junction between a pipe, a short connector, and a pipe. To analyze a cascade of joints, multiple partial reflectors may be modeled as multiple Fabry-Perot cavities. These reflectors would be expected to have similar impedance on either side of the joint, an uncommon arrangement. This arrangement requires S-parameter analysis to determine the likely nature of the transmission and reflection coefficients.

If a reflector is passive and lossless, its S-matrix is unitary. Consequently:

$$\boldsymbol{S}^{*T}\boldsymbol{S} = 1 = \begin{bmatrix} {S_{11}}^* & {S_{21}}^* \\ {S_{12}}^* & {S_{22}}^* \end{bmatrix}\begin{bmatrix} S_{11} & S_{12} \\ S_{21} & S_{22} \end{bmatrix} = \begin{bmatrix} 1 & 0 \\ 0 & 1 \end{bmatrix} \tag{4.16}$$

From the unitary relation, the moduli of the parameters are related as:

$$|S_{11}|^2 + |S_{21}|^2 = |S_{12}|^2 + |S_{22}|^2 = 1 \tag{4.17}$$

And the phases of the parameters are related as:

$$-\arg(S_{11}) + \arg(S_{12}) = -\arg(S_{21}) + \arg(S_{22}) + \pi \tag{4.18}$$

In addition, symmetry implies that:

$$S_{11} = S_{22},\ S_{12} = S_{21} \tag{4.19}$$

With these constraints, it is simple to show that transmission and reflection coefficients require a 90° phase shift between them in this case. For example, if R is real, then $T = jA$ where A is real, and vice versa. With these assumptions, it is simple to model a cascade of reflectors, without needing to know the exact values of the coefficients.

For example, Figure 4.3 shows a schematic of three partial reflectors; r_1 and r_2 are separated by distance d_a, while r_2 and r_3 are separated by d_b.

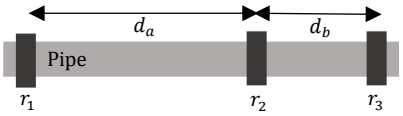

Figure 4.3: Schematic of a pipe with 3 partial reflectors.

Following the previous analysis, the transmission coefficient of a single cavity between r_2 and r_3 may first be found as:

$$T_{2,ref} = \frac{T_2 T_3 e^{-j\mathrm{k}d_b}}{(1 - R_2 R_3 e^{-j2\mathrm{k}d_b})} \tag{4.20}$$

Similarly, the reflection coefficient of the single cavity may be found as:

$$R_{2,ref} = R_2 + {T_2}^2 R_3 e^{-j2\mathrm{k}d_b} + {T_2}^2 R_3 R_2 R_3 e^{-j4\mathrm{k}d_b} + {T_2}^2 R_3 {R_2}^2 {R_3}^2 e^{-j6\mathrm{k}d_b} + \cdots \tag{4.21}$$

$$R_{2,ref} = R_2 + {T_2}^2 R_3 e^{-j2\mathrm{k}d_b}(1 + R_2 R_3 e^{-j2\mathrm{k}d_b} + {R_2}^2 {R_3}^2 e^{-j4\mathrm{k}d_b} + \cdots) \tag{4.22}$$

$$R_{2,ref} = R_2 + \frac{{T_2}^2 R_3 e^{-j2\mathrm{k}d_b}}{(1 - R_2 R_3 e^{-j2\mathrm{k}d_b})} \tag{4.23}$$

The overall response of the three-reflector system can then be modeled using the reflection and transmission coefficients above in a further Fabry-Perot model. The overall transmission coefficient is:

$$T_{3,ref} = \frac{T_1 T_{2,ref} e^{-jkd_a}}{\left(1 - R_1 R_{2,ref} e^{-j2kd_a}\right)} \tag{4.24}$$

Similarly, the overall reflection coefficient is:

$$R_{3,ref} = R_1 + \frac{{T_1}^2 R_{2,ref} e^{-j2kd_a}}{\left(1 - R_1 R_{2,ref} e^{-j2kd_a}\right)} \tag{4.25}$$

To illustrate this, we shall examine the difference in the transfer functions obtained with single and multiple resonant cavities. Figure 4.4a shows the relation between the transmitted (blue) and reflected (red) powers with kd_b/π for a two reflector system, where the cavity length is d_b. Figure 4.4b shows the corresponding result for a three-reflector system, where the cavity lengths are d_a and d_b. The sum of the powers (green) is unity in both cases, as expected in a lossless system. The transmission and reflection coefficients are assumed arbitrarily, as $T_1 = 0.8352$, $R_1 = -j0.55$, $T_2 = 0.9367$, $R_2 = -j0.35$, $T_3 = 0.8352$, and $R_3 = -j0.55$, and the distance between reflector 1 and 2, d_a, is 15m, while the distance between reflector 2 and 3, d_b, is 10m. In both cases, periodic fluctuations in power may be seen; however, there are clearly multiple periodicities in the two-cavity case.

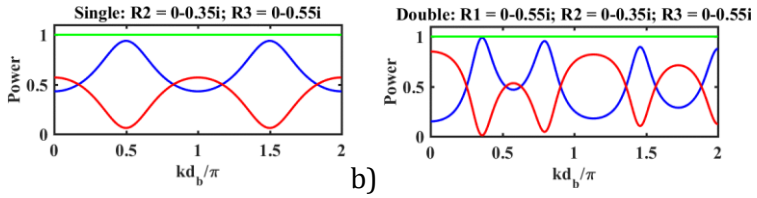

a) b)

Figure 4.4: Relation between transmitted and reflected power for a) two and b) three partial reflectors.

In contrast, a finite pipe (for example, as used in later experiments) may have open ends, as shown in Figure 4.5. Such a system may be considered as a single cavity with perfect reflectors, so that any acoustic wave present remains entirely trapped between them.

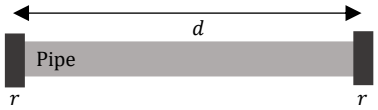

Figure 4.5: Schematic of a pipe with two perfect reflectors.

In this type of cavity, there is only a reflection coefficient, which has the value $R = 1$. In this case, the transfer function (now relating the wave amplitudes at either end of the cavity, just inside the reflectors) is given by:

$$T_{ch,r} = \frac{e^{-jkd}}{\left(1 - e^{-2jkd}\right)} \tag{4.26}$$

This transfer function can be related to the original channel transfer function in Equation 4.6 as:

$$T_{ch,r} = \frac{T_{ch}}{\left(1 - e^{-2jkd}\right)} \tag{4.27}$$

Moving forward, other effects must occur in a real pipe system. Particularly, there will be acoustic noise, so that a more realistic expression for the received signal is:

$$x_o''(t) = x''(t) + n(t) \tag{4.28}$$

Where $n(t)$ is white noise. If the spacing between nodes is large, the signal-to-noise ratio, SNR, may be low. However, a matched filter may be used to maximize SNR, by correlating the received signal with a reference signal [148] as shown in Figure 4.6.

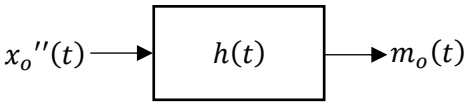

Figure 4.6: Block diagram of a matched filter.

The output of the correlator is a modified signal $m_o(t)$, given by [149]:

$$m_o(t) = x_o''(t) * h(t)$$

(4.29)

Here $h(t)$ is the impulse response of the filter and $*$ denotes convolution. The output signal can be described in terms of signal and noise components as:

$$m_o(t) = m(t) + n_o(t) = x''(t) * h(t) + n(t) * h(t)$$

(4.30)

Where $m(t)$ is the signal filter output and $n_o(t)$ is the noise filter output.

Examples of correlation detection in acoustics may be found in [150-152]. Correlation can be carried out on up-converted or baseband signals. Here we assume the former. In either case, it can be shown [153] that the optimum reference signal is a time-reversal of $x'(t)$ so the impulse response of the matched filter is:

$$h(t) = x'^{*}(T_R - t)$$

(4.31)

Where T_R is the pulse width at the receiver. A similar result may be achieved in the frequency domain by simple multiplication, as:

$$M(\omega) = X_o{}''(\omega)H(\omega)$$

(4.32)

Here $M(\omega)$ and $H(\omega)$ are the Fourier transforms of $m(t)$ and $h(t)$. The baseband signal may then be recovered by rectification and low pass filtering. For example, the received and reference signals may both have rectangular envelopes. In this case, the down-converted signal will have a triangular envelope with a duration of $2T$ and maximum amplitude AT at T. The input SNR to the filter is given by:

$$\text{SNR}_{in} = \frac{P_{x''}}{P_n} = \frac{\int_0^{T_R} x''^2(t)dt}{E\{|n(t)|^2\}}$$

(4.33)

Where $P_{x''}$ is the average filter input power, P_n is the average noise power and E refers to the expected value. The output SNR is given by:

$$\mathrm{SNR}_o = \frac{P_m}{P_{n_o}} = \frac{\int_0^{T_{R_o}} m^2(t)dt}{E\{|n_o(t)|^2\}}$$

(4.34)

Where P_m is the average filter output power, P_{n_o} is the average output noise power and T_{R_o} is the pulse width at the filter. The relation between SNR_o and SNR_{in} is known as the processing gain G, and is given by [154]:

$$G = \frac{\mathrm{SNR}_o}{\mathrm{SNR}_{in}}$$

(4.35)

This implies that the processing gain depends on the signal duration. Since the correlation peak is increased by a factor equal to the pulse width, the SNR_o is increased by the same factor. Correlation with a coherent signal yields a higher peak, while the correlation with non-coherent noise lowers the noise floor.

4.2 Dispersion-less Model Implementation

A discrete-time implementation of the above has been developed using MATLAB. The input signal is a complex time-domain pulse that is used to modulate a carrier. The fast Fourier transform function 'fft' is used to convert to the frequency domain. The 'fftshift' function is used to reorder the Fourier transform components in ascending order. The frequency domain signal is multiplied by the channel transfer function to simulate propagation and (if necessary) any reflections. The 'ifftshift' and 'ifft' functions are used for ordering and inverse transform respectively to transform the signal back to the time domain. The model uses a fixed phase velocity of $v_{ph} = 3578$ m/s, to mimic an acoustic wave in bulk copper.

Correlation detection is modeled as shown in Figure 4.7. A copy of the upshifted signal before transmission is correlated with the received signal using the 'xcorr' function. The function 'abs' is used for rectification. Low pass filtering is implemented by using the 'conv' routine, with a rectangular window; the result is equivalent to a filter with a 'sinc' function response, with a cutoff frequency that is inversely proportional to the window length.

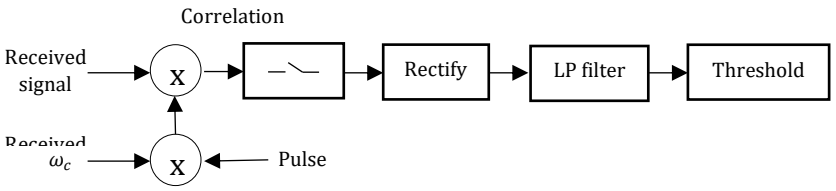

Figure 4.7: Block diagram of correlation and down-conversion.

As an example that would be used in later simulations and experiments, Figure 4.8 shows two time-domain signals, a baseband rectangular pulse with a 0.3 s pulse width (in red) and the upshifted signal (in black), assuming a 20 kHz carrier frequency. At this frequency, the upshifted pulse consists only of 6 cycles (in abbreviation cyc/chip, where chip is 1 in this example).

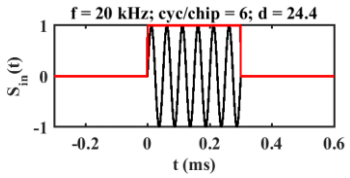

Figure 4.8: Example envelope (red) and a modulated signal (black) for typical signal parameters.

Figure 4.9 shows similar time-domain signals on an extended scale. Figure 4.9a shows the transmitted upshifted signal (6 cyc/chip at 20 kHz), and Figure 4.9b shows the received signal after propagating 24.4 m. The amplitude of the received signal is unchanged, and the only effect of a non-dispersive channel is a time delay (here, t_d = 6.81 ms).

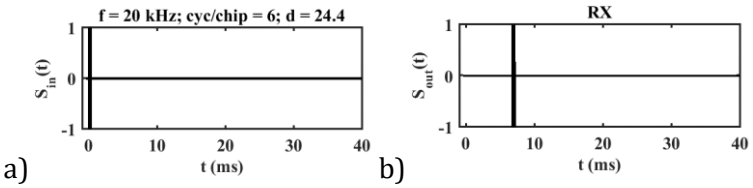

Figure 4.9: a) Transmitted and b) received signals, for example parameters.

Figures 4.10 a) and b) show the spectra of the two signals. Both are 'sinc' functions centered on the carrier frequency; however, the two spectra at the moment are identical, since the transfer function of the channel has unit modulus.

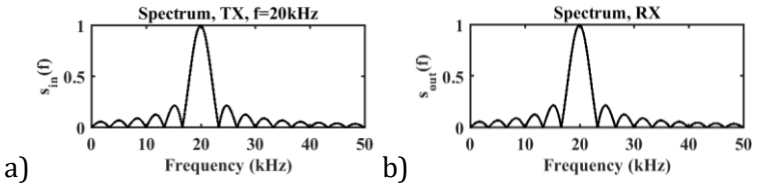

Figure 4.10: Spectra of a) a transmitted and b) a received signals, for example parameters.

Reflections may be modeled by using a modified transfer function that models a single Fabry-Perot cavity with perfect reflectors, as described above. In addition, attenuation may be added to mimic a practical single cavity with perfect reflectors (a piece of copper pipe). For example, Figure 4.11 shows the channel transfer function, assuming that d = 24.4 m. The effect of multiple reflections is to add amplitude oscillations. Attenuation α may control the minimum amplitude value (Here α is arbitrary assumed to be 0.03).

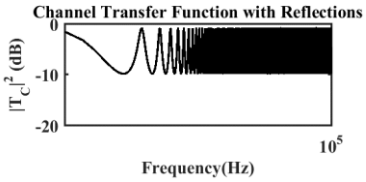

Figure 4.11: Channel transfer function with multiple reflections.

Figure 4.12 shows the effect of the Fabry-Perot response in the time domain. Figure 4.12a shows the transmitted pulse, and Figure 4.12b shows the pulse received at a distance of 24.4 m. Here the first two multiple reflected pulses can be seen at $t = 3t_d$ and $t = 5t_d$; both transmitted and reflected pulses clearly have reduced amplitudes that decay exponentially following a typical ring-down pattern.

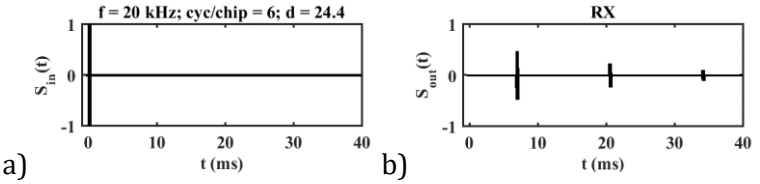

Figure 4.12: a) Transmitted and b) received signal in a system with multiple reflections.

We now consider other effects, ignoring reflections and attenuation for the time being, Figure 4.13 shows in the time-domain an autocorrelation signal (black) and down-converted envelope (red) of the previous example signal. A triangular signal is the

autocorrelation of a rectangular pulse and an upshifted triangle with a carrier frequency is the autocorrelation of an upshifted pulse with the same frequency. The correlation signal has twice the duration of the received and reference signals, and the correlation peak is at the center of the triangle. Note that the correlation signal has been normalized here.

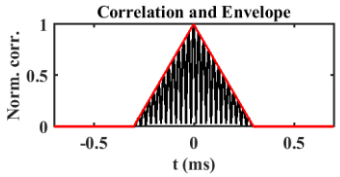

Figure 4.13: Autocorrelation of a pulse (black) and its envelope (red).

Figure 4.14 shows the effect of increasing the number of cycles in the transmitted signal. Results are shown for a) 1 cycle, and b) 2 cycles. In each case, the left-hand diagrams show the upshifted pulse, the central diagrams its frequency spectrum, and the right-hand diagrams show the correlation envelope (has a triangular shape). The spectra of upshifted pulses are 'sinc' functions centered on the carrier frequency with bandwidth relative to the number of cycles. As the number of cycles increases, the spectrum narrows while the correlation signal widens. To reduce the effects of dispersion (discussed later), long pulses will be required; this will inevitably lead to low data rates.

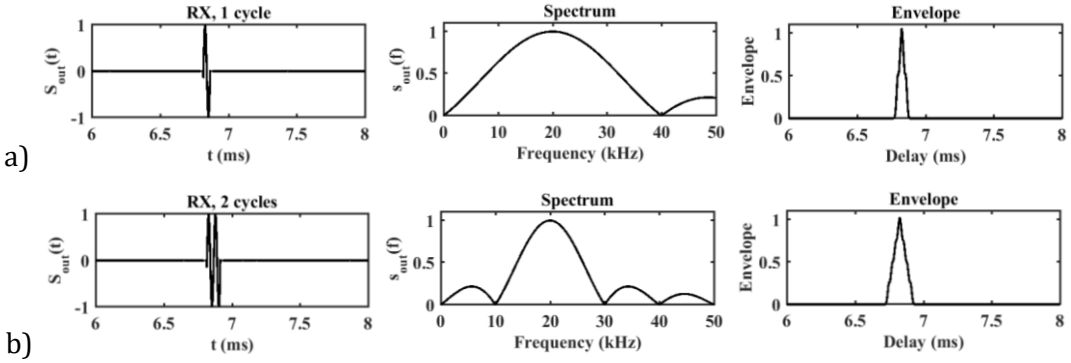

Figure 4.14: Received signal (left), its spectrum (center) and its autocorrelation envelope (right) for pulses containing a) 1 and b) 2 cycles.

Figure 4.15 shows the received frequency spectrum of a propagated signal, a) without and b) with multiple reflections and attenuation (and again in c), in an expanded view of the main lobe). In both cases, the spectra are 'sinc' functions centered on the carrier frequency

as expected for upshifted pulses. However, the effect of reflection is to introduce oscillations in the spectrum due to the coherent addition and cancellation of the incident and reflected pulse spectra. Although they must have the same frequency content in isolation, their sum must generally have a different spectrum since each frequency component in the reflected pulse will see a different phase delay.

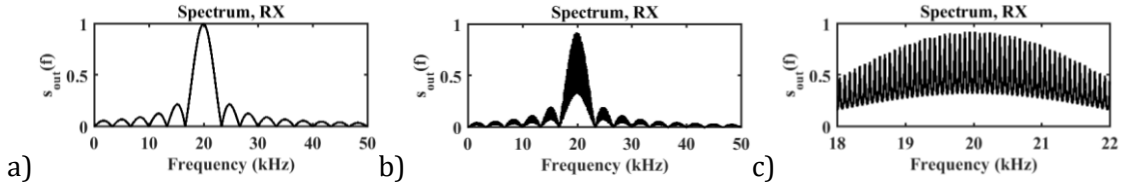

Figure 4.15: Frequency spectra of received signal a), and b) with reflections and attenuation; c) expanded view of the main lobe with reflections and attenuation.

Figure 4.16 a) shows the received noiseless signal (an incident and two reflected pulses) before signal processing, and b) its envelope after correlation and down-conversion. As expected, the incident and reflected pulses and their envelopes are both clear. Figure 4.16 c) shows a similar noisy signal with an SNR of 10dB, and d) its envelope after correlation and down-conversion. While the incident and reflected pulses are almost buried under noise, the SNR of their correlation envelopes has improved considerably by an amount equivalent to the processing gain.

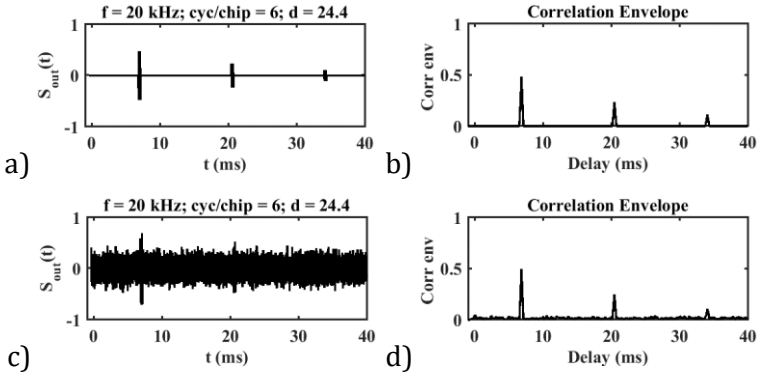

Figure 4.16: Multiply reflective system: a) received noiseless signal and b) its correlation envelope, c) received noisy signal and d) its correlation envelope.

Figure 4.17 shows the variation of processing gain with the number of bits (the length) of a baseband rectangular signal when SNR_{in} is 0.1 (red), 1 (blue) and 10 (black). It shows the

processing gain equals the number of bits, which in this numerical example is equal to the pulse width. Large SNR_{in} gives smoother lines than small SNR_{in} since the signal is buried in noise in the latter case. For similar reasons, small SNR_{in} gives inaccurate results at low processing gain.

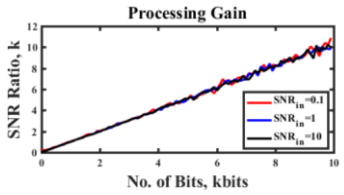

Figure 4.17: Relation between processing gain and number of bits when SNR_in is 0.1 (red), 1 (blue) and 10 (black).

4.3 Dispersive Model Analysis

To increase the realism of the system model, dispersion, multi-mode propagation and mode conversion must be incorporated, together with any frequency dependent effects due to the transducers. To simplify the additional explanations needed, we ignore the effect of reflections. Figure 4.18 shows the block diagram of the dispersive model. The baseband signal is first excited and up-converted. It is then transduced as an acoustic signal on a multi-moded, dispersive pipe. The propagated signal is transduced back and processed by correlation and then down-converted. Transduction, propagation, and detection are assumed to be implemented using a power amplifier for signal amplification, an EMAT for transmission, a copper pipe for propagation, a microphone for reception, and lastly a low-noise signal amplifier for amplification again. Each of these functions has a frequency response that will be described here. Further processing techniques such as short-time Fourier transform may also be applied.

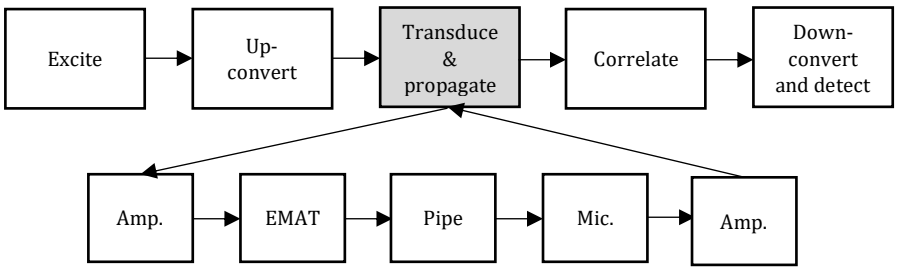

Figure 4.18: Block diagram of the dispersive system model.

Amplifier

An amplifier is needed to inject sufficient power into the EMAT to generate a detectable acoustic signal. For comparison with later experimental results, the amplifier transfer function is assumed to be given by:

$$T_a = \frac{j(\frac{\omega}{\omega_{a1}})^n}{(1+\frac{\omega}{\omega_{a1}})^n(1+\frac{\omega}{\omega_{a2}})^m} \tag{4.36}$$

This response describes an amplifier with low- and high-frequency cutoff points. The parameter ω_{a1} is the low cut off frequency, n controls the low-frequency roll-off, ω_{a2} is the high cut-off frequency, and m to controls the high frequency roll-off. Figure 4.19 shows the transfer function obtained when f_{a1}= 50 Hz, n=1, and f_{a2} = 300 kHz and m=2 to match later experiments. The response is clearly flat over more than the audible frequency range, falling off at low and high frequencies as expected for an audio amplifier.

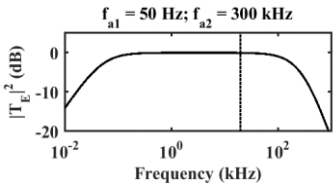

Figure 4.19: Power amplifier frequency response for typical simulation parameters.

EMAT

The operation of the EMAT has been described mathematically in Chapter 3, and a Lorentz force proportional both to angular frequency and to amplitude has been discussed. The EMAT impedance itself may be described as a resistance R_L, connected in parallel to a self-capacitance C and in series to an inductance L. Figure 4.20a shows an EMAT equivalent circuit connected to a source V_o with impedance Z_o.

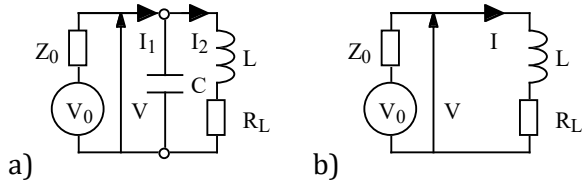

Figure 4.20: EMAT equivalent circuits: a) detailed, and b) simplified.

The full EMAT equivalent circuit is given by:

$$I_1 Z_o + I_2(R_L + j\omega L) = V_o \tag{4.37}$$

$$I_2(R_L + j\omega L) + \frac{(I_2 - I_1)}{\mathrm{j}\omega C} = 0 \tag{4.38}$$

Solving Equation 4.37 and 4.38 for $\frac{I_2}{V_0}$, we get:

$$\frac{I_2}{V_0} = \frac{1}{\{R_L + j\omega L + (j\omega C R_L + 1 - \omega^2 LC)Z_o\}} \tag{4.39}$$

Considering the angular frequency dependence previously mentioned, which implies that the volumetric Lorentz force is proportional to $j\omega L I_2$, the transfer function for electrical-to-acoustic transduction is given by:

$$T_e = kj\omega L \frac{I_2}{V_0} \tag{4.40}$$

Where k is constant. Substituting Equation 4.39 in Equation 4.40 then leads to a transfer function:

$$T_e = \frac{kj\omega L}{\{R_L + j\omega L + (j\omega C R_L + 1 - \omega^2 LC)Z_o\}} \tag{4.41}$$

This expression is relatively complicated. However, as found experimentally, the self-capacitance C is small at low frequencies. Figure 4.20b shows a simpler circuit that ignores this term. The transfer function of this simpler circuit is:

$$T_e = \frac{kj\omega L}{(Z_o + R_L + j\omega L)} \tag{4.42}$$

Since the EMAT is connected to a power amplifier, Z_o is the output impedance of the amplifier. Since Z_o will be small, to maximize the voltage and current delivered to the load, it can be considered negligible. Consequently, the simplest EMAT transfer function is:

$$T_e = \frac{kj\omega L}{(R_L + j\omega L)} \tag{4.43}$$

This result may be written as:

$$T_e = \frac{j(\frac{\omega}{\omega_e})}{1 + j\left(\frac{\omega}{\omega_e}\right)} \tag{4.44}$$

Where, ω_e is the low-frequency cutoff, and is determined by $\frac{L}{R_L}$. Figure 4.21 shows an example EMAT transfer function, assuming that the breakpoint lies at 5.7 kHz to match later experiments. Below the breakpoint, the response has a low frequency roll-off, while above the breakpoint the response is flat. The EMAT should clearly be operated in this regime.

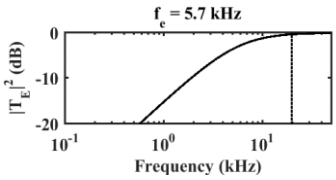

Figure 4.21: Example EMAT frequency response.

.

Channel

A copper pipe is used for signal propagation. Its transfer function is the same as the channel transfer function, T_{ch}, discussed previously. Since the pipe supports multiple modes, a transfer function may be found for each mode. In addition, a modified channel transfer function, T_{mc}, can be developed to model mode conversion, in the form:

$$T_{mc} = A_{mc} e^{-jk_1 d_1} e^{-jk_2 d_2} \tag{4.45}$$

Where A_{mc} is the mode conversion amplitude, both the wavenumber k_1 and the traveled distance d_1 are for the first mode, and both the wavenumber k_2 and the traveled distance d_2 are for the second mode.

Microphone

Finally, a microphone will be used to detect the signal. Commercially-available microphones typically operate over a frequency range of 2 Hz to 20 kHz, have a flat response between 0.3 kHz and 18.5 kHz, and have built-in amplifiers. The transfer function of such an amplifier can be written as:

$$T_m = \frac{j(\frac{\omega}{\omega_{m1}})}{(1+\frac{\omega}{\omega_{m1}})(1+\frac{\omega}{\omega_{m2}})} \tag{4.46}$$

Here, ω_{m1} is the low cut off frequency and ω_{m2} is the high cut-off frequency. Figure 4.22 shows a microphone transfer function, assuming that the low cut-off frequency is at 0.3 kHz and the high cut-off is at 18.5 kHz to match later experiments. There are three ranges: a low frequency roll-off range, a flat response range for the mid frequencies, and a high-frequency roll-off range. In reality, the flat response is an approximation since practical microphones may have resonances within due to their diaphragm construction. Clearly, the operating frequency should lie at intermediate frequencies, above the low-frequency cut-off of the EMAT and below the high frequency cut-off of the microphone

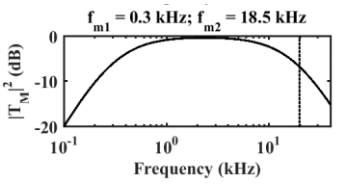

Figure 4.22: Example microphone frequency response.

4.4 Dispersive Model Implementation

A discrete-time implementation was also developed for dispersive systems using MATLAB, based on a modified transfer function that combined the transducer responses above with

the channel response of a particular mode. This MATLAB implementation can be found in Appendix 1. The overall response, T_{dm}, is given by:

$$T_{dm} = T_a . T_e . T_{ch} . T_m \tag{4.47}$$

Here T_{ch} represents the transfer function of a particular mode, or of a mode generated by conversion. For example, Figure 4.23 shows the transfer function of the dispersive model for a longitudinal mode in a copper pipe with 15mm OD and 1mm wall thickness. Due to the multiplications of multiple transfer functions of different blocks (devices), the channel response has a long low frequency roll-off range and a long high frequency roll-off range with a limited flat range response. In this example, the carrier frequency at 20 kHz lies in the high roll-off range.

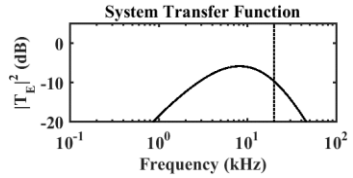

Figure 4.23: Dispersive model transfer function for the L(0,1) mode.

Other than dispersion, the implementation of the input signal, propagation, correlation, and down-conversion here are similar to the dispersion-less model. Dispersion data needed for this model are calculated using the numerical solver PCDisp, exported as .csv files, and read into the MATLAB simulator. Ignoring the torsional mode, two modes can propagate in a copper pipe with 15mm OD and 1mm wall thickness around the carrier frequency 20 kHz; longitudinal L(0,1) and flexural F(1,1) modes.

Wavenumbers k may be found from the dispersion curves of phase velocities v_{ph} as, $k = \omega / v_{ph}$. Using this data, a channel transfer function can be computed for each mode. For example, Figure 4.24a shows an example of an undispersed, upshifted rectangular pulse in the time domain, assuming 20 kHz carrier frequency and a pulse duration of 6 cycles. Figure 4.24b shows a similar pulse after propagation as the L(0,1) mode for a short distance. The pulse is now dispersed, so that the amplitude is reduced and the pulse is stretched in time.

Figure 4.24c shows a similar response after a larger propagation distance. The dispersed pulse is now stretched out much more in time, and its amplitude has reduced even further.

Dispersion has a considerable effect on correlation envelopes. For example, Figure 4.24d shows the correlation envelope of the non-dispersed pulse in Figure 4.24a, while Figures 4.24e and 4.24f show envelopes corresponding to Figures 4.24b and c. As the propagation distance increases, the correlation peak reduces in amplitude and loses its sharpness, reducing the effective processing gain and the associated discrimination against noise.

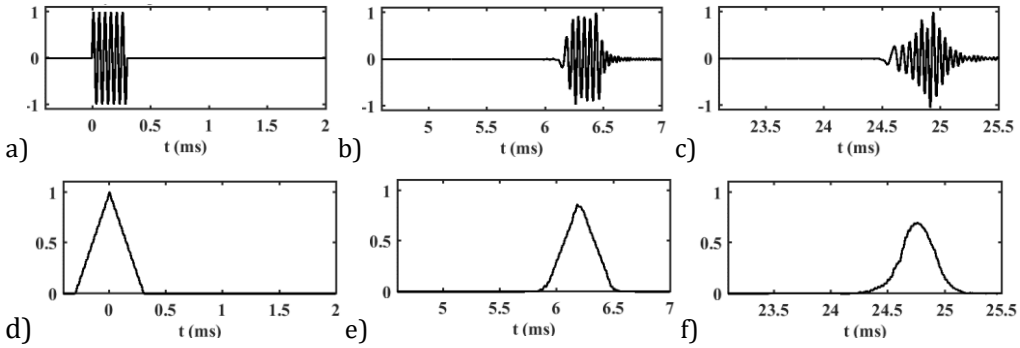

Figure 4.24: a) Non-dispersive, b) dispersive, and c) dispersive and delayed pulses; d) - f) the corresponding correlation envelopes.

Figure 4.25 shows similar time-domain signals on an extended scale, now assuming that the L(0,1) and F(1,1) modes are both excited and detected together. Since attenuation is not considered here, the total received amplitude is assumed to be 1: the L(0,1) mode is assumed to have 0.75 amplitude, and the F(1,1) mode has 0.25 amplitude. In this model, dispersion curves are again computed using PCDisp. However, the process of manufacturing copper pipes (smelting, casting, and annealing) may alter mechanical properties. Instead of using generic parameters for bulk copper, dispersion data are therefore adjusted slightly to match later experiments with real pipes. Figures 4.25a and 4.25b show the transmitted and received signals after propagating 24.4 m. The propagation distance is clearly sufficient to separate the two modes and the two delayed pulses represent the longitudinal mode (v_{ph}=3968 m/s at 20 kHz) and flexural mode (v_{ph}=1286 m/s). Clearly, F(1,1) has higher dispersion. Figure 4.25c shows the corresponding correlation envelope; the F(1,1) mode

has a considerably reduced (although still recognizable) correlation peak. These results emphasize the need for low-dispersion modes to achieve usable performance.

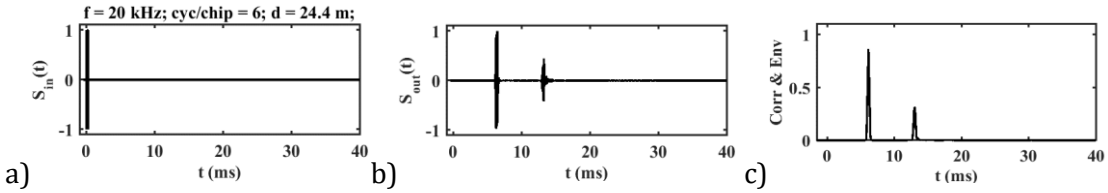

Figure 4.25: a) Transmitted b) received signals and c) their correlation envelopes assuming a pulse containing 6 cycles at 20 kHz.

Figures 4.26a and 4.26b show the spectra of the transmitted and received signals. Both are sinc functions centered on the carrier frequency. However, the received spectrum has oscillations. These are similar to reflected spectra, but the oscillations now arise from the coherent addition and cancellation of the longitudinal and flexural mode spectra. In each case, the signal bandwidth is extended.

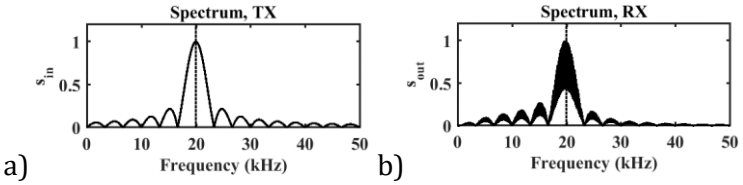

Figure 4.26: Spectra of a) a transmitted and b) a received signals of example parameters.

Figure 4.27 shows the effect of increasing the pulse length in the transmitted signal. Results are shown for a) 1 cycle, and b) 2 cycles. In each case, the left-hand diagrams show the received signals, and the right-hand diagrams show the correlation envelopes. In both cases, the first received pulse is the L(0,1) mode and the second pulse is the F(1,1) mode. As the number of cycles is increased, dispersion is reduced, and the correlation envelope is sharpened, even for the more dispersive mode. These results emphasize the need to reduce the signal bandwidth.

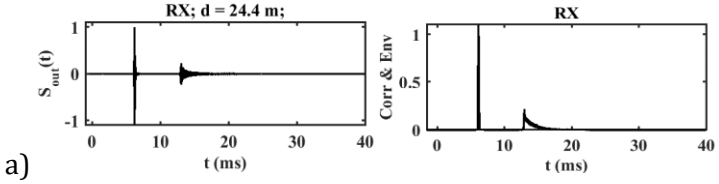

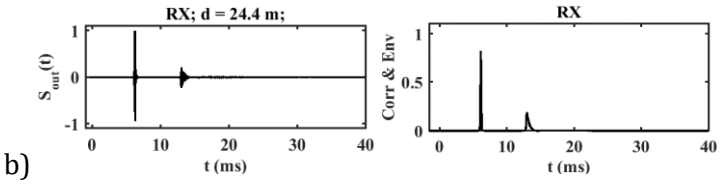

Figure 4.27: Received signal (left), and its autocorrelation envelope (right) for pulses containing a) 1 and b) 2 cycles.

If mode conversion occurs, results are more complicated, because signals propagate at different velocities in different sections of the pipe. For example, Figure 4.28 shows the dispersion curves for a) phase velocity, and b) group velocity, when mode conversion takes place at 9.8m from the transmitter (chosen to match the position of a mode conversion source in later experiments). In addition to the L(0,1) (blue), and F(1,1) (green) modes, conversions from longitudinal to flexural modes (cyan) and from flexural to longitudinal modes (magenta) are shown. Both of the mode conversion curves are similar to that of the F(1,1) mode but are faster.

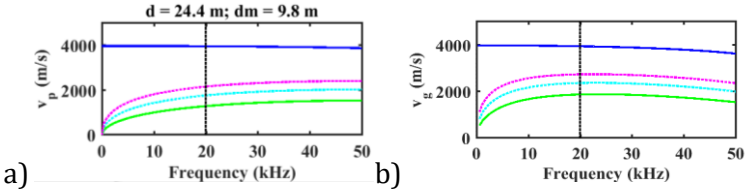

Figure 4.28: Dispersion curves, a) phase velocity, and b) group velocity including multi-mode propagation and mode conversion.

The existence of these components leads to additional delayed signals. For example, Figure 4.29a shows outputs obtained when mode conversion takes place at 9.8m from the transmitter. Figure 4.29b shows similar results when mode conversion takes place 22m from the transmitter, another location observed experimentally. In each case, the left-hand diagrams show the received signals, and the right-hand diagrams show the correlation envelopes. There are clearly four pulses, corresponding to the L(0,1) mode, L(0,1) -> F(1,1) mode conversion, F(1,1) -> L(0,1) mode conversion, and the F(1,1) mode, respectively. The amplitudes of both mode conversions are assumed to be 0.1. In addition, Figure 4.29b shows interference between different signal components, which may be challenging to analyze. The interference may worsen if additional sources of mode conversion or reflection exist.

In any such case, it is essential to maximize the sharpness of the correlation peak, to allow the different components to be separated.

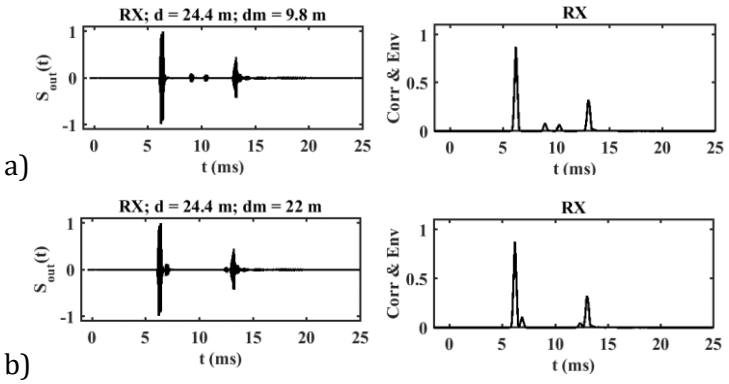

Figure 4.29: Received signal (left), and its autocorrelation envelope (right) for mode conversions at a) 9.8m and b) 22m from the detector.

Many signal processing techniques can be used to distinguish the sub-components of complicated signals. The FFT provides insight about frequency content but without any temporal information. In contrast, the short-time Fourier transform STFT [28] and the wavelet transform [155] are able to show when a certain frequency arrives as a function of time. These techniques may be useful in constructing partial group velocity dispersion curves. Particularly, the 2D Fourier transform (2DFFT) enables the construction of partial phase velocity dispersion curves when applied to temporally segmented signals [156]. The chirplet transform [157] and adaptive chirplet algorithm [158] may also be used to extract dispersion information from a signal.

For example, Figure 4.30 shows a graphical representation (spectrogram) of group velocity as a function of time, obtained using the STFT. It is demonstrated here by applying the 'FFT' routine to sequential windowed segments of the example signals previously shown a) without, and b) with mode conversions at 9.8m (as in Figure 4.25 and Figure 4.29a, respectively). Here v_g values from PCDisp are superimposed to validate the results. Bright colors indicate the existence of a certain v_g at a specific frequency while dark colors indicate its absence. In Figure 4.30a, bright yellow matches the dispersion curves of the L(0,1) mode (blue), and the F(1,1) mode (green) at the carrier frequency (dotted line). Figure 4.30b shows also bright colors that match the same modes in addition to L(0,1) -> F(1,1) conversion (magenta), and F(1,1) -> L(0,1) conversion (cyan) at the carrier frequency.

Although the correspondence is not always perfect, this method may be used to estimate dispersion curves from pulsed signal data.

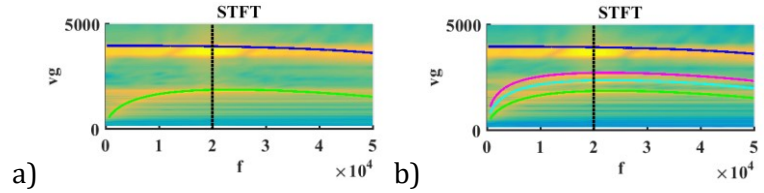

Figure 4.30: STFT Spectrogram and PCDisp group velocity dispersion curves of propagation a) without and b) with mode conversions at 9.8m.

4.5 Conclusion

In this chapter, a general transfer function model has been developed and used to simulate acoustic transmission between two sensor nodes. A transfer function for a dispersion-less system has been first discussed, and then developed to model a more realistic dispersive system. For clarity, reflections were considered in the former, while dispersion, multi-mode propagation, and mode conversion are considered in the latter; however, they may all be present in general. The dispersion-less system has been used to demonstrate signal recovery from noise using correlation detection.

Correlation detection has been shown to increase the signal-to-noise ratio, with a processing gain that increases with integration time. A reduction in signal bandwidth has been shown to mitigate dispersion. However, this reduces the bit rate, and there is an inherent incompatibility between the use of long signals for this purpose in a system with internal reflections, dispersion, and multiple modes, since there may be overlap between different received signal components. Although a long propagation distance mitigates some potential overlaps, compressed peaks are mandatory to reduce these further. In the next chapter, CDMA and codes will be discussed, including quasi-orthogonal codes and Golay complementary pairs to compress pulses and enable multiplexed transmission.

5 Multiplexed System

One aim of this research is to verify pipe continuity by allowing distributed nodes to communicate simultaneously using acoustic waves. There are several techniques for multiplexing, such as time division multiple access (TDMA), frequency division multiple access (FDMA), and code division multiple access (CDMA). TDMA assigns a time slot for each node. When one node is transmitting, all other nodes are silent. However, the requirement for synchronization introduces considerable unnecessary complexity. FDMA assigns a frequency band to each node and a guard band to avoid interference when transmitting simultaneously. Although it is suitable for a small number of nodes, the dispersion limitation of acoustic propagation does not allow the use of a wide spectrum. In contrast, CDMA assigns a code to each node that has a high autocorrelation and a low cross-correlation (ideally zero) to allow simultaneous transmission within the same frequency band. It is the most suitable method for asynchronous acoustic communication, and it is easily scalable. It is also flexible since codes may be assigned only to active nodes.

CDMA operates by correlation detection. A secondary aim is therefore to detect disturbances despite the high likelihood of overlaps between the correlation peaks caused by multipath effects. Mitigating overlaps can be achieved by sharp correlation peaks, using quasi-orthogonal Barker-like codes (QO) or bipolar Golay complementary pairs (GCP) instead of rectangular pulses. A QO pair or two orthogonal GCPs can be used to distinguish between two nodes in a multiplexed distributed sensor network. More realistically, a QO triplet may be used for a sensor node, n, to distinguish between three nodes: an adjacent node from each side, $n+1$ and $n-1$, and a reflection from node n itself. Such a triplet may be used cyclically, since attenuation sets an effective limit to the number of nodes that communicate. In a low attenuation system, a QO quadruplet or a 4-user complementary code set can be used to distinguish between 2 adjacent nodes from each side. In this chapter, multiplexing will be explored by utilizing two different CDMA schemes, quasi-orthogonal Barker-like code pairs, triplets, and quadruplets, and Golay complementary pairs and sets.

5.1 CDMA Overview

CDMA can be categorized into single-user and multi-user schemes. For single-user, the received signal has no other interfering signals and can, therefore, be demodulated by a

matched filter or correlation detection. In a multi-user scheme, each individual user has a distinguished code that is supposed to be known to the intended receiver [159]. CDMA may also be categorized into synchronous and asynchronous schemes. In synchronous CDMA, codes are orthogonal to each other and a dot product between two different codes is zero. Many low cross-correlation orthogonal codes have been explored in the literature. Welsh codes are well-known examples, and are based on a Hadamard matrix that has +1,-1 entries with mutually orthogonal rows. Their cross-correlations are zero at shift number zero. However, for other shift numbers, the cross-correlation can reach almost the maximum of the autocorrelation, making them unsuitable for asynchronous CDMA. Furthermore, there are only a fixed number of codes, limiting scalability.

In asynchronous CDMA, codes can only be quasi-orthogonal rather than perfectly orthogonal for all relative time shifts. Generally, a pseudo-random code is used as a spreading code to generate a quasi-orthogonal code. The main challenge is the non-zero values of cross-correlation and the sidelobes of the autocorrelation function. Many techniques have been developed to improve orthogonality.

A code designed for a single user is normally quasi-orthogonal with itself, while code sets designed for multiple users contain a similar number of quasi-orthogonal codes. Single codes have been heavily researched in radar applications [160, 161]. The time taken to identify any set of suitable codes is very long. For multiple codes, the authors in [162] discovered a length of 40 to 48 minimum peak sidelobe bipolar codes by utilizing recursive algorithms to reduce exhaustive searches from 2^N code possibilities to 1.4^N, reducing run times from 50 days to 14 days for codes of length 40 [163]. Alternatives of poly-phase codes were proposed by Lewis et al. [164] with a reduction in peak noise spikes. Gartz [165] proposed a method to identify poly-phase codes with low correlation side lobes of uniform amplitude.

Common CDMA applications have complexities beyond this research. For example, mobile networks have many users with multiple paths and fading factors. In this research, the network has a small number of nodes and a limited number of paths. However, node *n* has to distinguish between signals from nodes *n-1* and *n+1* in addition to its own reflection. Although a node may receive signals from less immediately adjacent nodes, attenuation will

weaken the signal significantly. Specific factors must be considered in such a network. The optimal correlation properties for a family of asynchronous codes may be maximum main-lobe autocorrelation, minimum side lobe autocorrelation, and minimum cross-correlation. A variable code number is needed for scalability. Minimum code length is needed for complexity reduction and the maximum balancing factor is needed to distinguish between ones and zeros in a noisy environment.

5.2 Encoding

There are different mechanisms to encode digital data such as non-return-to-zero (NRZ) and return-to-zero (RZ). NRZ represents 1s and 0s by high and low values while RZ requires a clock to latch the high value before returning to the low value. Encoding can be unipolar when the values are zero and positive, and bipolar when the values are negative and positive. Furthermore, encoding can be multiphase (or poly-phase) when representing values with a base of more than 2. In CDMA, phase-shift keying (PSK) is used to digitally modulate the code. Gold codes use unipolar encoding, while other shorter codes such as Barker codes use bipolar encoding. Bipolar encoding may be used to achieve asynchronous CDMA minimum cross-correlation and maximum autocorrelation with the least number of bits. Codes may be represented in a binary form, particularly, 1s and -1s, and, therefore, PSK will have two distinguished phases. The carrier will be of $\theta = 0^0$ for 1, and $\theta = 180^0$ for -1.

In contrast to unipolar and bipolar codes, multiphase codes allow more information with the same data rate [160, 161]. Instead of representing 0 and 1 with -1 and +1 respectively, complex numbers can be used. For example, (0, 1, 2) may be represented by [+1, -0.5+0.866j, -0.5-0.866j] and (0, 1, 2, 3) may be represented by [+1, +j, -1, -j]. Authors in [166] examined the effect of using four phases in Barker codes when the absolute value of the correlation is unaltered, then exhibiting constructions for generalized Barker sequences of a variety of lengths and all possible alphabet sizes.

A review and comparison between Barker codes, Gold codes, Kasami codes, and others are presented in [167] and [168]. Barker codes, which were discovered in 1953 [169], are only appropriate for single-user systems. They are used in radar systems that have narrow bandwidth and side lobe peaks of maximum 1. Barker codes have the advantage of a sharp main lobe and low sidelobes in autocorrelation. The number of known binary Barker codes

is limited, with a maximum of 13 bits length. Figure 5.1 shows examples of the autocorrelation of binary Barker codes containing a) 3 bits (decimal 3), b) 11 bits (decimal 583), and c) 13 bits (decimal 5535). In all cases, the processing gain is equal to the number of bits, and the correlation vector length is proportional to the number of bits. The peaks become sharper as the number of bits increases, and the ratio between the main lobe and side lobes is improved. Since the number of known Barker codes that have optimum correlation properties is limited, some relaxation on the correlation values can generate more Barker-like sequences. We term such codes Barker-Type.

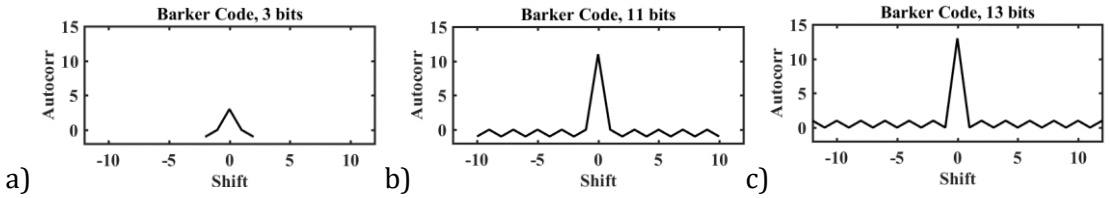

Figure 5.1: Example binary Barker codes containing a) 3, b) 11 and c) 13 bits.

For multi-user codes, Hadamard (Walsh) codes are considered relatively short and as mentioned before may be orthogonal in synchronous systems. Gold codes have a higher number of sequences for a specific word length than Kasami codes, but a high probability of errors. Kasami codes have optimal correlation properties but a small number of sequences. The so-called Kasami 'large set' can be obtained by a relaxation in correlation values. Both Gold and Kasami codes are also extremely long, which may cause overlaps between directly transmitted and multiply reflected signals.

Figure 5.2 shows an example of a comparison between normalized absolute auto- (black) and cross- (blue) correlation values of bipolar a) Hadamard, b) Gold codes, and c) Kasami (small set). To generate the same number of sequences (8), Hadamard codes require 8 bits while Kasami codes (small set) require 63 bits. Gold codes are long, with 31 bits, but have a high number of sequences (33). Examples here of 8-bit Hadamard code sequences C1 (for autocorrelation) and C2 (for cross-correlation) in binary form are:

$$C1 = 11001100$$
$$C2 = 10011001 \qquad (5.1)$$

Similarly, examples of 31-bit Gold code sequences C1 (for autocorrelation) and C2 (for cross-correlation) in binary form are:

$$C1 = 1000010100111100011100010011111$$
$$C2 = 0010011010000010001111010001001 \quad (5.2)$$

Finally, examples of 63-bit Kasami code sequences C1 (for autocorrelation) and C2 (for cross-correlation) in binary form are:

$$C1 = 111111010101100110111011010010011100010111100101000110000100000$$
$$C2 = 011010100111011111100111111100001011011100000000110100111101011 \quad (5.3)$$

In all cases, an autocorrelation peak is obtained when the sequences overlap fully. The maximum cross-correlation value of Hadamard codes is relatively high when both sequences are asynchronous. Codes have relatively low cross-correlations. However, they are very long. Hadamard codes have high side lobes in their autocorrelation, while Gold and Kasami codes have low side lobes. However, increasing the number of bits may improve the ratio between the main lobe and side lobes in the autocorrelation. In summary, these types of codes are not suitable for distributed sensor networks due to either the high values of cross-correlations or the high number of bits.

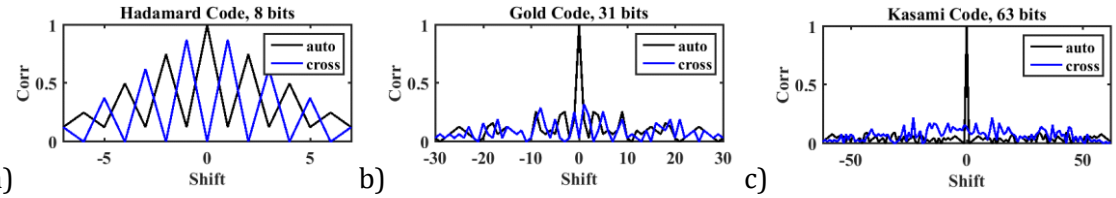

Figure 5.2: Example comparison between auto and cross-correlations of a) Hadamard, b) Gold codes, and c) Kasami (small set).

5.3 Multiphase Quasi-Orthogonal (QO) Codes

Barker-type codes must be short and quasi-orthogonal. Pairs of QO codes can be used to distinguish between the two adjacent transmitters in a transmission scheme. However, in a more realistic network, triples of QO codes are needed to allow each sensor node to distinguish between the two adjacent nodes and its own reflection. Pairs and triplets of QO

polyphase Barker-type codes can be found by searching numerically for codes that satisfy specified criteria for the maximum absolute cross-correlation and maximum absolute autocorrelation side lobes. To conduct a search, let N be a decimal number, M be the number of bits, and B be the base. A code $C_N^{B,M}$ is obtained as a set of complex numbers by:

$$C_N^{B,M} = \left[e^{\frac{j2\pi d_M}{B}}, e^{\frac{j2\pi d_{M-1}}{B}}, \dots\ e^{\frac{j2\pi d_1}{B}}\right] \tag{5.4}$$

Where d_M is the m^{th} digit of M in Base B, so that $C_N^{B,M}$ lies in the range $0 \leq N \leq N_{max}$, where $N_{max} = B^M - 1$. To search this space, a B^M matrix of all possible multiphase codes is first constructed in MATLAB. When B = 2, the matrix contains bipolar conventional codes such as Hadamard and Gold codes. However, 0 and 1 must now be represented as +1 and -1. After constructing multiphase codes, another B^M matrix of autocorrelations is computed to select only those codes that satisfy the autocorrelation sidelobe constraint. Then, a matrix of correlations between each pair of such codes is computed to identify those that also satisfy the cross-correlation constraint. A similar search process can be used to search for triplets and quadruplets.

To increase the number of QO Barker-like codes in a set, the constraint on maximum absolute cross-correlation must be relaxed. In the process, the discrimination factor (the ratio between the autocorrelation peak and the absolute values of cross-correlation) must decrease. Increasing the number of bits can restore the discrimination factor. However, an increase in bits will increase the search time exponentially, since the cross-correlation possibilities increase by 2^{2M}. To reduce the search time, a reduced code list may be constructed, by eliminating redundant codes with common phase shifts. These redundant codes are the codes above $C_{N'_{max}}^{B,M}$, for a given N, M, and B, when:

$$N'_{max} = \frac{B^M - 1}{B - 1} - 1 \tag{5.5}$$

We can illustrate the above using an example. If $B = 10$, and $M = 3$, then $C_0^{10,3} = [e^{j0}, e^{j0}, e^{j0}]$, and $C_{111}^{10,3} = [e^{\frac{j2\pi}{10}}, e^{\frac{j2\pi}{10}}, e^{\frac{j2\pi}{10}}]$. Consequently:

$$C_{111}^{10,3} = e^{\frac{j2\pi}{10}} C_0^{10,3}$$

(5.6)

Similarly:

$$C_{N+111}^{10,3} = e^{\frac{j2\pi}{10}} C_N^{10,3}$$
$$C_{N+111P}^{10,3} = e^{\frac{j2P\pi}{10}} C_N^{10,3}$$

(5.7)

Here $N < 111$, and $P \leq 8$ in this example. Now, the autocorrelation of a code and the phase-shifted equivalents are identical, since correlation involves taking the conjugate of the second term. Consequently, the autocorrelation of the codes in Equation (5.7) are given by:

$$C_{N+111P}^{10,3} * C_{N+111P}^{10,3} = \left(e^{\frac{j2P\pi}{10}} C_N^{10,3}\right) * \left(e^{\frac{j2P\pi}{10}} C_N^{10,3}\right)$$
$$C_{N+111P}^{10,3} * C_{N+111P}^{10,3} = e^{\frac{j2P\pi}{10}} e^{\frac{-j2P\pi}{10}} \left(C_N^{10,3} * C_N^{10,3}\right)$$
$$C_{N+111P}^{10,3} * C_{N+111P}^{10,3} = C_N^{10,3} * C_N^{10,3}$$

(5.8)

Thus, the autocorrelations of $C_{N+111P}^{10,3}$ and $C_N^{10,3}$ are identical. Similarly, the cross-correlation of codes $C_{N1}^{10,3}$ and $C_{N2+111P}^{10,3}$ will lead to:

$$C_{N1}^{10,3} * C_{N2+111P}^{10,3} = C_{N1}^{10,3} * \left(e^{\frac{j2P\pi}{10}} C_{N2}^{10,3}\right)$$
$$C_{N1}^{10,3} * C_{N2+111P}^{10,3} = e^{\frac{-j2P\pi}{10}} \left(C_{N1}^{10,3} * C_{N2}^{10,3}\right)$$
$$\left|C_{N1}^{10,3} * C_{N2+111P}^{10,3}\right| = \left|C_{N1}^{10,3} * C_{N2}^{10,3}\right|$$

(5.9)

Thus, the cross-correlation magnitudes of $C_{N1}^{10,3}$ and $C_{N2+111P}^{10,3}$ and $C_{N1}^{10,3}$ and $C_{N2}^{10,3}$ are also identical. Since the numerical search is constrained by magnitude values of cross-correlation and autocorrelation side lobes, the reduced code list will produce the same results as the full list in a significantly reduced search time. The reduction factor is given by:

$$\frac{N'_{max}}{N_{max}} \approx \frac{1}{B-1}$$

(5.10)

To ensure the algorithm finds the best possible codes for the searched range, the lowest possible autocorrelation sidelobes, and cross-correlation constraints must be determined, instead of relying on an arbitrary initial selection of these constraints. Hence, the algorithm may conduct multiple fast searches and a single exhaustive search to select the lowest. As the search terminates once the first set of codes is found, a fast search with an arbitrary selection will let the algorithm reduce the constraints if the autocorrelation sidelobes and cross-correlation maxima are lower than the arbitrary values. The process may be repeated until the unwanted maxima and the constraints are equal. This MATLAB algorithm is presented in appendix 2.

A simple example is when *M* is 2 and *B* is 2, and the possible QO codes in decimal are 0, 1, 2, and 3. In this case, the possible bipolar codes are [+1,+1], [+1,-1], [-1,+1], and [-1,-1]. Figure 6.3 shows the correlation results of the QO pair (0, 1). In this and the following examples, diagonal plots are autocorrelations while off-diagonal plots are cross-correlations. The autocorrelation is 2 as expected while the cross-correlation is 1 (dashed line). The autocorrelation side lobes can also reach up to 1. The discrimination factor is therefore only 2, and the other QO pair (2, 3) have a similar poor performance.

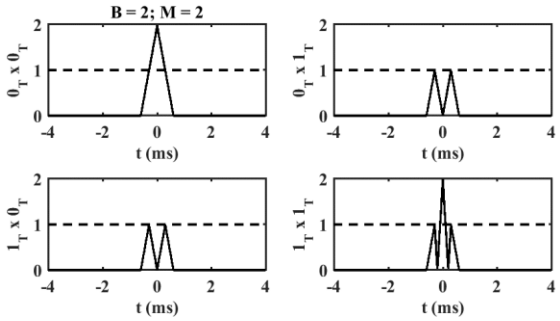

Figure 5.3: Auto and cross-correlations of the 2-bit QO bipolar pair (0, 1).

The QO search algorithm was conducted for up to base 14 for pairs and up to base 8 for triplets, with a range between 2 and 17 bits for each base. A restricted list of suitable QO codes with variable performance was identified. Figure 5.4 compares the discrimination factor (*D*) for multiphase pairs with different numbers of bits. Here base 2 is shown in green, base 3 in blue, base 4 in red, base 5 in magenta, base 6 in black, and base 7 in yellow. For bases 2, 3, 4, and 6, the variations consist of straight lines with well-defined slopes (*L*) which can be expressed as: $L = \frac{D}{M} = \frac{1}{A}$, where *A* is the minimum constraint on autocorrelation

sidelobes and cross-correlation. The values of the slopes are $\frac{1}{\sqrt{9}}, \frac{1}{\sqrt{7}}, \frac{1}{\sqrt{5}}, \frac{1}{\sqrt{4}}, \frac{1}{\sqrt{3}}, \frac{1}{\sqrt{2}}$, and $\frac{1}{\sqrt{1}}$, which are reciprocals of the square roots of specific integers. Performance improvement or decline therefore corresponds to a jump from one such line to another due to the integer value of A; a property that codes of bases 5 and 7 do not share.

To elaborate on this, autocorrelation sidelobes and cross-correlation can be expressed as:

$$|S_M|^2 = \sum_{m=1}^{M} e^{\frac{j2\pi d_{1m}}{B}} e^{\frac{-j2\pi d_{2m}}{B}}, \text{ or}$$
$$|S_M|^2 = \sum_{m=1}^{M} e^{\frac{j2\pi (d_{1m}-d_{2m})}{B}} = \sum_{m=1}^{M} e^{\frac{j2\pi C_m}{B}} \tag{5.11}$$

Where d_{1m} and d_{2m} are the m^{th} digits of the two correlated codes, and $C_m = d_{1m} - d_{2m}$. For instance, if M = 2, correlations are given by:

$$|S_2|^2 = \left\{\cos\left(\frac{2\pi C_1}{B}\right) + \cos\left(\frac{2\pi C_2}{B}\right)\right\}^2 + \left\{\sin\left(\frac{2\pi C_1}{B}\right) + \sin\left(\frac{2\pi C_2}{B}\right)\right\}^2, \text{ or}$$
$$|S_2|^2 = 2 + 2\left\{\cos\left(\frac{2\pi C_1}{B}\right)\cos\left(\frac{2\pi C_2}{B}\right) + \sin\left(\frac{2\pi C_1}{B}\right)\sin\left(\frac{2\pi C_2}{B}\right)\right\} \tag{5.12}$$

We now define:

$$\cos\left(\frac{2\pi[C_1 - C_2]}{B}\right) = \cos\left(\frac{2\pi C_1}{B}\right)\cos\left(\frac{2\pi C_2}{B}\right) + \sin\left(\frac{2\pi C_1}{B}\right)\sin\left(\frac{2\pi C_2}{B}\right) = c_{1-2} \tag{5.13}$$

The possible values for c_{1-2} are (-1, +1) when B = 2, (-1/2, +1) when B = 3, (-1, 0, +1) when B = 4, and (-1, -1/2, +1/2, +1) when B = 6. Since $2c_{1-2}$ must be therefore integer, so must $|S_2|^2$. Similarly, if M = 3, it is simple to show that the correlations are given by:

$$|S_3|^2 = 3 + 2(c_{1-2} + c_{1-3} + c_{2-3}) \tag{5.14}$$

Clearly, $2c_{i-j}$ can only be -2, -1, 0, +1 or +2 for $1 \leq i, j \leq M$. These two results prove that $|S_M|^2$ must be an integer for B = 2, 3, 4, and 6 when M = 2, 3. Numerical investigation shows that the same conclusion holds true for larger M, so the value of A above must be the square

root of an integer for these bases. However, the same is not true for other bases, since the possible values of $2c_{i-j}$ are no longer so convenient.

However, the discrimination factor variations indicate complexity in the underlying properties which makes it difficult to predict the performance of higher bases. Consequently, an exhaustive time-consuming search is inevitable. Nevertheless, base 6 clearly demonstrates better performance when the number of bits is 6, 8, and 9. Bases 4, 5, and 7 exceed this performance, but only in a relatively unimportant special case (when M = 10 for Base 4, when M = 5 for Base 5, and when M = 7 for Base 7).

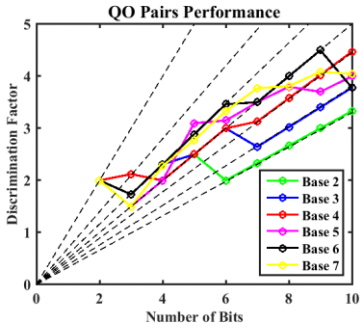

Figure 5.4: Variation of discrimination factor of multiphase QO pairs with number of bits.

Table 5.1 shows the same results, now presented as a table. Once again, the best performance offered by B = 6, with a discrimination factor up to 4.5 for 9-bit codes. In some of the pairs, the maximum autocorrelation sidelobes are less than the cross-correlation (for example, when B = 2 and M = 7). Varying the two constraints might allow discovery of pairs with better performance. However, the gains are likely to be small.

Base	Number of bits	Max auto-correlation	Max auto side lobes	Max cross-correlation	Discrimination Factor
2	2	2.00	1.00	1.00	2.00
	3	3.00	2.00	2.00	1.50
	4	4.00	2.00	2.00	2.00
	5	5.00	2.00	2.00	2.50
	6	6.00	3.00	3.00	2.00
	7	7.00	2.00	3.00	2.33
3	3	3.00	1.00	1.00	2.00
	4	4.00	2.00	2.00	2.00
	5	5.00	2.00	2.00	2.50
	6	6.00	2.00	2.00	3.03

	7	7.00	2.00	3.00	2.33
4	4	4.00	1.00	2.00	2.00
	5	5.00	2.00	2.00	2.50
	6	6.00	2.00	2.00	3.03
	7	7.00	2.00	3.00	2.33
5	4	4.00	2.00	2.00	2.00
	5	5.00	1.61	1.61	3.10
	6	6.00	1.61	1.61	3.10
	7	7.00	2.00	2.00	3.50
6	6	6.00	1.73	1.73	3.46
	7	7.00	2.00	2.00	3.50
	8	8.00	2.00	2.00	4.00
	9	9.00	2.00	2.00	**4.50**
7	7	7.00	1.85	1.85	3.77
	8	8.00	2.10	2.10	3.81
	9	9.00	2.20	2.20	4.08

Table 5.1: Discrimination factors of multiphase QO codes with different numbers of bits.

Figure 5.5 shows the autocorrelation functions of known generalized Barker sequences for B = 6 [160]. In decimal, these are a) 638, b) 751, and c) 3482 when M = 7, 8, and 9 respectively. In all cases, the main peak is sharp, with a maximum value equivalent to the number of bits, while sidelobes are constantly low. The disadvantage of increasing the number of bits, however, is widening the sidelobes.

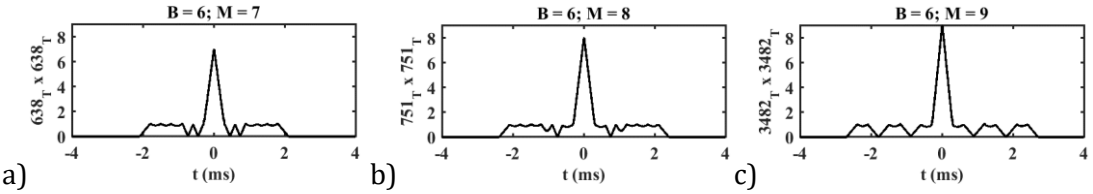

a) b) c)

Figure 5.5: Phase-six Barker codes a) 638, b) 751, and c) 3482 for 7, 8, and 9 bits respectively.

Table 5.2 summarizes the best results discovered by the QO search algorithm of base 6 for Barker-like pairs, triplets, and quadruplets. The best results are obtained using long codes. Obviously, the discrimination factor is reduced when the number of codes is increased. Pairs and triplet codes each have sufficient performance to allow correct detection with two and three simultaneously interfering users of equal strength; however, quadruplet codes do not, since the discrimination factor is less than the number of users in this case.

Base	Type	Number of bits	C1	C2	C3	C4	Discrimination factor
6	Pair	8	626	52775	-	-	4.00
	Pair	9	8564	1040855	-	-	4.50
	Triplet	7	2519	15783	36528	-	3.50
	Triplet	10	5099	918088	989300	-	3.78
	Quadruplet	8	97	4528	35070	145245	3.02
	Quadruplet	9	378	25059	125625	255234	3.00

Table 5.2: Examples of the best pairs, triplets, quadruplets in base 6.

To illustrate base 6 results, Figure 5.6 shows the correlation results of the QO pair (8564, 1040855) when *M*=9 and B=6. The autocorrelation is 9 as expected while the sidelobes and cross-correlation is 2 (dashed line) demonstrating a discrimination factor of 4.5, the best performance found from any such code set to date.

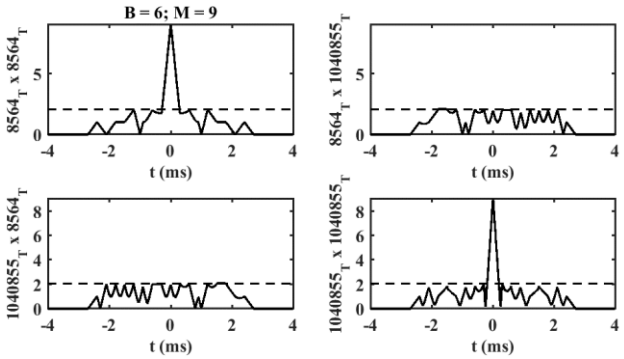

Figure 5.6: Auto and cross-correlations of base 6, 9-bit QO pair (8564, 1040855).

As another example, Figure 5.7 shows the correlation results of the QO triplet (5099, 918088, 989300) when *M*=10 and *B*=6. The autocorrelation is 10 as expected while the sidelobes and cross-correlation is 2.65 (dashed line). This triplet achieves a discrimination factor of 3.78, lower than the performance of the best pair above.

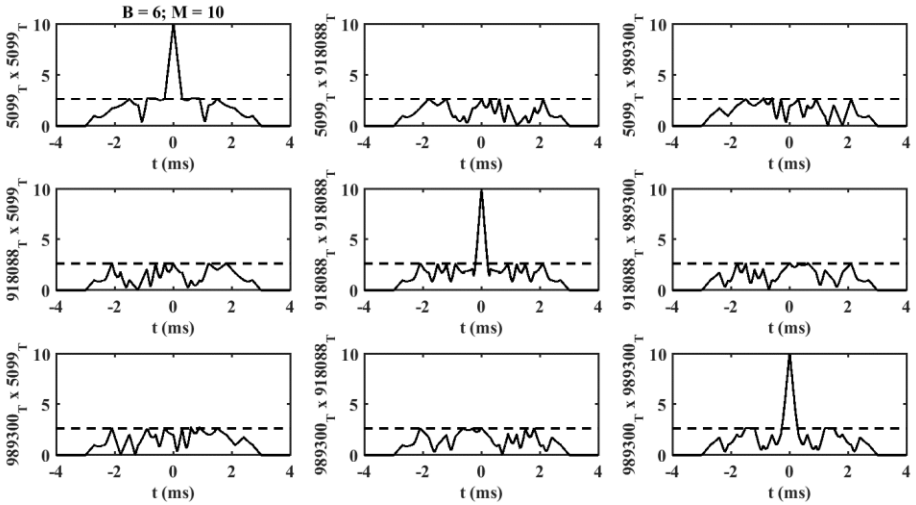

Figure 5.7: Auto and cross-correlations of base 6, 10-bit QO triplet (5099, 918088, 989300).

Finally, Figure 5.8 shows the correlation results of the QO quadruplet (378, 25059, 125625, 255234) when $M = 8$ and $B = 6$. The autocorrelation is 8 as expected while the sidelobes and cross-correlation is 2.65 (dash line). This quadruplet achieved a discrimination factor of 3.02, lower than the best pairs and triplets.

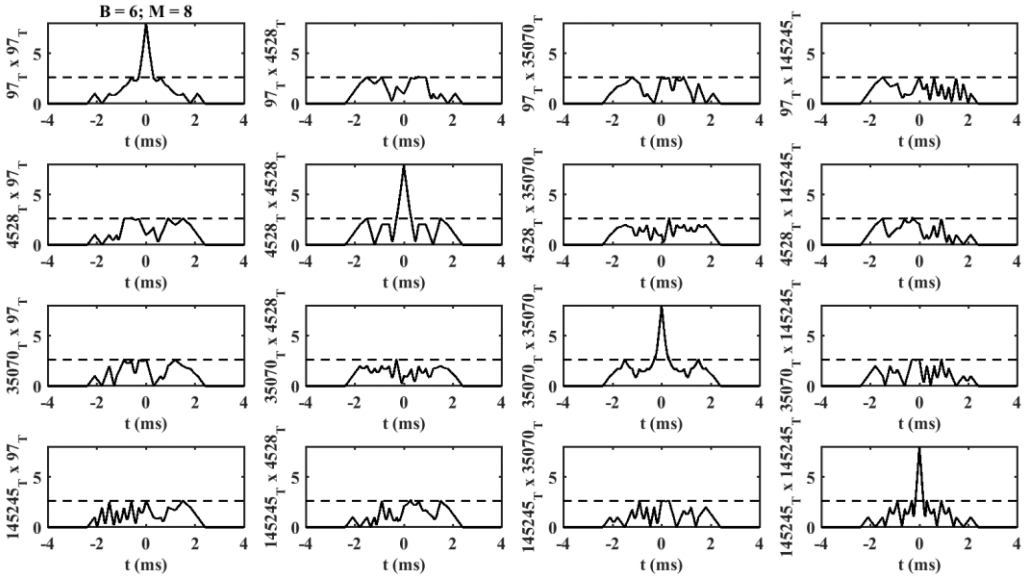

Figure 5.8: Auto and cross-correlations of base 6, 8-bit, QO quadruplet (378, 25059, 125625, 255234).

Since the system model presented in the previous chapter uses a carrier to transmit the signal, the effect of up-conversion should be investigated. Figure 5.9 shows a modulated

signal (black) of 2-bit QO codes (red) defined by vectors a) [+1,+1] and b) [+1,-1] with a carrier of 20 kHz. The modulated signal clearly changes its phase to represent a multiphase code. More complex codes can be up-converted in a similar way.

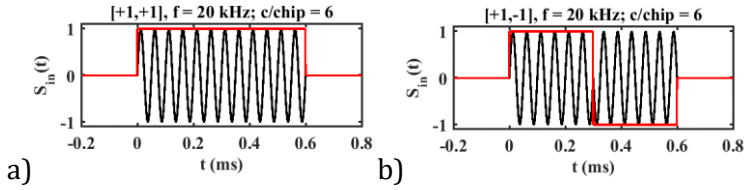

Figure 5.9: Modulated codes: a) (+1,+1) and b)(+1,-1) with a 20 kHz carrier.

Ideally, the envelopes obtained after cross-correlation and down-conversion should be similar to the cross-correlations of baseband signals. Figure 5.10 shows the result of down-converting the cross-correlations shown in the previous example in Figure 5.9, namely an 8-bit quadruplet, after up-conversion using a 20 kHz carrier. The envelope of the correlation function (red) is indeed identical to the previous example, confirming that the up-conversion process does not affect the basic properties of orthogonal codes.

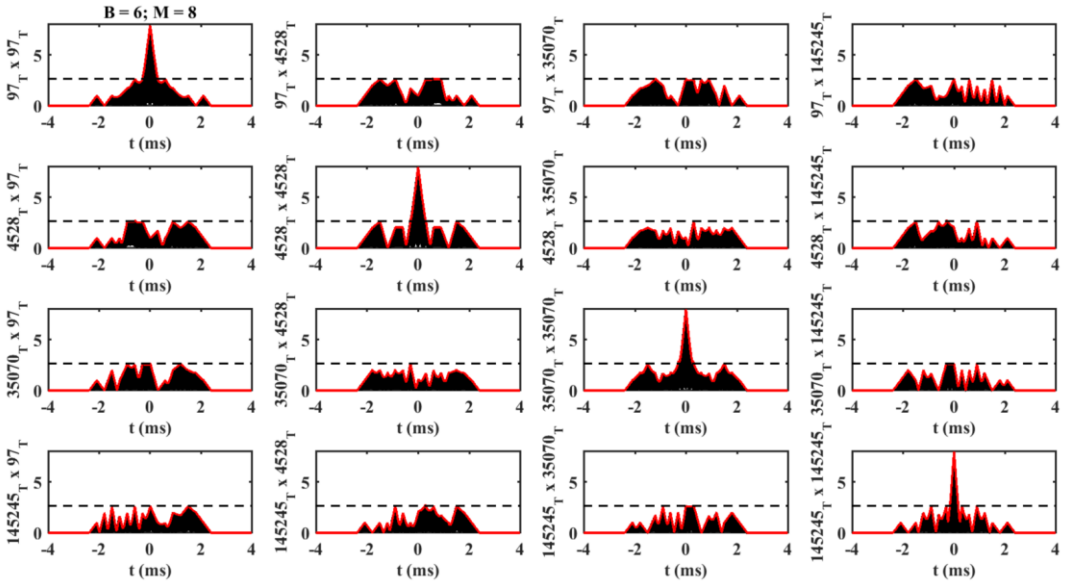

Figure 5.10: Baseband auto and cross-correlation envelopes (red) obtained after down-converting base 6, 8-bit, QO quadruplets, assuming a 20 kHz carrier.

5.4 Golay Complementary Pairs

As mentioned before, the autocorrelation sidelobes and non-zero cross-correlations that are unavoidable in QO codes may degrade multiplexed communication. An alternative approach, the Golay complementary pair, has the property of reducing unwanted correlations to zero by using two sequences instead of one. It doubles the processing gain, potentially allowing an increase in the distance between sensor nodes; however, transmission time is clearly also doubled. Golay introduced these sequences for an application in infrared multi-slit spectrometry in 1949 [170], and defined complementary sequences more formally in 1961 [171]. Since then, bipolar and complex GCPs have been studied extensively [172, 173] and have been applied in different domains including orthogonal frequency-division multiplexing [172, 174], CDMA [175], and acoustics [176, 177].

Golay described bipolar complementary series as a pair of equally long, finite sequences with the property that the number of pairs of like elements in one series, with any given separation *j*, is equal to the number of pairs of unlike elements with the same separation in the other series [171]. Based on that definition; $(1, 1, -1, 1)$ and $(1, 1, 1, -1)$ are examples of GCPs.

Bipolar GCPs have a restricted number of possible lengths, typically a power of 2. To identify suitable codes numerically, an extensive search can be conducted to find pairs that satisfy the basic GCP properties which are zero autocorrelation sidelobes and zero cross-correlations. Let $A = (A_1\ A_2 \cdots A_M)$, and $B = (B_1\ B_2 \cdots B_M)$ be two M-length GCPs, where $A_i, B_i \in \{-1, 1\}\ \forall\ 1 \leq i \leq M$. The basic property is expressed by Golay in autocorrelative terms, under any given separation *j,* as:

$$X_i = \sum_{i=1}^{i=M-j} A_i A_{i+j}$$
$$Y_i = \sum_{i=1}^{i=M-j} B_i B_{i+j} \tag{5.15}$$

Then:

$$X_i + Y_i = 0 \qquad j \neq 0$$
$$X_0 + Y_0 = 2M$$

(5.16)

Once again, the search time increases rapidly with the number of bits. Therefore, Golay proposed a simple algorithm that can find bipolar GCPs for longer codes faster [171]. The algorithm operates by appending, as follows. If A_0 and B_0 are pair with length unity, longer codes can be found by recursion as:

$$A_{i+1} = A_i, B_i$$
$$B_{i+1} = A_i, -B_i$$

(5.17)

In addition, orthogonal bipolar GCPs with length M for a 2-user network can be found by searching for the first pair (A, B) as before, then constructing the second pair (C, D) as:

$$C_i = -B_{M-i+1}$$
$$D_i = A_{M-i+1}$$

(5.18)

For a system with additional users, a complementary set of sequences [178, 179] can be constructed from a known 2-bit GCP. The number of sequences required to find a set with zero autocorrelation sidelobes and zero cross-correlations is equal to the number of users. To generate a bipolar 4-user code set from GCP, (A, B), with M=2, a matrix is first formed as:

$$\Delta = \begin{bmatrix} A & \tilde{B} \\ B & -\tilde{A} \end{bmatrix}$$

(5.19)

Where ~ means to flip a code from left to right. A second matrix is then formed as:

$$\Delta' = \begin{bmatrix} \Delta \otimes \Delta & -\Delta \otimes \Delta \\ -\Delta \otimes \Delta & \Delta \otimes \Delta \end{bmatrix}$$

(5.20)

Where the operator $\otimes$ means interleave elements. The matrix Δ' is a 4-user code set that has a total of 16 codes with a minimum length of 4 bits each. For an 8-user system, a similar code set can be repeated 4 times to have a bipolar code set of 64 codes total constructed

from a 4-bit GCP with a minimum length of 8 bits each. Codes for a larger number of users can be obtained similarly. However, since the GCP lengths are restricted, the possible number of orthogonal users is also limited which reduces the versatility of the method.

Table 5.3 shows bipolar orthogonal GCPs (*A, B*) and (*C, D*) found using the 2-user algorithm discussed above for *M*=4, 8, 16, and 32 bits. These orthogonal complementary pairs are suitable for distinguishing signals from 2 nodes, with a processing gain that depends on the number of bits.

Base	**Number of bits**	***A***	***B***	***C***	***D***
2	4	1	2	11	8
	8	18	29	71	72
	16	4637	4834	47287	47176
	32	303895266	303951133	1195919287	1195948104

Table 5.3: Bipolar orthogonal GCPs of multiple numbers of bits for 2-user systems.

To illustrate the results of orthogonal GCPs for 2-user systems, Figure 5.11 shows correlation results for the bipolar orthogonal GCPs (1, 2) and (11, 8) when *M* is 4. Once again, diagonal plots are autocorrelations while off-diagonal plots are cross-correlations. In contrast to QO codes, the autocorrelations now have clear main lobes without sidelobes, and the cross-correlations are perfectly zero, so the discrimination factor is infinite. In each case, the processing gain is 2*M* (here, 8). Orthogonal GCPs therefore have obvious advantages over QO codes, achieved at a price of increasing the number of codes that must be transmitted.

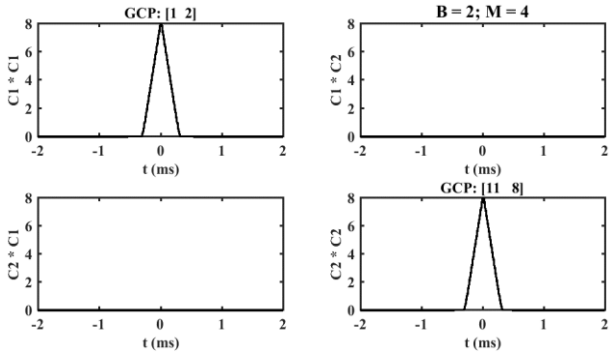

Figure 5.11: Auto and cross-correlations of the 4-bit orthogonal GCPs (1, 2) and (11, 8) for 2-user systems.

To improve the processing gain further, Figure 5.12 shows the correlation results of the bipolar orthogonal GCPs (4637, 4834) and (47287, 47176) when M this time is 16 and assuming a 20 kHz carrier. Once again, the down-converted autocorrelations (red) and the up-converted autocorrelations (black) have clear main lobes without sidelobes, and the cross-correlations are perfectly zero. However, the processing gain is now 32 as expected. This example shows how the processing gain may be increased simply by extending the code length. It also confirms that the carrier does not affect this multiplexing method.

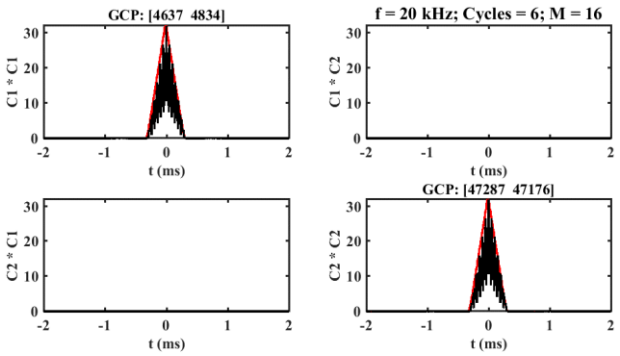

Figure 5.12: Auto and cross-correlations of 16-bit orthogonal GCPs (4637, 4834) and (47287, 47176) for 2-user systems, assuming a 20 kHz carrier.

It is easy to extend the same approach to allow additional users, using a so-called complementary code set (CCS) [178, 179]. For example, Table 5.4 shows the CCS for a 4-user system (16 codes, 4 codes for each user) when M = 4, obtained using the 4-user algorithm above.

User	Code 1	Code 2	Code 3	Code 4
1	0	3	10	9
2	12	15	6	5
3	10	9	0	3
4	6	5	12	15

Table 5.4: 4-bit complementary code set for 4-user systems.

Figure 5.13 shows the correlation results of the complementary code set for the 4-user system in the table above. As expected, the cross-correlations are perfectly zero and the autocorrelations have clear main lobes without sidelobes and with a processing gain of 16,

a significant advantage of the increment in the number of users (4 times improvement in comparison with a corresponding QO quadruplet system).

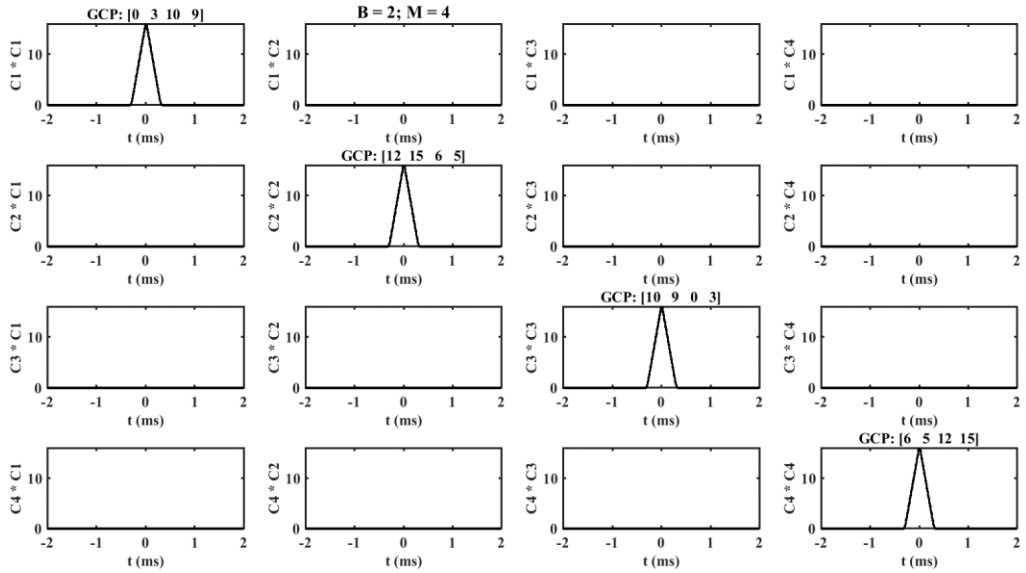

Figure 5.13: Auto and cross-correlations of the 4-bit complementary code set for 4-users.

Similarly, Table 5.5 shows a complementary code set for an 8-user system (64 codes, 8 codes for each user) when M = 8. The set is obtained using the 8-user algorithm that is discussed above.

User	Code 1	Code 2	Code 3	Code 4	Code 5	Code 6	Code 7	Code 8
1	0	15	204	195	170	165	102	105
2	240	255	60	51	90	85	150	153
3	204	195	0	15	102	105	170	165
4	60	51	240	255	150	153	90	85
5	170	165	102	105	0	15	204	195
6	90	85	150	153	240	255	60	51
7	102	105	170	165	204	195	0	15
8	150	153	90	85	60	51	240	255

Table 5.5: 8-bit complementary code set for 8-user systems.

Figure 5.14 shows the correlation results of the complementary code set for an 8-user system in the previous table when M here is 8. The correlations are as expected with a processing gain of 64 while the cross-correlations are perfectly zero. Although increasing the number of orthogonal users improves the processing gain, the time to transmit the 8 sequences is increased linearly which slows the communication.

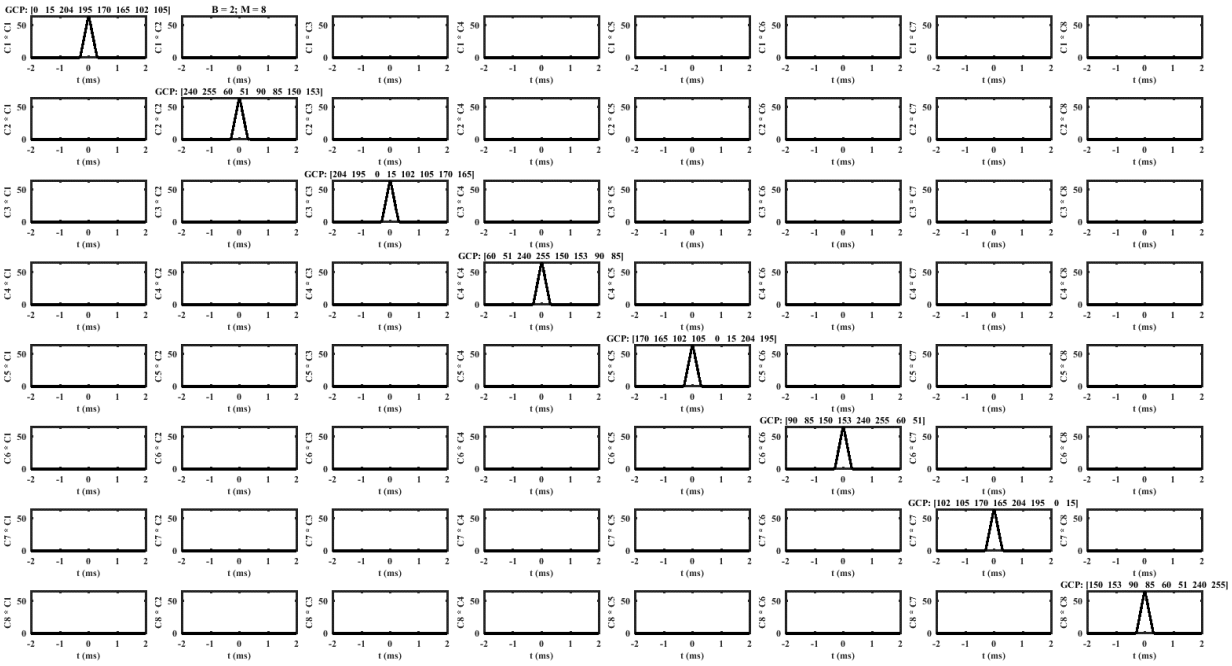

Figure 5.14: Correlations of the 8-bit complementary code set for 8-user systems.

5.5 Conclusion

In this chapter, CDMA communication codes for multiple users in an asynchronous acoustic monitoring system have been discussed. Since common codes such as Hadamard, Kasami, Gold and Barker codes are unsuitable, an efficient algorithm to search for short codes in the form of multiphase, quasi-orthogonal, Barker-like pairs, triplets, and quadruplets has been developed. QO pairs may be used to distinguish between two sensor nodes, while QO triplets and quadruplets may be used for three and four sensor nodes respectively. Base 6 codes show the best performance, particularly 9-bit pairs, 10-bit triplets, and 8-bit quadruplets. However, in addition to the restricted code set, all QO codes have non-zero autocorrelation sidelobes and cross-correlation. Bipolar Golay complementary pairs have therefore been investigated as alternatives. GCPs are completely orthogonal, and offer improved processing gain when compared with QO codes of similar length. Orthogonal GCPs and complementary code sets obtained from GCPs have been constructed for 2-, 4-, and 8-user systems. In contrast to QO codes, increasing the number of users will significantly increase the transmitting time. In the next chapter, CDMA techniques discussed here will be integrated with the dispersive system model in a full simulation.

6 Multiplexed Dispersive Model

In this chapter, a full-system simulation of the propagation of quasi-orthogonal Barker Type (QO) codes and Golay Complementary Pairs (GCPs) will be presented, using a dispersive model. This simulation is built on top of the model presented in Chapter 4, considering multimode propagation, multiple reflections, and mode conversion. Hence, this short chapter is intended to integrate the results of Chapters 4 and 5 together.

6.1 Numerical Simulation of Code Propagation

To begin with, we will explore the effects of dispersion and multimode effects on code propagation. Figure 6.1 compares the dispersion-less propagation of multiplexed signals with a dispersive model, where the latter is represented as an amplifier with EMAT and a microphone attached to a copper pipe with 15 mm OD and 1 mm wall thickness (or simply a transducer-pipe-transducer model) to match later experiments. Figure 6.1a shows the generalized Barker code 3482 with base B = 6 and length M = 9 after up-conversion onto a 20 kHz carrier, using 6 cycles per chip. This code demonstrated the best discrimination factor in Chapter 5. Figure 6.1b shows the up-converted code after 24.4 m propagation, and Figure 6.1c shows the recovered signal after correlation and down-conversion. The result shows a clear autocorrelation peak with a sharp main lobe and wide, but low, sidelobes.

In Figure 6.1d, the same Barker code is transmitted in the dispersive model as two modes that initially cannot be distinguished, the L(0,1) mode with a nominal amplitude of 0.75 and the F(1,1) mode with an amplitude of 0.25. Figure 6.1e shows the received signal after 24.4 m propagation. The two modes have separated out; the L(0,1) pulse has clearly experienced little dispersion, whereas the F(1,1) pulse has stretched out rather more. Figure 6.1f shows the recovered signal after correlation and down-conversion. There are clearly two correlation peaks, but both of the correlation envelopes are recognisable.

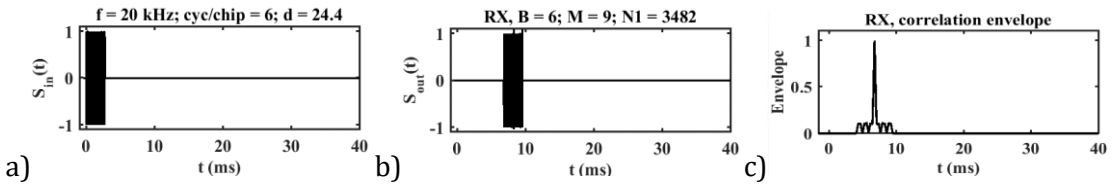

a) b) c)

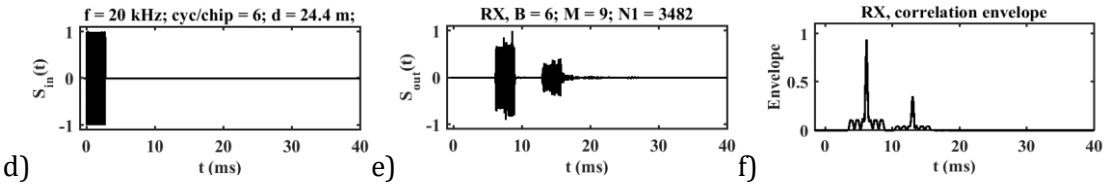

Figure 6.1: Comparison of multiplexed propagation between dispersion-less and dispersive models: a) code, b) propagated signal, c) correlation envelope for dispersion-less model; d) code, e) propagated signal, and f) correlation envelope for dispersive model.

Figure 6.2 shows the corresponding frequency responses of a) the transmitted code and b) the received signal. In contrast to a simple pulse, the code example here has a distorted sinc function spectrum with an asymmetric peak at the carrier frequency, 20 kHz. The additional oscillations in the received response arise from beating between the two modes.

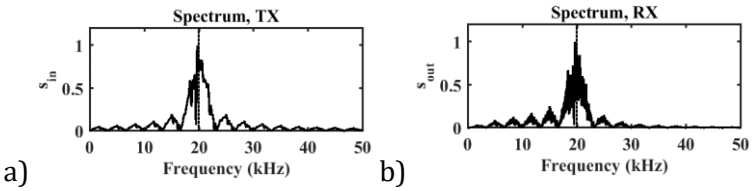

Figure 6.2: Frequency spectrum of a) the transmitted general Barker code and b) the received signal.

We now illustrate the propagation of a QO pair. The two-moded pipeline system is again assumed, with no reflection or mode conversion. The QO codes concerned are 9-bit equivalents of the decimal numbers 8564 and 1040855 in base 6, and the propagation distance is again 24.4 m. Figure 6.3 shows the full set of autocorrelation envelopes (diagonal plots) and cross-correlation envelopes (off-diagonal plots), after correlation and down-conversion. The autocorrelations and cross-correlations are as expected for both modes. However, the longitudinal mode has a higher discrimination factor, due to its reduced dispersion. These results highlight the need to choose a low dispersion mode for communication. In addition, the wide spread of the autocorrelation sidelobes and the cross-correlations indicate the inevitability of the overlaps when any disturbances or discontinuities are present in the system.

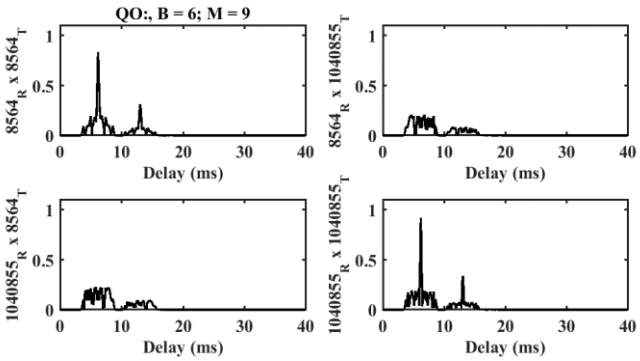

Figure 6.3: Received auto- and cross-correlation envelopes of the 9-bit QO pair 8564 and 1040855 with base 6 in a 2-moded system.

We now demonstrate the propagation of GCPs in the same 2-moded system model. Figure 6.4 shows the received full set of autocorrelation envelopes (diagonal plots) and cross-correlation envelopes (off-diagonal plots) of the bipolar GCPs (1, 2) and (11, 8) with M=4. The results are similar to single pulse propagation, and the adverse effect of the dispersion is barely noticeable. The possibility of overlaps from the disturbances or discontinuities is also significantly reduced. However, the distribution of the original energy into two modes has diminished the processing gain.

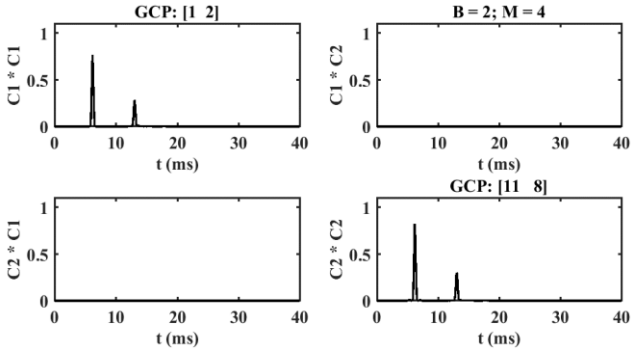

Figure 6.4: Received auto- and cross-correlation envelopes of the 4-bit orthogonal GCPs (1, 2) and (11, 8) in a 2-moded system.

6.2 Numerical Simulation of Channel Discontinuities

We now consider the additional effects on multiplexed propagation likely to be experienced due to channel discontinuities, including reflection and mode conversion. The L(0,1) and F(1,1) modes are assumed again to be launched, with amplitudes of 0.75 and 0.25,

respectively, but are now propagated for 24.4 m in a dispersive model based on a single Fabry-Perot cavity consisting of perfect reflectors. Attenuation is also considered, with attenuation coefficients of 0.03 m^{-1} for the L(0,1) mode and 0.07 m^{-1} for the F(1,1) mode. These assumptions are consistent with later experiments, which suggest that the flexural mode has higher attenuation.

Figure 6.5 shows the full set of received correlation envelopes for the 9-bit QO pair 8564 and 1040855 in base 6. Four sharp main lobes can be identified in the autocorrelation plots. The first two represent the direct transmission of the L(0,1) and F(1,1) modes, respectively, while the second two represent multiple L(0,1) reflections that follow a classic ring-down pattern. Multiple reflections of the flexural mode are also expected, but these are delayed more than 40 ms and consequently cannot be seen here; furthermore, their amplitudes are very low due to their relatively higher attenuation. In all cases, the autocorrelation sidelobes and cross-correlation signals are stretched out in the time domain.

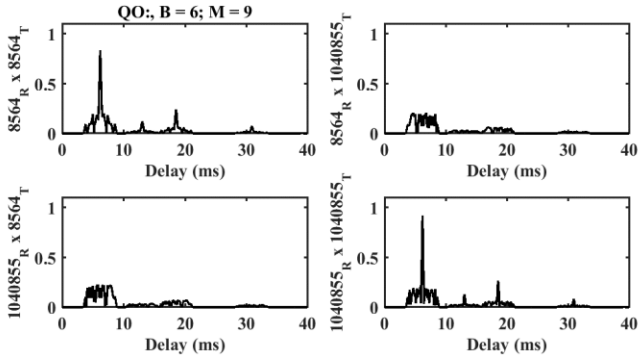

Figure 6.5: Received auto- and cross-correlation envelopes of the QO pair 8564 and 1040855 with multiple reflections.

Figure 6.6 shows the received full set of correlation envelopes of the bipolar GCPs (1, 2) and (11, 8) for *M*=4, in the same multiple reflection system. The four distinct peaks in the autocorrelation plots here correspond to multiple reflections of the two different modes as in the QO pair results. As expected, the main difference is the complete absence of autocorrelation sidelobes and cross-correlation signals, greatly simplifying the identification of the different signal components.

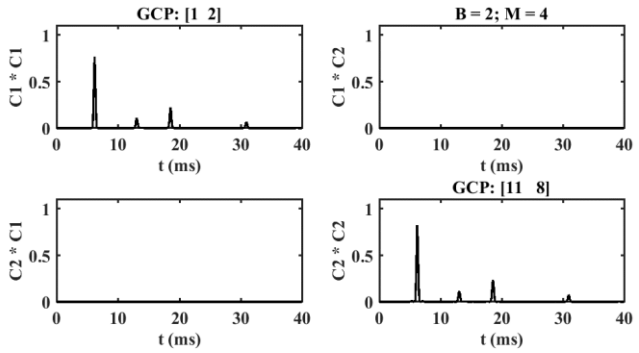

Figure 6.6: Received auto- and cross-correlation envelopes of the 4-bit orthogonal GCPs (1, 2) and (11, 8) with multiple reflections.

Mode conversion effects (which may be expected from dents or other localised modifications to the pipeline, such as supports or bends) may easily be incorporated into the numerical model. To demonstrate this, a mode conversion source is added at a distance of 9.8 m from the transmitter, simulating a real dent observed on the pipe used in later experiments. The mode conversion amplitude is assumed to be 0.2.

Figure 6.7 shows the full set of received correlation envelopes for a) the 9-bit QO pair 8564 and 1040855 in base 6, and b) the bipolar orthogonal GCPs (1, 2) and (11, 8) when *M* is 4 (their peaks are numbered in the figure). The results presented here now demonstrate the cumulative effects of dispersion, multimode propagation, multiple reflection, attenuation, and mode conversion. Clearly, identification of the separate pulses obtained using QO pairs has become much more difficult, and the discrimination factor has been degraded further due to overlaps between differentially delayed signals.

These effects are much less severe with orthogonal GCPs, again highlighting the advantages of this coding method. In the GCP autocorrelations , the second and third distinct peaks are the converted modes L(0,1) -> F(1,1) and F(1,1) -> L(0,1), while the rest of the peaks are as discussed before. However, the peak amplitudes have been decreased because the power is now distributed over a longer time. Multiple reflections of mode converted signals are not visible due to their low amplitude and high attenuation.

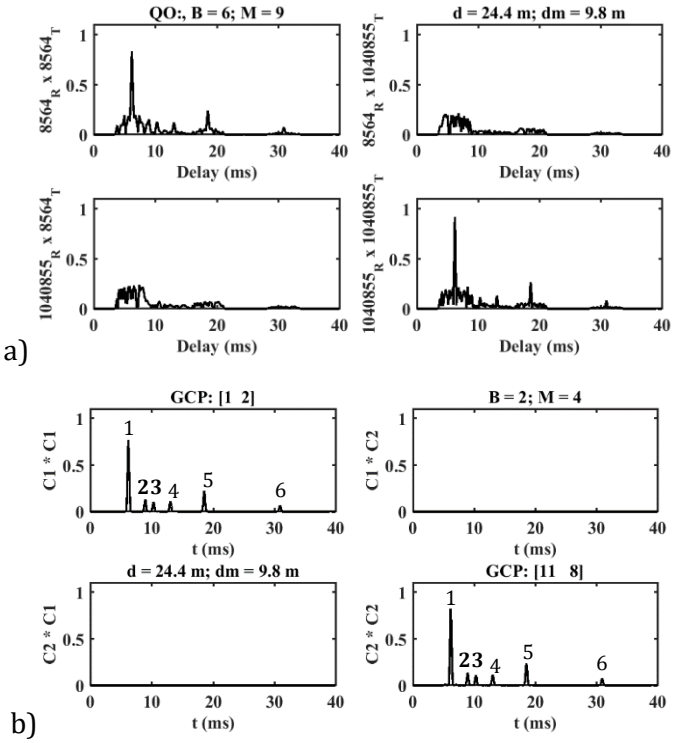

Figure 6.7: Received auto- and cross-correlation envelopes of the a) QO pair and b) orthogonal GCPs in a dispersive model with multiple reflections and mode conversion.

A mode converter may act as a partial reflector as well. Experimentally, this effect can only be observed for the L(0,1) longitudinal mode, due to its low attenuation. To include this effect in the model, a double Fabry-Perot cavity of 2 perfect end-reflectors and 1 intermediate partial reflector can be modeled as discussed in Chapter 4. Figure 6.8 shows the full set of received correlation envelopes for the orthogonal GCPs mentioned before with a partial reflector at 9.8 m from the transmitter, but ignoring mode conversion for simplicity. The transmission coefficient of the partial reflector is arbitrarily chosen to be 0.76 while its reflection coefficient is chosen to be $-j0.65$ to match later experiments. The first peak is the L(0,1) mode, the second and fourth peaks are L(0,1) reflections by the partial reflector. The third peak is the F(1,1) mode, and the rest are the multiple reflections caused by the perfect reflectors. One of the partial reflections is overlapping with the flexural mode. Combining the effects of multiple reflections, mode conversion, and partial reflections portrays the complexity of the problem. Nevertheless, the effects of pipe discontinuities can be mitigated by separating signals further with increasing time delay and the use of Golay codes in multiplexed systems.

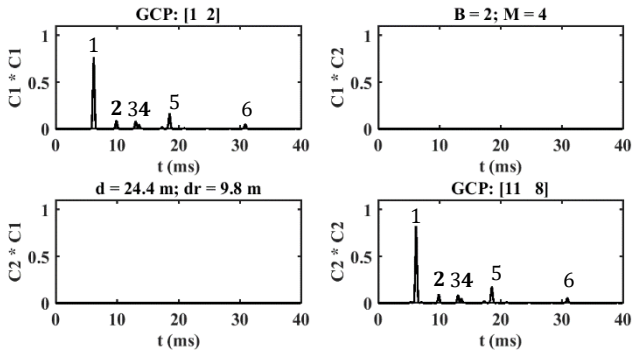

Figure 6.8: Received auto- and cross-correlation envelopes of the orthogonal GCPs in a dispersive model with partial reflections.

6.3 Conclusion

This chapter has described the simulation of QO codes and orthogonal GCPs in an extended model containing dispersion, multimode propagation, multiple perfect and partial reflections, mode conversion, and attenuation. The effect of dispersion is to smear out and reduce the height of correlation peaks, while the effect of multimode propagation, mode conversion, and multiple reflections is to introduce additional, weaker correlation signals that may overlap with and obscure the desired signal. Consequently, a reduction of main lobe energy and a lower discrimination factor may be expected using QO codes . Increasing time delay and Golay multiplexing may be used to mitigate these cumulative effects. In the next chapter, experimental results obtained using both coding systems will be discussed and compared with numerical results.

7 Experimental System

Previous chapters have presented a theoretical model of multiplexed communication in pipes, including the likely accompanying effects of dispersion, multimode propagation, mode conversion, multiple reflections, and attenuation. In this chapter, the system will be demonstrated experimentally, and the results will be compared to theoretical predictions.

7.1 Laboratory Setup

The laboratory apparatus was constructed iteratively until realistic results were obtained. The initial aim was to demonstrate transmission and reception of up-converted encoded acoustic signals via a pipe, and hence to verify continuity. Figure 7.1 shows a schematic of the apparatus, which illustrates the functions from generating a transmitted signal to processing a received signal. The system flow starts with a signal generator that is programmed by a PC to produce pulse, Barker, QO, or GCP codes. Each such signal is up-converted, amplified by an audio amplifier and transduced from the electrical to the acoustic domain using an EMAT. After a few milliseconds of propagation along a long copper pipe, the signal is detected using a receiver unit containing up to four microphones with built-in amplifiers. The microphones are connected to shielded connector converters and then to an oscilloscope for recording. Signal processing is carried out in software.

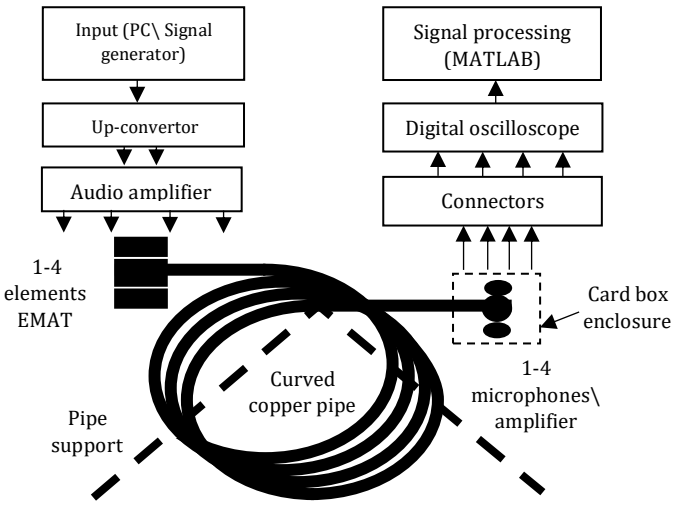

Figure 7.1: Laboratory setup for experimental demonstration of code propagation.

Figure 7.2a shows the Thurlby Thandar (TTi) TG4042 dual function generator used for the

generation of modulated signals, which is controlled by a PC through a USB interface using the standard commands for programmable instruments (SCPI). The PC (running MATLAB and Waveform Manager Plus software) is used for programming up-converted square pulses or codes, and then passing them as arbitrary waveforms to the function generator for a burst-type generation. The unit can operate up to 40 MHz and has an output impedance of 50 Ω. Figure 7.2b shows the Sony TAF2460E audio amplifier used to amplify the input and drive the EMAT with sufficient current for acoustic wave excitation. The amplifier has 150 W power output and can amplify a signal amplitude from below 1 V up to 50 V. It has 8 Ω output impedance, which is useful in reducing the mismatch between the EMAT and the function generator. It has two-channel (stereo) input and four-channel output, and each output channel is connected to one element of the EMAT via a coaxial cable.

a)  b) 

Figure 7.2: a) Function generator and b) audio power amplifier used in the experiments.

The input transducer is a 4-element EMAT containing four cuboid solenoids mounted at 90° spacings around the pipe as described in Chapter 3. Each element consists of a square solenoid coil with an identical number of turns (90) and wire diameter (0.56 mm), wrapped around a square bar magnet. Because a suitable magnet was not commercially available, the required cross-section was formed from multiple parts, forcibly held together in a frame. The required cross-section was achieved using three Neodymium bar magnets with a 4.9 kg pull force (Eclipse Neodymium Magnets, part No.: N818RS). Each magnet bar has a length of 25 mm, a width of 10 mm, and a height of 5 mm, while each coil has a length of 25 mm, a width of 16.1 mm, and a height of 15.1 mm.

Figure 7.3a shows a schematic of the structural components of the EMAT, which consist of two main elements: a set of 3D printed plastic holders to hold the coils and magnets, and a split clamp to attach the entire unit to a pipe. Plastic cross-clamping screws are used to fix the EMAT position on the pipe and minimize unwanted vibrations. Figure 7.3 also shows the top (b) and side (c) views of a complete EMAT mounted on a copper pipe. Four SMA-

type coaxial cables that provide the solenoid drive may be seen in these views; these are connected in parallel using SMA tees.

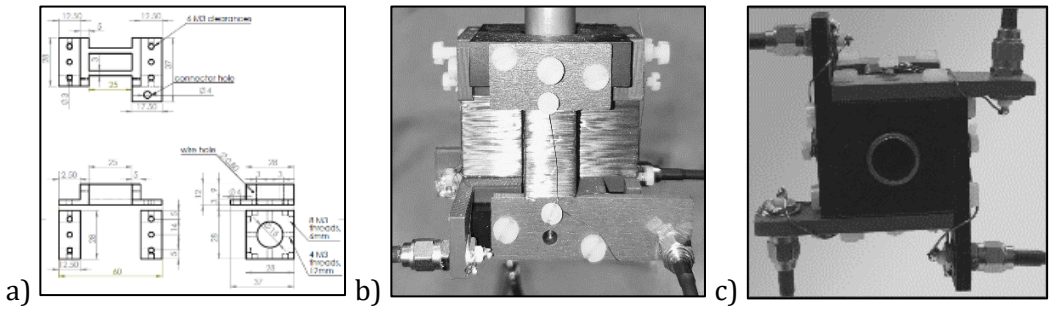

Figure 7.3: a) EMAT holder schematic; b) top c) and side views of a 4-element EMAT.

Multiple EMAT versions were constructed, and each was an improvement on the previous one. The first step was to increase the number of elements from one to four, which yielded an improvement in the signal-to-noise ratio and a reduction in flexural mode generation due to the increase in symmetry. The second was to increase the number of turns and decrease the wire thickness to raise the turn density, which again resulted in a better SNR. The third was to increase the pull force of each permanent magnet bar from 4 kg to 4.9 kg, which again increased SNR. The final improvement was to ensure a high symmetry of the coil windings. Figure 7.4 shows close-up photographs of two EMAT iterations, with a) poor symmetry and a low number of turns, and b) high symmetry and a larger number of turns.

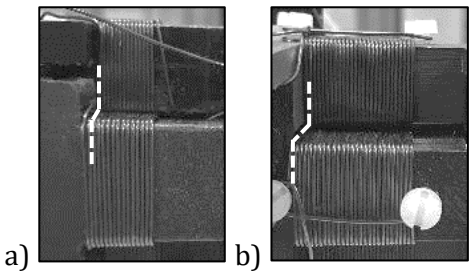

Figure 7.4: EMAT windings with a) low and b) high symmetry.

The microphones used for output transduction were commercially available units. Figure 7.5 shows a) a single microphone, b) top, and c) side views of the complete receiver, which allows up to four microphones to be mounted around the pipe using 3D-printed plastic holders. Single receiver elements are sufficient for basic measurements and multiple elements for identifying unsymmetrical modes, such as the F(1,1) mode. The position of

each microphone is adjusted to minimize the distance to the pipe surface, and hence increase acoustic coupling. Another enhancement to the acoustic coupling is by allowing adjustment of the microphone position using a rapid prototyped flexure driven by 2 screws. The microphone is an omnidirectional electret condenser (SmartLav+, manufactured by RODE) with a junction-gate field-effect transistor (JFET) for amplification and a 3 kΩ impedance. It has small dimensions of 24 mm by 5 mm. The output connector is a 3.5 mm jack with tip, ring, ring, and sleeve (TRRS). Since the microphone can detect sounds equally from all sides, the overall assembly is enclosed by a soundproofed box to block air reception and ensure that any detected signals are only those that have propagated along the pipe.

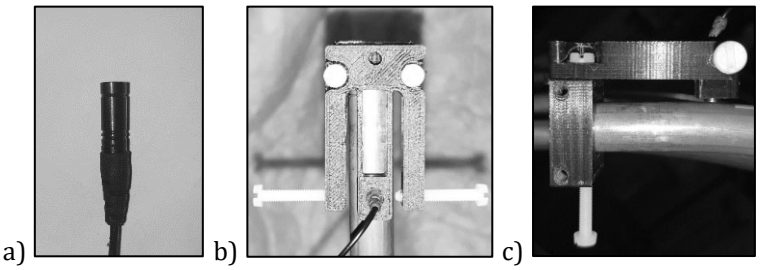

Figure 7.5: Photographs of a) a microphone, b) top, and c) side views of the complete receiver containing a flexure positioning system.

Figure 7.6a shows the shielded enclosures used to mate 3.5 mm TRRS audio jack ports with Bayonet Neill–Concelman (BNC) ports and hence allow connection of the microphones to the oscilloscope. Figure 7.6b shows the digital scope used to monitor the output signals from the microphones and export them to the PC via a USB port. The oscilloscope is a 4-channel unit (DSO5012A) from Agilent Technologies, which has a 2 Gsa/s sample rate and can detect frequencies up to 200 MHz. The instrument settings are controlled by the PC using SCPI commands.

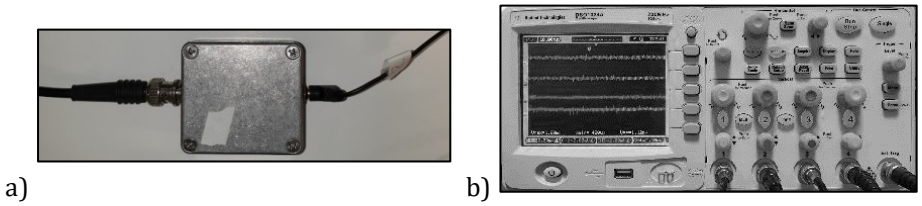

Figure 7.6: a) Shielded microphone interface box; b) four-channel digital oscilloscope.

Figure 7.7 shows a photograph of the rig from the top, including the transmitter (EMAT), the pipe, 2 trestles, and 1 horizontal beam to support the pipe, and the receiver (microphone). The copper pipe used has a 24.4 m length, 15 mm OD, and 1 mm wall thickness matching the simulations presented earlier. The pipe is joint-free and bent into a spiral shape of 10 turns with a diameter of approximately 0.8 m. Layers of acoustic absorbing material were wrapped around the beam to reduce cross-talk between adjacent turns, and minimize reflection and mode conversion arising from local support constraints. This arrangement allows long-distance propagation in a compact rig.

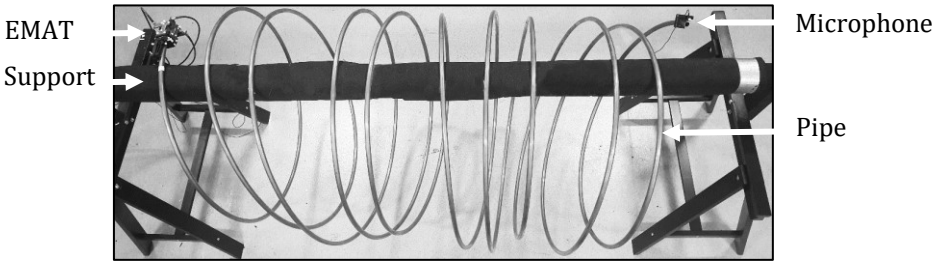

Figure 7.7: 24.4 m long spiral copper pipe.

The experimental pipe was carefully inspected to identify any discontinuities. For example, Figure 7.8 shows a photograph of a small dent located in the middle of the pipe created during manufacturing. Any such defect may be expected to induce mode conversion and reflections. Two further dents were observed close to the end of the pipe, and were removed easily by shortening the pipe. Due to the relative ductility of the thin copper wall, it may be distorted by clamping screws, especially at the elevated temperatures caused by eddy current generation at high power. Hence, care must be taken when conducting experiments by using plastic screws instead of metallic screws and controlling the EMAT drive power.

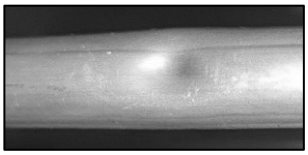

Figure 7.8: Photograph of an observed pipe dent.

7.2 Component Measurements

In this section, we present the results of preliminary component characterization. The 90-turn, 4-element cuboid EMAT was first characterized in isolation using an LCR meter, and found to have an inductance, L, of 57 μH, a resistance, R, of 3.5 Ω and a capacitance, C, of 200 pF. Its AC response was then measured in more detail using the circuit in Figure 7.9a, which contains a signal generator, V_S, with impedance, z_o, and an EMAT connected via a coaxial cable. An oscilloscope was used to measure the load voltage, V_L. Figure 7.9b compares the measured (red and solid black) and simulated (dashed) normalized responses of the EMAT. The red data was measured with a long cable, and the black with a short cable; similar results were obtained in each case. The simulated response was computed using the circuit analysis in Chapter 5. The experimental and theoretical responses are very similar, with a low frequency cut-off at about 5.7 kHz, and a flat band between 0.8 MHz and 9 MHz. Minor differences at high frequency can be ignored.

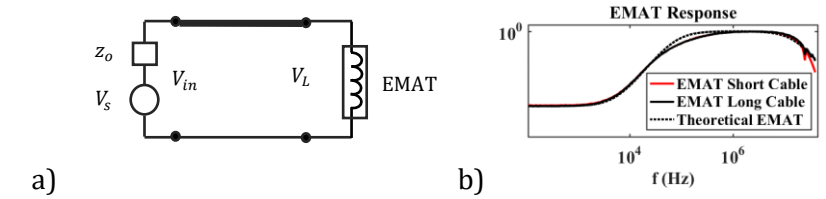

a) b)

Figure 7.9: a) Circuit for EMAT measurement, and b) comparison between experimental and theoretical frequency responses.

The EMAT was then characterized together with the audio power amplifier. Figure 7.10a shows the circuit, which contains a signal source, an amplifier, a 2.18 Ω, 50 W test resistor R_t for protection, and the EMAT. Figure 7.10b shows the responses of the amplifier (red), the amplifier and EMAT (black), and the theoretical amplifier response (dashed), again computed using the analysis of Chapter 5. All three results have an almost identical low frequency roll-off (at 50 Hz) and a flat response in the mid-frequency range. There are small differences at high frequency, and the measured high frequency cut-off increases from 300 kHz to 500 kHz after connecting the EMAT to the amplifier. Again, these details are unimportant at audio frequencies.

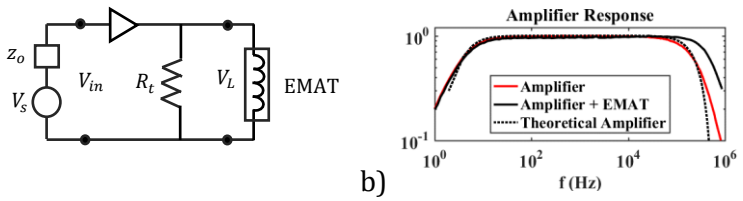

Figure 7.10: a) Circuit to measure the overall transducer response, and b) comparison between experimental and theoretical responses.

The linearity of the EMAT was explored by varying the input voltage over the excited frequency range. Figure 7.11 shows the relationship between the voltage across the EMAT and the input voltage at 1 (black), 10 (blue), 20 (green), and 30 (red) kHz. The interpolated lines are extended to start from (0,0) (dashed lines), confirming that the EMAT has linear behavior over the whole of the important acoustic frequency range.

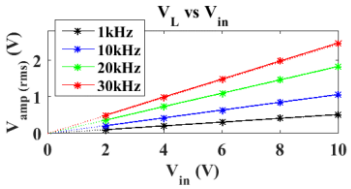

Figure 7.11: Comparison between input and output voltages of the EMAT driver circuit.

Measuring the response of the microphones and their built-in amplifiers is challenging. However, the necessary data was kindly made available by the manufacturer. Figure 7.12 shows a comparison between this data and the theoretical responses, with the latter again being computed as described in Chapter 5. A small rise can be seen in the experimental data between 3 kHz and 13 kHz, presumably due to diaphragm resonances; however, these are both small and damped, and amount to <2 dB signal enhancement at resonance.

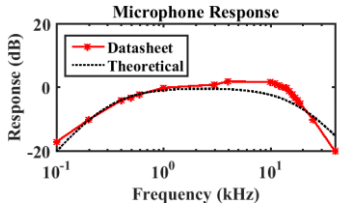

Figure 7.12: Comparison between manufacturer's data and the theoretical frequency response of the microphone.

7.3 System Trials

Results of complete system trials will now be presented. A rig consisting of a 4-element EMAT, a spiral copper pipe, and a single microphone were first used to demonstrate propagation of uniform pulses. Additional experiments suggested that the attenuation coefficient of the flexural mode (the most likely unwanted mode) is proportional to frequency between 300 Hz and 20 kHz. Since the microphone has its desired response in the audible range, operating at the maximum detectable frequency will maximise attenuation of undesirable components. A 20 kHz carrier was therefore used throughout.

Figure 7.13 shows a) the input signal (TX), and b) the received signal (RX) over 100 ms acquisition time, with the oscilloscope sampling rate set to 200 k cycles per second. The input signal amplitude was 5 V_{pp} while the received signal was about 4 mV_{pp}, indicating a significant amplitude reduction. The received signal was therefore corrected in post-processing due to its low amplitude by subtracting the mean of the first few samples to eliminate the offset and reduce the drift. Pulse spreading and additional pulses in the received signal can be ascribed to channel effects (including dispersion and multimode propagation) and discontinuity effects (including mode conversion and multiple reflections) respectively.

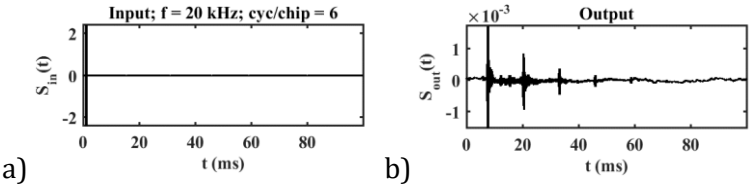

Figure 7.13: a) Transmitted and b) received experimental signals for a uniform pulse.

Figure 7.14 shows the normalized spectra of a) the transmitted and b) the received signals. While both are expected to be sinc functions centered on the carrier frequency (20 kHz), the received spectrum has oscillations due to the superimposition of the spectra of multiple components generated by channel features. Moreover, there are clear spikes around 3, 5, and 13 kHz, which are due to the resonance of individual devices in the system around these frequencies including the microphone as described above.

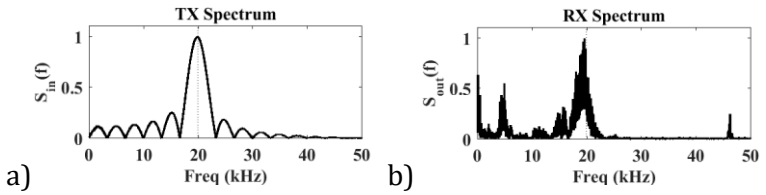

Figure 7.14: Spectra of a) transmitted and b) received experimental signals.

To improve interpretation of the received signal, the correlation detection and down-conversion processes used in the numerical model of previous chapters were applied to the experimental measurements. Figure 7.15 shows the normalized correlation envelopes of a) the transmitted and b) the received signals measured above. The received envelope clearly has one major peak, two small peaks, and multiple smaller peaks that appear up to 84 ms delay, the last of which corresponds to a propagation distance of over 319 m at a velocity is 3800 m/s. The major peak arriving at 6.5 ms is certainly the longitudinal mode L(0,1).

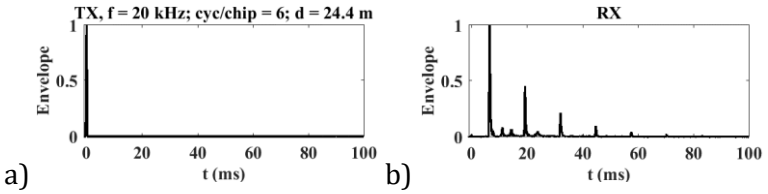

Figure 7.15: a) Transmitted and b) received experimental correlation envelopes.

Prior to a precise identification of the different pulses in the received signal, velocities of modes must be approximated or extracted. A group velocity spectrogram was therefore computed by applying the short-time Fourier Transform (STFT) to the received signal to compare experimental and numerical dispersion curves. Figure 7.16 shows the results obtained, together with numerical group velocity variations calculated using PCDisp. The group velocity at the carrier frequency (highlighted by a black line) of the experimental longitudinal mode (brightest spot) is around 3790 m/s while the corresponding theoretical velocity (blue) is 3800 m/s. The experimental flexural mode velocity is around 1320 m/s while the corresponding theoretical velocity (green) is 1360 m/s. The marginal mismatch between experimental and numerical velocities is likely to be justified due to the material treatment and small variations of the pipe diameter and thickness along its length.

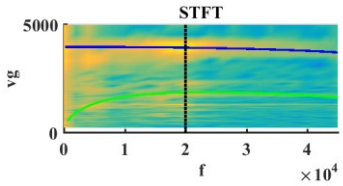

Figure 7.16: Comparison between the experimental spectrogram and theoretical group velocity dispersion curves. V_g for L(0,1) and F(1,1) are shown in blue and green.

Returning to the received signal analysis, to identify the main pulses more exactly, Figure 7.17a shows markers using the group velocities extracted above on the received signal for multimode propagation and reflections in a shorter time scale. The blue markers show estimated time delays for the L(0,1) mode and its end reflections at 3t, 5t, and 7t while the green markers show estimated delays for the F(1,1) mode and its end reflection. Attenuation is noticeably higher for the flexural mode, whose ring-down decays quickly.

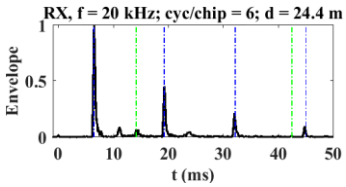

Figure 7.17: Received experimental correlation envelope with markers for additional signal components arising from multimode propagation and end reflections.

Figure 7.18 now shows additional markers highlighting signal components arising from channel discontinuity effects on the same signal, in a) similar and b) expanded scales. For example, mode conversion and reflections would be expected to arise from the dent previously shown in Figure 7.8, which is located at 8.9 m from the transmitter. The magenta marker shows L(0,1) -> F(1,1) mode conversion, the cyan marker shows F(1,1) -> L(0,1) mode conversion, and the red marker shows L(0,1) partial reflections. Here, one of the partial reflections is almost overlapping with the L(0,1) -> F(1,1) mode conversion while the other partial reflection is very close to the F(1,1) mode. However, F(1,1) -> L(0,1) mode conversion appears almost non-existent. These results are entirely as expected; the dent is an asymmetric distortion and may very easily convert a symmetric mode to an antisymmetric one, but not vice versa.

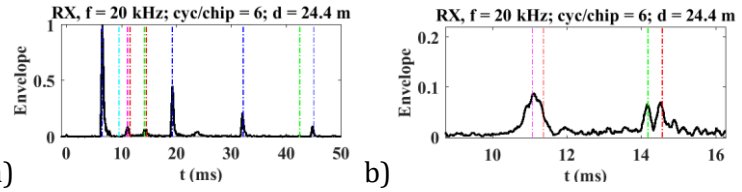

a) b)

Figure 7.18: a) The received experimental correlation envelope and b) its expanded view with markers for multimode and reflections.

Figure 7.19a compares the normalized experimental (black) and theoretical (red) correlation envelopes of the same transmitted signal. The model assumes the same pipe parameters, and includes channel and discontinuity effects observed experimentally, namely dispersion, multimode propagation, L(0,1) -> F(1,1) mode conversion, multiple reflections (using double Fabry-Perot cavity of two perfect end-reflectors and one intermediate reflector), and attenuation. The assumed relative amplitudes are 0.85 for the L(0,1) mode and 0.15 for the F(1,1) mode and the attenuation coefficients are 0.03 m^{-1} for the L(0,1) mode and 0.07 m^{-1} for the F(1,1) mode. The mode conversion amplitude is 0.2 and the partial reflection amplitude is 0.18. In addition, the transmission and reflection coefficients of the partial reflector are assumed to be $T = 0.76$ and $R = -j0.65$.

These parameters demonstrate a clear match between the experimental and theoretical signals for L(0,1) (blue markers) and F(1,1) (green markers) modes, mode conversion (magenta marker), and partial reflections (red markers) in both time and amplitude, confirming the analysis above. However, a small timing difference (larger for F(1,1) mode) is due to the mismatch between the experimental and theoretical dispersion curves. Any small difference in assumed group velocity can result in a noticeable mismatch in reflection timing, due to the large distance traveled. Figure 7.19b shows the same comparison, but in an expanded view of the main L(0,1) peak. The experimental peak is marginally wider than the theoretical one. Multiple experiments were conducted to investigate the matter. To lower the frequency of mechanical vibrations from the transducers that might widen the main peak, additional masses were attached to the EMAT. Additional support bands were also used to hold the microphone holder parts together firmly, and clamping screws were gradually tightened to monitor any change introduced. The slow decay of the main peak can be ascribed to multiple reflections over the short distance between the pipe end and the microphone. Further discussion of additional noise will be presented later.

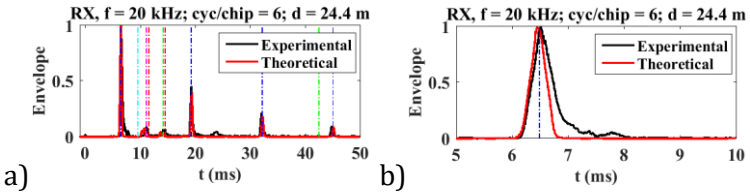

Figure 7.19: Comparison between theoretical and experimental received envelopes on a) long and b) short timescales.

7.4 Multiplexed Signals

In this section, an experimental demonstration of Barker code, QO, and GCP propagation will be presented using the same apparatus. Figure 7.20 shows a) transmitted and b) received experimental correlation envelopes of the 9-bit generalized Barker code 3482 with base B = 6 using 6 cycles of a 20 kHz carrier per chip. While the transmitted envelope has a clear and recognizable autocorrelation shape for this particular code, the received envelope has a distinguishable major peak with a sharp main lobe but distorted sidelobes. In addition, the received signal contains smaller peaks arising from the flexural mode, mode conversion, and reflections whose wide sidelobes that overlap noticeably. Figure 7.20c compares the same experimental Barker code envelope with its corresponding theoretical envelope, generated using the dispersive model with the parameters above. The experimental and theoretical envelopes again are well matched. However, a small mismatch in some of the mode conversion and reflections can be seen. The most likely explanation is overlap with smaller peaks generated by other features in the pipe, such as mode conversion and partial reflections by the support and transducer holders. Because of their low amplitude, these effects were not incorporated into the model. They became more noticeable in experimental coded propagation since the signal duration is significantly increased.

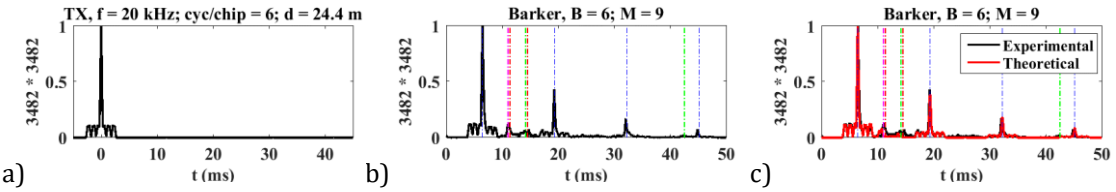

Figure 7.20: a) Transmitted, and b) received correlation envelopes of experimental generalized Barker code at 20 kHz; c) comparison with theory.

We now demonstrate multiplexed code propagation, using the best codes identified in Chapter 5. We start with quasi-orthogonal codes. Figure 7.21a shows the full set of autocorrelation envelopes (diagonal plots) and cross-correlation envelopes (off-diagonal plots), after correlation and down-conversion, for the best QO Barker-Type pair, namely the 9-bit pair equivalents of the decimal numbers 8564 and 1040855 in base 6. In each case, each chip contained 6 cycles of a 20 kHz carrier as before. Figure 7.21b compares the same experimental code set and the corresponding theoretical envelopes using the dispersive model with the aforementioned parameters. The experimental signal components arising from longitudinal and flexural mode propagation, mode conversion, and multiple reflections all match the theoretical predictions, as expected. A marginal mismatch in the generalized Barker code comparison between the main peak and the first L(0,1) reflection can be seen again here, but with slight variations based on the coherent addition and subtraction of the overlaps in every pair. There are other differences in the sidelobes of the main peaks and the main cross correlation components; experimental signal amplitudes are higher than theoretical amplitudes, presumably due to the overlap with the additional slow decay effect mentioned above. Thus, the main cross-correlation of any experimental pair is not a perfect mirror of its reciprocal. The cumulative effect is to reduce the discrimination factor from the predicted value of 4.5.

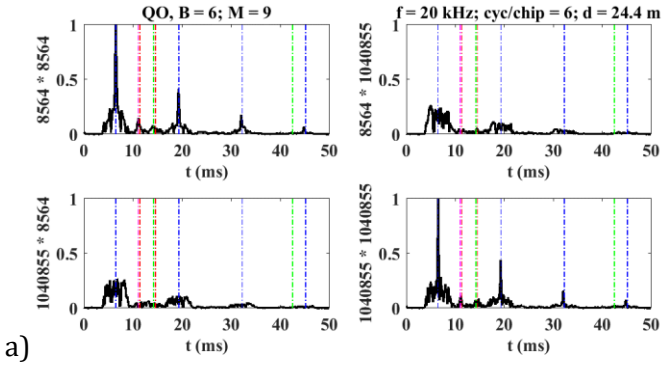

a)

b)

Figure 7.21: a) Experimental auto- and cross-correlation envelopes of QO pair; b) comparison with theory.

The results above indicate that a QO pair with a high discrimination factor can be integrated into a cyclic distributed network consists of a receiving node with adjacent transmitting node on either side. However, codes may still arrive simultaneously, and we therefore now demonstrate the effects of code collision. To do so, a composite signal containing both the codes 8564 and 1040855 was constructed, with equal strength but a variable delay of $2M$ digits (0% overlap), M digits (50% overlap), and 0 digits (100% overlap).

Figure 7.22 shows the composite experimental signals after correlation processing. Figures 7.22a)-c) shows results after correlation with code 8564, for a) 0%, b) 50%, and c) 100% overlap, while Figures 7.22d)-f) show results after correlation with 1040855 . The QO codes are clearly still detectable. However, overlaps with unwanted signal components are now more detrimental. When the collision is 0% (a and d) and 50% (b and e), the sidelobes and cross-correlations exceed the discrimination threshold, and unwanted components merge with the main component. When the collision is 100% (c and f), sidelobes exceed 0.5 normalized amplitude. At this point, users can no longer be distinguished. These results highlight how sidelobes and unwanted cross-correlations rapidly deteriorate the discrimination factor. One solution is to use a handshake to ensure that only one node can transmit at any time. Handshake protocols are well-known in communication and digital design domains and can be applied asynchronously in ways beyond the scope of this thesis.

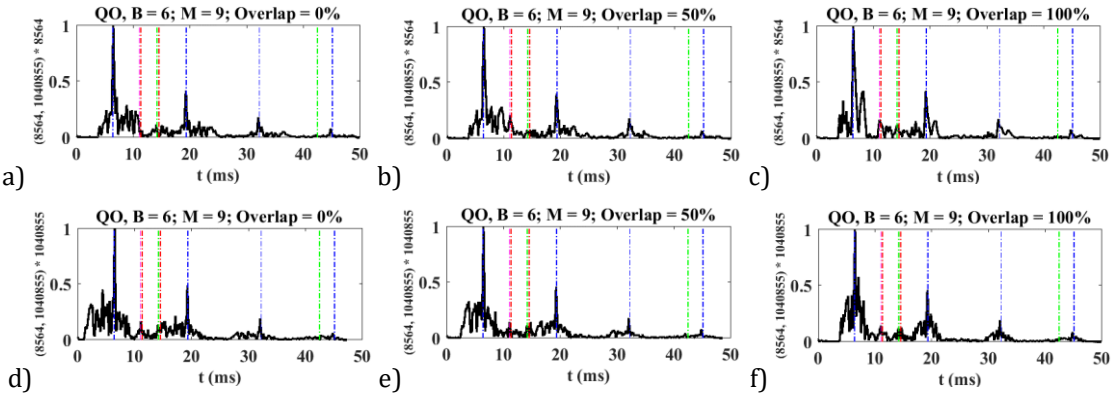

Figure 7.22: QO pair 8564, 1040855 with a) 0%, b) 50%, and c) 100% overlap correlated with 8564, and with d) 0%, e) 50%, and f) 100% overlap, correlated with 1040855.

Returning now to propagation of individual codes, Figure 7.23 shows experimental auto- and cross-correlation envelopes for the 10-bit triplet equivalents of 5099, 918088, and 989300 in base 6. Here the increased code length has slightly increased overlap between unwanted signal components. The effect can be seen clearly in the cross-correlation of the two codes 5099, 989300, where the envelope marginally exceeds the expected 3.78 discrimination threshold. Again, the cross-correlations components of reciprocal pairs are not perfectly mirrored. However, distinguishing between three equal-strength users remains possible, since the discrimination factor is still higher than the number of users. Such a triplet therefore allows network based on a set of three cyclically distributed codes.

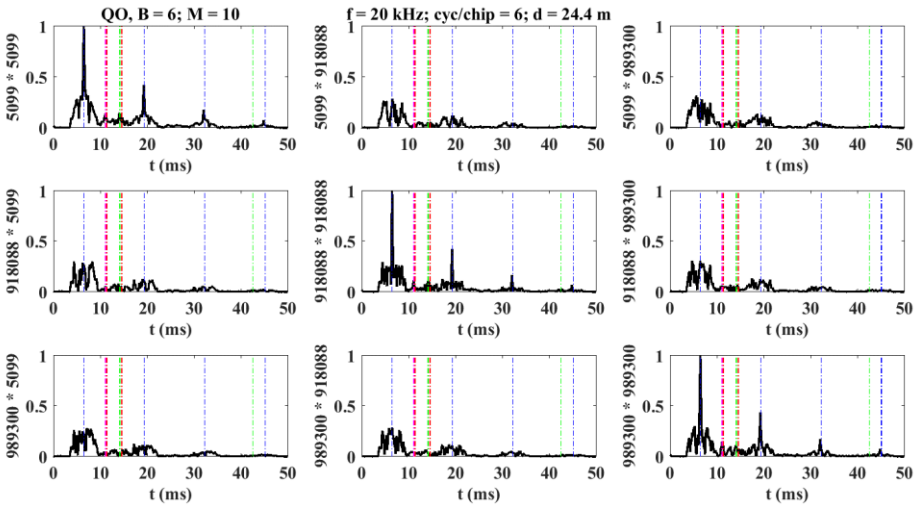

Figure 7.23: Experimental auto- and cross-correlation envelopes of QO triplet 5099, 918088, and 989300 in base 6.

Finally, Figure 7.24 shows experimental auto- and cross-correlation envelopes for the 8-bit QO quadruplet equivalents of 97, 4528, 35070, and 145245 in base 6. The code correlations and channel and discontinuity effects are again all as expected, including a sharp main peak with wide sidelobes in autocorrelations and relatively high cross-correlations. Once again, cross-correlations of reciprocal pairs are not perfectly mirrored. Some of the sidelobes in both autocorrelations and cross-correlations are now above 0.33 normalized amplitude. Hence, the discrimination factor is now too low for successful separation of 4 equal-strength users. The chance of code collision with four users is clearly higher. Once again, a handshake mechanism may be used in mitigation. However, this overhead implies a longer

communication time. These results confirm the need for full orthogonality to minimize signal overlaps and allow code sets supporting increased user numbers.

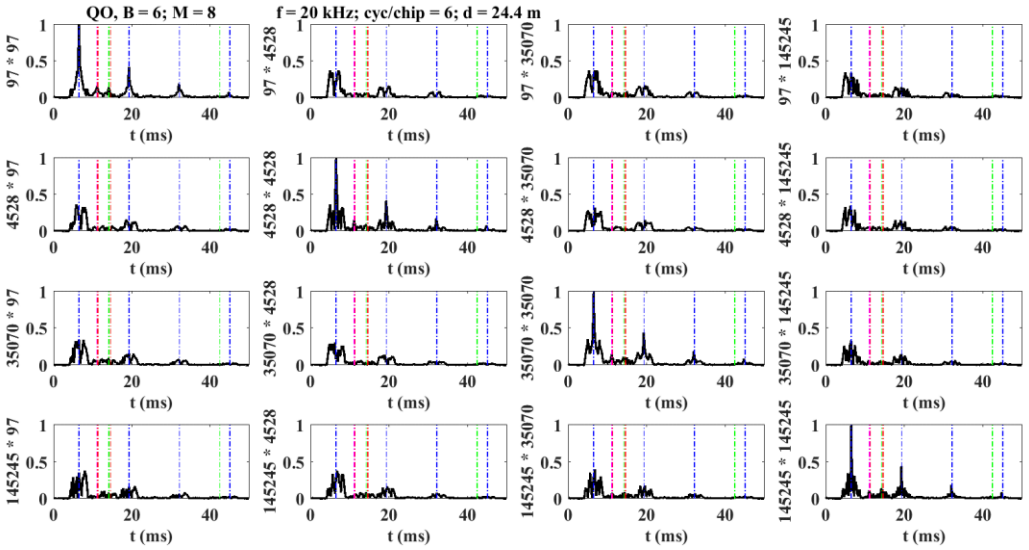

Figure 7.24: Experimental auto- and cross-correlation envelopes of QO quadruplet 97, 4528, 35070, and 145245 in base 6.

We therefore now demonstrate the propagation of Golay complementary pairs and complementary code sets. Experimentally, there are several difficulties. To achieve full orthogonality, the sampling rate of the software, function generator, and the oscilloscope must all be equal or multiples of each other, and synchronization between instruments is mandatory. Otherwise, the autocorrelation sidelobes and the cross-correlation signals will not be completely canceled. These aspects were investigated extensively.

To begin with, Figure 7.25a shows the full set of autocorrelation envelopes (diagonal plots) and cross-correlation envelopes (off-diagonal plots) after correlation and down-conversion of the bipolar orthogonal GCP (1, 2) and (11, 8) with M=4. As usual, the results show the main longitudinal mode, the flexural mode, and additional signal components arising from mode conversion, and multiple reflections. However, the autocorrelation peaks are now clear with no sidelobes, and the cross-correlation envelopes are zero as expected. The main features that can be seen on the diagonal plots are the ring-down pattern of the L(0,1) mode. These components may be removed by time-gating, following detection of the main peak

using a threshold detector set to a suitable level. These results show the immediate benefit of full orthogonality, enabling precise discrimination between users even if codes collide.

Figure 7.25b compares between the same full set of the experimental GCP pair (black) and their corresponding theoretical envelopes (red) using the dispersive model. There is again a good match, which was achieved using the same numerical parameters as before, apart from a minor reduction in the attenuation coefficients from 0.03 to 0.025 m^{-1} for the L(0,1) mode, and from 0.07 to 0.06 m^{-1} for the F(1,1) mode needed to obtain a good amplitude match. One possible explanation is a change in temperature, arising from eddy current heating during the extended experiments required to demonstrate GCP codes.

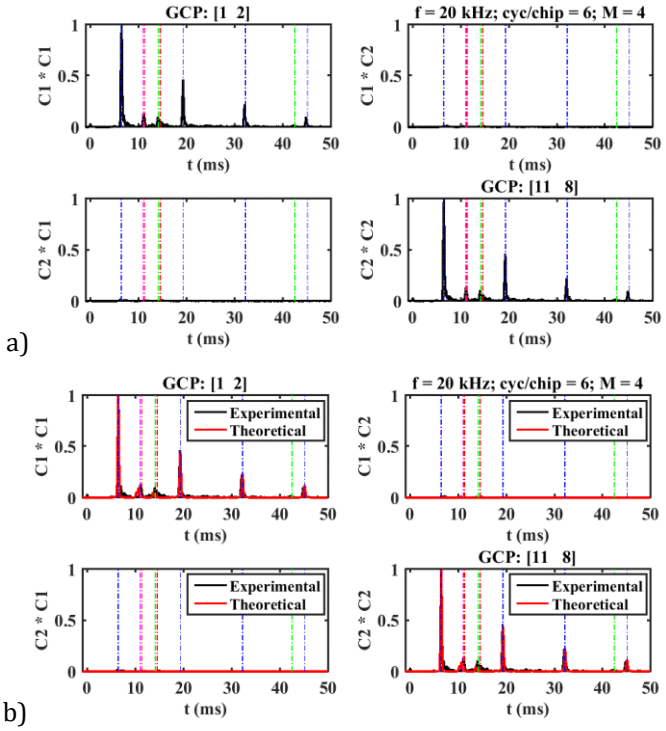

Figure 7.25: a) Experimental auto- and cross-correlation envelopes of orthogonal GCPs pair; b) comparison with theory.

Similarly, Figure 7.26 shows the full set of auto- and cross-correlation envelopes for a 4-user complementary code set with *M*=4. In each case, the codes used are listed on the diagonal plots. These results should be compared with those obtained for the 4-user QO code set above. There is a very significant improvement in separation of the main signal component and any unwanted components. The time separation between the first main

peak and the second arrival peak is about 2 ms, compared with less than 0.7 ms separation in the corresponding QO code set due to the code length and the sidelobes. Cancellation of sidelobes in GCPs has not only reduced overlaps but also has reduced power distribution and has therefore improved the main peak and L(0,1) reflections. Distinguishing these reflections is important in a reflection scheme as discussed in the next chapter. This code set may be used to configure a cyclic network with 4 distinguished nodes, or a 5-node network containing a listening node with 2 adjacent transmitting nodes on each side.

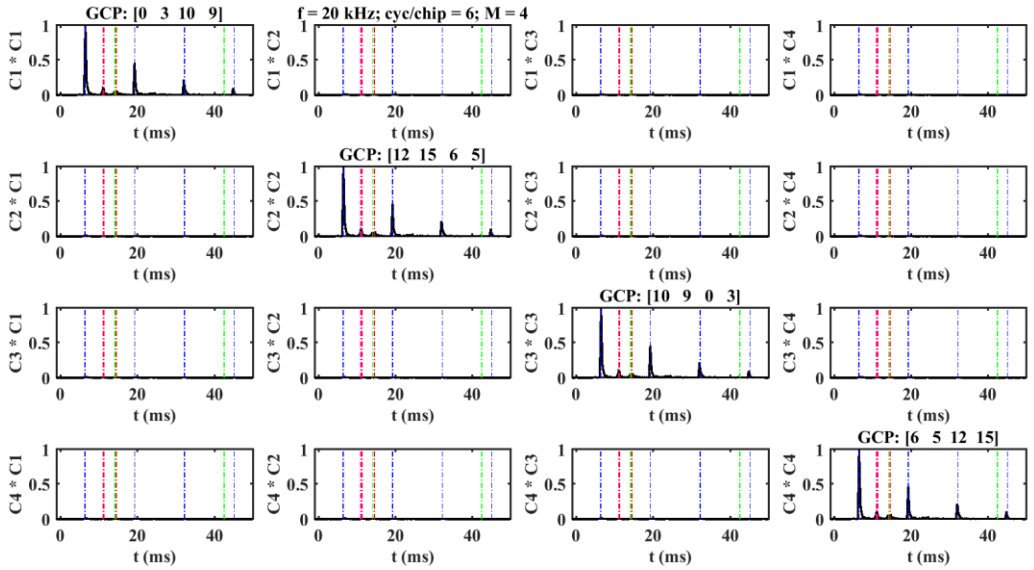

Figure 7.26: Experimental auto- and cross-correlation envelopes of a 4-user CCS.

Finally, Figure 7.27 shows the full set of auto- and cross-correlation envelopes for an 8-user complementary code set with *M*=8 (in a landscape view). These results represent a doubling of the number of allowed users, making the benefits of full orthogonality very clear. Complementary code sets for even higher numbers of users may be constructed in the same way, using a simple algorithm. In contrast, finding corresponding QO codes for such a large number of users is likely to require an unfeasible amount of time or computing resources, and the resulting codes may be expected to have a poor discrimination factor. However, it should not be forgotten that the advantage of complementary code sets has been achieved through the propagation of additional codes and subsequent complex signal processing. Furthermore, cyclic distribution of codes makes it unlikely that such a large number of distinct users will need to be supported.

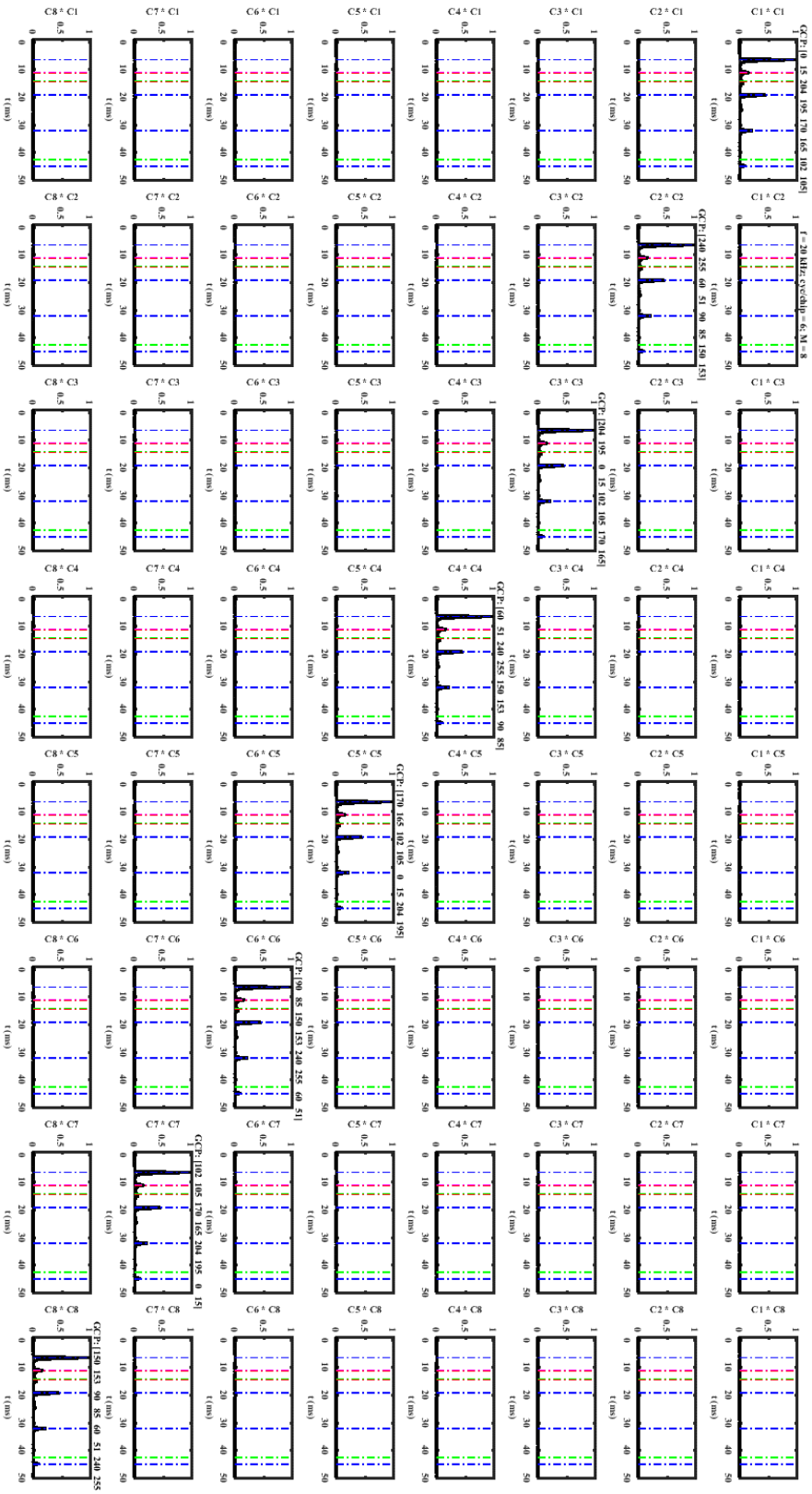

Figure 7.27: Experimental auto- and cross-correlation envelopes of an 8-user CCS.

We now consider a previously highlighted property of Golay code pairs: if the number of bits is increased, the SNR should increase proportionally. However, overlap with additional signals generated by mode conversion and reflection will raise the effective noise floor. In such a case, realizing the potential SNR gains offered by longer signals becomes impossible, since the noise is no longer random. For example, Figure 7.28a shows a comparison between autocorrelations of the GCP (1, 2) for 4 and 16 bits. The 16-bit envelope has 4 times higher processing gain. However, Figure 7.28b shows a comparison between the same GCP envelopes after normalization. Figure 7.28c shows the same data on an expanded scale. Here it is clear that increasing the code length has increased rather than decreased the effective noise floor.

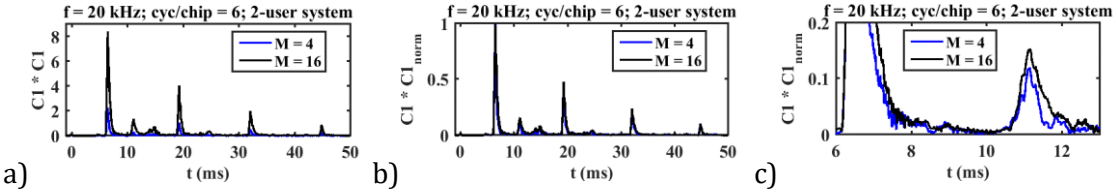

Figure 7.28: Comparison between autocorrelations of GCPs with 4 and 16 bits.

To illustrate this further, Figure 7.29 shows the experimental noise floor of a) the autocorrelation of the GCP (1, 2) and b) the cross-correlation of the orthogonal GCPs (1, 2) and (11, 8) on expanded scales chosen to lie between the arrivals of the main peak and mode conversion component (the second arrival peak). The autocorrelation shows a relatively high signal that exists in between these two pulses. This 'noise floor' has periodic local peaks, and hence cannot be random. In contrast, the cross-correlation envelope has a much lower noise floor since the additional signals are fully canceled.

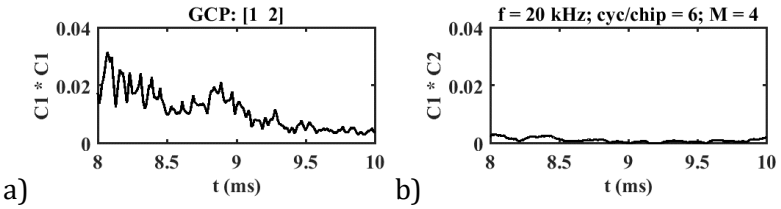

Figure 7.29: Experimental 'noise floors' of a) auto- and b) cross-correlations of GCPs.

These results also confirm the existence of very low amplitude channel discontinuity effects, in addition to the other major effects discussed previously. Such low amplitude effects are

generally unimportant; however, they may limit the performance of GCP multiplexing, since they introduce additional correlated noise that cannot be removed by signal processing. These effects are likely to exist in any practical pipeline that has additional structural features such as connectors or supports.

7.5 Conclusion

This chapter has described laboratory apparatus to successfully demonstrate pulse and coded propagation along a pipe. The experimental results agree well with the theoretical simulations, validating the analysis of channel and discontinuity effects including dispersion, multimode propagation, mode conversion, and multiple reflections discussed in previous chapters. In addition, signal transmission experiments confirm the feasibility of exploiting quasi-orthogonal codes and Golay complementary pairs in monitoring pipelines to verify continuity using multiple sensing nodes. QO codes performance may be degraded by overlaps with unwanted signal components and codes collisions while perfectly orthogonal GCPs require longer transmitting times. In addition, other low amplitude discontinuity effects are likely to exist and may limit the performance of GCP multiplexing. The next chapter will discuss the feasibility of using such a system to allow the detection of changes, for example, caused by tampering.

8 Change Detection

Previous chapters have investigated theoretically and experimentally a system for verifying pipeline continuity using Quasi-Orthogonal codes and Golay Complementary Pairs in a transmission scheme. Status monitoring is important to anticipate potential destructive attacks, which this research is primarily concerned about. In this chapter, a system will be demonstrated for detecting changes in both transmission and reflection.

To detect anomalies or a changes in engineering structures, non-destructive testing (NDT) uses time-consuming approaches involving ultrasound, eddy currents, or x-rays that usually involve disruption to operation [180]. In contrast, structural health monitoring (SHM) methods use distributed sensors for continuous monitoring and change detection [181]. For example, signal processing algorithms have been developed for guided acoustic wave systems to extract information about changes in plates [182], rails [183], and pipes [184]. In pipelines, changes mostly take the form of internal and external corrosion that thins the pipe wall. This can grow and eventually cause complete system failure.

A mathematical and numerical analysis of changes in transmission and reflection will first be elaborated, then numerical and experimental results will be compared. Lastly, potential automated algorithms will be explored to decide if a change occurs. As discussed in Chapter 1, transmission schemes have transmitting and receiving nodes spaced along the pipeline, while reflection schemes have transmission and reception combined in the same node. The latter is commonly used in industry for detecting changes.

8.1 Theoretical Analysis

Here we assume that the most potentially disruptive changes may involve deliberate external disturbances. These amount to adding a reflector to the pipe, which will induce additional reflection and mode conversion. The induced changes can be understood in terms of timing diagrams. As an example, we assume, a pipe of length d with perfect end reflectors, one asymmetrical partial reflector at a distance d_m, and the possibility to attach a removable reflector at a distance d_r. This configuration resembles the experimental pipe discussed before. We assume a simple pulse which starts from the origin and travels to the end reflector. Figure 8.1 shows the timing diagram, with assumed signal paths for some of

the propagated, reflected and mode converted waves. The received signal is the combination of waves at d in a transmission scheme, and at the origin in reflection.

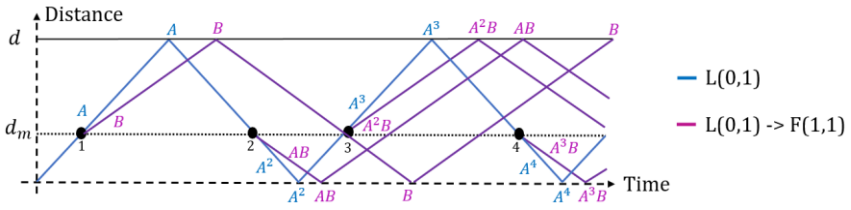

Figure 8.1: Timing diagram showing L(0,1) mode propagation and L(0,1) -> F(1,1) mode conversion by a dent.

In this example, a scattering event at point 1 at distance d_m will split the incident signal into an L(0,1) mode (blue) with amplitude A and a converted F(1,1) mode (magenta) with amplitude B. The reflected L(0,1) mode must split again at scattering point 2 after a distance $2d - d_m$, into an L(0,1) mode with amplitude A^2 and a converted F(1,1) mode with amplitude AB. Ignoring the attenuation, the same scattering events may happen again at points 3, 4, … etc. Other excitations and scattering events are possible but will be considered later. As in earlier analysis, the sum of all L(0,1) waves in transmission can be written as:

$$X_{T,L} = Ae^{-jk_l d}\{1 + A^2e^{-j2k_l d} + A^4e^{-j4k_l d} \ldots\} \tag{8.1}$$

In a similar way, the combined L(0,1) -> F(1,1) mode converted waves with scattering at odd-numbered points (1, 3, 5 … etc.) can be written as:

$$X_{T,L-F(o)} = Be^{-jk_l d_m}e^{-jk_f(d-d_m)}\{1 + e^{-j2k_f d} + e^{-j4k_f d} \ldots\}\{1 + A^2e^{-j2k_l d} + A^4e^{-j4k_l d} \ldots\} \tag{8.2}$$

In addition, the combined L(0,1) to F(1,1) mode converted waves with scattering at even-numbered points (2, 4, 6 … etc.) can be written as:

$$X_{T,L-F(e)} = ABe^{-jk_l(2d-d_m)}e^{-jk_f(d+d_m)}\{1 + e^{-j2k_f d} + e^{-j4k_f d} \ldots\}\{1 + A^2e^{-j2k_l d} + A^4e^{-j4k_l d} \ldots\} \tag{8.3}$$

Energy conservation requires that amplitudes are related by an expression of the form:

$$\sqrt{|A^2| + |B^2|} = 1$$

(8.4)

Now, some of the previous terms may be simplified as:

$$\{1 + A^2 e^{-j2k_l d} + A^4 e^{-j4k_l d} \ldots\} = \frac{1}{1 - A^2 e^{-j2k_l d}}$$
$$\{1 + e^{-j2k_f d} + e^{-j4k_f d} \ldots\} = \frac{1}{1 - e^{-j2k_f d}}$$

(8.5)

Consequently, the two L(0,1) -> F(1,1) converted modes can be summed to obtain:

$$X_{T,L-F} = X_{T,L-F(o)} + X_{T,L-F(e)} = \frac{Be^{-jk_l d_m} e^{-jk_f (d-d_m)} + ABe^{-jk_l (2d-d_m)} e^{-jk_f (d+d_m)}}{(1 - A^2 e^{-j2k_l d})(1 - e^{-j2k_f d})}$$

(8.6)

These expressions may be incorporated into a numerical model similar to the one discussed before, consisting of an EMAT and microphone attached to a copper pipe with 15 mm OD, 1 mm wall thickness, and 24.4 m length and with an existing dent at 9.8 m. The excitation is a 6-cycle pulse at 20 kHz, and the L(0,1) mode is assumed to be excited with unit amplitude. Attenuation values are assumed as 0.03 for the L(0,1) mode and 0.07 for the F(1,1) mode, while the mode conversion amplitude is taken as 0.2 to match later experiments. Figure 8.2 shows the received correlation envelope in transmission, with no reflector, highlighting a) the L(0,1) mode (blue) and b) L(0,1) -> F(1,1) mode conversion by the dent (magenta). As expected from the timing diagram, the time plot shows the L(0,1) mode with an amplitude of about 0.8, its ring-down pattern, and L(0,1) -> F(1,1) mode conversion by the first odd and even scattering points. The mode conversion quickly disappears due to its low amplitude and high flexural mode attenuation.

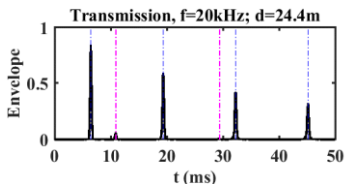

Figure 8.2: Numerical correlation envelope in transmission with no reflector. Markers show a) longitudinal propagation and b) mode conversion by the dent.

A comparable analysis can be applied in a reflection scheme. The combined propagated L(0,1) waves are then:

$$X_{R,L} = 1 + A^2 e^{-j2k_l d}\{1 \ + \ A^2 e^{-j2k_l d} + \ A^4 e^{-j4k_l d} \ \ldots\}$$

(8.7)

Similarly, the combined L(0,1) ->F(1,1) mode converted waves with scattering at points (1, 2, 3 … etc.) are:

$$X_{R,L-F} = \frac{Be^{-jk_l d_m} e^{-jk_f(2d-d_m)} + ABe^{-jk_l(2d-d_m)} e^{-jk_f(d_m)}}{(1 - A^2 e^{-j2k_l d})(1 - e^{-j2k_f d})}$$

(8.8)

Next, L(0,1) partial reflections will be incorporated. Figure 8.3 shows a timing diagram for the same launched L(0,1) mode with partial reflection paths highlighted in red. The L(0,1) reflection at point 1 is assumed to have an amplitude of R, while L(0,1) reflections at points 2, 3, 4, … etc. have amplitudes of AR, A^2R, A^3R, … etc.. In reflection, a partial reflection may arrive considerably before any mode conversion, in contrast to a transmission scheme.

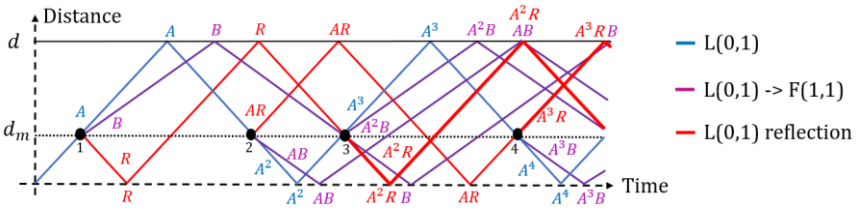

Figure 8.3: Timing diagram showing L(0,1) mode, L(0,1) -> F(1,1) mode conversion, and L(0,1) partial reflection by the dent.

The combined partially reflected waves of the L(0,1) mode that are reflected at even and odd scattering points in a transmission scheme are given by:

$$X_{T,Lm} = \frac{Re^{-jk_l(d+2d_m)} + ARe^{-jk_l(3d-2d_m)}}{(1 - A^2 e^{-j2k_l d})(1 - e^{-j2k_l d})}$$

(8.9)

Adding this response to the numerical model, Figure 8.4 shows the received correlation envelope in transmission on an extended amplitude scale, highlighting the L(0,1) mode,

L(0,1) -> F(1,1) mode conversion, and L(0,1) partial reflection by the dent (red). The partial reflection from the first scattering point almost overlaps with the mode conversion, making it difficult to distinguish between them. There are perfect overlaps between multiple partial reflection paths.

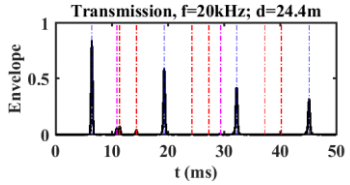

Figure 8.4: Numerical correlation envelope in transmission with no reflector. Markers show longitudinal propagation and mode conversion and partial reflection by the dent.

Alternatively, in reflection, the combined partial reflection waves of the L(0,1) mode are:

$$X_{R,Lm} = \frac{Re^{-jk_l 2d_m} + ARe^{-jk_l(4d-2d_m)}}{(1-A^2e^{-j2k_l d})(1-e^{-j2k_l d})} \tag{8.10}$$

We now consider the changes that arise when a partial reflector is attached. Figure 8.5 shows a timing diagram for the same pipe, with a partial reflector at a distance d_r, here assumed to be equal to or greater than d_m. Focusing only on L(0,1) -> F(1,1) mode conversions, the diagram shows the L(0,1) mode in blue, L(0,1) -> F(1,1) mode conversion by the dent in magenta, and L(0,1) -> F(1,1) by the reflector in cyan. The scattering points now have doubled; 1m, 2m, 3m, … etc. are the scatterings due to the dent, and 1r, 2r, 3r, … etc. are those due to the reflector (with an assumed amplitude of C). Since there are more scattering events, a reduced main wave amplitude and more scattered waves are expected.

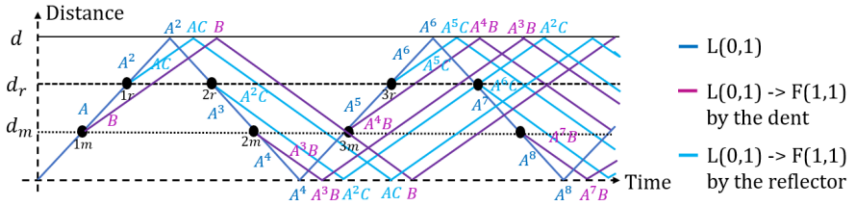

Figure 8.5: Timing diagram showing L(0,1) mode, L(0,1) -> F(1,1) by the dent, and L(0,1) -> F(1,1) mode conversion by the reflector.

Here, the combined propagated L(0,1) waves in a transmission scheme are modified to:

$$X_{T,L} = A^2 e^{-jk_l d}\{1 \ + \ A^4 e^{-j2k_l d} + \ A^8 e^{-j4k_l d} \ \ldots\} \tag{8.11}$$

In contrast, the combined L(0,1) waves in a reflection scheme are:

$$X_{R,L} = 1 + [A^4 e^{-j2k_l d}\{1 \ + \ A^4 e^{-j2k_l d} + \ A^8 e^{-j4k_l d} \ \ldots\}] \tag{8.12}$$

Intuitively, the combined mode conversion L(0,1) to F(1,1) by the dent in both schemes can be modified to include altered variables of amplitudes and distances by attaching a reflector. In addition, the combined L(0,1) -> F(1,1) mode conversion by the reflector in both schemes can be synthesized similar to previous mode conversion analysis. There are many other possible pathways, and these quickly complicate the analysis even in the simple example above. However, any other experimentally observed paths can be included in a similar way.

Considering L(0,1) partial reflections, Figure 8.6 shows the previous paths of the dented pipe with an attached reflector, in addition to L(0,1) partial reflections from the dent (red) and the reflector (yellow). Here, the amplitude of the partial reflection by the dent at scattering point $1m$ is R_1, while the amplitude by the reflector at scattering point $1r$ is R_2. There is now an increased number of waves, and consequently an increased number and extent of signal overlaps is to be expected. For this arrangement, all the partially reflected waves generated by the reflector and the dent in both schemes can easily be synthesized.

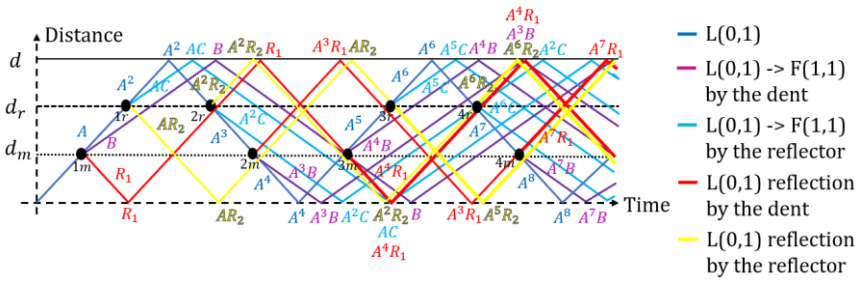

Figure 8.6: Timing diagram for L(0,1) mode, L(0,1) -> F(1,1) and L(0,1) partial reflection by the dent, and L(0,1) -> F(1,1) and L(0,1) partial reflection by the reflector.

To elaborate more on the L(0,1) -> F(1,1) mode conversion and L(0,1) partial reflection, we add a reflector to the numerical model above. To match later experiments, the reflector is attached at 18.5 m from the transmitter with an assumed reflectivity of 0.3, higher than that of the dent. Figure 8.7 shows in transmission a) the received correlation envelope, highlighting the channel and discontinuity effects, and b) a difference envelope highlighting L(0,1) -> F(1,1) mode conversion (cyan) and L(0,1) partial reflection (yellow) by the reflector. The difference envelope is acquired by subtracting the signal with a reflector from the signal without it. Since the reflector is closer to the receiver, reflector effects arrive earlier than discontinuity effects. The first peak after the main peak is F(1,1) -> L(0,1) mode conversion by the first scattering point. The difference envelope shows that L(0,1) partial reflections by the odd and even scattering points have less dispersion and attenuation and consequently have more potential for use in change detection.

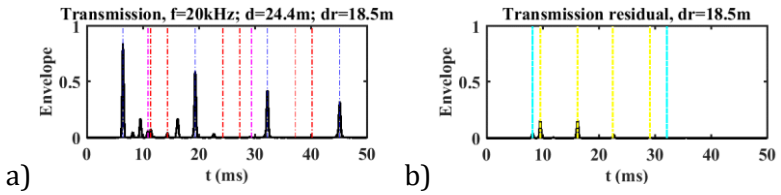

Figure 8.7: Numerical correlation envelope in transmission with a reflector at 3.95 m. Markers show a) longitudinal propagation, mode conversion, and partial reflections by the dent, and b) mode conversion and partial reflections by the reflector.

Although the analysis above assumed $d_r \geq d_m$, the case when $d_r < d_m$ deserves attention. Reflectors may also induce reciprocal effects such as F(1,1) -> L(0,1) mode conversion. In such a case, the analysis is similar, but the launched mode may be F(1,1) and scattering points convert the asymmetric flexural mode to the symmetrical longitudinal mode. Figure 8.8 shows a timing diagram assuming initial F(1,1) excitation with a partial reflector at a distance d_r. The partial reflector scatters the F(1,1) mode into the F(1,1) mode with an assumed amplitude of D (green) and into the L(0,1) mode with an amplitude of E (orange). Further partial reflections of the flexural mode may take place but may be ignored due to expected high attenuation. The combined propagated F(1,1) waves and the converted mode F(1,1) to L(0,1) in both schemes can be again similarly found.

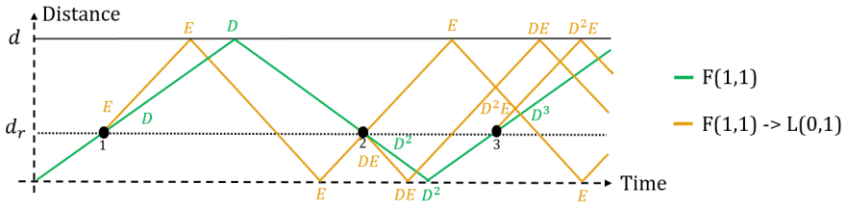

Figure 8.8: Timing diagram for F(1,1) mode and F(1,1) -> L(0,1) mode conversion by the reflector.

The previous analysis will allow features in experimental signals to be identified. However, while the time order of scattered components is likely to match theoretical estimates, their amplitudes are likely to differ, due to inaccurate estimation of attenuation and scattering coefficients. Other probable discrepancies are due to unconsidered pathways, low amplitude scatterings by the supports, and thermal and environmental effects.

8.2 Experimental Transmission Scheme

Experiments with a removable reflector were made using the same rig as before. Figure 8.9 shows schematics of a) transmission and b) reflection schemes. These show the laboratory arrangement of the 4-element EMAT, the microphone, the spiral copper pipe and its dent, the 10 points of contact between the support and the pipe, and the removable reflector. The transmission scheme has the microphone at the far end of the pipe while the reflection scheme has it next to the EMAT. In the reflection scheme, the clamps mounting the EMAT and microphone are joined to minimize reflections. However, since the microphone is not exactly collocated with the EMAT, some small signals trapped between the microphone and the pipe end may be expected.

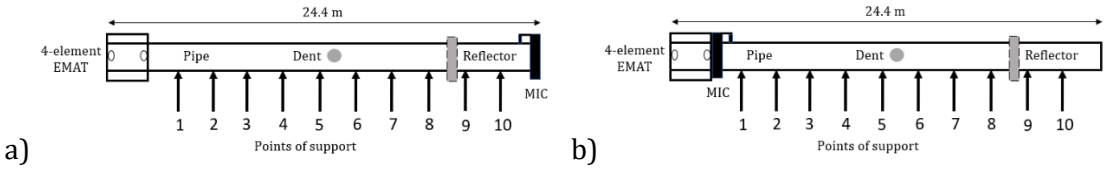

Figure 8.9: Laboratory apparatus for a) transmission and b) reflection schemes.

Figure 8.10 shows photographs of a copper pipe a) without, and b) with the reflector. The reflector is flexible, metallic, and has a semi-symmetric ring shape of 2 mm thickness and a thicker lock with a screw to control the reflection and transmission coefficients. To avoid

permanent damage to the ductile copper pipe, the clamping force must be limited. Unlike the asymmetric dent, the semi-symmetric reflector may induce flexural to longitudinal mode conversion, although with relatively higher flexural modes due to its semi-symmetry. Reflector attachment locations are chosen to be close to the transmitter, the dent, or the receiver to highlight different features and confirm the analysis. To keep the coefficients consistent, the clamping screw is tightened with a consistent number of turns (8).

a) 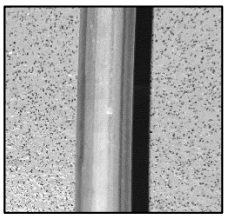 b) 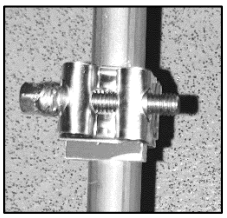

Figure 8.10: Photographs of a pipe a) without and b) with a removable reflector.

We present experimental results for a single-node system first, assuming a uniform pulse of 5 V_{pp} with a 20 kHz up-conversion and 6 cycles period. The scattered components are identified by comparison with the simulations above and highlighted with the same color code. Figure 8.11 shows the experimental correlation envelope in transmission with no reflector attached, highlighting the channel and discontinuity effects. The experimental envelope matches the numerical envelope shown above, with a main L(0,1) peak and a small number of unwanted peaks caused by channel and discontinuity effects. This result may be used as a baseline for comparison with later modified states.

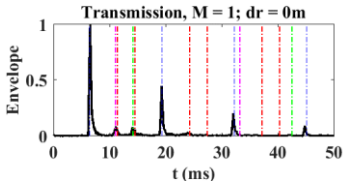

Figure 8.11: Experimental correlation envelope in transmission with no reflector. Markers show multimode propagation, mode conversion, and partial reflections.

Figure 8.12 shows the effect on the correlation envelope of adding a removable reflector at 3.95 m from the transmitter, highlighting a) channel and discontinuity effects and b) the reflector effects including the mode conversions and L(0,1) partial reflections. In

comparison with the experimental baseline, channel and discontinuity effects are noticeably reduced because of the energy distribution by the reflector, making reflector effects more significant due to their earlier arrival and their relatively high reflection coefficient. Estimating reflector coefficients requires identification of all of the reflection effects. This is a complicated process since they are spread in both time and relative amplitude. However, the main paths of mode conversions and partial reflections by the reflector discussed above can be extracted. The first reflector effect that arrives after the main L(0,1) peak is F(1,1) -> L(0,1) mode conversion, and has low amplitude due to the high flexural mode attenuation. This component has traveled mostly with L(0,1) mode velocity since the reflector is close to the transmitter. Changing the reflector location may change its arrival time and hence its order. The second identified effect, and the largest one, is a partial reflection with a normalized amplitude of about 0.3. When monitoring a pipe in a normal state (baseline), such a detectable amplitude that arrives at an unexpected time should suggest a significant change in the pipe state.

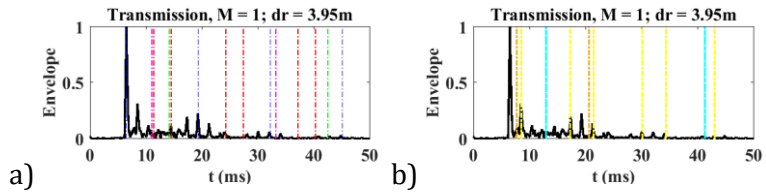

Figure 8.12: Experimental correlation envelope in transmission with a reflector at 3.95 m. Markers show a) multimode propagation, mode conversion, and partial reflections by the dent, and b) mode conversion and partial reflections by the reflector.

Figure 8.13 shows the effect on the correlation envelope of moving the reflector forward, highlighting again a) channel and discontinuity effects and b) reflector effects when the reflector is 11 m from the transmitter. Again, the F(1,1) -> L(0,1) mode conversion arrives first after the main peak. Despite that, the reflector effects are minimized here due to overlap with the discontinuity effects, since the dent is close by (about 1 m distance) and the transducers are relatively far away. However, the L(0,1) partial reflections and their ring-down pattern can be recognized. Comparison with the baseline shows that a change can be detected by identifying these extra peaks. Due to the low partial reflection coefficient, they have low amplitudes. Nevertheless, a signal with a reasonably small number of

unwanted peaks allows low amplitude changes to be identified without using any detection algorithms even when the effect is almost overlapping with a pre-existing discontinuity.

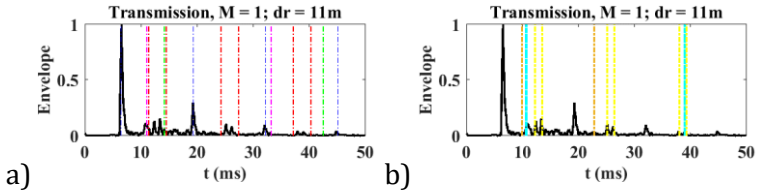

Figure 8.13: Experimental correlation envelope in transmission with a reflector at 11 m, with markers for a) multimode propagation, mode conversion, and partial reflections by the dent, and b) mode conversion and partial reflections by the reflector.

Figure 8.14 shows the correlation envelope when the reflector is at 18.5 m from the transmitter, highlighting again a) the channel and discontinuity effects and b) the reflector effects. Clearly, the order and time of the peaks by these effects are matching its corresponding numerical result presented above. However, the amplitudes are different due to the experimental low-amplitude discontinuities effects which mentioned in Chapter 7. This time, the first arrival after the main peak is the L(0,1) -> F(1,1) mode conversion by the reflector, since the reflector is close by. The second arrival is a partial reflection with a high amplitude. However, this partial reflection has a different path than its corresponding high amplitude partial reflection when the reflector is close to the transmitter. The induced reflector peaks clearly demonstrate that partial reflection paths are more detectable than mode conversion paths in transmission when a change occurs. However, the alteration in peak order induced by the reflector indicates the impracticality of using this method to locate the change.

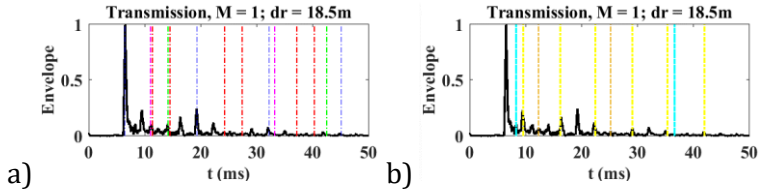

Figure 8.14: Experimental correlation envelope transmission with a reflector at 18.5 m, with markers for a) multimode propagation, mode conversion, and partial reflections by the dent, and b) mode conversion and partial reflections by the reflector.

8.3 Experimental Reflection Scheme

Similar trials were conducted in reflection. Figure 8.15 shows a) the received signal for the same previous input and b) its correlation envelope, with no reflector. The amplitude of the received signal is about 8 mV_{pp} arriving at almost zero delay. There is an immediate blast of overlapping peaks that include L(0,1) and F(1,1) modes and trapped reflections. Short distance reflections by supports or pipe clamps, even with low amplitudes, are expected to become more noticeable. These peaks are difficult to separate for analysis. However, some distinct peaks with low amplitudes arrive later and can be exploited for detecting changes as shown in the next attempts.

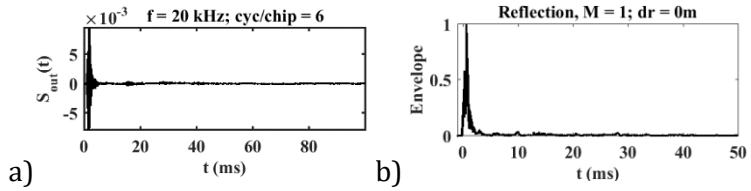

Figure 8.15: a) Experimental received signal in reflection with no reflector; and b) correlation envelope.

Figure 8.16 shows the previous baseline envelope on an extended amplitude scale, highlighting major peaks including a) channel and b) discontinuity effects. The L(0,1) and F(1,1) end reflections and the L(0,1) -> F(1,1) mode conversion have lower amplitudes than their corresponding peaks in transmission due to their longer travel distances. The first peak after the initial blast is an L(0,1) partial reflection caused by the dent. In reflection, the experimental result suggests that reflections trapped between the transmitter and the dent are significant due to their short travel time, and trapped partial reflections can be identified, here at periodic intervals. These intervals are marked in a darker red to distinguish them from other partial reflections. From the timing diagram, some of the partial reflections are perfectly overlapping. Consequently, the amplitude of the first partial reflector is lower than the second one since it has two overlapping reflections.

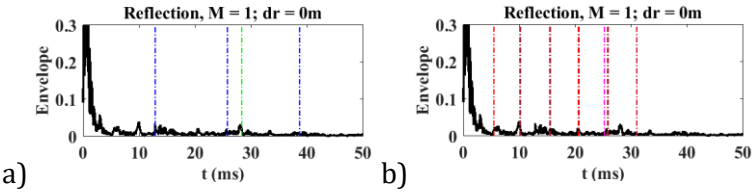

Figure 8.16: Experimental correlation envelope in reflection with no reflector, with markers for a) multimode propagation and b) mode conversion and partial reflections by the dent.

Figure 8.17 shows the effect on the experimental correlation envelope of attaching a removable reflector at 3.95 m from the transmitter, highlighting a) channel and discontinuity effects and b) reflector effects. The channel and discontinuity effects are overlapping heavily with the partial reflections trapped in the short space between the transducers and the reflector and are marked here in a darker yellow to differentiate them from other partial reflection paths. Many other reflector effects are also induced which also overlap and create oscillations. Despite that, peaks of partial reflection and mode conversion by the reflector can be recognized from the theoretical analysis. The earliest arrival of a partial reflection by the reflector is merging with the main blast due to the oscillation effect of the main peak. The L(0,1) -> F(1,1) and F(1,1) -> L(0,1) mode conversions by the reflector are perfectly overlapping, as expected in a reflection scheme.

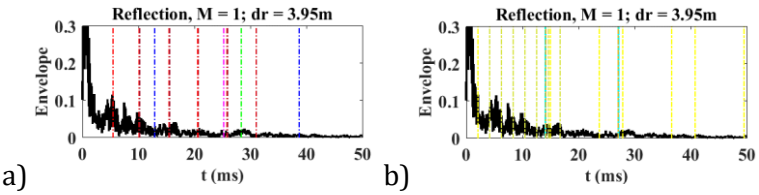

Figure 8.17: Experimental correlation envelope in reflection with a reflector at 3.95 m, with markers for a) multimode propagation, mode conversion, and partial reflections by the dent, and b) mode conversion and partial reflections by the reflector.

Figure 8.18 shows the effect on the correlation envelope of moving the removable reflector forward, highlighting again a) channel and discontinuity effects and b) reflector effects. This time, the removable reflector is at 11 m from the transmitter. As with the corresponding transmission signal, proximity between the dent and the reflector reduces the induced peaks. Consequently, the first detectable peak after the main blast is an overlap between the partial reflections by the dent and by the reflector. The partial reflections trapped between

the transducers and the reflector (dark yellow) are now separated and attenuated, since the distance between the transducers and the reflector is increased. A similar effect can be seen in the ring-down pattern induced by the reflector. Once again, the L(0,1) -> F(1,1) and F(1,1) -> L(0,1) mode conversions by the reflector are overlapping. The markers here highlight the major peaks; however, other unmarked reflection paths are possible but may have low amplitudes and appear as oscillations. In this case, change detection is challenging.

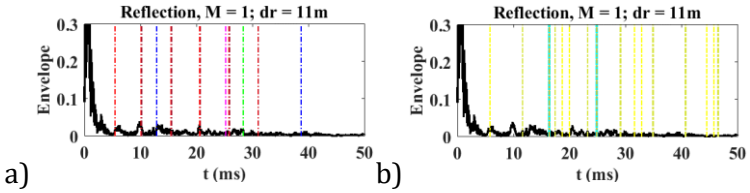

Figure 8.18: Experimental correlation envelope in reflection with a reflector at 11 m, with markers for a) multimode propagation, mode conversion, and partial reflections by the dent, and b) mode conversion and partial reflections by the reflector.

Finally, Figure 8.19 shows the correlation envelope when the reflector is 18.5 m away from the transmitter, highlighting again a) channel and discontinuity effects and b) reflector effects. Multimode propagation, mode conversion, and partial reflections by the dent are all as expected theoretically. Reflector effects now arrive much later, due to the large separation between the reflector and the transducers. The L(0,1) -> F(1,1) and F(1,1) -> L(0,1) mode conversions by the reflector have low amplitudes and again are perfectly overlapping. The first partial reflection by the reflector is overlapping with a partial reflection by the dent. In addition, the second reflector effect is an overlap between at least 2 partial reflection peaks by the reflector and 2 partial reflection peaks by the dent, and therefore it has the highest amplitude of any reflector effects. All these overlaps cause ambiguity in distinguishing between them. Indeed, only the high delayed partial reflection peaks and the high oscillations are discriminating this envelope from a baseline envelope. The timing of the partial reflection peaks is as shown in the timing diagram. The high oscillations can be ascribed to two factors: signals trapped between the clamps of the EMAT and the microphone, and signals trapped between the reflector and the nearer pipe end.

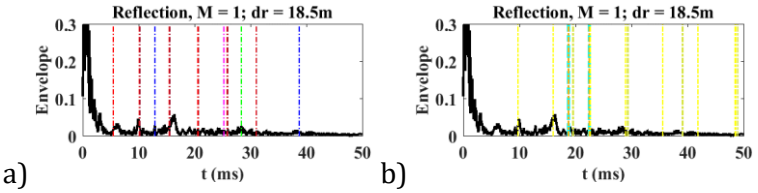

a) b)

Figure 8.19: Experimental correlation envelope in reflection with a reflector at 18.5 m, with markers for a) multimode propagation, mode conversion, and partial reflections by the dent, and b) mode conversion and partial reflections by the reflector.

The results show that partial reflections have potentially the most detectable amplitudes while mode conversion peaks are almost negligible. In this scheme, attenuation plays an important role and therefore farther reflectors (changes) from the transducers are harder to detect. Consequently, the reflection scheme may have more amplitude and distance limitations in detecting changes when compared with the transmission scheme.

We now briefly consider a multi-node system, where codes are used to distinguish transmitters. Detecting a change with QO codes is difficult, as expected, due to the heavy overlap between QO sidelobes and partial reflection and mode conversion induced by a change. Considerably better performance is to be expected from Golay Code Pairs. Figure 8.20 shows a comparison between the experimental baseline correlation envelopes of the previous uniform pulse (black) and the orthogonal GCP (1, 2) (red) at 20 kHz in a) transmission and b) in reflection with an extended amplitude scale, highlighting channel and discontinuity effects. The GCP has 4 bits and hence its signal is 4 times wider than the uniform pulse. Despite that, the envelopes in both cases show matching effects, suggesting that change detection with GCPs and Complementary Code Sets may operate as before. These experimental results show many overlapping signals which initially appear complex and ambiguous. However, careful analysis shows meaningful and consistent results especially after using a movable reflector. Such an analysis may allow both schemes to be used for change detection, for example using changes to the coefficients of a tapped delay line filter for multipath correction as will be discussed next.

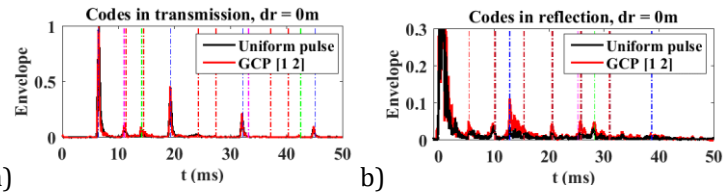

a) b)

Figure 8.20: Comparison between experimental correlation envelopes of baseline GCP and uniform pulse in a) transmission and b) reflection.

8.4 Potential Detection Algorithms

In 1993, Rytter [185] classified systems that monitor changes into 4 main levels: identifying a change, locating it, quantifying its severity, and predicting the remaining service life (prognosis). Levels 3 and 4 are not directly relevant to changes caused by destructive attacks. Identification and location have been addressed extensively in the literature [186] and even have been commercialized in the gas and oil industry [187]. A set of processes are used to decide if a change occurs. Figure 8.21 shows an example of the so-called waterfall model used for change detection since the 1990s [188]. The first steps of sensing, signal processing, and feature extraction have been covered previously. An automated algorithm is then required for pattern processing, situation assessment, and decision-making processes. The detection algorithm is typically specified per application. Assessment of a change entails a comparison between a system state before (baseline) and after the change. Consequently, common change detection algorithms process a residual signal acquired by subtracting the measurement after the change from the baseline. The ideal residual signal contains only extra components that are induced by the change as shown numerically.

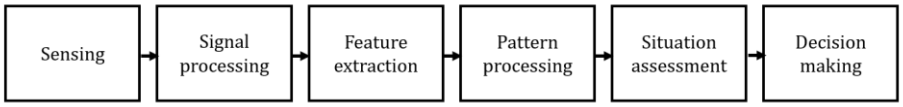

Figure 8.21: Algorithm processes for change detection [188].

For example, Figure 8.22 shows the residual signals from the transmission trials above, highlighting the reflector effects when the change occurs at a) 3.95, b) 11, and c) 18.5 m. In the absence of multimode and dent effects, the reflector effects can be clearly observed. In all cases, the residual partial reflections have the highest amplitudes, while mode conversions are much lower. The ring-down pattern of the partial reflections can be also

observed. Other lower amplitude components are insignificant, suggesting that the number of major paths induced by a reflector is limited and its location can be determined as in the corresponding numerical result. Consequently, an algorithm can automatically process residual signals with extracted features to assess the situation and make a decision. Furthermore, the order of the limited components is changing based on the location of the reflector, therefore, the algorithm can recognize patterns by processing some residual training signals to identify the reflector location.

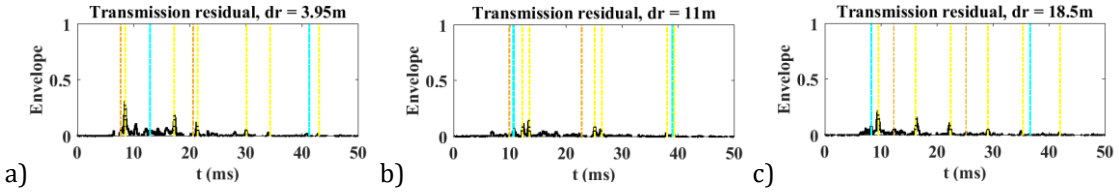

Figure 8.22: Residual experimental signals in transmission when the change is at a) 3.95, b) 11, and c) 18.5 m

Similarly, Figure 8.23 shows the residual signals from reflection measurements when the change is attached again at 3.95, 11, 18.5 m. Here, some of the residual partial reflection and mode conversion induced by the reflector can be observed in the absence of multimode and dent effects. The periodic trapped reflections between the reflector and the transducers are higher in amplitudes when the distance is short as expected. However, farther reflectors from the transducers have fewer residual components. Therefore, the algorithm may find difficulty in assessing a change in reflection when its location is far, or when it is overlapping with a pre-existing discontinuity.

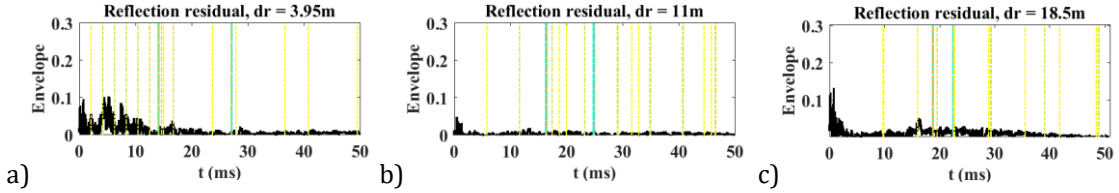

Figure 8.23: Residual experimental signals in reflection when the change is at a) 3.95, b) 11, and c) 18.5 m.

Experimental residual signals typically show additional noise due to thermal and environmental factors, which can induce effects similar to disturbances. A large number of baseline samples are required for compensation [181]. A well-known method of processing

residual signals is the cumulative sum (CUMSUM) algorithm, which can detect changes that are formerly anticipated [189]. Another is the generalized likelihood ratio (GLR) test, which uses intensive computations on a high number of residual signals to detect unexpected changes. Recently, the GLR algorithm becomes a standard tool for change detection [190]. Supervised and unsupervised machine learning algorithms are also used in damage detection [191]. These algorithms are data-driven and construct a statistical model of the system such as a probability density function of a normal condition. Subsequently, changes can appear in regions with very low density.

Alternative approaches involve equalization filters, widely used in wireless communication to compensate for channel multipath effects [192]. Equalization filters have been used in acoustics, particularly in underwater transmission of telemetry signals, speech and images [193, 194]. In acoustic waveguides, multimode propagation, mode conversion, and reflection are obvious multipath effects that in principle can be reversed by equalization filters. Moreover, multipath propagation is less complicated since paths are limited, can be determined to some extent, and are stationary. However, the adverse features are dispersion and multimode excitation. Since equalization filters are uncommon in acoustics, this approach will be considered here.

Equalizers are categorized as static or adaptive, and adaptive equalizers have a key advantage of being effective in channels with unknown characteristics. To implement adaptive equalization, a Finite Impulse Response (FIR) filter in the form of a weighted tapped delay line is commonly used. Figure 8.24 shows a block diagram of an equalization filter consists of N number of taps to delay the received samples, $x(n)$, by T s per tap, a set of weighting coefficients, W_n, and a summing block to equalize the received signal by effectively reverse channel delay and amplitude effects. Adaptive equalizers first operate in a training mode, where known baseline sequences are used to identify weighting coefficients that can compensate for initial channel effects. Then, the filter tracks channel changes by continuously adjusting the weights, either by finding the least mean square (LMS) of the difference between the equalized signal and the training signal, or by using a complex and computationally costly recursive least square algorithm [195].

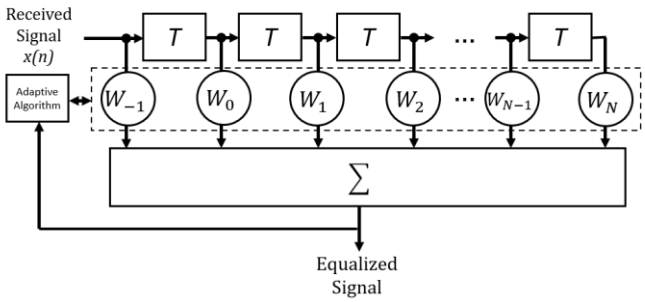

Figure 8.24: A block diagram of a weighted tapped delay line.

Here, since dispersed multimode and discontinuity effects have been accurately extracted, it may be possible to train an equalization filter to reverse them. Delayed multipath effects caused by a disturbance can then be identified with a threshold detector, without acquiring a residual signal. Changes in filter weightings can be estimated blindly in a feedback loop to identify the location and magnitude of the disturbance, provided dispersion is limited.

For example, we have attempted to implement a weighted tapped delay line numerically for a dispersion-less system by using the recursive least square algorithm 'dsp.RLSFilter' in MATLAB to compute the weighting coefficients. The signal is a uniform pulse of 6 cycles with 2048 samples; and the received signal has 2 components: a delayed dispersion-less pulse and delayed, attenuated pulse. The forgetting factor is set to 0.9. Figure 8.25 shows a) the transmitted $d(n)$, b) the received baseline, $x_1(n)$, correlation envelopes in normalized scales, and c) the weighting coefficients, $w_1(n)$, computed by the algorithm, where n is the number of samples. Clearly, the algorithm identifies the taps and matches the coefficient weights with those of the received signal components.

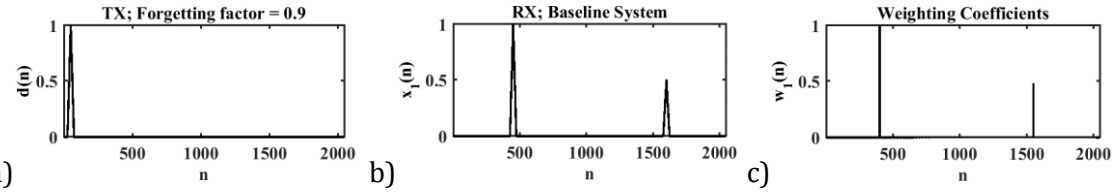

Figure 8.25: a) Transmitted, b) received baseline correlation envelopes in a dispersion-less system, c) and its filter weighting coefficients.

The system is now modified by some form of disturbance that generates and additional pulse between the two original pulses. Figure 8.26 shows a) the transmitted $d(n)$, b) the

received modified $x_2(n)$ correlation envelopes in normalized scales, and c) the weighting coefficients $w_2(n)$ computed by the algorithm. Again, the algorithm computes the taps and their weighting coefficients efficiently.

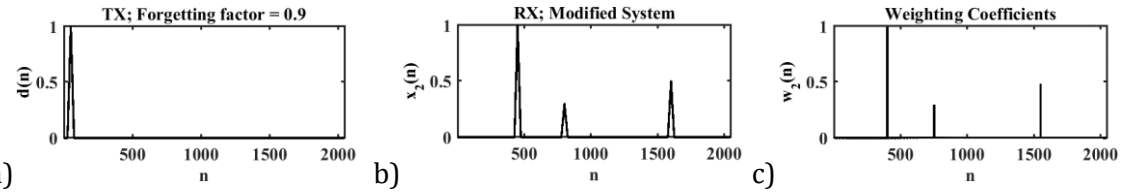

Figure 8.26: a) Transmitted, b) received modified correlation envelopes in a dispersion-less system, c) and its filter weighting coefficients.

Figure 8.27 shows the difference between the weighting coefficients before and after the change. The algorithm can clearly detect the change and locate it. However, other known effects may complicate decision-making and increase the probability of false alarms. In acoustic waveguides, multiple dispersive modes may propagate, and signal components may overlap. Because of dispersion, the tapped delay line must assign multiple weights for each signal component, and it will fail to distinguish between overlapped components. Other approaches are needed in mitigation. For example, with a priori knowledge, dispersion can be compensated using an algorithm that maps the signal from the time domain to the distance domain [196]. However, the accuracy of this algorithm is dependent on the precision of the dispersion curves, which must be estimated theoretically or extracted experimentally using processing techniques such as STFT.

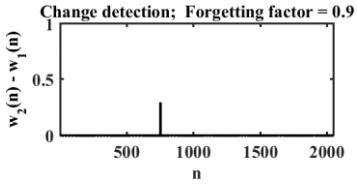

Figure 8.27: Difference in weighting coefficients between baseline and modified systems.

8.5 Conclusion

In this chapter, change detection was considered in transmission and reflection schemes, using a pipe with a removable reflector. Measurements with multiple reflector locations validated the analysis of channel, discontinuity, and reflector effects. Similar results are

expected for multi-user GCPs with lengths comparable to uniform pulses. A semi-symmetric reflector can modify the pipe state by inducing multiple L(1,0) partial reflections and L(1,0) -> F(1,1) and F(1,1) -> L(0,1) mode conversions. The shortest partial reflection paths introduced by the reflector are the most detectable in both schemes. Due to the reduction in attenuation, transmission is better for detecting farther and weaker amplitude changes when the monitoring signal has a reasonably low number of unwanted peaks, even if the change is physically overlapping with one caused by an existing discontinuity. Dispersion and multimode propagation limit the ability of adaptive filters to detect and locate such changes. The final chapter will summarize progress to date and discuss future work.

9 Conclusion

The principal aim of this research was to propose a monitoring system to verify continuity of long-distance pipelines and detect disturbances. The system involves deploying distributed acoustic nodes spaced along the pipe and using QO or GCP codes to communicate asynchronously and distinguish between neighboring nodes. The need for such a system is vital for many types of long-distance pipelines subject to destructive attacks, such as water pipes in arid countries and oil and gas pipes in countries dependent on energy sector, or in inhabited regions where leaks and explosions may endanger lives. In this last chapter, the main contributions will be highlighted first, followed by a thesis summary. Then, a discussion of possible directions for future work will be presented.

9.1 Main Contributions

The literature review showed an extensive focus on monitoring approaches for defects in pipelines, such as leak detection systems and SHM methods, which allow the system to continue functioning safely but below its optimum performance. In contrast, monitoring systems for severe structural damage to long-distance pipelines have received limited attention. These failures are more discussed in NDT where monitoring methods are invasive and involve disruption to operation. This research was primarily concerned with investigating a monitoring system that may contribute to filling this gap.

Many aspects contribute to the lack of research in this area. One is the expected absence of the signal carrier (the transported product) in structural damage. Another is the likely overlap between multiple excited modes, multiple channel modes, and mode conversion and reflections by discontinuities. Moreover, dispersion smears out the propagated signals. Additional aspects include attenuation, the requirement of low-power transducers for safety reasons, and noise from thermal and environmental factors and the product.

Despite that, in theoretical simulations and experiments, we successfully demonstrated a novel approach to monitor a pipe in both transmission and reflection. The pipe wall was used as a signal carrier to avoid the problem of product loss. The overlap, dispersion, and attenuation are mitigated by selecting a low-frequency carrier and a metallic gas-filled pipe with a small diameter to support a low number of modes. In addition, the pipe length is

maximized, and the supports and connectors are minimized to reduce overlap between modes of different velocities and reduce discontinuities effects. Signal bandwidth was reduced by optimizing the signal duration and using peak compression to reduce dispersion. A matched filter implemented by correlation detection and Golay Complementary Pairs were used to improve SNR. This proposed approach allowed continuity verification and showed encouraging performance in detecting changes, especially in transmission.

To multiple nodes, CDMA was implemented using new quasi-orthogonal codes in base 6, which had a high discrimination factor. Base 6 codes showed the best performance, particularly in the form of 9-bit pairs, 10-bit triplets, and 8-bit quadruplets. Nevertheless, the autocorrelation sidelobes and cross-correlation caused high overlaps. As a result, CDMA was also implemented with perfectly orthogonal GCPs instead. The multiplexed system allowed distinguishing between sets of 2-, 4-, and 8-users. These are the key contributions that were discussed throughout the former chapters of this thesis.

9.2 Thesis Review

The thesis was divided into three main parts. The first discussed the theoretical background of acoustics in waveguides, acoustic transducers and existing systems, the second demonstrated the proposed monitoring system numerically, and the third demonstrated the system experimentally.

Chapter 1 first highlighted the importance of protecting critical pipeline infrastructure, and reviewed monitoring systems including systems using acoustic waves. Then, the chapter presented the main aims of the research and briefly highlighted the building blocks of the proposed system which include signal encoding, up-conversion, and amplification, transduction using an EMAT and propagation along the pipe. At the receiver, reverse transduction, down-conversion, and decoding by correlation detection were carried out.

Chapter 2 discussed the theory behind propagation in cylindrical acoustic waveguides including modes, numerical solvers, dispersion characteristics, and effects of discontinuities. It emphasized the adverse effects of dispersion on the implementation of an acoustic monitoring system, due to the rapid increase of the number of acoustic modes at

high frequencies and common features of existing pipelines such as large diameter, bends, supports, liquid fills, and surrounds. Computed dispersion curves obtained using the freeware PCDisp showed that limited number of modes can be obtained by a combination of low frequency and small pipe diameter.

Chapter 3 introduced the principles of piezoelectric transducers and EMATs. It proposed a design of a 4-element cuboid EMAT, with analytical and numerical models for coils and permanent magnets. The numerical analysis showed the fields of solenoids and magnets may excite primarily the longitudinal mode, and possibly may excite flexural modes. Investigation of EMAT modification showed that wider cuboid solenoids increase acoustic signals while curved-pole solenoids and magnets improve uniformity.

In Chapter 4, the complete system, including channel and discontinuity effects, was simulated. The propagation channel was a copper pipe with 15 mm OD and 1 mm wall thickness to match experiments. The numerical results showed that correlation detection may improve SNR, integration time may increase processing gain, and reduction in signal bandwidth may mitigate dispersion, but with a reduction in the bit rate.

In Chapter 5, code division multiplexing was investigated as a method of allowing an asynchronous multi-user system. Common codes were found to be unsuitable, and an efficient algorithm to search for short codes in the form of multiphase, quasi-orthogonal, and Barker-like, pairs, triplets, and quadruplets was developed. Since all QO codes have non-zero autocorrelation sidelobes and cross-correlation, Bipolar GCPs were then investigated as alternatives, which are completely orthogonal and offer improved processing gain. Orthogonal GCPs and complementary code sets were obtained for up to 8 users. Chapter 6 integrated the QO codes and orthogonal GCPs in an extended model containing channel and discontinuity effects.

Chapter 7 described laboratory apparatus to demonstrate pulse and coded propagation along an air-filled pipe. The rig consisted of a 4-element EMAT, a long spiral copper pipe, and a single microphone detector. Experiments were conducted at carrier frequencies between 2 – 20 kHz, and the best results were obtained at 20 kHz, where system performance was optimum. The experimental results were consistent with the simulations,

confirming the previous analysis of channel and discontinuity effects. Experimental QO code performance was degraded by overlaps with unwanted signal components while perfectly orthogonal GCPs required longer transmitting times. In addition, other low amplitude discontinuity effects were expected to limit the performance of GCP multiplexing.

Finally, Chapter 8 considered using the multiplexed system for detecting changes in transmission and reflection schemes with a removable reflector. Measurements of uniform pulses with multiple reflector locations validated the mathematical and numerical analysis of the reflector effects. Similar results were expected for multi-user GCPs with lengths comparable to uniform pulses. A semi-symmetric reflector modified the pipe state by inducing multiple L(1,0) partial reflections and L(1,0) -> F(1,1), F(1,1) -> L(0,1) mode conversions. Due to the reduction in attenuation, the transmission scheme was better for detecting farther and weaker amplitude changes. Then, potential automated algorithms including equalization adaptive filters were explored to decide if a change occurs. Indeed, the experimental demonstration in the last two chapters accomplished the thesis's aim of verifying pipe continuity and detecting changes.

9.3 Future Work

We now conclude with some directions for future work. As previously stated, the investigations above were carried out on a small, metallic, unburied, gas-filled pipe. Further investigation with larger pipes is necessary, since these pipes are employed in industry. The key anticipated challenge is the increased number of modes. Nevertheless, searching for a frequency range of a limited number of modes with negligible dispersion, or a large velocity gap between non-dispersive and dispersive modes is worthwhile. Alternatively, zero-dispersion modes such as the torsional modes can be used. Another approach is to examine algorithms to reverse dispersion effectively. Such changes obviously may alter other aspects of the system such as transducer design, the spacing between nodes, attenuation, skin depth, …, etc. Furthermore, the effect of pipe products and surrounds require analytical and experimental investigation. They are expected to introduce multimode propagation, attenuation and noise. The channel response may also alter with filling depth.

Improving SNR is another subject worth exploring. Higher SNR may allow for higher performance in reflection and transmission, better sensitivity in change detection, and

larger separation between nodes. One method was demonstrated theoretically by using longer GCPs, or Complementary Code Set (CCS) for a higher number of users. The method was experimentally limited due to the low amplitude discontinuity effects. Nevertheless, even without such effects, the number of users is restricted by the allowed code length, which must be shorter than the transit time to avoid information loss.

Manipulating a code set by stacking, shifting, and then assigning the codes to only one user may improve the SNR greatly, much more than a CCS with equal length. For example, a CCS of 4 users has 16 codes, where each user has 4 codes as illustrated before. A code stack can be formed by stacking code n of each user in turn, to have a total of 4 stacked codes, where $n = 1, 2, 3, 4$. Code stacks of this type were constructed, theoretically simulated, and experimentally propagated. Simulated results showed a high improvement in SNR, but experimental results unfortunately failed due to the same effects above. However, attempting to remove these effects should improve processing gain and SNR.

Another area worthy of more detailed investigation is the EMAT design. Here, we implemented a 4-element, narrow, cuboid EMAT and evaluated wider and curved pole EMATs. Their magnetic field uniformity and strength are affected by factors such as lift-off distance, number of elements, curvature, number of turns, current, and permanent magnet pull force. These can be tuned to increase longitudinal mode excitation while minimizing the magnetic field reversals that excite unwanted flexural modes.

Finally, the model system could be improved by incorporating more elements, with each element using an anti-collision algorithm and executing a monitoring strategy that verifies continuity, and detects, locates, and quantifies changes. The system demonstrated here acquired data and then processed it later in software. Implementing signal processing such as down-conversion, correlation detection, and a change detection algorithm in hardware should then allow real-time monitoring.

10 References

1 US Government Accountability Office, Department of Transportation Is Taking Actions To Address Rail Safety, But Additional Actions Are Needed To Improve Pipeline Safety. *GAO*, 14, p.667, 2014.

2 Schmura, E. and Klingenberg, M., Existing Natural Gas Pipeline Materials and Associated Operational Characteristics. *FY 2005 Progress Report.* Concurrent Technologies Corp, 2005.

3 Braiundt, J., Johnson, M., Elphinston, J. and Ratnayaka, D., Pipeline Design and Construction. Twort's Water Supply, pp.693–742, 2017.

4 https://www.aquasure.com.au/pipeline-powerline, visited on 21/3/2020.

5 https://maghrebwatch.com/2018/10/05/morocco-get-full-ownership-gas-pipeline-linking-algeria-europe/, visited on 21/3/2020.

6 https://www.theprocesspiping.com/introduction-to-piping-system/, visited on 21/3/2020.

7 Shibata, A., Konishi, M., Abe, Y., Hasegawa, R., Watanabe, M. and Kamijo, H., Neuro Based Classification of Gas Leakage Sounds in Pipeline. In Proc. IEEE Int. Conf. on Networking, Sensing and Control, Okayama, Japan, 26–29 March, pp.298–302, 2009.

8 http://www.fao.org/faostat/en/#home, visited on 13/2/2018.

9 https://www.arabnews.com/saudi-arabia/news/866376, visited on 21/3/2020.

10 https://www.eia.gov/international/analysis/country/SAU, visited on 18/3/2020.

11 https://www.cia.gov/, visited on 18/3/2020.

12 https://www.bloomberg.com/news/articles/2020-02-22/saudi-arabia-plans-to-invest-110-billion-in-jafurah-gas-field, visited on 18/3/2020.

13 Chowdhury S. and Al-Zahrani M., Characterizing Water Resources and Trends of Sectorwise Water Consumption in Saudi Arabia. *King Saud University - Engineering Sciences*, 27, pp.68-82, 2015.

14 https://eu.usatoday.com/story/money/2019/05/22/largest-oil-reserves-in-world-15-countries-that-control-the-worlds-oil/39497945/, visited on 23/3/2020.

15 https://igarape.org.br/startling-maps-show-every-terrorist-attack-worldwide-for-the-last-20-years/ , visited on 20/3/2022.

16 https://www.start.umd.edu/gtd/ , visited on 20/3/2022.

17 https://www.theguardian.com/world/2019/sep/16/trump-says-us-locked-and-loaded-after-saudi-arabia-oil-attack-as-crude-prices-soar-iran-aramco, visited on 18/3/2020.

18 https://www.telegraph.co.uk/news/worldnews/northamerica/usa/7809748/Three-killed-in-Texas-gas-pipe-explosion.html, visited on 18/3/2020.

19 https://libyanfreepress.wordpress.com/2012/03/20/water-pipeline-in-bani-walid-sabotaged-from-nato-mercenaries-1932012/, visited on 20/2/2018.

20 Kwun, H. and Bartels, K., Experimental Observation of Wave Dispersion in Cylindrical Shells Via Time-Frequency Analysis. *The Acoustical Society of America*, 97(6), pp.3905-3907, 1995.

21 Kim, J., Sharma, G., Boudriga, N. and Iyengar, S., SPAMMS: A Sensor-Based Pipeline Autonomous Monitoring and Maintenance System, Proc. 2nd Int. Conf. *on Communication Systems and Networks (COMSNETS10)*, pp.1-10, 2010.

22 Watanabe, K. and Himmelblau, D., Detection and Location of a Leak in a Gas-Transport Pipeline by a New Acoustic Method. *AIChE Journal*, 32(10), pp.1690-1702, 1986.

23 Hough, E., Leak Testing of Pipelines Using Pressure and Acoustic Velocity. *Oil and Gas*, 86, pp.35-41, 1988.

24 Ishimatsu, T., Doufene, A., Alawad, A. and de Weck, O., Desalination Network Model Driven Decision Support System: A Case Study of Saudi Arabia. *Desalination*, 423, pp.65-78, 2017.

25 Babbitt, H., The Detection of Leaks in Underground Pipes. *American Water Works Association*, 7(4), pp.589-595, 1920.

26 Pudar, R. and Liggett, J., Leaks in Pipe Networks. *Hydraulic Engineering*, 118(7), pp.1031-1046, 1992.

27 Liou, J. and Tian, J., Leak Detection-Transient Flow Simulation Approaches. *Energy Resources Technology*, 117(3), pp.243-248, 1995.

28 Rose J., Ultrasonic Guided Waves in Solid Medi. *Cambridge University Press*, Cambridge, 2014.

29 Karli, R., Bouchalkha, A. and Alhammadi, K., Investigation of Electromagnetic (EM) Wave Attenuation in Oil Pipeline. Conf. *Electrical and Computing Technologies and Applications (ICECTA)*, Ras Al Khaimah, pp.1-4, 2017.

30 Jacobi, W., Propagation of Sound Waves Along Liquid Cylinders. *The Acoustical Society of America*, 21(2), pp.120-127, 1949.

31 Greenspon, J., Axially Symmetric Vibrations of a Thick Cylindrical Shell in an Acoustic Medium. *The Acoustical Society of America*, 32(8), pp.1017-1025, 1960.

32 Greenspon, J., Vibrations of Thick and Thin Cylindrical Shells Surrounded by Water. *The Acoustical Society of America*, 33(10), pp.1321-1328, 1961.

33 Gazis, D., Three-Dimensional Investigation of the Propagation of Waves in Hollow Circular Cylinders. II. Numerical Results. *The Acoustical Society of America*, 31(5), pp.568-573, 1959.

34 Fuller, C. and Fahy, F., Characteristics of Wave Propagation and Energy Distributions in Cylindrical Elastic Shells Filled with Fluid. *Sound and Vibration*, 81(4), pp.501-518, 1982.

35 Riemsdijk, J. and Bosserlaar, H., On-Stream Detection of Small Leaks in Crude Oil Pipeline. Proc. *7th World Pet*, Cong., 1960.

36 Decker, W., Pipeline Leak Detection Using Nitrous Oxide Method. *ASNT Conf*. (U.S.A.), p.358, 1978.

37 Scott, I., *Basic Acoustic Emission*. New York: Gordon and Breach Science, 1991.

38 Blitz, J. and Simpson, G., *Ultrasonic Methods of Non-Destructive Testing*. London: Chapman and Hall, 1996.

39 Jones, R., The Non-Destructive Testing of Concrete. *Mag. Concrete Research*, 1(2), pp.67-78, 1949.

40 Alleyne, D. and Cawley, P., Optimization of Lamb Wave Inspection Techniques. *NDT & E International*, 25(1), pp.11-22, 1992.

41 Kehlenbach, M., Kohler, B., Cao, X. and Hanselka, H., Numerical and Experimental Investigation of Lamb Wave Interaction with Discontinuities. In: Proc. 4th Int. *Workshop on Structural Health Monitoring, Stanford*, California. pp.421-429, 2003.

42 Staszewski, W., Lee, B., Mallet, L. and Scarpa, F., Structural Health Monitoring Using Scanning Laser Vibrometry: I. Lamb Wave Sensing. *Smart Materials and Structures*, 13(2), pp.251-260, 2004.

43 Kwun, H. and Holt, A., Feasibility of Under-Lagging Corrosion Detection in Steel Pipe Using the Magnetostrictive Sensor Technique. *NDT & E International*, 28(4), pp.211-214, 1995.

44 Leutenegger TF., Detection of Defects in Cylindrical Structures Using a Time Reverse Numerical Simulation Method. PhD Thesis No. 14833. *Swiss Federal Institute of Technology, Zurich*, 2002.

45 Rose, J., Ditri, J., Pilarski, A., Rajana, K. and Carr, F., A Guided Wave Inspection Technique for Nuclear Steam Generator Tubing. *NDT & E International*, 27(6), pp.307-310, 1994.

46 Wenhao Zhu and Rose, J., Lamb Wave Generation and Reception with Time-Delay Periodic Linear Arrays: a BEM Simulation and Experimental Study. *IEEE Transactions on Ultrasonics, Ferroelectrics and Frequency Control*, 46(3), pp.654-664, 1999.

47 Li, J. and Rose, J., Implementing Guided Wave Mode Control by Use of a Phased Transducer Array. *IEEE Transactions on Ultrasonics, Ferroelectrics and Frequency Control*, 48(3), pp.761-768, 2001.

48 Duan, W., Kirby, R., Mudge, P. and Gan, T., A One Dimensional Numerical Approach for Computing the Eigenmodes of Elastic Waves in Buried Pipelines. *Sound and Vibration*, 384, pp.177-193, 2016.

49 Muggleton, J. and Brennan, M., Leak Noise Propagation and Attenuation in Submerged Plastic Water Pipes. *Sound and Vibration*, 278(3), pp.527-537, 2004.

50 Meribout, M., Abdu Galeel, M., Al Marzouqi, M. and Abu Aasi, M., A New Concept for an Effective Leak Detection in Multiphase Fluid Pipelines. 2010 First Int. Conf. *on Sensor Device Technologies and Applications*, pp.206-210, 2010.

51 Lin, W., Jiang, L. and Wu, H., Study of Non-Intrusive Gas Pipeline Leak Detection with Acoustic Sensor. *IFAC Proceedings Volumes*, 46(20), pp.27-32, 2013.

52 Xu, Q., Zhang, L. and Liang, W., Acoustic Detection Technology for Gas Pipeline Leakage. *Process Safety and Environmental Protection*, 91(4), pp.253-261, 2013.

53 Fuchs, H. and Riehle, R., Ten Years of Experience with Leak Detection by Acoustic Signal Analysis. *Applied Acoustics*, 33(1), pp.1-19, 1991.

54 Liou, C., Pipeline Leak Detection by Impulse Response Extraction. *Fluids Engineering*, 120(4), pp.833-838, 1998.

55 Goh, H. et al., Underwater Wireless Communication System. *Phys*. Conf. Ser. 178, 012029, 2009.

56 Goh, H. et al., Water Pipe Leak Detection Using Electromagnetic Wave Sensor for the Water Industry. IEEE Symp. *on Computers & Informatics,* Kuala Lumpur, pp.290-295, 2011.

57 Hunaidi, O. and Chu, W., Acoustical Characteristics of Leak Signals in Plastic Water Distribution Pipes. *Applied Acoustics*, 58(3), pp.235-254, 1999.

58 Mellett, J., Ground Penetrating Radar Applications in Engineering, Environmental Management, and Geology. *Applied Geophysics*, 33(1-3), pp.157-166, 1995.

59 Ayala–Cabrera, D., Herrera, M., Izquierdo, J., Ocaña–Levario, S. and Pérez–García, R., GPR-Based Water Leak Models in Water Distribution Systems. *Sensors*, 13(12), pp.15912-15936, 2013.

60 Inagaki, T. and Okamoto, Y., Diagnosis of the Leakage Point on a Structure Surface Using Infrared Thermography in Near Ambient conditions. *NDT & E International*, 30(3), pp.135-142, 1997.

61 Stoianov, I., Nachman, L., Madden, S. and Tokmouline, T., PIPENET: A Wireless Sensor Network for Pipeline Monitoring, in IPSN 07: Proc. 6th Int. Conf. *on Information Processing in Sensor Networks*, New York, NY, pp.264-273, 2007.

62 Jawhar, I., Mohamed, N. and Shuaib, K., A Framework for Pipeline Infrastructure Monitoring Using Wireless Sensor Networks, Proc. *Wireless Telecomm*. Symp. (WTS07), April, pp.1-7, 2007.

63 Kurmer, P., Kinsgley, A., Laudo, S. and Krak, J., Distributed Fiber Optic Acoustic Sensor for Leak Detection. Proc. *SPIE* 1586, pp.117-128, 1991.

64 Dakin, J., Pratt, D., Bibby, G. and Ross, J., Distributed Optical Fibre Raman Temperature Sensor Using a Semiconductor Light Source and Detector. *Electronics Letters*, 21(13), p.569, 1985.

65 Adrian-Martinez, S., Ardid, M., Bou-Cabo, M. et al., Acoustic Signal Detection Through the Cross-Correlation Method in Experiments with Different Signal to Noise Ratio and

Reverberation Conditions. (Eds) Ad-Hoc Networks and Wireless, ADHOC-NOW 2014, *Springer Lecture Notes in Computer Science* 8629, 2015.

66 Gao, Y., Liu, Y., Ma, Y., Cheng, X. and Yang, J., Application of the Differentiation Process into the Correlation-Based Leak Detection in Urban Pipeline Networks. *Mechanical Systems and Signal Processing*, 112, pp.251-264, 2018.

67 Peng, Z., Wang, J. and Han, X., A Study of Negative Pressure Wave Method Based on HAAR Wavelet Transform in Ship Piping Leakage Detection System. In Proc. 2nd Int. Conf. *on Computing, Control and Industrial Engineering (CCIE),* Wuhan, China, 20–21 August, pp.111–113, 2011.

68 Yonghong, S. and Zhenhua, W., Detection of Small Leakage from Pipeline Based on Improved Harmonic Wavelet. Proc. 2012 7th Int. Conf. *on Computer Science & Education (ICCSE),* Melbourne, VIC, Australia, 14–17 July, pp.45–49, 2012.

69 Wang, H., Ye, H. and Wang, G., Oil Pipeline Leakage Detection Based on Wavelet Algorithm. *Inf. Control-Shenyang*, 31, pp.456–460, 2002.

70 Lay-Ekuakille, A., Vendramin, G. and Trotta, A., Spectral Analysis of Leak Detection in a Zigzag Pipeline: A Filter Diagonalization Method-Based Algorithm Application. *Measurement*, 42(3), pp.358-367, 2009.

71 N. Won-Bae, R. Yeon-Sun, K. Jeong-Tae, Attenuation of Fundamental Longitudinal Cylindrical Guided Wave Propagating in Liquid-Filled Steel Pipes. *Journal of Ocean Engineering and Technology*, 19, 2005.

72 Pochhammer, L., Ueber die Fortpflanzungsgeschwindigkeiten kleiner Schwingungen in einem unbegrenzten isotropen Kreiscylinder. *Journal für die reine und angewandte Mathematik (Crelles Journal)*, (81), pp.324-336, 1876.

73 Chree, C., The Equations of an Isotropic Elastic Solid in Polar and Cylindrical Coordinates, Their Solutions and Applications. *Transactions of the Cambridge Philosophical Society*, 14, pp.50-309, 1889.

74 Ghosh, J., Longitudinal Vibrations of a Hollow Cylinder. *Bulletin of the Calcutta Mathematical Society*, 14, pp31-40, 1923.

75 Adem, J., On the Axially-symmetric Steady Wave Propagation in Elastic Circular Rods. *Quarterly of Applied Mathematics*, 12(3), pp.261-275, 1954.

76 Gazis, D., Three-Dimensional Investigation of the Propagation of Waves in Hollow Circular Cylinders. I. Analytical Foundation. *The Journal of the Acoustical Society of America*, 31(5), pp.568-573, 1959.

77 Gazis, D., Three-Dimensional Investigation of the Propagation of Waves in Hollow Circular Cylinders. II. Numerical Results. *The Journal of the Acoustical Society of America*, 31(5), pp.573-578, 1959.

78 Mirsky, I., Pulse Velocities in an Orthotropic Elastic Tube. *The Bulletin of Mathematical Biophysics*, 29(2), pp.311-318, 1967.

79 Mirsky, I., Wave Propagation in a Viscous Fluid Contained in an Orthotropic Elastic Tube. *Biophysical Journal*, 7(2), pp.165-186, 1967.

80 Fuller, C. and Fahy, F., Characteristics of Wave Propagation and Energy Distributions in Cylindrical Elastic Shells Filled with Fluid. *Journal of Sound and Vibration*, 81(4), pp.501-518, 1982.

81 Long, R., Cawley, P. and Lowe, M., Acoustic Wave Propagation in Buried Iron Water Pipes. *Proceedings of the Royal Society of London. Series A: Mathematical, Physical and Engineering Sciences*, 459(2039), pp.2749-2770, 2003.

82 Seco, F. and Jiménez, A., *Modelling the Generation and Propagation of Ultrasonic Signals in Cylindrical Waveguides*. INTECH, 2012.

83 Silk, M. and Bainton, K., The Propagation in Metal Tubing of Ultrasonic Wave Modes Equivalent to Lamb Waves. *Ultrasonics*, 17(1), pp.11-19, 1979.

84 Mohr, W. and Holler, P., On Inspection of Thin-Walled Tubes for Transverse and Longitudinal Flaws by Guided Ultrasonic Waves. *IEEE Transactions on Sonics and Ultrasonics*, 23(5), pp.369-373, 1976.

85 Agarwal, N. and Bull, M., Acoustic Wave Propagation in a Pipe with Fully Developed Turbulent Flow. *Journal of Sound and Vibration*, 132(2), pp.275-298, 1989.

86 https://en.wikipedia.org/wiki/Lamb_waves, visited on 4/09/2019.

87 Maji, A., Satpathi, D. and Kratochvil, T., Acoustic Emission Source Location Using Lamb Wave Modes. *Journal of Engineering Mechanics*, 123(2), pp.154-161, 1997.

88 Gupta, A. and Duke, J., Identifying the Arrival of Extensional and Flexural Wave Modes Using Wavelet Decomposition of Ultrasonic Signals. *Ultrasonics*, 82, pp.261-271, 2018.

89 Prosser, W. and Gorman, M., Plate Mode Velocities in Graphite/Epoxy Plates. *The Journal of the Acoustical Society of America*, 96(2), pp.902-907, 1994.

90 Oliver, J., Elastic Wave Dispersion in a Cylindrical Rod by a Wide-Band Short-Duration Pulse Technique. *The Journal of the Acoustical Society of America*, 29(2), pp.189-194, 1957.

91 Sachse, W. and Pao, Y., On the Determination of Phase and Group Velocities of Dispersive Waves in Solids. *Journal of Applied Physics*, 49(8), pp.4320-4327, 1978.

92 Pialucha, T., Guyott, C. and Cawley, P., Amplitude Spectrum Method for the Measurement of Phase Velocity. *Ultrasonics*, 27(5), pp.270-279, 1989.

93 Alleyne, D. and Cawley, P., Two-Dimensional Fourier Transform Method for the Quantitative Measurement of Lamb Modes. *Proc. Ultrasonics Symp, Honolulu, HI, 4-7 Dec*, pp1143-1146, 1990.

94 Hong, J., Sun, K. and Kim, Y., Dispersion-Based Short-Time Fourier Transform Applied to Dispersive Wave Analysis. *The Journal of the Acoustical Society of America*, 117(5), pp.2949-2960, 2005.

95 Alleyne, D. and Cawley, P., The Excitation of Lamb Waves in Pipes Using Dry-Coupled Piezoelectric Transducers. *Journal of Nondestructive Evaluation*, 15(1), pp.11-20, 1996.

96 Pavlakovic, B., Lowe, M., Alleyne, D. and Cawley, P., Disperse: a General Purpose Program for Creating Dispersion Curves, *Annual Review of Progress in Quantitative NDE*, Plenum Press, New York, pp.185–192, 1997.

97 Demma, A., *The Interaction of Guided Waves with Discontinuities in Structures*, PhD Thesis, Imperial College of Science, Technology and Medicine, University of London, 2003.

98 Marzani, A., Bocchini, P., Viola, E., Bartoli, I., Coccia, S., Salamone, S., Lanza, F. and Scalea, D., *A Software for the Computation of Acoustic Waves in Cylindrical, Plate and Arbitrary Cross-Section Waveguides*. Attidella 13a Congresso Nazionale Sulle Prove non Distruttive Monitoraggio e Diagnostica AIPnD, Roma, Italia, 2009.

99 Demma, A., Cawley, P., Lowe, M., Roosenbrand, A. and Pavlakovic, B., The Reflection of Guided Waves from Notches in Pipes: a Guide for Interpreting Corrosion Measurements. *NDT & E International*, 37(3), pp.167-180, 2004.

100 Kwun, H. and Bartels, K., Experimental Observation of Wave Dispersion in Cylindrical Shells via Time-Frequency Analysis. *The Journal of the Acoustical Society of America*, 97(6), pp.3905-3907, 1995.

101 Zemanek, J. and Rudnick, I., Attenuation and Dispersion of Elastic Waves in a Cylindrical Bar. *The Journal of the Acoustical Society of America*, 33(10), pp.1283-1288, 1961.

102 O'Donnell, M., Jaynes, E. and Miller, J., Kramers–Kronig Relationship between Ultrasonic Attenuation and Phase Velocity. *The Journal of the Acoustical Society of America*, 69(3), pp.696-701, 1981.

103 Long, R., Vogt, T., Lowe, M. and Cawley, P., Measurement of Acoustic Properties of Near-Surface Soils Using an Ultrasonic Waveguide. *GEOPHYSICS*, 69(2), pp.460-465, 2004.

104 Rayleigh, L., The Problem of the Whispering Gallery, In Scientific Papers, *Cambridge University, Cambridge*, 5, pp.617–620, 1912.

105 Demma A., Cawley P. and Lowe S., Mode Conversion of Longitudinal and Torsional Guided Modes Due to Pipe Bends, *Review of Progress in Quantitative Nondestructive Evaluation,* 20, pp.172–179, 2001.

106 Demma, A., Cawley, P., Lowe, M. and Pavlakovic, B., The Effect of Bends on the Propagation of Guided Waves in Pipes. *Journal of Pressure Vessel Technology*, 127(3), pp.328-335, 2005.

107 Nishino, H., Yoshida, K., Cho, H. and Takemoto, M., Propagation Phenomena of Wideband Guided Waves in a Bended Pipe. *Ultrasonics*, 44, pp.e1139-e1143, 2006.

108 Sanderson, R., Hutchins, D., Billson, D. and Mudge, P., The Investigation of Guided Wave Propagation around a Pipe Bend Using an Analytical Modeling Approach. *The Journal of the Acoustical Society of America*, 133(3), pp.1404-1414, 2013.

109 Baik, J. and Thompson, R., Ultrasonic Scattering from Imperfect Interfaces: A Quasi-Static Model. *Journal of Nondestructive Evaluation*, 4(3-4), pp.177-196, 1984.

110 Alleyne, D. and Cawley, P., The Interaction of Lamb Waves with Defects. *IEEE Transactions on Ultrasonics, Ferroelectrics and Frequency Control*, 39(3), pp.381-397, 1992.

111 Alleyne, D. and Cawley, P., The Long Range Detection of Corrosion in Pipes Using Lamb Waves, *Review of Progress in Quantitative Nondestructive Evaluation*, New York: Plenum Press, pp.2073-2080, 1995.

112 Sun, F., Sun, Z., Chen, Q., Murayama, R. and Nishino, H., Mode Conversion Behavior of Guided Wave in a Pipe Inspection System Based on a Long Waveguide. *Sensors*, 16(10), p.1737, 2016.

113 Torvik, P., Reflection of Wave Trains in Semi-Infinite Plates. *The Journal of the Acoustical Society of America*, 41(2), pp.346-353, 1967.

114 Yu, J., Lefebvre, J., Xu, W., Benmeddour, F. and Zhang, X., Propagating and Non-Propagating Waves in Infinite Plates and Rectangular Cross Section Plates: Orthogonal Polynomial Approach. *Acta Mechanica*, 228(11), pp.3755-3769, 2017.

115 Diligint, O., *Interaction between Fundamental Lamb Modes and Defects in Plates*, PhD Thesis, Imperial College London, 2003.

116 Morvan, B., Wilkie-Chancellier, N., Duflo, H., Tinel, A. and Duclos, J., Lamb Wave Reflection at the Free Edge of a Plate. *The Journal of the Acoustical Society of America*, 113(3), pp.1417-1425, 2003.

117 Alleyne, D. and Cawley, P., The Interaction of Lamb Waves with Defects. *IEEE Transactions on Ultrasonics, Ferroelectrics and Frequency Control*, 39(3), pp.381-397, 1992.

118 Alleyne, D., Lowe, M. and Cawley, P., The Reflection of Guided Waves from Circumferential Notches in Pipes. *Journal of Applied Mechanics*, 65(3), pp.635-641, 1998.

119 Diligent, O., Grahn, T., Boström, A., Cawley, P. and Lowe, M., The Low-Frequency Reflection and Scattering of the S0 Lamb Mode from a Circular Through-Thickness Hole in a Plate: Finite Element, Analytical and Experimental Studies. *The Journal of the Acoustical Society of America*, 112(6), pp.2589-2601, 2002.

120 Blitz, J. and Simpson, G., *Ultrasonic Methods of Non-Destructive Testing*. London: Chapman and Hall, 1996.

121 Khalili, P. and Cawley, P., Relative Ability of Wedge-Coupled Piezoelectric and Meander Coil EMAT Probes to Generate Single-Mode Lamb Waves. *IEEE Transactions on Ultrasonics, Ferroelectrics, and Frequency Control*, 65(4), pp.648-656, 2018.

122 Thurston, R. and Pierce, A., *Ultrasonic Measurement Methods*. San Diego: Academic Press, 1990.

123 Frost, H., Electromagnetic-Ultrasound Transducers: Principles, Practice, and Applications. *Physical Acoustics*, Academic, New York, 14, pp.179-275, 1979.

124 Maxfield, B. and Fortunko, C., The Design and Use of Electromagnetic Acoustic Wave Transducers (EMATs). *Materials Evaluation*, 41, p.1399, 1983.

125 Thompson, R., A Model for the Electromagnetic Generation and Detection of Rayleigh and Lamb Waves. *IEEE Transactions on Sonics and Ultrasonics*, 20(4), pp.340-346, 1973.

126 Zhichao, L., Kang, L., Shujuan, W. and Guofu, Z., Modeling and Analysis of Surface Wave EMAT and its Acoustic Field. *2010 5th IEEE Conference on Industrial Electronics and Applications*, Taichung, pp.89-93, 2010.

127 Jian, X., Dixon, S. and Edwards, R., Optimising Ultrasonic Wideband Rayleigh Wave Generation by Pulsed Electromagnetic Coils. *Nondestructive Testing and Evaluation*, 20(1), pp.43-62, 2005.

128 Hirao, M. and Ogi, H., *Electromagnetic Acoustic Transducers*. Tokyo, Springer, 2017.

129 Kwun, H. and Teller, C., Magnetostrictive Generation and Detection of Longitudinal, Torsional, and Flexural Waves in a Steel Rod. *The Journal of the Acoustical Society of America*, 96(2), pp.1202-1204, 1994.

130 Wang, Y., Wu, X., Sun, P. and Li, J., Enhancement of the Excitation Efficiency of a Torsional Wave PPM EMAT Array for Pipe Inspection by Optimizing the Element Number of the Array Based on 3-D FEM. *Sensors*, 15(2), pp.3471-3490, 2015.

131 Lieberherr, M., The Magnetic Field Lines of a Helical Coil are Not Simple Loops. *American Journal of Physics*, 78(11), pp.1117-1119, 2010.

132 Lerner, L., Magnetic Field of a Finite Solenoid with a Linear Permeable Core. *American Journal of Physics*, 79(10), pp.1030-1035, 2011.

133 Epstein, C. and Davey, K., Iron-Core Coils for Transcranial Magnetic Stimulation. *Journal of Clinical Neurophysiology*, 19(4), pp.376-381, 2002.

134 Dodd, C. and Deeds, W., Analytical Solutions to Eddy-Current Probe-Coil Problems. *Journal of Applied Physics*, 39(6), pp.2829-2838, 1968.

135 Ludwig, R. and Dai, X., Numerical Simulation of Electromagnetic Acoustic Transducer in the Time Domain. *Journal of Applied Physics*, 69(1), pp.89-98, 1991.

136 Kaltenbacher, M., Ettinger, K., Lerch, R. and Tittmann, B., Finite Element Analysis of Coupled Electromagnetic Acoustic Systems. *IEEE Transactions on Magnetics*, 35(3), pp.1610-1613, 1999.

137 Dwight, H., The Magnetic Field of a Circular Cylindrical Coil. *The London, Edinburgh, and Dublin Philosophical Magazine and Journal of Science*, 11(72), pp.948-957, 1931.

138 Garrett, M., An Elliptic Integral Computer Package for Magnetic Fields, Forces and Mutual Inductances of Axisymmetric Systems. *Oak Ridge Nat. Lab., Oakridge, TN, Tech. Rep*. ORNL-3318, 1962.

139 Rusinov, A., High Precision Computation of Solenoid Magnetic Fields by Garrett's Methods. *IEEE Transactions on Magnetics*, 30(4), pp.2685-2688, 1994.

140 Jackson, J., *Classical Electrodynamics*. New York, John Wiley, pp.168-268, 1975.

141 Weber, E., *Electromagnetic Theory*. New York, Dover, p.131, 1965.

142 Misakian, M., Equations for the Magnetic Field Produced by One or More Rectangular Loops of Wire in the Same Plane. *Journal of Research of the National Institute of Standards and Technology*, 105(4), pp.557-564, 2000.

143 Camacho, J. and Sosa, V., Alternative Method to Calculate the Magnetic Field of Permanent Magnets with Azimuthal Symmetry. *Revista Mexicana de F´ısica*, 59, pp.8-17, 2013.

144 Fabry C. and Perot, A, *Theorie et Applications D'une Nouvelle Methode de Spectroscopie Interferentielle*. Ann. Chim. Phys. 16 (7), 1899.

145 Perot, A. and Fabry, C., On the Application of Interference Phenomena to the Solution of Various Problems of Spectroscopy and Metrology. *The Astrophysical Journal*, 9, p.87, 1899.

146 Schütz M. J. A., Universal Quantum Transducers Based on Surface Acoustic Waves, *in Quantum Dots for Quantum Information Processing: Controlling and Exploiting the Quantum Dot Environment* (Springer International Publishing, Cham), pp. 143–196, 2017.

147 Xu, Y., Fu, W., Zou, C., Shen, Z. and Tang, H., High Quality Factor Surface Fabry-Perot Cavity of Acoustic Waves. *Applied Physics Letters*, 112(7), p.073505, 2018.

148 Turin, G. L., An Introduction to Matched Filters. *IRE Transactions on Information Theory*. 6 (3): 311–329, 1960.

149 Bracewell, R., *The Fourier Transform And Its Applications*. New York: McGraw-Hill, 1986.

150 Cutard, T., Fargeot, D., Gault, C. and Huger, M., Time delay and phase shift measurements for ultrasonic pulses using autocorrelation methods. *Journal of Applied Physics*, 75(4), pp.1909-1913, 1994.

151 Ho, K., Gan, T., Billson, D. and Hutchins, D., Application of Pulse Compression Signal Processing Techniques to Electromagnetic Acoustic Transducers for Noncontact Thickness Measurements and Imaging. *Review of Scientific Instruments*, 76(5), p.054902, 2005.

152 Li, F., Su, Z., Ye, L. and Meng, G., A Correlation Filtering-based Matching Pursuit (CF-MP) for Damage Identification Using Lamb Waves. *Smart Materials and Structures*, 15(6), pp.1585-1594, 2006.

153 Ziemer, R. and Tranter, W., *Principles Of Communications*. Boston, Mass. [u.a.]: Mifflin, 1988.

154 Dixon R. C., *Spread Spectrum Systems*, New York: Wiley, 1984.

155 Serrano, E. and Fabio, M., Application of the Wavelet Transform to Acoustic Emission Signals Processing. *IEEE Transactions on Signal Processing*, 44(5), pp.1270-1275, 1996.

156 Alleyne, D. N. and Cawley P., A 2-dimensional Fourier Transform Method for the Quantitative Measurement of Lamb Modes, *IEEE Symposium on Ultrasonics*, Honolulu, HI, USA, 1990.

157 Mann, S. and Haykin, S., The Chirplet Transform: A Generalization of Gabor's logon Transform, *Vision Interface* '91, p. 205–212, 1991.

158 Kuttig, H., Niethammer, M., Hurlebaus, S. and Jacobs, L., Model-based Analysis of Dispersion Curves Using Chirplets. *The Journal of the Acoustical Society of America*, 119(4), pp.2122-2130, 2006.T.

159 Koulakiotis, D. and Aghvami, A., Data Detection Techniques for DS/CDMA Mobile Systems: a Review. *IEEE Personal Communications*, 7(3), pp.24-34, 2000.

160 Golomb, S. and Scholtz, R., Generalized Barker Sequences. *IEEE Transactions on Information Theory*, 11(4), pp.533-537, 1965.

161 Chu, D., Polyphase Codes with Good Periodic Correlation Properties (Corresp.). *IEEE Transactions on Information Theory*, 18(4), pp.531-532, 1972.

162 Cohen, M., Fox, M. and Baden, J., Minimum Peak Sidelobes Pulse Compression Codes. *Proc. IEEE Int. Radar Conf.*, pp.633-638, 1990.

163 Lindner, J., Binary Sequences up to Length 40 with Best Possible Autocorrelation Function. *Electronics Letters*, 11(21), p.507, 1975.

164 Lewis, B., Kretschmer, F. and Shelton, W., *Aspects of Radar Signal Processing*. Norwood, MA: Artech House, 1986.

165 Gartz, K., Generation of Uniform Amplitude Complex Code Sets with Low Correlation Sidelobes. *IEEE Transactions on Signal Processing*, 40(2), pp.343-351, 1992.

166 Turyn, R., Four-Phase Barker Codes. *IEEE Transactions on Information Theory*, 20(3), pp.366-371, 1974.

167 Dinan, E. and Jabbari, B., Spreading Codes for Direct Sequence CDMA and Wideband CDMA Cellular Networks. *IEEE Communications Magazine*, 36(9), pp.48-54, 1998.

168 Ziani, A., Medouri, A. and Essaaidi, M., Performance Comparison of Pseudo-Random and Orthogonal Spreading Sequences. *International Journal of Engineering and Innovative Technology (IJEIT)*, 4(12), 2015.

169 Barker, R., Group Synchronizing of Binary Digital Systems, Communication Theory. *Academic Press, Inc*, New York, pp.273-287, 1953.

170 Golay, M. Multi-Slit Spectrometry. *Journal of The Optical Society of America*, *39*(6), pp.437, 1949.

171 Golay, M. Complementary Series. *IEEE Transactions on Information Theory*, *7*(2), pp.82-87, 1961.

172 Parker, M.G., Paterson, K.G., Tellambura, C. Golay Complementary Sequences. *Wiley Encyclopedia of Telecommunications*, *John Wiley and Sons*, Hoboken, NJ, 2003.

173 Borwein, P., & Ferguson, R. A Complete Description of Golay Pairs for Lengths Up to 100. *Mathematics of Computation*, *73*(246), pp.967-985, 2003.

174 Ochiai, H., & Imai, H. Block Coding Scheme Based on Complementary Sequences for Multicarrier Signals. *IEICE Transactions on Fundamentals of Electronics, Communications and Computer Sciences, 80*, pp.2136-2143, 1997.

175 Shu-Ming Tseng, & Bell, M. Asynchronous Multicarrier DS-CDMA Using Mutually Orthogonal Complementary Sets of Sequences. *IEEE Transactions on Communications*, *48*(1), pp.53-59, 2000.

176 White, J.D.H., Challis, R.E. A Golay Sequencer Based NDT System for Highly Attenuating Materials. *IEE Coll. on Non-Contacting and Remote NDT*, London, Nov. 10, 1992.

177 Mienkina, M., Friedrich, C., Gerhardt, N., Wilkening, W., Hofmann, M., & Schmitz, G. Experimental Evaluation of Photoacoustic Coded Excitation Using Unipolar Golay Codes. *IEEE Transactions on Ultrasonics, Ferroelectrics and Frequency Control*, *57*(7), pp.1583-1593, 2010.

178 Tseng, C.C., Liu, C.L. Complementary Sets of Sequences. *IEEE Trans. Inf. Theory,* 18, pp.644–652, 1972.

179 Suehiro, N., & Hatori, M. N-Shift Cross-Orthogonal Sequences. *IEEE Transactions on Information Theory*, *34*(1), pp.143-146, 1988.

180 Shull, P. *Nondestructive Evaluation: Theory, Techniques, and Applications*. New York, NY: Marcel Dekker, Inc., 2002.

181 Worden, K., Farrar, C., Manson, G., & Park, G. The Fundamental Axioms of Structural Health Monitoring. *Proceedings of the Royal Society a Mathematical, Physical and Engineering Sciences*, 463(2082), pp.1639-1664, 2007.

182 Sohn, H., Wait, J., Park, G. & Farrar, C. Multi-Scale Structural Health Monitoring for Composite Structures. Composite Structures. *In Proc. 2nd Eur. Workshop on Structural Health Monitoring*, Munich, Germany, 2004.

183 Wilcox, P., Evans, M., Pavlakovic, B., Alleyne, D., Vine, K., Cawley, P., & Lowe, M. Guided Wave Testing of Rail. *Insight - Non-Destructive Testing and Condition* Monitoring, 45(6), pp.413-420, 2003.

184 Zhuang, W., Shah, A., & Datta, S. (1997). Axisymmetric Guided Wave Scattering by Cracks in Welded Steel Pipes. *Journal of Pressure Vessel Technology,* 119(4), pp.401-406, 1997.

185 Rytter, A. Vibration based inspection of civil engineering structures. Ph.D. Dissertation, Department of Building Technology and Structural Engineering, *Aalborg University*, Denmark, 1993.

186 Croxford, A., Wilcox, P., Drinkwater, B., & Konstantinidis, G. Strategies for Guided-Wave Structural Health Monitoring. *Proceedings of the Royal Society a Mathematical, Physical and Engineering Sciences*, 463(2087), pp.2961-2981, 2007.

187 https://www.emerson.com/en-us/automation/measurement-instrumentation/corrosion-erosion-monitoring/about-rosemount-wireless-corrosion-erosion-monitoring, visited on 2/11/2021.

188 Bedworth, M., & O'Brien, J. The Omnibus Model: A New Model of Data Fusion?. *IEEE Aerospace and Electronic Systems Magazine*, 15(4), pp.30-36, 2000.

189 Page, E. Continuous Inspection Schemes. *Biometrika*, *41*(1/2), pp.100-115, 1954.

190 Willsky, A., & Jones, H. A Generalized Likelihood Ratio Approach to the Detection and Estimation of Jumps in Linear Systems. *IEEE Transactions on Automatic Control*, 21(1), pp.108-112, 1976.

191 Worden, K., & Manson, G. The Application of Machine Learning to Structural Health Monitoring. *Philosophical Transactions of the Royal Society a Mathematical, Physical and Engineering Sciences*, 365(1851), pp.515-537, 2007.

192 Turin, G. Introduction to Spread-Spectrum Antimultipath Techniques and their Application to Urban Digital Radio. *Proceedings Of The IEEE*, 68(3), pp.328-353, 1980.

193 Stojanovic, M., Catipovic, J., & Proakis, J. Adaptive Multichannel Combining and Equalization for Underwater Acoustic Communications. *The Journal of the Acoustical Society of America*, 94(3), pp.1621-1631, 1993.

194 Stojanovic, M., Freitag, L., and Johnson, M. Channel-Estimation-Based Adaptive Equalization of Underwater Acoustic Signals. *Oceans' 99. MTS/IEEE. Riding the Crest into the 21st Century. Conference and Exhibition. Conference Proceedings (IEEE Cat. No. 99CH37008)*. Vol. 2. IEEE, 1999.

195 Haykin, S. *Adaptive Filter Theory*. Upper Saddle River, NJ: Prentice-Hall, Inc., 1996.

196 Wilcox, P. A rapid signal processing technique to remove the effect of dispersion from guided wave signals. *IEEE Transactions on Ultrasonics, Ferroelectrics, and Frequency Control*, vol. 50, no. 4, pp. 419-427, 2003.

11 Appendices

11.1 Appendix 1

The MATLAB algorithm developed to implement the dispersive model of the pipe with multimode, mode conversion, reflection and attenuation effects is supplemented here.

```
clear all;
clc;
close all;
format long;

fonts1=16;
%Program to model acoustic pipe monitoring system;
%PHD Student: Aiman Noorwali
%Supervisor: R.R.A.Syms
%Imperial College London;

%Models transmission and detection of quasi orthogonal codes;
%Through system containing amplifier, EMAT, pipe and microphone;
%Propagates L(0,1), F(1,1), FC(1,1) and LC(1,1) with reflections;
%using computed data (vp, vg, and k) by PCDISP to estimate velocities;
%Polyphase codes transmitted and correlated with each other;
%Upconversion, correlation detection and downconversion all included;

%Codeset - select from set of generalised Barker QO codes;
%Can have 1, 2 or 3 codes in codeset;
codeset=3;
%Path to read PCDISP data
%(phase and group velocities and wavenumbers are extracted)
addpath('C:\xxx')

if codeset==1;
    %Uniform pulse
    B=2; M=2;
    ncodes=1; ncycles=6;
    N=[0];
end;

if codeset==2;
    %Barker
    B=2; M=5;
    ncodes=1; ncycles=2;
    N=[29];
    am=1; xm1=1; xm2=1;
end;
if codeset==3;
    %QO pair
    B=6; M=9;
    ncodes=2; ncycles=6;
    N=[8564; 1040855];
    am=M/4.5; xm1=am; xm2=am;
end;
if codeset==4;
    %QO triplet
    B=6; M=10;
    ncodes=3;ncycles=6;
    N=[5099;    918088; 989300];
   am=sqrt(7); xm1=am; xm2=am;
end;
%Signal frequency;
f=20e3;
%Input noise level;
sigma=0;
%Propagation distance;
d=24.4;
%dent distance from the RX end
dm_dnt=d-9.8;
%partial reflector distance from the RX end
dr=0;
%Component responses;
%Amplifier;
fA1=50;
fA2=300e3;
%EMAT;
fE1=5.7e3;

%Import PCDISP data for f and k;
```

```
f_k1=csvread('L01_fk.csv');
f_k2=csvread('F11_fk.csv');
%Import PCDISP data for f and vp;
f_vp1=csvread('L01_fvp.csv');
f_vp2=csvread('F11_fvp.csv');
%Import PCDISP data for f and vg;
f_vg1=csvread('L01_fvg.csv');
f_vg2=csvread('F11_fvg.csv');
%Estimate vp values at carrier frequency;
vp1=interp1(f_vp1(:,1),f_vp1(:,2),f);
vp2=interp1(f_vp2(:,1),f_vp2(:,2),f);
%Estimate vg values at carrier frequency;
vg1=interp1(f_vg1(:,1),f_vg1(:,2),f);
vg2=interp1(f_vg2(:,1),f_vg2(:,2),f);

%Estimate propagation time for L01;
tprop1=d/vg1;
%Estimate propagation time for F11;
tprop2=d/vg2;
%Estimate propagation time for L01->F11;
tprop12=(d-dm_dnt)/vg1 + dm_dnt/vg2;
%Estimate propagation time for F11->L01;
tprop21=(d-dm_dnt)/vg2 + dm_dnt/vg1;

%Microphone transfer function;
fM1=300;
%fM2=17.5e3;
fM2=18.5e3;

%Plotting parameters for transfer functions;
%Maximum and minimum values for signals etc;
max_sig_in=1.1;
max_sig_out=1.1;
startsig=-1;
stopsig=40;

%FFT parameters;
%Number of samples per cycle;
nsamp=16*2;
%Sampling frequency;
Fs = f*nsamp;
%Sampling period;
T = 1/Fs;
%Total number of samples;
L = nsamp*1024*7;
%Length of moving average filter;
nwindow=nsamp/2;
%Length of auto- and cross-correlations;
LC=2*L-1;
%Length of filtered auto- and cross-correlations;
LF=LC+nwindow-1;
%Moving average filter;
filt=ones(1,nwindow)*pi/(2*nwindow);

%Transmission parameters;
%Time per chip;
tbit=ncycles/f;
%Total number of cycles;
cycles=ncycles*M;
%Time offset for signal start;
timeshift=8*tbit/ncycles;
%Time vector for signals
t=linspace(0,(L-1)*T,L)-timeshift;
%Time vector for auto- and cross-correlations;
t2=linspace(0,(LC-1)*T,LC);
%Time vector for filtered correlations;
t3=linspace(0,(LF-1)*T,LF);

%Allocate arrays;
E=zeros(ncodes,L);
C=zeros(ncodes,L);
S=zeros(ncodes,L);
X=zeros(ncodes,L);
Y=zeros(ncodes,L);
Z=zeros(ncodes,L);

Exc=zeros(ncodes,ncodes,LC);
Sxc=zeros(ncodes,ncodes,LC);
FSxc=zeros(ncodes,ncodes,LF);

U1=zeros(ncodes,L);
```

```
U2=zeros(ncodes,L);
U1_m1tr=zeros(ncodes,L);
U2_m1tr=zeros(ncodes,L);
U12=zeros(ncodes,L);
U21=zeros(ncodes,L);
U=zeros(ncodes,L);

V1=zeros(ncodes,L);
V2=zeros(ncodes,L);
V1_m1tr=zeros(ncodes,L);
V2_m1tr=zeros(ncodes,L);
V12=zeros(ncodes,L);
V21=zeros(ncodes,L);
V=zeros(ncodes,L);

W1=zeros(ncodes,L);
W2=zeros(ncodes,L);
W1_m1tr=zeros(ncodes,L);
W2_m1tr=zeros(ncodes,L);
W12=zeros(ncodes,L);
W21=zeros(ncodes,L);
W=zeros(ncodes,L);

VSxc1=zeros(ncodes,ncodes,LC);
VSxc2=zeros(ncodes,ncodes,LC);
VSxc1_m1tr=zeros(ncodes,ncodes,LC);
VSxc2_m1tr=zeros(ncodes,ncodes,LC);
VSxc12=zeros(ncodes,ncodes,LC);
VSxc21=zeros(ncodes,ncodes,LC);
VSxc=zeros(ncodes,ncodes,LC);

FVSxc1=zeros(ncodes,ncodes,LF);
FVSxc2=zeros(ncodes,ncodes,LF);
FVSxc1_m1tr=zeros(ncodes,ncodes,LF);
FVSxc2_m1tr=zeros(ncodes,ncodes,LF);
FVSxc12=zeros(ncodes,ncodes,LF);
FVSxc21=zeros(ncodes,ncodes,LF);
FVSxc=zeros(ncodes,ncodes,LF);

%Plotting parameters for time responses;
%Time start and end for plotting;
tstart=-timeshift;
tend=tbit*M+timeshift;
%Start and stop for time responses before transmission;
start0=tstart*1000;
stop0=tend*1000;
%Total time duration;
TD=L*T;

%Construct polyphase codes
Nbase=dec2base(N,B,M);
Nnum=zeros(ncodes,M);
    for i=1:ncodes
        for m=1:M;
            Nnum(i,m)=str2double(Nbase(i,m:m));
        end;
    end;
codes=exp(1j*2*pi*Nnum/B);


%Construct complex signals;
for k=1:ncodes
    for i=1:L
        tau=(i-1)*T-timeshift;
        bitnum=fix(1+tau/tbit);
        if bitnum>0;
            if bitnum<=M;
                %Envelope;
                E(k,i)=codes(k,bitnum);
                %Signal with sine carrier;
                S(k,i) = exp(1j*(2*pi*f*(tau-timeshift)-pi/2))*codes(k,bitnum);
            end;
        end;
    end;
end;

%%%%%%%%% Add non-linearity if needed %%%%%%%%%%%%%%%
%NLC=16
%S = S + (NLC.*(S.^2));
%%%%%%%%%%%%%%%%%%%%%%%%%%%%%%%%%%%%%%%%%%%%%%%%%%%%
%Add noise if needed;
```

```
X = S + sigma*(rand(ncodes,L))+1j*sigma*(rand(ncodes,L));
snr1=1000;
X = awgn(S,snr1);
Ns=X-S;
snrin=snr(S,Ns)
%Auto- and cross-correlations of envelopes before transmission;
for i=1:ncodes
    for j=1:ncodes
        %NB need to scale envelope by factor of 2 to agree with signal;
        Exc(i,j,:)=abs(xcorr(real(E(i,:)),real(E(j,:))))/2;
        Sxc(i,j,:)=abs(xcorr(real(S(i,:)),real(S(j,:))));
    end;
end;
max_Ecorr=max(max(max(Exc)));
%max_Ecorr=1;
%Downconvert auto- and cross-correlations of signals before transmission;
for i=1:ncodes
    for j=1:ncodes
        FSxc(i,j,:)=conv(squeeze(Sxc(i,j,:)),filt);
    end;
end;

%Frequencies for single-sided and double-sided spectra;
F_sing = Fs*(0:(L/2))/L;
F_doub =[-fliplr(F_sing(2:end-1)),F_sing];

%FFTs;
for i=1:ncodes
    Y(i,:)=fft(X(i,:));
end;
%Spectra of initial signals;
YM_doub = abs(Y/L);
%Single-sided spectra of initial signal;
YM_sing = YM_doub(:,1:L/2+1);
YM_sing(:,2:end-1) = 2*YM_sing(:,2:end-1);

%Shift FFT to form full spectra;
for i=1:ncodes;
    Z(i,:)=fftshift(Y(i,:));
end

%Amplifier transfer functions;
TF_AMP_doub=1j*(F_doub/fA1)./((1+1j*F_doub/fA1).*(1+1j*F_doub/fA2).^2);

%EMAT transfer function;
TF_EMAT_doub=1j*(F_doub/fE1)./(1+1j*(F_doub/fE1));

%Channel transfer function;
%Interpolate vp and vg data;
vp1_sing=interp1(f_vp1(:,1).',f_vp1(:,2).',F_sing);
vp2_sing=interp1(f_vp2(:,1).',f_vp2(:,2).',F_sing);
vg1_sing=interp1(f_vg1(:,1).',f_vg1(:,2).',F_sing);
vg2_sing=interp1(f_vg2(:,1).',f_vg2(:,2).',F_sing);

%Construct values for L01->F11;
vp12_sing=1./((1-dm_dnt/d)./vp1_sing+(dm_dnt/d)./vp2_sing);
vg12_sing=1./((1-dm_dnt/d)./vg1_sing+(dm_dnt/d)./vg2_sing);
%Construct values for F11->L01;
vp21_sing=1./((1-dm_dnt/d)./vp2_sing+(dm_dnt/d)./vp1_sing);
vg21_sing=1./((1-dm_dnt/d)./vg2_sing+(dm_dnt/d)./vg1_sing);

%Construct double sided f-k data for L01 mode and interpolate;
f_k1=[-flipud(f_k1);
              f_k1];
k_doub1=interp1(f_k1(:,1).',f_k1(:,2).',F_doub,'linear','extrap');
%Construct double sided f-k data for F11 mode and interpolate;
f_k2=[-flipud(f_k2);
              f_k2];
k_doub2=interp1(f_k2(:,1).',f_k2(:,2).',F_doub,'linear','extrap');

%%%%attenuation%%%%
Latt=0.012;
Fatt=0.067;
%%%%%%%%%%%%%%%%%%
%Construct transfer function for L01;
AL01=1;
%TF_CH_double=AL01.*exp(-1j*k_doub1*d); %If no end reflections
TF_CH_double = (AL01.*exp(-1j*k_doub1*d).*exp(-Latt*d))./(1 - (AL01^2).*(exp(-2*1j*k_doub1*d).*exp(-Latt*d)));
%%%%%%%%%%
%Construct transfer function for F11;
AF11=0.35;
```

```
%TF_CH_double2=AF11*exp(-1j*k_doub2*d); %If no end reflections
TF_CH_double2 = (AF11.*exp(-1j*k_doub2*d).*exp(-Fatt*d))./(1 - (AF11^2).*(exp(-2*1j*k_doub2*d).*exp(-Fatt*d)));

%%%%%%%%%% mode conversion by dent %%%%%%%%%%%%%%%
%Construct transfer function for mode conversion from pipe dent L01->F11;
AF1dnt=0.19;
%odd
TF_CH_double12_dnt1 = (AF1dnt.*exp(-1j*k_doub1*(d-dm_dnt)).*exp(-1j*k_doub2*dm_dnt).*exp(-Latt*(d-
dm_dnt)).*exp(-Fatt*(dm_dnt))./(1 - (exp(-2*1j*k_doub2*d).*exp(-Fatt*d))).*(1./(1 - (AL01^2).*(exp(-
2*1j*k_doub1*d).*exp(-Latt*d))));
%even
TF_CH_double12_dnt2 = (AF1dnt.*AL01.*exp(-1j*k_doub1*(2*d-(d-dm_dnt))).*exp(-1j*k_doub2*((d+(d-
dm_dnt)))).*exp(-Latt*(2*d-(d-dm_dnt))).*exp(-Fatt*(d+dm_dnt)))./(1 - (exp(-2*1j*k_doub2*d).*exp(-
Fatt*d))).*(1./(1 - (AL01^2).*(exp(-2*1j*k_doub1*d).*exp(-Latt*d))));
%sum
TF_CH_double12_dnt=TF_CH_double12_dnt1+TF_CH_double12_dnt2;

%Construct transfer function for mode conversion from pipe dent F11->L01;
AF2dnt=0.19;
%odd
TF_CH_double21_dnt1 = (AF2dnt.*exp(-1j*k_doub2*(d-dm_dnt)).*exp(-1j*k_doub1*dm_dnt).*exp(-Fatt*(d-
dm_dnt)).*exp(-Latt*(dm_dnt)))./(1 - (exp(-2*1j*k_doub1*d).*exp(-Latt*d))).*(1./(1 - (AF11^2).*(exp(-
2*1j*k_doub2*d).*exp(-Fatt*d))));
%even
TF_CH_double21_dnt2 = (AF2dnt.*AF11.*exp(-1j*k_doub2*(2*d-(d-dm_dnt))).*exp(-1j*k_doub1*(dm_dnt)).*exp(-
Fatt*(2*d-(d-dm_dnt))).*exp(-Latt*(dm_dnt)))./(1 - (exp(-2*1j*k_doub1*d).*exp(-Latt*d))).*(1./(1 -
(AF11^2).*(exp(-2*1j*k_doub2*d).*exp(-Fatt*d))));
%sum
TF_CH_double21_dnt=TF_CH_double21_dnt1+TF_CH_double21_dnt2;

%%%%%Inserting partial reflectors
AFrf=0.4; %L01 partial reflection amplitude
%Coefficients by the reflector
Rm = -1j*0.5;
Tm = sqrt(1 - abs(Rm)^2);
%Construct transfer function for first L01 partial reflector;
TF_CH_double12_ref = (Tm*AFrf*exp(-1j*k_doub1*(d-dr)).*exp(-1j*k_doub2*dr))./(1 - (Rm.*exp(-1j*2*k_doub1*(d-
dr)).*exp(-1j*2*k_doub2*dr))).*exp(-Latt*(d-dr)).*exp(-Fatt*dr);

%%%%%%%%%%%%%%%%%%%%%%%%%%%%%%%
%Microphone transfer function;
TF_MICR_doub=1j*(F_doub/fM1) .^2 ./ ( (1+1j*(F_doub/fM1)) .^2 .* (1+1j*(F_doub/fM2)).^2);
%TF_MICR_doub=ones(size(F_doub)); %displess
%Overall transfer function for L01;
TF_doub1=TF_AMP_doub.*TF_EMAT_doub.*TF_MICR_doub.*TF_CH_double;
%TF_REF_doub1=TF_AMP_doub.*TF_EMAT_doub.*TF_REF_double1.*TF_MICR_doub; %ref

%Overall transfer function for F11;
TF_doub2=TF_AMP_doub.*TF_EMAT_doub.*TF_CH_double2.*TF_MICR_doub;
%Overall transfer function for mode conversion from dent L01->F11;
TF_doub12_dnt=TF_AMP_doub.*TF_EMAT_doub.*TF_CH_double12_dnt.*TF_MICR_doub;
%Overall transfer function for mode conversion from dent F11->L01;
TF_doub21_dnt=TF_AMP_doub.*TF_EMAT_doub.*TF_CH_double21_dnt.*TF_MICR_doub;
%Overall transfer function for first L01 reflection;
TF_doub12_ref=TF_AMP_doub.*TF_EMAT_doub.*TF_CH_double12_ref.*TF_MICR_doub;

%Single-sided transfer functions for plotting;
TF_AMP_sing=TF_AMP_doub(L/2:end);
TF_EMAT_sing=TF_EMAT_doub(L/2:end);
%VPH_sing=VPH(L/2:end);
TF_CH_sing=TF_CH_double(L/2:end);
TF_MICR_sing=TF_MICR_doub(L/2:end);
TF_sing=TF_doub1(L/2:end);

%Multiply FFTs by system transfer function;
for i=1:ncodes;
    W1(i,:)=Z(i,:).*TF_doub1;
    W2(i,:)=Z(i,:).*TF_doub2;
    W1_dnt12(i,:)=Z(i,:).*TF_doub12_dnt; %md L->F
    W1_dnt21(i,:)=Z(i,:).*TF_doub21_dnt; %md F->L
    W12_ref(i,:)=Z(i,:).*TF_doub12_ref; %reflections

    W(i,:)=W1(i,:)+W2(i,:)+W1_dnt12(i,:)+W12_ref(i,:); %dent with reflection
end;

%Shift back;
for i=1:ncodes;
    U1(i,:)=ifftshift(W1(i,:));
    U2(i,:)=ifftshift(W2(i,:));
    U12(i,:)=ifftshift(W12(i,:));
    U21(i,:)=ifftshift(W21(i,:));
```

```
    U(i,:)=ifftshift(W(i,:));
end;

%Single-sided spectra;
UM_sing1 = abs(U1(:,1:L/2+1))/L;
UM_sing1(:,2:end-1) = 2*UM_sing1(:,2:end-1);
UM_sing2 = abs(U2(:,1:L/2+1))/L;
UM_sing2(:,2:end-1) = 2*UM_sing2(:,2:end-1);

UM_sing12 = abs(U12(:,1:L/2+1))/L;
UM_sing12(:,2:end-1) = 2*UM_sing12(:,2:end-1);
UM_sing21 = abs(U21(:,1:L/2+1))/L;
UM_sing21(:,2:end-1) = 2*UM_sing21(:,2:end-1);

UM_sing = abs(U(:,1:L/2+1))/L;
UM_sing(:,2:end-1) = 2*UM_sing(:,2:end-1);

%Inverse FFT to find time responses after transmission;
for i=1:ncodes;
    V1(i,:)=ifft(U1(i,:));
    V2(i,:)=ifft(U2(i,:));
    V12(i,:)=ifft(U12(i,:));
    V21(i,:)=ifft(U21(i,:));
    V(i,:)=ifft(U(i,:));
    %normalize
    V(i,:)=real(V(i,:))./max(real(V(i,:)));

end;

%Auto- and cross-correlations after transmission;
for i=1:ncodes
    for j=1:ncodes
        VSxc1(i,j,:)=abs(xcorr(real(V1(i,:)),real(S(j,:))));
        VSxc2(i,j,:)=abs(xcorr(real(V2(i,:)),real(S(j,:))));
        VSxc12(i,j,:)=abs(xcorr(real(V12(i,:)),real(S(j,:))));
        VSxc21(i,j,:)=abs(xcorr(real(V21(i,:)),real(S(j,:))));
        VSxc(i,j,:)=abs(xcorr(real(V(i,:)),real(S(j,:))));
    end;
end;
%Downconvert auto- and cross-correlations after transmission;
for i=1:ncodes
    for j=1:ncodes
        FVSxc1(i,j,:)=conv(squeeze(VSxc1(i,j,:)),filt);
        FVSxc2(i,j,:)=conv(squeeze(VSxc2(i,j,:)),filt);
        FVSxc12(i,j,:)=conv(squeeze(VSxc12(i,j,:)),filt);
        FVSxc21(i,j,:)=conv(squeeze(VSxc21(i,j,:)),filt);
        FVSxc(i,j,:)=conv(squeeze(VSxc(i,j,:)),filt);
    end;
end;

%%%%%%%%%%%%%%%%%%%%%%%%%%%%%%%%%%%%%%%%%%%%%%%%%%%%%%%%%%%%%%%%%%%%%%%
%%%%%%%%%%%%%%%%%%%%%%%%PLOTS%%%%%%%%%%%%%%%%%%%%%%%%%%%%%%%%%%%%%%%%%
%transmitted and recieved signal plots
    figure('Position', [0,10,450*ncodes,450]);
for i=1:ncodes
    %Signals and envelopes before transmission;
    subplot(2,ncodes,i);
    p=plot(t*1000,real(S(i,:)));
    set(p,'Color','black','LineWidth',2);
    hold on;
    if B==2;
        p=plot(t*1000,E(i,:));
        set(p,'Color','red','LineWidth',2);
    end;
    axis([-1 40 -max_sig_in max_sig_in]);
    %axis([-0.2 0.8 -max_sig_in max_sig_in]);
    set(gca,'Fontname','Times','FontSize',fonts1,'FontWeight','bold','LineWidth',2);
    xlabel('t (ms)','Fontname','Times','Fontsize',fonts1,'Fontweight','bold');
    ylabel('S_i_n(t)','Fontname','Times','Fontsize',fonts1,'Fontweight','bold');
    if i==1;
        params0=['d = ',num2str(d),' m; dm = ',num2str(d-dm_dnt),' m'];
        params1=['f = ',num2str(f/1000),' kHz','; cyc/chip = ',num2str(ncycles),'; ',params0];
        title(params1,'Fontname','Times','Fontsize',fonts1,'Fontweight','bold');
    end;
    if i==2;
        params2=['d = ',num2str(d),' m; dm_dnt = ',num2str(dm_dnt),' m'];
        title(params2,'Fontname','Times','Fontsize',fonts1,'Fontweight','bold');
    end;
    set(gcf,'color','w');
    %Signals after transmission;
    subplot(2,ncodes,i+ncodes);
```

```
        p=plot((t*1000),real(V(i,:)));
        set(p,'Color','black','LineWidth',2);
    hold on;
    %axis([startsig stopsig -max_sig_out max_sig_out]);
    axis([-1 40 -max_sig_out max_sig_out]);
    %axis([23.1 25.5 -max_sig_out max_sig_out]);
    set(gca,'Fontname','Times','FontSize',fonts1,'FontWeight','bold','LineWidth',2);
    xlabel('t (ms)','Fontname','Times','Fontsize',fonts1,'Fontweight','bold');
    ylabel('S_o_u_t(t)','Fontname','Times','Fontsize',fonts1,'Fontweight','bold');
    TITLE=['RX, B = ',num2str(B),'; M = ',num2str(M),'; N1 = ', num2str(N(i,1))];
    title(TITLE,'Fontname','Times','Fontsize',fonts1,'Fontweight','bold');
    %title(params9,'Fontname','Times','Fontsize',fonts1,'Fontweight','bold');
    set(gcf,'color','w');
end;


%%%%Correlation Detection plot%%%%
figure('Position', [0,50,450*ncodes,225*ncodes]);
for i=1:ncodes
    for j=1:ncodes
        plotnum=j+ncodes*(i-1);
        subplot(ncodes,ncodes,plotnum);
                if i==j;
            p=plot((t3-TD)*1000,squeeze(FVSxc(i,j,:))/(max_Ecorr));
            set(p,'Color','black','LineWidth',2);
                else
            p=plot((t3-TD)*1000,squeeze(FVSxc(i,j,:))/max(FVSxc(2,2,:)));
            set(p,'Color','black','LineWidth',2);
                end;
        %%%%%%MARKERS%%%%%%%%%%
        vgL01=3.780e3;
        vgF11=1.780e3;
        tpropvectL01=ones(1,2)*d/vgL01;
        tpropvectF11=ones(1,2)*d/vgF11;
        mpropvect=linspace(0,1,2);
        lwidth=1;
        %L01
        hold on;
        p1=plot(tpropvectL01*1000,mpropvect,'-.');
        set(p1,'Color','b','LineWidth',lwidth);
        hold on;
        p=plot(3*tpropvectL01*1000,mpropvect,'-.');
        set(p,'Color','b','LineWidth',lwidth);
        hold on;
        p=plot(5*tpropvectL01*1000,mpropvect,'-.');
        set(p,'Color','b','LineWidth',lwidth);
        hold on;
        p=plot(7*tpropvectL01*1000,mpropvect,'-.');
        set(p,'Color','b','LineWidth',lwidth);
        %F11
        hold on;
        p2=plot(tpropvectF11*1000,mpropvect,'-.');
        set(p2,'Color','g','LineWidth',lwidth);
        hold on;
        p=plot(3*tpropvectF11*1000,mpropvect,'-.');
        set(p,'Color','g','LineWidth',lwidth);
        %markers of the dent
        %md L01 -> F11
        hold on;
        %odd
        dent=ones(1,2)*(((d-dm_dnt)/vgL01)+(dm_dnt)/vgF11); %odd
        p=plot(dent*1000,mpropvect,'-.');
        set(p,'Color','m','LineWidth',lwidth);
        %even
        hold on;
        dent=ones(1,2)*(((d+dm_dnt)/vgL01)+(2*d-dm_dnt)/vgF11); %even
        p=plot(dent*1000,mpropvect,'-.');
        set(p,'Color','m','LineWidth',lwidth);
        axis([0 50 0 1]);
        set(gca,'Fontname','Times','FontSize',fonts1,'FontWeight','bold','LineWidth',2);
        xlabel('t (ms)','Fontname','Times','Fontsize',fonts1,'Fontweight','bold');
        ylabel('Envelope','Fontname','Times','Fontsize',fonts1,'Fontweight','bold');
        TITLE=['Correlation, f=',num2str(f/1000),'kHz; d=',num2str(d),'m; dr=',num2str(dr),'m'];
        title(TITLE,'Fontname','Times','Fontsize',fonts1,'Fontweight','bold');
        set(gcf,'color','w');
    end
end
```

11.2 Appendix 2

The MATLAB algorithm developed to search numerically for pairs and triplets of QO polyphase Barker-type codes, that satisfy specified criteria for the maximum absolute cross-correlation and maximum absolute autocorrelation side lobes, is supplemented here.

```
clear all;
clc;
close all;
format long;
tic;
%Program to find generalized Barker codes (pairs and triplets);
%PHD Student: Aiman Noorwali
%Supervisor: R.R.A.Syms
%Imperial College London;

%Select Base (B), Code length (M) and allowed autocorrelation (AM)
%NB Scaling of run-time increases very rapidly with B and M
%Define base;
B=3
%Define length;
M=2
%Define thresholds for selection;
AM=2
ratio=M/AM
%Error margin - needed for numerical reasons;
tol=1e-10;
AM=AM+tol;
%Set search range
Nmax=B^M
limit=50000;
if Nmax>limit
    Nmax=limit;
end
%Generate elementary codes
for i=0:B-1
    cn(i+1,1)=exp(1j*2*pi*i/B);
end

%Generate codes and select on the basis of auto-correlations;
num_singles_OK=0;
for N0=0:Nmax-1
    Nbase=dec2base(N0,B,M);
    for m=1:M
        Nnum=str2num(Nbase(m:m));
        c0(m,1)=cn(Nnum+1,1);
    end
    ac=abs(xcorr(c0,c0));
    if max(ac(1:M-1,1))<AM
        num_singles_OK=num_singles_OK+1;
        code_singles(num_singles_OK,1)=N0;
        C(num_singles_OK,:)=c0;
    end
end
num_singles_OK

%Select further on the basis of cross-correlations;
num_pairs_OK=0;
num_triple_OK=0;
if num_singles_OK>2
    for NA=1:num_singles_OK-2
     if NA <= num_singles_OK
        N1=code_singles(NA,1);
        c1=C(NA,:);
        for NB=NA+1:num_singles_OK-1
            N2=code_singles(NB,1);
            c2=C(NB,:);
            xc=abs(xcorr(c1,c2));
            if max(xc)<AM
                num_pairs_OK=num_pairs_OK+1
                pair=[N1, N2]
                %return
                for NC=NB+1:num_singles_OK
```

```
                    N3=code_singles(NC,1);
                    c3=C(NC,:);
                    xc13=abs(xcorr(c1,c3));
                    if max(xc13)<AM
                        xc23=abs(xcorr(c2,c3));
                        if max(xc23)<AM
                            triple=[N1, N2, N3]
                            num_triple_OK=num_triple_OK+1;
                            return
                        end
                    end
                end
            end
        end
    end
  end
end
toc
```